

**Direct Synthesis of Few-layer 2D Transition Metal
Dichalcogenides by Mist CVD and Their Application to
MOSFET and Photovoltaic Devices**

ミスト **CVD** 法による 2D 遷移金属ダイカルコゲナイド極
薄層の直接合成と **MOSFET** および太陽電池への応用



*A Dissertation Submitted to the Graduate School of Science and
Engineering of Saitama University in Partial Fulfillment of the
Requirements for the Degree Doctor of Philosophy*

By

Abdul Kuddus

Recommended for the Acceptance by the Department of
Functional Materials Science

Supervisor: Hajime Shirai

September 2022

© *Copyright by Abdul Kuddus, 2022*

All Rights Reserved

Dedicated to my beloved

Father and Mother

MD AFJAL HOSSEN AND KULSUM BIBI

DECLARATION

This thesis is the result of my work and includes nothing which is the outcome of work done by other contributor(s). It is not substantially the same as any that I have submitted for a degree or diploma or other qualification at the Saitama University or any other University or similar institution. I further state that no substantial part of my thesis has already been submitted, or is being concurrently submitted for any such degree, or other qualification at the Saitama University or any other University.

Abdul Kuddus

September, 2022

ABSTRACT

The direct synthesis of submillimeter-sized mono/few-layer 2D transition metal dichalcogenide such as molybdenum disulfide (MoS_2), tungsten disulfide (WS_2), and tungsten sulphoselenide ($\text{WS}_{0.3}\text{Se}_{1.7}$) on high- κ amorphous aluminum titanium oxide ($\text{a-Al}_{0.74}\text{Ti}_{0.26}\text{O}_y$)/ p^+ -Si substrates by mist CVD has been investigated and applied in metal-oxide-semiconductor field effect transistors (MOSFETs), complementary metal-oxide-semiconductor logic circuit (CMOS), and photovoltaic devices. The deposition of atomic mono/bilayer MoS_2 and $\text{WS}_2/\text{WS}_{0.3}\text{Se}_{1.7}$ was performed from a single precursor of $(\text{NH}_4)_2\text{MoS}_4$ and $(\text{NH}_4)_2\text{WS}_4$ respectively dissolved in N-methyl-2-pyrrolidone (NMP) by an intermittent mist supply in the closed quartz tube at different furnace temperatures, storage times of the precursor mist into the closed chamber, number of repetitions cycles, precursor concentration and sulfurization or selenization conditions as variables. Submillimeter-size few-layer MoS_2 , WS_2 , and $\text{WS}_{0.3}\text{Se}_{1.7}$ were obtained on mist CVD deposited ~ 45 nm-thick- $\text{Al}_{0.74}\text{Ti}_{0.26}\text{O}_y$ (ATO) layer by adjusting furnace temperature and the storage time of mist in the closed quartz tube with no use of alkali halide salt or seed layer. The synthesized atomic mono/bilayer MoS_2 , WS_2 , and $\text{WS}_{0.3}\text{Se}_{1.7}$ were applied as a channel layer in FETs. The MoS_2 and WS_2 channel FETs with gold source/drain electrodes showed n-type behaviors, while p-type behavior by $\text{WS}_{0.3}\text{Se}_{1.7}$ channel FET with platinum source/drain electrodes. A consistent manufacturing technique for both channel and gate insulating layers was applied using transition metal dichalcogenide atomic mono/bilayer WS_2 and $\text{WS}_{0.3}\text{Se}_{1.7}$, and thin high- κ $\text{Al}_{0.74}\text{Ti}_{0.26}\text{O}_y$ layers in field-effect transistors as well as a complementary metal-oxide-semiconductor logic circuit by mist CVD.

Further, the carrier transport properties of the few-layer $\text{WS}_{0.3}\text{Se}_{1.7}/(\text{WO}_x)\text{WS}_{0.3}\text{Se}_{1.7}$ channel FETs and the photovoltaic effect of $\text{WS}_{0.3}\text{Se}_{1.7}/(\text{WO}_x)\text{WS}_{0.3}\text{Se}_{1.7}$ lateral $\text{p}^+\text{-n}$ junction via field-effect transistor structures has been investigated. The $\text{p}^+\text{-n}$ lateral junction was formed on the few layers $\text{WS}_{0.3}\text{Se}_{1.7}$ by a combination of the O_2/He plasma and laser irradiations with different excitation wavelengths using a metal mask. A combination of O_2/He plasma and the shorter wavelength of 420 nm (0.1mW) laser irradiation provided the promoted generation of WO_x -related defects, results in an oxidation of top $\text{WS}_{0.3}\text{Se}_{1.7}$ layers. The FETs with $\text{WS}_{0.3}\text{Se}_{1.7}/\text{WO}_x$ lateral $\text{p}^+\text{-n}$ junction channel layer and asymmetrical Au and Pt source/drain electrodes showed a unipolar p-channel behavior from ambipolar owing to the strong hole doping from high affinity WO_x layer to the underneath $\text{WS}_{0.3}\text{Se}_{1.7}$ by plasma/laser oxidation. They also show a photovoltaic effect with a short-circuit current (I_{sc}) of an order of 10^{-9} A with an open-circuit voltage of 0.788 V. Further, an increase of I_{sc} of an order of several 10^{-6} A under AM1.5G solar simulator light exposure was obtained using a silver mirror back reflector sandwiched between the dielectric ($\text{Al}_{0.74}\text{Ti}_{0.26}\text{O}_y$) layer and the c-Si substrate, which was originated from the high reflectance of Ag, results in, an enhanced light absorption in $\text{WS}_{0.3}\text{Se}_{1.7}$.

ACKNOWLEDGMENTS

First, I would like to express my overwhelming gratitude to my supervisor, Professor Dr. Hajime Shirai who selected me as a doctoral student and gave me a chance to work with his bright group and make this thesis under his supervision. I am very much appreciative of his scholastic guidance, advice, and fruitful discussions.

Besides my supervisor, I express my deepest thank to Professor Keiji Ueno for the helpful suggestion, and discussion, and provide me with a rich device fabrication laboratory during my research tenure.

I would like to thank Professor Masamichi Sakai, Professor Keiji Ueno, and Professor Kenji Kamishima for consenting to be a member of my thesis committee and for their constructive advice and comments.

I would like to thank all of the former and current members of Shirai Lab; Kazusi Shimomura, Yuki Nasuno, Koki Imai, Koki Kawamura, Yuma Moriya, Kojun Yokoyama, Ryota Sato, Ryuichi Ukai, Yoshikazu Ikeno, Yuya Urushido, Ryotaro Kizaki, Sora Sakai, Hirotaka Tokuta, Tomohiro Hirai, Wenbo Fan, Matsuda Nozomi, Hasegawa Daiki, Date Masaki, and Yagi Kazuya for their support and create a nice environment for research. I also want to thank the members of Ueno Lab; Tomohiro Shida, Takuya Mori, Takafumi Fukushima, Nonaka Nanako, Sasaki Ken, Kawamura Manaka, and Kikuchi Toyama for helping me in AFM measurement, Hall effect measurement and for fabricating the Metal-oxide Semiconductor Field Effect Transistor (MOSFET). I find it immensely enjoyable working with my dear lab colleagues.

I am also indebted to Assistant Professor Dr. Ryo Ishikawa for his suggestions during my experiment and weekly meeting. I am also thankful to all staff of the Department of Functional Materials Science, Saitama University for their support. A special thank goes to Mrs. Izumi Inomori, Foreign Student Office (FSO) for conveying all information related to my education and supporting me to solve my numerous personal and academic issues as the nearest person during this long journey.

I must acknowledge the generosity of all funding agencies. This study was partially supported by a Japan Science and Technology Agency (JST) grant, a Grant-in-Aid for

Scientific Research from the Ministry of Education, Culture, Sports, Science and Technology (MEXT) of Japan. I am also grateful to MEXT for offering me the scholarship for my Ph.D. program in the program of Renewable Energy System Engineering (RESE) at the Graduate School of Science and Engineering at Saitama University.

I would like to thank Assistant Professor Shunji Kurosu, Toyo University (present Osaka University), Kawagoe campus, for allowing me to use SEM and EDS machines and teach me how to analyze and characterize. A deep thanks to K. Funato of Tokyo Dylec Corp. for allowing me to use their Fast-Scanning Mobility Particle Analyzer and Mr. Yoshiharu Iwai of Riken Keiki Co. Ltd, for UPS and Kelvin probe measurement, CW Wu, Ma-Tek, Materials Analysis Technology Inc. for TEM measurement.

I express my deepest thank from the core of my heart to Professor Abu Bakar Md Ismail and Dr. Jaker Hossain, Dr. A. T. M. Saiful Islam and Dr. Enamul Karim for the helpful suggestion, discussion, inspiration, and encouragement in every moment of this journey. My special gratitude to Dr. Md. Arifuzzaman Rajib and no thanks could be enough for his uncountable support, suggestions, and cooperation during my PhD journey.

In the end, I want to acknowledge my parents, my younger brother, and family members of my in-law, from the bottom of my heart. No gratitude could not be enough to express the dedication that they have been given to look after me at every moment. I want to acknowledge my lovely wife, Sadia Afrin; no thanks could be enough for her patience and unconditional support during this long and tough journey.

Finally, I would like to thank all friends, neighbors, and well-wishers, who live in Japan or Bangladesh, or anywhere in the world for their supports.

Above all, I thank almighty Allah.

List of Publications and Presentations

Article Publications

- 1) **A. Kuddus**, A. Rajib, K. Yokoyama, T. Shida, K. Ueno, and H. Shirai, “*Mist chemical vapor deposition of crystalline MoS₂ atomic layer films using sequential mist supply mode and its application in field-effect transistors*” *Nanotechnology*, 33 045601 (2022).
- 2) **A. Kuddus**, K. Yokoyama, A. Rajib, and H. Shirai, “*Mist Chemical Vapor Deposition of Crystalline WS₂ and WS_{2-x}Se_x Atomic Mono/Bilayer Films and their Applications in Complementary MOS Inverter*” *Semicond. Sci. Technol.* 37, 095020 (2022).
- 3) **A. Kuddus**, K. Yokoyama, K. Ueno, and H. Shirai, “*Improved photovoltaic properties of few-layer WS_{0.3}Se_{1.7}/WO_x lateral p-n junctions using gold mirror layer*”, (to be submitted) September, (2022).
- 4) K. Yokoyama, **A. Kuddus**, Faruk Hossain, and H. Shirai, “*Mesh Bias Controlled Synthesis of TiO₂ and Al_{0.74}Ti_{0.26}O₃ Thin Films by Mist Chemical Vapor Deposition and Its Applications in Gate Dielectric Layer for Field-Effect Transistors*” *ACS Applied Electronic Materials* 4, 5, 2516–2524 (2022).
- 5) A. Rajib, **A. Kuddus**, K. Yokoyama, T. Shida, K. Ueno, and H. Shirai, “*Mist chemical vapor deposition of Al_{1-x}Ti_xO_y thin films and their application to a high dielectric material*” *J. App. Phys.* 131, 105301 (2022).
- 6) A. Rajib, **A. Kuddus**, T. Shida, K. Ueno, and H. Shirai, “*Mist Chemical Vapor Deposition of AlO_x Thin Films Monitored by a Scanning Mobility Particle Analyzer and its Application to the Gate Insulating Layer of Field-effect Transistors*” *ACS Applied Electronic Materials* 3, 2, 658-667 (2021)
- 7) M. E. Karim, Y. Nasuno, **A. Kuddus**, T. Ukai, S. Kurosu, M. Tokuda, Y. Fujii, T. Hanajiri, R. Ishikawa, K. Ueno, and H. Shirai, “*Effect of thermally annealed atomic-layer-deposited AlO_x/chemical tunnel oxide stack layer at the PEDOT:PSS/n-type Si interface to improve its junction quality*” *Journal of Applied Physics* 128, 045305 (2020).

- 8) M. E. Karim, A.T.M. S. Islam, Y. Nasuno, **A. Kuddus**, R. Ishikawa, and H. Shirai, “*Chemical mist deposition of organic for efficient front- and back-PEDOT:PSS/crystalline Si heterojunction solar cells*”, EPJ Photovoltaics 11, 7 (2020).

Conference Presentations

- 1) **A. Kuddus**, K. Yokoyama and H. Shirai “*Photovoltaic Effect of Few-layer $WS_{0.3}Se_{1.7}$ -based lateral $p^+ -n$ Junctions using MOSFET Structure*” The 29th International Conference on Amorphous and Nano-crystalline Semiconductors (ICANS29), 23-26 August 2022, Nanjing, China.
- 2) K. Yokoyama, **A. Kuddus**, K. Ueno, and H. Shirai “*Effect of Mesh bias supply during synthesis of AlO_x , TiO_x and $Al_{1-x}Ti_xO_y$ thin films by a mist chemical vapor deposition*” The 29th International Conference on Amorphous and Nano-crystalline Semiconductors (ICANS29), 23-26 August 2022, Nanjing, China.
- 3) **A. Kuddus**, K. Yokoyama and H. Shirai “*Mist Chemical Vapor Deposition of Atomic Layer Crystalline WS_2 and $WS_{2-x}Se_x$ Films and Their Applications in MOSFETs*” 5th International conference of young researcher on advanced materials (IUMRS-ICYRAM), 3-6 August 2022, Fukuoka, Japan.
- 4) K. Yokoyama, **A. Kuddus**, K. Ueno, and H. Shirai “*Mesh Bias Controlled Synthesis of TiO_2 Thin Films by Mist Chemical Vapor Deposition and Its Applications in Gate Dielectric Layer for Field-Effect Transistors*” 5th International conference of young researcher on advanced materials (IUMRS-ICYRAM), 3-6 August 2022, Fukuoka, Japan.
- 5) **A. Kuddus**, R. Kizaki, K. Yokoyama, and H. Shirai “*Carrier transport in 2D $WS_{2-x}Se_x$ FETs*” The 69th JSAP Spring Meeting, March 22-26, 2022, Kanagawa, Japan.
- 6) **A. Kuddus**, R. Kizaki, K. Yokoyama, and H. Shirai “*PEDOT:PSS/2D $WS_{2-x}Se_x$ /n-Si Heterojunction Solar Cells*” The 69th JSAP Spring Meeting, March 22-26, 2022, Kanagawa, Japan.

- 7) **A. Kuddus**, and H. Shirai “*Synthesis of Two-Dimensional Transition-Metal Dichalcogenides by Mist Chemical Vapor Deposition for Field-Effect Transistors*” 6th World Congress on Nanomaterials, January 14-15, 2022, Online, UK.
- 8) **A. Kuddus**, A. Rajib, R. Kizaki, K. Yokoyama, K. Ueno, H. Shirai “*Mist Chemical Vapor Deposition of Crystalline MoS₂*” International Conference and Expo on Catalysis, Chemical Engineering, and Technology, October 28-30, 2021, Online, Vancouver, Canada.
- 9) K. Yokoyama, A. Rajib, **A. Kuddus**, T. Shida, K. Ueno, and H. Shirai “*Synthesis of Aluminum Titanium oxide thin films by a mist chemical vapor deposition and their potential as High-K dielectric material*” International Conference and Expo on Catalysis, Chemical Engineering and Technology, October 28-30, 2021, Online, Vancouver, Canada.
- 10) **A. Kuddus**, A. Rajib, R. Kizaki, K. Yokoyama, K. Ueno, H. Shirai “*Synthesis of 2D MoS₂ and WS_{1-x}Se_x thin films by Mist-CVD*” The 82nd JSAP Autumn Meeting, September 10-13, 2021, Online, Japan.
- 11) K. Yokoyama, A. Rajib, **A. Kuddus**, T. Shida, K. Ueno, and H. Shirai “*Effect of mesh bias supply during synthesis of AlO_x and TiO_x thin films by a mist chemical vapor deposition*” The 82nd JSAP Autumn Meeting, September 10-13, 2021, Online, Japan.
- 12) A. Rajib, **A. Kuddus**, T. Shida, K. Yokoyama, K. Ueno, and H. Shirai “*Al_{1-x}Ti_xO_y Thin Films Synthesized by Mist-CVD and Applied as a Gate Insulating Layer*” The 68th JSAP Spring Meeting, March 16-19, 2021, Tokyo, Japan.
- 13) **A. Kuddus**, A. Rajib, K. Shimomura, K. Yokoyama, K. Ueno, H. Shirai “*Digitalized Mist-Chemical Vapor Deposition of atomic-layer Molybdenum Disulfide (MoS₂) Flakes at Low Temperatures*” The 68th JSAP Spring Meeting, March 16-19, 2021, Tokyo, Japan.
- 14) A. Rajib, **A. Kuddus**, and H. Shirai “*Al_{1-x}Ti_xO_y Thin Films Synthesized by Mist-CVD and Applied as a Gate Insulating Layer*” International Conference on

Science and Technology for Celebrating the Birth Centenary of Bangabandhu (ICSTB-2021, March 11-13, 2021, BCSIR, Bangladesh.

- 15) A. Rajib, **A. Kuddus**, K. Enamul, S. Kurosu, T. Ukai, M. Tokuda, Y. Fujii, T. Hanajiri, R. Ishikawa, K. Ueno, and H. Shirai, “*The role of water in the synthesis of AlO_x thin films by a mist chemical vapor deposition*”, The 67th JSAP Spring Meeting, March 12-15, 2020, Tokyo, Japan.
- 16) A. Rajib, **A. Kuddus**, T. Shida, K. Ueno, and H. Shirai, “*Mist-CVD of AlO_x thin films monitored by fast scanning mobility particle analyzer and its application to FETs*” The 30th Materials Research Meeting, December 9-11, 2020, Yokohama, Japan.
- 17) A. Rajib, T. Shida, **A. Kuddus**, K. Ueno, and H. Shirai, “*Synthesis of AlO_x thin films by mist-CVD and its application to dielectric layer for MIS-FET*” The 51st The Society of Chemical Engineers SCEJ Autumn Meeting, September 24-26, 2020, Japan.

Table of Contents

ABSTRACT	I
ACKNOWLEDGEMENTS	III
LIST OF PUBLICATIONS AND PRESENTATIONS	V
LIST OF TABLES	XII
LIST OF FIGURES	XIV
LIST OF ABBREVIATIONS	XXVII
CHAPTER 1 GENERAL INTRODUCTION	2
1.1 A smart two-dimensional materials system beyond silicon	2
1.2 Properties of 2D TMDCs semiconductors: MoS ₂ , WS ₂ , WSe ₂ and WS _{2-x} Se _x	8
1.3 Techniques for the synthesis of 2D TMDCs and benefits of Mist-CVD	15
1.4 Metal oxide field effect transistors (MOSFETs), Complementary MOS circuit and their electrical parameters .	19
1.5 Motivation and objectives of this study	23
1.6 Structure of this dissertation	24
CHAPTER 2 EXPERIMENTAL AND ANALYTICAL METHODOLOGIES	33
2.1 EXPERIMENTAL	33
2.1.1 <i>Hot-wall Mist-CVD system</i>	33
2.1.1.1 <i>Mist generation unit</i>	34
2.1.1.2 <i>Reaction unit</i>	35
2.1.1.3 <i>ventilation unit</i>	36
2.1.1.4 <i>Sulfurization/selenization set up</i>	37
2.1.2 <i>Synthesis of MoS₂, WS₂ and WS_{2-x}Se_x films by Mist CVD.....</i>	37

2.1.3	<i>Fabrication of MoS₂, WS₂ and WS_{2-x}Se_x- channel MOSFETs and design of CMOS circuit</i>	38
2.1.4	<i>Fabrication of WS_{0.3}Se_{1.7}/WO_x based lateral p⁺-n junction solar cells.....</i>	40
2.2	ANALYTICAL METHODOLOGIES	41
2.2.1	<i>Optical Microscopy</i>	41
2.2.2	<i>Atomic Force Microscopy (AFM)</i>	43
2.2.3	<i>Scanning Electron Microscopy (SEM)</i>	44
2.2.4	<i>Transmission Electron Spectroscopy (TEM)</i>	45
2.2.5	<i>Raman and Photoluminescence (PL) spectroscopy</i>	46
2.2.6	<i>X-ray Photoelectron Spectroscopy (XPS)</i>	50
2.2.7	<i>Auger electron spectroscopy (AES)</i>	52
2.2.8	<i>Ultraviolet Photoelectron Spectroscopy (UPS)</i>	54
2.2.9	<i>Kelvin Probe Measurement (KPFM)</i>	55
2.2.10	<i>Time-of-Flight Secondary Ion Mass Spectrometry (ToF-SIMS)</i>	56
2.2.11	<i>Fast Mobility Particle Sizer (FMPS)</i>	57
2.2.12	<i>Spectroscopic Ellipsometry (SE)</i>	60
2.2.13	<i>Hall Measurement</i>	62
2.2.14	<i>Electrical Characterizations of MOSFET, CMOS and Solar cells.....</i>	65
CHAPTER 3 RESULTS AND DISCUSSIONS		74
3.1	MIST CHEMICAL VAPOR DEPOSITION OF CRYSTALLINE MoS₂ ATOMIC LAYER FILMS USING SEQUENTIAL MIST SUPPLY MODE AND ITS APPLICATION IN FIELD-EFFECT TRANSISTORS	75
3.1.1	<i>Growth of MoS₂ thin films under sequential mist supply mode</i>	76
3.1.2	<i>Role of sulfurization of MoS_x films</i>	85
3.1.3	<i>Synthesis of MoS₂ by intermittent and continuous mode</i>	88
3.1.4	<i>Synthesis of atomic mono/bilayer MoS₂ on mist CVD Al_{0.74}Ti_{0.26}O_y dielectric layer.....</i>	90

3.1.5	<i>Fabrication of atomic mono/bilayer MoS₂ channel MOSFETs</i>	92
3.2	DIRECT SYNTHESIS OF SUBMILLIMETER-SIZED FEW-LAYER WS₂ AND WS_{0.3}Se_{1.7} BY MIST CHEMICAL VAPOR DEPOSITION AND ITS APPLICATION TO COMPLEMENTARY MOS INVERTER	95
3.2.1	<i>Synthesis of few-layer WS_{2-x}Se_x flake under intermittent mist CVD mode</i>	95
3.2.2	<i>Effect of selenization and sulfurization of WS_x films ...</i>	102
3.2.3	<i>Growth of submillimeter-size few-layer WS_{0.3}Se_{1.7} flakes by mist CVD on a-Al_{0.74}Ti_{0.26}O_y dielectric layer ..</i>	105
3.2.4	<i>Growth of submillimeter size few-layer WS₂ flakes on a-Al_{0.74}Ti_{0.26}O_y dielectric layer</i>	108
3.2.5	<i>Fabrication of FETs and CMOS using mist CVD WS₂ and WS_{0.3}Se_{1.7} on a-Al_{0.74}Ti_{0.26}O_y dielectric layer</i>	110
3.3	PHOTOVOLTAIC PROPERTIES OF FEW-LAYER WS_{0.3}Se_{1.7}/WO_x LATERAL P⁺-N JUNCTIONS USING METAL MIRROR LAYER	115
3.3.1	<i>Fabrication of WS_{0.3}Se_{1.7}/WO_x(WS_{0.3}Se_{1.7}) lateral p⁺-n junction device with a FETs structure</i>	115
3.3.2	<i>Carrier transport properties in WS_{0.3}Se_{1.7}/WO_x (WS_{0.3}Se_{1.7}) channel MOSFETs</i>	122
3.3.3	<i>Photovoltaic properties in the FETs with lateral WS_{0.3}Se_{1.7}/WO_x(WS_{0.3}Se_{1.7}) p⁺-n junction</i>	125
3.3.4	<i>PEDOT:PSS/2D WS_{0.3}Se_{1.7}/n-Si heterojunction solar cells</i>	133
3.3.5	<i>Growth of few-layer triangle-shape WS_{0.3}Se_{1.7} flakes.....</i>	133
	CHAPTER 4 SUMMARY AND FUTURE WORK	140
4.1	Summary of experimental results	140
4.2	Future works	140

List of Tables

Table 1.1.	The lattice constants of bulk TMDs (Experimental and theoretical). Lattice constants are provided in Å.	13
Table 1.2.	Theoretical in-plane lattice constants of monolayer TMDs with hexagonal symmetry, were obtained from different numerical calculations of PBE, LDA, and HSE. Lattice constants (a) are provided in Å.	14
Table 1.3.	Spin-orbit splitting at K and VBM at Γ and K was obtained from the experimental ARPES data for mono, bi-, and tri-layer $W_{2(1-x)}Se_{2x}$ ($x=0.8$).	15
Table 2.1.	Wave number differences ($\Delta\omega$) between in-plane E_{2g}^1 and out-off plane A_{1g} modes of MoS_2 and WS_2 .	49
Table 3.1.1.	MoS ₂ deposition and sulfurization conditions	77
Table 3.1.2.	Summary of XPS Analysis: atomic ratio S/M and position of Mo and S.	88
Table 3.1.3.	Summary of layer thickness, maximum flake size, frequency difference $\Delta\omega$ value, intensity ratio A/B, and PL emission energy.	90
Table 3.1.4.	FET parameters are determined from the transfer characteristics.	94
Table 3.1.5.	FET parameters for different deposition techniques of atomic mono/bilayer MoS ₂ .	94
Table 3.2.1.	The deposition conditions of atomic layer WS ₂ and WS _{2-x} Se _x films.	96
Table 3.2.2.	Summary of XPS observation of WS _{2-x} Se _x for Se vapor exposure period $t = 1200$ and 2400 s.	104
Table 3.2.3.	Summary of XPS results of as-deposited and sulfurized WS _x films for $t=1200$ s.	110
Table 3.2.4.	The electrical characteristics of WS ₂ and WS _{0.3} Se _{1.7} atomic bi/monolayers-based MOSFETs with mist-CVD Al _{0.74} Ti _{0.26} O _y as a dielectric layer.	112

Table 3.2.5.	A comparative study on electrical parameters of atomic mono/bilayer WS ₂ - and WSe ₂ - channel FETs for different synthesis techniques.	112
Table 3.3.1.	WS _{2-x} Se _x deposition and sulfurization conditions	117
Table 3.3.2.	Summary of XPS observation of synthesized WS _{0.3} Se _{1.7} film with Se-exposure at 600 °C for 60 minutes.	119
Table 3.3.3.	Summary of photovoltaic performance of WS _{0.3} Se _{1.7} /WO _x lateral p ⁺ -n junction device.	128

List of Figures

- Figure 1.1.** (a) 50 Years of Microprocessor Trend Data: Number of transistors per microprocessor chip, Frequency, typical power, and the number of logical cores; (b) miniaturization of the transistor gate length in different technology nodes and production years. (c) short channel effect and punch through; (d) drain-induced barrier lowering. **2**
- Figure 1.2.** 2D materials families. **4**
- Figure 1.3.** Crystal structure of graphene, boron nitride, black phosphorus and 2D TMDCs and polymorphs (phases) of 1H phase, 1T phase (ideal), distorted 1T', 2H phase, 3R phase **5**
- Figure 1.4.** Applications of 2D transition metal dichalcogenides in electronic, optoelectronic, and energy devices. **6**
- Figure 1.5.** Evolution of 2D heterostructure-based devices with the features of being ultrafast and weakly light sensitive properties, low power consumption and biocompatibility. **7**
- Figure 1.6.** Band structure of bulk, multilayer, and monolayer MoS₂ film. **8**
- Figure 1.7.** (a) Bulk 2H-MoS₂ side and top view of single MoS₂ monolayer (3×3-unit cells); (b) Polytypes of TMDs: 2H, 3R, and 1T lattice; (c) The graphical depiction of d-orbitals in TMDs. **9**
- Figure 1.8.** Band structure of WS₂ in bulk, multilayer, and monolayer. The arrow highlights the fundamental band gap. **10**
- Figure 1.9.** Crystal structure of WS₂; (a) Schematic view of the layered structure; (b) schematic view from the c-axis; (c) unit cell of the trigonal prismatic structure; (d) unit cell of the octahedral structure. **11**
- Figure 1.10.** The crystal structure of single-layer tungsten diselenide (WSe₂) **12**

Figure 1.11.	Electronic band structure of bulk and monolayer WSe ₂ . The valence band maximum and the conduction band minimum are highlighted in blue and red, respectively.	12
Figure 1.12.	Classification diagram of functional thin-film fabrication method.	16
Figure 1.13.	Schematic of the development of the vapor-phase synthesis of WS ₂ . The upper side indicates the development of single domain size, the lower side indicates the development of the growth of large-area WS ₂ film by various methods.	17
Figure 1.14.	Chemical structure of (NH ₄) ₂ MeS ₄ precursor and the different solvents of N-Methyl-2-Pyrrolidone (NMP), Dimethylformamide (DMF), Dimethyl sulfoxide (DMSO), and Ethylene glycol (EG).	19
Figure 1.15.	Key parameters of 2D FETs and relevant electrical characterization methods.	19
Figure 1.16.	Band alignment of various 2D materials and elemental contact metals. Schematic of bandgap, electron affinity, ionization potential, and charge neutrality level (CNL) for multilayer 2D materials including the work functions Φ_M of common contact metals.	20
Figure 1.17.	Typical $I_{ds}-V_{gs}$ characteristics of an n-MOSFET; drain current I_{ds} plotted against gate voltage V_s on a log-lin. and a lin.-lin. scale. The most important parameters threshold voltage V_{th} , subthreshold slope SS, off-current I_{OFF} , and on-current I_{ON} in the $I_{ds}-V_g$ curve.	22
Figure 1.18.	(a) Schematic of CMOS inverter circuit (b) standard symbol (c) different operating regions of CMOS circuit.	23
Figure 2.1.	Camera image and a schematic of the mist CVD system and its different units.	34
Figure 2.2.	Schematic of an ultrasonic mist generator and its principal components.	35
Figure 2.3.	Schematic diagram of different types of reaction units of mist CVD system.	36

Figure 2.4.	Camera image and a schematic diagram of sulfurization/ selenization setup.	37
Figure 2.5.	AFM and microscopic images of mist CVD MoS ₂ , and WS _{2-x} Se _x flakes synthesized by mist-CVD.	38
Figure 2.6.	(a) 3D schematic and microscopic images of MX ₂ channel FETs: (a) MoS ₂ , (b) WS ₂ , and (c) WS _{2-x} Se _x channel MOSFETs. The MoS ₂ and WS ₂ channel n-FETs with Au as S/D electrodes and WS _{2-x} Se _x channel p-FET with Pt source/drain electrodes.	39
Figure 2.7.	(a) Complementary inverter circuit comprising p- WS _{0.3} Se _{1.7} and n- WS ₂ channel MOSFETs with a common gate as the input voltage, V _{IN} , and common source as the output, V _{OUT} ; (b) voltage transfer characteristics (VTC) at different V _{DD} .	40
Figure 2.8.	Camera images of (a) 10 kV, 10 kHz O ₂ /He plasma exposure system and lasers of different oscillation wavelengths of 420, 532, and 650 nm; (b) Set-up of laser irradiation and I-V measurement; (c) schematic of WS _{0.3} Se _{1.7} /WO _x lateral p ⁺ -n junction solar cells.	40
Figure 2.9.	(a) Optical microscopy (OM) system; (b) OM internal diagram; (c) schematic of optical reflection and transmission for a TMDCs film with thickness d ₁ and refraction index n ₁ on SiO ₂ /Si substrate (the thickness, and refraction index of SiO ₂ are d ₂ and n ₂ and refraction index of Si is n ₃) and optical image of mono/bilayer of WS _{0.3} S _{1.7} flakes on ATO substrate.	41
Figure 2.10.	Schematic diagram of atomic force microscopy (AFM) system.	43
Figure 2.11.	Force curve of atomic force microscopy: contact and non-contact scanning mode.	44
Figure 2.12.	(a) Schematic of an internal diagram of scanning electron microscopy (SEM) system and (b) SEM image of MoS ₂ film	45
Figure 2.13.	(a) Schematic of a TEM measurement system and (b) TEM image of single-crystal 2H-phase MoS ₂ .	46

Figure 2.14.	Renishaw InVia Raman spectroscopy system and its internal schematic diagram with laser wavelength 532 nm.	47
Figure 2.15.	Raman spectra of (a) MoS ₂ ; (b) WS ₂ ; (c) WSe ₂ at different number of layers; (d) WS _{2(1-x)} Se _{2x} at different Se-composition.	48
Figure 2.16.	PL spectra of (a) MoS ₂ ; (b) WS ₂ ; (c) WSe ₂ at different number of layers and (d) WS _{2(1-x)} Se _{2x} at different Se-composition	50
Figure 2.17.	AXIS Nova, Kratos Axis Ultra XPS system, and its internal diagram.	51
Figure 2.18.	Schematic of photoemission excitation and survey spectra obtained from XPS observation.	51
Figure 2.19.	(a) The internal diagram of the AES system, (b) AES experimental setup with a cylindrical mirror analyzer (CMA), and (c) a typical AES spectrum of MoS ₂ .	53
Figure 2.20.	(a) Work function spectrum of a chemical element obtained from UPS observation and (b) information depth for UPS compare with XPS.	55
Figure 2.21.	The schematic of the KPFM system; scanning a WSe ₂ film surface retaining at a constant height and corresponding KPFM profile spectra.	56
Figure 2.22.	(a) A particle beam interaction in ToF-SIMS with liberation of single ions (+/-) and molecular compounds; (b) a TOF-SIMS depth profiles spectra of S ⁻ , MoS ₂ ⁻ , and MoO ⁻ ions.	57
Figure 2.23.	(a) Fast Scanning Mobility Particle Sizer (FMPS), Model-3091 image; (b) Schematic of the aerosol flow diagram and (c) data representation by FMPS-3091.	58
Figure 2.24.	Schematic of an (a) cascade impactor; (b) differential mobility analyzer; (c) continuous flow condensation particle counter (CPC); (d) measurable ranges of solution concentration by FMPS 3091: the maximum (red) and the minimum (green) RMS noise level.	60

Figure 2.25.	Beam geometry for light and its electric field in spectroscopic ellipsometry.	61
Figure 2.26.	A configuration of the Van der Pauw measurement system for the Hall coefficient measurement without and with the perpendicularly applied magnetic field (0.5 T) to the sample surface and the associated experimental set-up.	63
Figure 2.27.	Schematic of (a) MOSFET structure with different terminals and (b) device measurement system with Keithley 2100	65
Figure 2.28.	A typical transfer characteristic of MOSFET and its respective electrical parameters.	66
Figure 2.29.	Photogenerated carrier transport in a typical p-n junction, J-V characteristics and different parameters of a solar cell device.	68
Figure 3.1.1.	(a) Schematic representation of the mist CVD system; (b) The sequential MoS ₂ precursor mist supply mode; (c) sulfurization setup.	76
Figure 3.1.2.	(a) Size distribution of mist particle monitored at the inlet and outlet positions of the tubular furnace for different N ₂ flow rates for a T _f of 850 °C and different T _s of 700 to 900 °C under an N ₂ gas flow of 2500 sccm, (b) Size distribution of mist particle monitored at the inlet and outlet positions for different H ₂ /Ar mixing ratios at a T _f of 850 °C, and at a different T _s of 200 to 850 °C under steady flow of an H ₂ /Ar mixture gas at a 150/200 sccm.	79
Figure 3.1.3.	Optical microscope image and Raman spectra of as-deposited MoS _x layers (without sulfurization) synthesized at different T _s of 400– 600 °C at mist supply time of 300 s.	80
Figure 3.1.4.	Optical microscope images of MoS ₂ flake synthesized at different mist supply times t _{1s} = 30- 75 s under the t ₂ = 150 s, N = 7 cycles at a T _f = 500 °C followed by sulfurization at 600 °C for 1200 s. The scale bar is 25 μm.	80

- Figure 3.1.5.** (a) AFM images of MoS₂ layers synthesized at different T_f s of 400–600 °C for $t_1= 50$ s, $t_2 = 150$ s, and $N= 7$ cycles (the insets show the optical microscope image and height profile of the corresponding samples); (b) Variations of the layer thickness, the average size of the MoS₂ flake, and area ratio of the MoS₂ flake with T_f s; (c) Raman and PL spectra of the corresponding samples. **82**
- Figure 3.1.6** (a) AFM images of MoS₂ flakes synthesized at different t_2 for $t_1 = 50$ s, $N = 7$ cycles, and $T_f = 500$ °C; (b) Variations of layer thickness, area ratio, and an average size of the MoS₂ flakes with t_2 ; (c) Raman and PL spectra of the corresponding samples. **83**
- Figure 3.1.7.** (a) AFM images of MoS₂ flakes fabricated at different N for $t_1 = 50$ s, $t_2 = 150$ s, and $T_f = 500$ °C (the inset shows the optical microscope image and height profile of the corresponding samples); (b) variations of the layer thickness, area ratio, and average size of the MoS₂ flakes with N ; (c) Raman and PL spectra of the corresponding samples. **84**
- Figure 3.1.8.** (a) AFM image of MoS₂ samples exposed to sulfur vapor using H₂/Ar (5/95 sccm) gases at different sulfidation temperatures $T_f = 600- 650$ °C for 20 min. synthesized for a $t_1 = 50$ s, $t_2 = 150$ s, $N= 7$ cycles, $T_f = 500$ °C; (b) the area ratio of MoS₂ flake to the observation area of $270 \times 180 \mu\text{m}^2$, layer thickness, and grain size determined from the optical microscope and AFM observations; (c) Raman and PL spectra of the corresponding samples. **85**
- Figure 3.1.9.** (a) AFM images of MoS₂ flakes exposed to sulfur vapor using H₂/Ar (5/95 sccm) mixture for different times at $T_f = 600$ °C synthesized at for a $t_1 = 50$ s, $t_2 = 150$ s, $N= 7$ cycles, $T_f = 500$ °C; (b) Variations of the area ratio, layer thickness, and grain size of MoS₂ flakes with sulfurization time; (c) Raman and PL spectra of the corresponding samples. **86**

- Figure 3.1.10.** XPS survey spectra of (a) as-deposited MoS_x; (b) sulfurized MoS_x films at a T_f= 600 °C for 1200 s and high-resolution spectra of (c) Mo 3d; (d) S 2p doublet of corresponding samples synthesized at a t₁ = 50 s, t₂ = 150 s, N= 7 cycles, T_f = 500 °C. **87**
- Figure 3.1.11.** (a) AFM and optical microscope images of MoS₂ layers fabricated by the sequential and continuous mist supply modes under the optimized condition at a precursor concentration of 0.05 M/L and a T_f of 500 °C followed by the sulfurization at 600 °C for 1200 s. **89**
- Figure 3.1.12.** (a) AFM and optical microscope images of MoS₂ flake fabricated from 0.05 and 0.01 M/L precursor solutions on the *th*-SiO₂/P⁺-Si substrate followed by exposure to sulfur vapor using H₂/Ar (5/95 sccm) at a T_f of 600 °C for 1200 s and PL mapping for a sample of 0.01 M/L, and (b) Raman spectra of corresponding samples. **90**
- Figure 3.1.13.** AFM and optical microscope images of MoS₂ flakes fabricated from 0.01 M/L precursor solutions on (a) ATO substrate without plasma treatment, plasma-treated (30 s) ATO using sequential mist supply mode, and plasma-treated (30 s) ATO using continuous mode followed by exposure to sulfur vapor using H₂/Ar (5/95 sccm) mixture at a T_f of 600 °C for 1200 s; (b) Raman and PL spectra of the corresponding samples; (c) Plot of an area of a single MoS₂ flake vs. corresponding flake size. **91**
- Figure 3.1.14.** Contact angle (wettability) of (NH₄)₂MoS₄ precursor solution (2μL) dropped on (a) ATO substrate before and after plasma treatment, and (b) AFM image of corresponding substrates. **92**
- Figure 3.1.15.** Transfer characteristics and √I_{ds}-V_{gs} curves of atomic MoS₂ mono/bilayer-based FET devices on *th*-SiO₂ and mist- CVD grown ATO dielectric layers (L/W= 16/12 μm). **93**

- Figure 3.2.1.** (a) Schematic diagram of the mist-CVD system; (b) Flow chart of sequential mist precursor supply; (c) Schematic of sulfurization/selenization set-up. **96**
- Figure 3.2.2.** (a) Optical microscope images of $WS_{2-x}Se_x$ flakes synthesized at different mist supply times $t_{1S} = 10-70$ s per one cycle under the $t_2 = 210$ s, $N = 7$ cycles at a $T_f = 475$ °C followed by selenization at 600 °C for 1200 s and (b) An estimated incubation time of $WS_{2-x}Se_x$ determined by the extrapolation from flake size to deposition times (t_1+t_2) plot. **97**
- Figure 3.2.3.** AFM image, average layer thickness, median of integrated area ratio, and average size of $WS_{2-x}Se_x$ flakes synthesized at different (a) T_f for $t_2 = 150$ s, and (b) t_2 at a $T_f = 475$ °C, $t_1 = 50$ s, and $N=7$ cycles. The inset shows the optical microscope images and height profiles for corresponding samples. **99**
- Figure 3.2.4.** (a) Raman and PL spectra of $WS_{2-x}Se_x$ layers synthesized at different (b) T_f s for $t_2 = 150$ and (b) t_2 for $T_f = 475$ °C, with $t_1 = 50$ s, $N = 7$ cycles, precursor concentration of 0.01 M/L and followed by selenization at 600 °C for 1200 s. **100**
- Figure 3.2.5.** Histogram of integrated area ratio for mist storage time, $t_2 = 210$ and 270 s, $WS_{2-x}Se_x$ flakes synthesized at different t_2 for $t_1 = 50$ s, $N = 7$ cycles, $T_f = 475$ °C, and precursor concentration of 0.01 M/L, selenization at 600 °C for 1200 s. **101**
- Figure 3.2.6.** (a) AFM images of $WS_{2-x}Se_x$ flakes synthesized at different N for $t_1 = 50$ s, $t_2 = 210$ s, and $T_f = 475$ °C (the inset shows optical microscope images of the corresponding samples); (b) the variations of the layer thickness, median of integrated area ratio, and an average size of the $WS_{2-x}Se_x$ flakes with N ; (c) Raman and PL spectra of the corresponding $WS_{2-x}Se_x$ samples. **102**
- Figure 3.2.7.** (a) AFM images of $WS_{0.3}Se_{1.7}$ flakes exposed to selenium (Se) vapor for different times at a $T_f = 600$ °C under the steady flow of H_2/Ar (5/95 sccm) mixture gas with 0.01 M/L $(NH_4)_2WS_4$; (b) The variations of an integrated area ratio, **103**

layer thickness, and grain size of $WS_{2-x}Se_x$ flakes for different exposure time; (c) Raman and PL spectra of the corresponding samples.

- Figure 3.2.8.** XPS observation: a high-resolution core-spectra of W $4f$ and Se $3d$ doublets of $WS_{2-x}Se_x$ samples with selenium vapor exposure for 1200 s and 2400 s at 600 °C; WS_x synthesized at a $T_f = 475$ °C, for $t_1 = 50$ s, $t_2 = 210$ s and $N = 7$ cycles. **104**
- Figure 3.2.9.** (a) Optical microscope and AFM images of $WS_{0.3}Se_{1.7}$ flakes for different precursor concentration of (a) 0.01 and (b) 0.035 M/L on $Al_{0.76}Ti_{0.24}O_y/p^+$ -Si substrate at mist supply times $t_1 = 50$ s, $t_2 = 210$ s, $N = 7$ cycles at a $T_f = 475$ °C followed by selenization at 600 °C for 2400 s. **105**
- Figure 3.2.10.** (a) Optical microscope and AFM images of few-layer $WS_{0.3}Se_{1.7}$ on $Al_{0.74}Ti_{0.26}O_3/p^+$ -Si substrate synthesized for $t_2 = 210$ s, at $T_f = 475$ °C, $t_1 = 50$ s, $N = 7$, and $C = 0.025$ M/L; (inset AFM height profile) and PL mapping of corresponding samples; (b) Raman and PL spectra of the corresponding samples; (c) Contact angle of $(NH_4)_2WS_4$ precursor dissolved in NMP dropped (2 μ L) on mist CVD $Al_{0.74}Ti_{0.26}O_y$ and thermally grown *th*- SiO_2 (285 nm) coated $/p^+$ -Si substrates. **106**
- Figure 3.2.11.** Optical microscope and AFM images of $WS_{0.3}Se_{1.7}$ film synthesized using continuous mist supply mode for equal mist supply time of (50 \times 7 cycles) 350 s at a $T_f = 475$ °C, 0.025 M/L on a- $Al_{0.76}Ti_{0.24}O_y/p^+$ -Si substrate followed by selenization at 600 °C for 2400 s. **108**
- Figure 3.2.12.** (a) Optical microscope and AFM images of few-layer WS_2 on $Al_{0.74}Ti_{0.26}O_y/p^+$ -Si substrate synthesized for $t_2 = 210$ s, at $T_f = 475$ °C, $t_1 = 50$ s, $N = 7$, and $C = 0.025$ M/L (inset AFM height profile) and PL mapping of corresponding samples; (b) Raman and PL spectra of the corresponding samples. **109**
- Figure 3.2.13.** XPS observation: The high-resolution core-spectra of (a) W $4f$ and (b) S $2p$ doublets of as-deposited and S- vapor exposed WS_x films for 1200 s at 600 °C; the WS_x films was **110**

synthesized at a $T_f = 475$ °C, $t_1 = 50$ s, $t_2 = 210$ s, $N = 7$ cycles and 0.025 M/L.

- Figure 3.2.14.** (a) Output and transfer characteristics of an atomic tri/bilayer p-channel $WS_{0.3}Se_{1.7}$ transistor on a linear and logarithmic scale in the positive and negative V_{ds} regimes; (b) Output and transfer characteristics of an atomic bi/monolayer WS_2 channel FETs with S/D gold electrodes on a linear and logarithmic scale; Inset shows the optical images of WS_2 and $WS_{0.3}Se_{1.7}$ MOSFETs with S/D gold and platinum electrodes, respectively, on ~ 45 -nm-thick $Al_{0.74}Ti_{0.26}O_y$ gate dielectric layer. **111**
- Figure 3.2.15.** The histogram of threshold voltage V_{th} , on-off ratio I_{ON}/I_{OFF} , subthreshold swing SS , and mobility μ_{lin} . calculated at V_G sweeping range of 0.5 V at a fixed V_{DD} of 0.2 V for $WS_{2-x}Se_x$ channel (red curve) and WS_2 channel (blue curve) bottom-gate FETs on mist- CVD grown $a-A_{0.74}T_{0.26}O_y$ (~ 45 nm)/ p^+ -Si substrates with platinum (Pt) and gold (Au) S-D electrodes, respectively. **113**
- Figure 3.2.16.** A typical energy band diagram for metal/TMDCs contact (Au/WS_2 and $Pt/WS_{0.4}Se_{0.6}$) at thermal equilibrium. **114**
- Figure 3.2.17.** (a) Complementary MOS characteristics where V_{IN} and V_{DD} were both positively biased (inset schematic of a complementary inverter circuit comprising p- channel $WS_{0.3}Se_{1.7}$ and n- channel WS_2 -channel FETs), and (b) the corresponding voltage gain ($\Delta V_{OUT}/\Delta V_{IN}$) at V_{dd} of 1 to 5 V. **115**
- Figure 3.3.1.** (a) Flowchart of the $WS_{2-x}Se_x$ synthesis steps, (b) $WS_{2-x}Se_x/WO_x$ lateral p^+ -n junction device fabrication, He/ O_2 plasma exposure system, Laser of 420, 532, and 650 oscillation wavelengths with 4 mm spot diameter, and with a FET structure. **116**
- Figure 3.3.2.** (a) AFM, and TEM images of synthesized $WS_{2-x}Se_x$ (the inset shows the line profile, optical microscope, and SEM **118**

- images); (b) Raman spectra (the inset shows the PL spectra); (c) PL map of the corresponding $WS_{2-x}Se_x$ sample.
- Figure 3.3.3.** XPS observation; a core energy spectrum of Se W 4f and 3d of $WS_{0.3}Se_{1.7}$ film with Se-exposure at 600 °C for 60 minutes. **119**
- Figure 3.3.4.** Micro-Raman spectra of few-layers $WS_{0.3}Se_{1.7}$ normalized by the TO phonon mode intensity at 520 cm^{-1} of c-Si at different 420 nm laser irradiation time $t = 0-120\text{ s}$ and PL spectra of corresponding samples. **120**
- Figure 3.3.5.** Micro-Raman spectra of few-layers $WS_{0.3}Se_{1.7}$ normalized by the TO phonon mode intensity at 520 cm^{-1} of a c-Si (a) before and after the He/ O_2 plasma exposure for 30 and 60s; (b) before and after laser exposure for 60 s after the He/ O_2 plasma exposure; (c) PL spectra; (d) PL map and AFM images of the corresponding $WS_{0.3}Se_{1.7}/WO_x$ lateral p^+-n junction area (the inset shows the line profile of the $WS_{0.3}Se_{1.7}$ layer); (e) TEM observation of plasma (60 s) and 420 nm laser (60 s) irradiated $WS_{0.3}Se_{1.7}$ film. **121**
- Figure 3.3.6.** The degree of oxidation; TOF-SIMS, XPS, and AES (inset AES map for oxygen “O”) observation of few-layers $WS_{0.3}Se_{1.7}$ before and after the He/ O_2 plasma exposure for 30 and 60s and subsequent 420 nm laser irradiation for 60 s. **122**
- Figure 3.3.7.** (a) Schematic of FETs with a channel of few-layers $WS_{0.3}Se_{1.7}$ having an oxidized region between source and drain (S/D) electrodes generated by the O_2/He plasma exposure and the PL map; (b) transfer characteristics of FETs with gold (S/D) electrodes; (c) transfer characteristics of FETs without and with O_2/He plasma exposure with platinum (S/D) electrodes. **123**
- Figure 3.3.8.** (a) The schematic of the FETs structure associated circuit configuration, and barrier height obtained from temperature dependent $I_{ds}-V_g$ characteristics using thermionic emission model; (b) transfer characteristics; (c) output characteristics **125**

of the corresponding laser-irradiated $\text{WS}_{0.3}\text{Se}_{1.7}/\text{WO}_x$ FETs at three different excitation wavelengths of 420, 532, and 650 nm for 60 s after the O_2/He plasma exposure.

- Figure 3.3.9.** I_{ph} -V curves in the dark for the as-deposited $\text{WS}_{0.3}\text{Se}_{1.7}$ few-layers and the O_2/He plasma-treated devices for the 60 s with gold and platinum electrodes when $V_g = 0$ V and under AM1.5G simulated solar light exposure for the device with a O_2/He plasma exposure for 60 s. **126**
- Figure 3.3.10.** (a) Raman spectra for the laser irradiation with three different wavelengths of 650, 532, and 420 nm after the plasma treatment of few-layers $\text{WS}_{0.3}\text{Se}_{1.7}$ film; (b) I_{ph} -V curves for the $\text{WS}_{0.3}\text{Se}_{1.7}/\text{WO}_x$ lateral p^+ -n junction devices treated by the O_2/He plasma exposure for 60 s and followed by the laser irradiation at excitation wavelengths of 420 ($r = 9.60$), 532 ($r = 3.90$), and 650 nm ($r = 1.01$); (c) EQE for the corresponding $\text{WS}_{0.3}\text{Se}_{1.7}/\text{WO}_x$ lateral p^+ -n junction device with Au/Pt as S/D electrodes under zero, at a 0 and ± 0.5 V at a $V_g = 0$ V bias. **127**
- Figure 3.3.11.** (a) The I_{ph} -V curves for the well-oxidized lateral p^+ -n junction devices at a different light intensity at no gate bias and photocurrent I_{ph} as a function of light intensity at 650 nm. (a) I_{ph} -V curves of the $\text{WS}_{0.3}\text{Se}_{1.7}/\text{WO}_x$ lateral p^+ -n junction FETs were measured at 532 nm light exposure under different gate bias V_g conditions. **129**
- Figure 3.3.12.** A band diagram and the schematic of $\text{WS}_{0.3}\text{Se}_{1.7}/\text{WO}_x$ lateral p^+ -n junction at thermal equilibrium state under illumination. The change of depletion layer width with gate bias V_g under dark and illumination. **130**
- Figure 3.3.13.** The simulation of optical reflectance at the normal incidence for the $\text{Al}_{0.74}\text{Ti}_{0.26}\text{O}_y(\text{ATO})/\text{Ag}/\text{Si}$ stacked structures, the bulk extinction coefficient k-spectra corresponding to the optical absorption of ATO and Ag used in the simulation and its schematic diagram. **131**

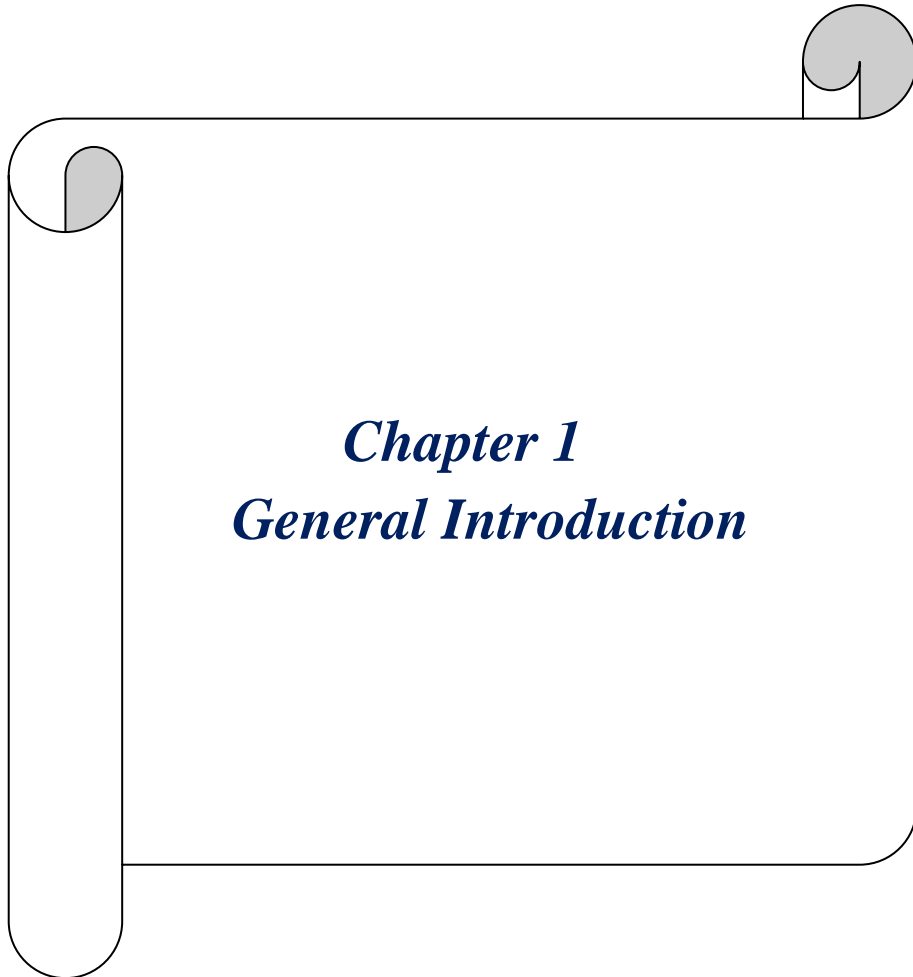
- Figure 3.3.14.** (a) PL spectra for few-layer $\text{WS}_{0.3}\text{Se}_{1.7}$ on 40-nm- thick ATO/p-Si with and without inserting gold mirror layer inserted between ATO dielectric layer and p-Si substrate; (b) $I_{\text{ph}}-V$ curve in the dark and under simulated AM1.5G illumination solar light exposure for $\text{WS}_{0.3}\text{Se}_{1.7}/\text{WO}_x$ lateral p^+-n junction device fabricated on ATO/Au/c-Si and (c) ATO/Ag/c-Si substrate; (d) the preliminary result of series connected two solar cells. **132**
- Figure 3.3.15.** (a) Transfer and (b) output characteristics of $\text{WS}_{0.3}\text{Se}_{1.7}$ p-channel MOSFETs with and without PEDOT: PSS cap layer near one side and both sides at the source/drain electrodes. **134**
- Figure 3.3.16.** The I-V characteristics of PEDOT:PSS/ $\text{WS}_{0.3}\text{Se}_{1.7}$ lateral p^+-n junction solar cell fabricated on *th*- SiO_2 (285 nm)/ p^+-Si in the dark and under AM1.5G simulated solar light exposure. **135**
- Figure 3.3.17.** (a) AFM images of tri-angle shape $\text{WS}_{0.3}\text{Se}_{1.7}$ (the inset shows the line profile) and (b) Raman spectra and PL spectra of the corresponding $\text{WS}_{0.3}\text{Se}_{1.7}$ samples. **136**

List of Abbreviation

2D	Two-Dimensional
TMDCs	Transition Metal Dichalcogenides
Mist-CVD	Mist Chemical Vapor Deposition
$(\text{NH}_4)_2\text{MoS}_4$	Ammonium tetrathiomolybdate
NMP	N-methyl-2-pyrrolidone
$(\text{NH}_4)_2\text{WS}_4$	Ammonium tetrathiotungstate
CH_3NH_2	Methylamine
2-C ₂ H ₇ NO	2-Aminoethanol
DMF	Dimethylformamide
DMSO	Dimethyl sulfoxide
EG	Ethylene glycol
$\text{Al}_{1-x}\text{Ti}_x\text{O}_y$	Aluminum titanium oxide
MoS_2	Molybdenum Disulfide
WS_2	Tungsten Disulfide
WSe_2	Tungsten Selenide
$\text{WS}_{2-x}\text{Se}_x$	Tungsten Sulfoselenide
MOSFETs	Metal Insulator Semiconductor FETs
CMOS	Complementary MOS
CBM	Conduction band minimum
VBM	Valence band maximum
E _g	Energy band gap
PMMA	Poly-methyl Methacrylate
PDMS	Polydimethylsiloxane
SiO_2	Silicon Dioxide
ATO	Aluminium Titanium Oxide
rpm	Rotation Per Minute
sccm	Standard cubic centimeter per minute
OM	Optical Microscope
SEM	Scanning Electron Microscope
TEM	Transmission Electron Microscope
AFM	Atomic force microscopy

PL	Photoluminescence
UV-Vis	Ultraviolet-visible
XPS	X-ray photoelectron spectroscopy
AES	Auger electron spectroscopy
UPS	Ultraviolet photoelectron spectroscopy
KPM	Kelvin probe microscope
FT-IR Spectroscopy	Fourier Transform Infrared Spectroscopy
FMPS	Fast Mobility Particle Sizer
SE	Spectroscopic Ellipsometry
XRD	X-ray Diffraction
PVD	Physical Vapor Deposition
MBE	Molecular Beam Epitaxy
PLD	Pulsed Laser Deposition
CVD	Chemical Vapor Deposition
PECVD	Plasma Enhanced CVD
MOCVD	Metal-Organic CVD
ALD	Atomic Layer Deposition
N ₂	Nitrogen
Ar	Argon
H ₂	Hydrogen
He	Helium
T _f	Tabular Furnace Temperature
F _d	Dilution Gas Flow Rate of N ₂
n/p-Si	n/p-type Silicon
Al _{1-x} Ti _x O _y	Aluminum Titanium Oxide
D _p	Droplet Size
nm, μm	Nanometer, Micrometer
M/L	Mole/Litre
sccm	Standard cubic centimeter per minute
MHz	Mega Hertz
E _f	Fermi Level
E _i	Intrinsic Level
μ	Carrier Mobility

C_{ox}	Oxide capacitance
I_{DS}	Drain to Source Current
V_g	Gate Voltage
V_{DS}	Drain to Source Voltage
L	Length of Channel
W	Width of the Channel
V_{th}	Threshold Voltage
SS	Subthreshold Voltage
RMS	Root means square
κ	Boltzmann Constant
g_m	Gain



Chapter 1
General Introduction

Chapter 1: General Introduction

1.1 A smart two-dimensional materials system beyond silicon

Modern electronics was started from the discovery of the transistor operation by John Bardeen, Walter Brattain, and Wiliam Shockley in the late 1940s. It aims to provide new functionalities and improve user interaction and experiences. To the initial development of integrated circuits (ICs) technologies in the early 1950s, silicon-based semiconductor devices soon replaced germanium-based transistors developed by Kilby (2000 Nobel Prize in Physics)^{1,2}. The demand for the miniaturization of the chip size and the increase of computing power is the driving force for the development of advanced silicon technology. As suggested by Gordon Moore in 1965, the co-founder of Intel, the number of transistors in dense integrated circuits doubles every 18 months (Figure 1.1a)^{3,4}. Since the gate length L_g of the MOSFET is approaching below 10 nm (Figure 1.1b), the size of individual silicon atoms (0.2 nm) would be a hard physical limit because of short channel effects, although the use of tri-gate structure Fin-FET overcomes this short channel effects partially. The short channel effect includes a series of effects such as a reverse leakage current, threshold voltage roll-off, mobility reduction, velocity saturation, hot carrier effects, drain-induced barrier lowering (DIBL), and punch through (Figure 1.1c-d) that affect severely the FETs performance.

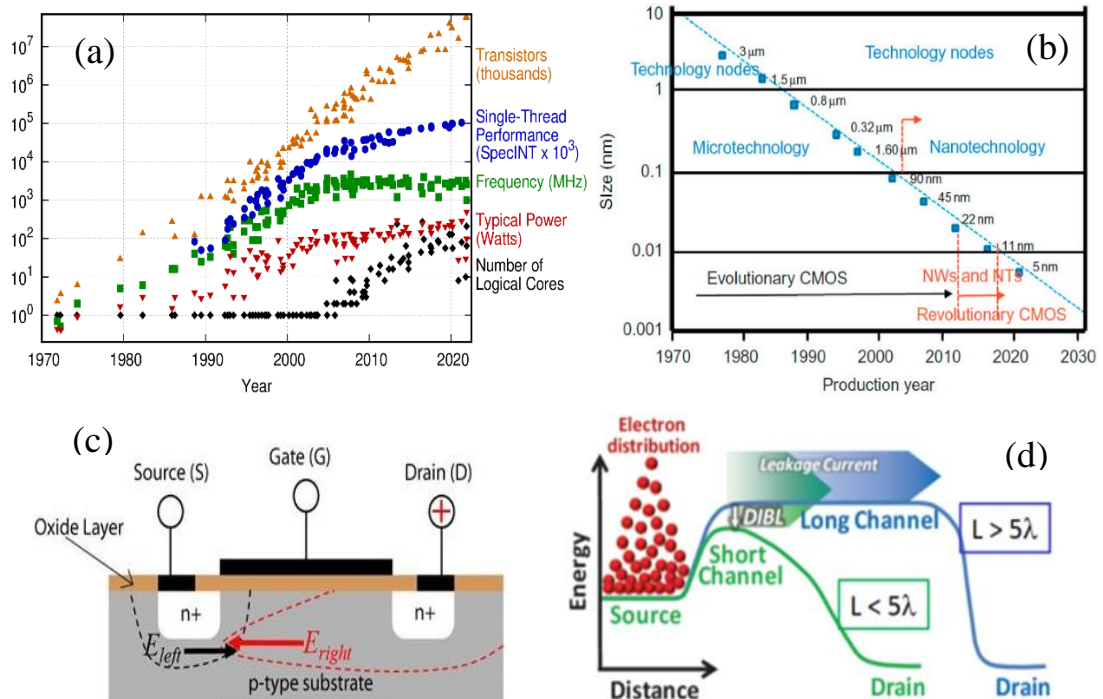


Figure 1.1. (a) 50 Years of microprocessor trend data: the number of transistors per microprocessor chip, frequency, typical power, and the number of logical cores; (b) miniaturization of the transistor gate length in different technology nodes and production years; (c) short channel effect and punch through; (d) drain induced barrier lowering. Reprinted with permission from references^{5,6}.

The leakage current increases the power dissipation, threshold voltage reduction makes it difficult to turn the transistor off completely, the velocity saturation decreases the current drive, and electrostatic coupling between the source and drain by the DIBL effect, makes the gate ineffective (punch through). Surface scattering degrades the mobility of charge carriers. Apart from these factors, impact ionization and hot carrier effects seriously impair the performance by diverging MOSFET behavior. However, when the channel thickness scaling below 10 nm in silicon-based FETs degrades the carrier mobility severely due to the roughness-induced fluctuation of the electron charge density⁷. To overcome these series of impacts and pursue Moore's law, the numerous actions have been taken to scale down the devices and to use the space on the chip more efficiently including the exploration of new materials, adoption of new chip designs, shortening the channel length, 3D structures FETs, etc.^{8,9}. So far, the transformation of the conventional planar metal-oxide-silicon field-effect transistor (MOSFET) structure to three-dimension (3D) structures such as tri-gate fin-FET and vertical TFT will face the same limitation of short channel effect, since they are also fabricated based on silicon MOSFET concept.

In recent years, there is much interest in new applications for smart systems including flexible circuits, wearable sensors for health monitoring, wearable electronics, biomedical devices, flexible display, and human-machine interfaces together with the non-planar devices^{10,11}. These wide applications are also a critical direction of semiconductor technology of conventional wafer-based silicon electronics. Thus, applying new material instead of silicon such as two-dimension (2D) TMDCs materials including graphene, MoS₂, WS₂, MoSe₂, WSe₂, and MoTe₂ are considered to be an ideal candidate due to their naturally passivated surface, ultra-thin body thickness and higher electron effective mass than silicon¹². A list of the 2D materials family is shown in [Figure 1.2](#). Additionally, the development of compliant fabrication methods including well-controllability, high growth rate, and low growth temperature with stoichiometry composition is also an important issue.

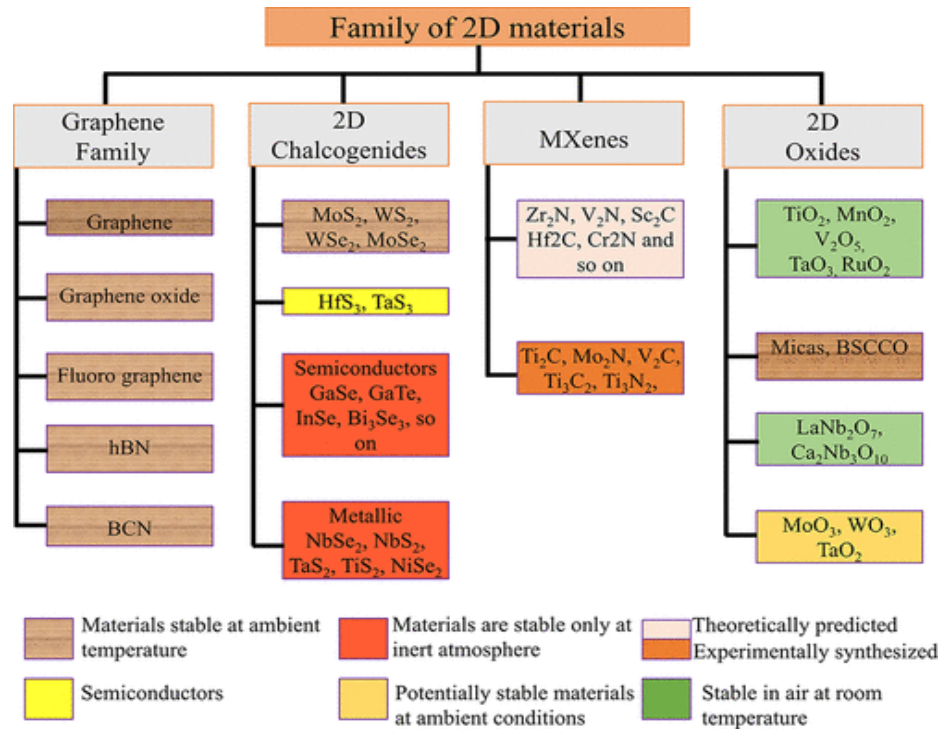


Figure 1.2. 2D materials families. (BSCCO is bismuth strontium calcium copper oxide, and BCN or borocarbonitride). Reprinted from references¹³.

The development of graphene and the nanotechnology revolution brought new interest in layered 2D materials. As a 2D crystal, graphene firstly attracted significant attention by showing possibilities for the development of faster transistors with high mobility, large gain, and low consumption energy¹⁴. In 1962, graphene was observed first in electron microscopes by Russian scientists, but only studied the material supported on metal surfaces. The successful isolation of graphene was conducted in 2004 by Andre Geim and Konstantin Novoselov at the University of Manchester were awarded the Nobel Prize in Physics in 2010 for their groundbreaking experiments regarding the two-dimensional material graphene¹⁵. The graphene has a hexagonal lattice structure with two carbon atoms in each unit cell and it has a Brillion zone (BZ) at six corners with degenerate conduction and valance bands, thus it has no energy band gap. The graphene-channel transistors usually show ambipolar behavior with a low on/off current ratio¹⁶. Numerous investigations are continuing to generate a sufficiently large bandgap for practical applications.

In the latter, the hexagonal boron nitride (h BN) has a repeated hexagon structure with atomic sheets with each side of the hexagon being a boron and nitrogen combination instead of the carbon. The h-BN is an insulator with a 4.5 eV band gap (mono layer) even though it has the same structure, therefore limiting its application in MOSFETs. On the other hand, the black phosphorus (BP) is consisted of only phosphorus atoms and has a layered structure. Among many types of phosphorous structure, the most stable structure for an allotrope is orthorhombic with unique angle-dependent in-plane conductivities. Each phosphorus atom is connected to two parallel adjacent atoms and a downward or upward one in black phosphorus forming ring oscillation. The BP has a band gap between graphene and BN but dispersed band structure in bulk form and comparatively strong coupling among layers^{17,18}. The crystal structure of graphene, boron nitride, black phosphorus, and 2D TMDCs with different polymorphs (phases) are shown in [Figure 1.3](#).

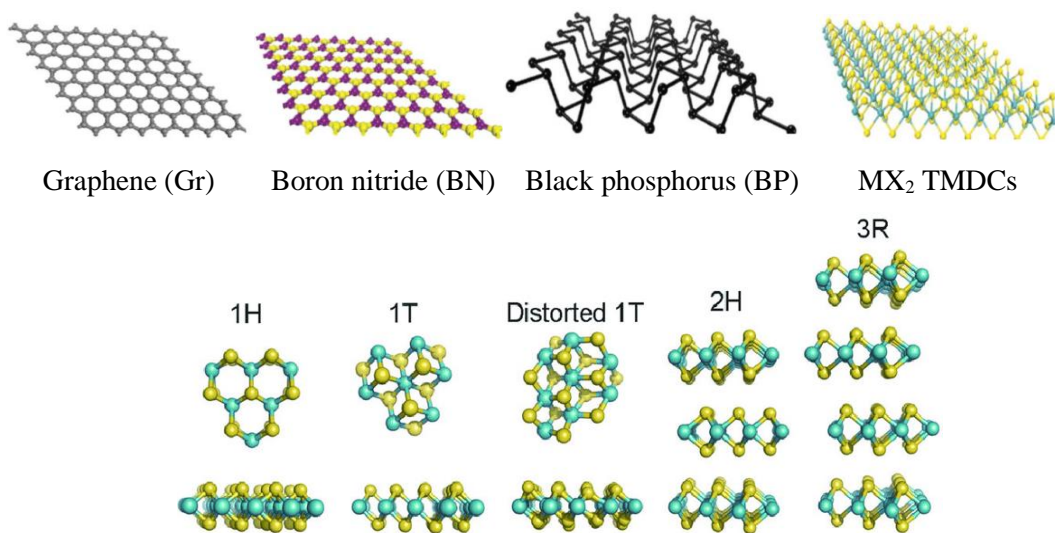


Figure 1.3. Crystal structures of graphene, boron nitride, black phosphorus, and 2D TMDCs and polymorphs (phases) of 1H phase, 1T phase (ideal), distorted 1T', 2H phase, 3R phase^{18,19}.

On the other hand, 2D materials such as transition metal dichalcogenide (TMDC) have properties that are different from the graphene and low band gap Boron nitride (BN) and Boron phosphide (BP). In the 1960s-1980s, TMDs were a subject of interest due to their wide range of material properties from semiconductors, metals, semimetals, and even superconductor²⁰. The atomically thin 2D TMDs materials offer a comparable electrical property to conventional bulk semiconductors and provide an extra advantage like flexibility, transparency, and controllable electrical and optical properties through the engineering of layer thickness, composition, and configuration²¹⁻²³. TMDC

materials have a bandgap, therefore, it is much easier to obtain transistors with a large on/off ratio. In addition, the TMDC monolayer does not have an inversion region that allows generating a new degree of freedom of carriers²⁴. TMDs have the chemical formula MX_2 , where M is a transition metal element from group VI (Mo, W) as well as, from group IV (Ti, Hf, etc.), group V (Ta, V, etc.), and X is chalcogen (S, Se or Te). The lattice structure of the TMDs is generally an X-M-X “sandwich” structure, where metal atoms sit in between the top and bottom hexagonally ordered chalcogen atoms, and the oxidation states of M and X are +4 and -2, respectively. The lone-pair electrons of the chalcogen atoms self-terminate the surfaces and eliminate dangling bonds and each TMD layer is around 6 - 7 Å thick^{25,26}. The monolayers TMDC have an energy band gap because of the strong spin-orbit coupling. It makes a spin-orbit splitting of several hundred meV in the valence region and a few meV in the conduction. The bonding force between the layers for TMDC is Vander Waals force²⁷. It was demonstrated that TMD semiconductors can undergo indirect-to-direct bandgap transition when decreasing the thickness from bulk to monolayer. Furthermore, the bandgap can be tuned by applying strain or by doping external elements, resulting in tunable electric and magnetic properties²⁸. Several selective applications of 2D TMDCs in electronic, optoelectronic, and energy devices are depicted in Figure 1.4.

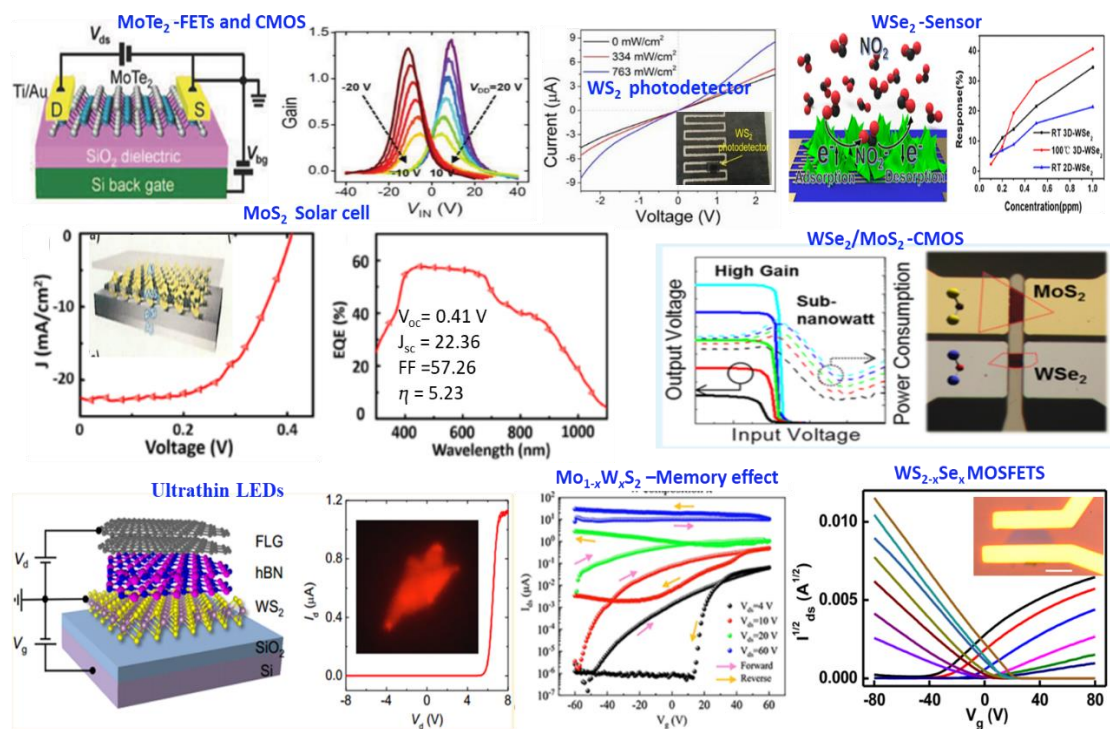


Figure 1.4. 2D transition metal dichalcogenides based electronic, optoelectronic, and energy devices. Reprinted with permission from references²⁹⁻³⁵.

Large-area, twisted TMDCs show unique optical properties and charge transport such as tunable photoluminescence, higher carrier multiplication, and topological superconductivity, which are essential to realizing high-frequency electronics and photodetection with ultrahigh sensitivity. This can potentially extend the horizons of present device structures by either the development of all 2D devices or a synergistic combination of 3D and 2D systems and thus understand high-performance optoelectronics including the hot-electron transistors (HETs), broadband ultrafast photodetection, or photo gain via carrier multiplication (Figure 1.5)³⁶. The evolution of 2D heterostructure-based devices with the features of being ultrafast and weakly light sensitive and having low power consumption and biocompatibility.

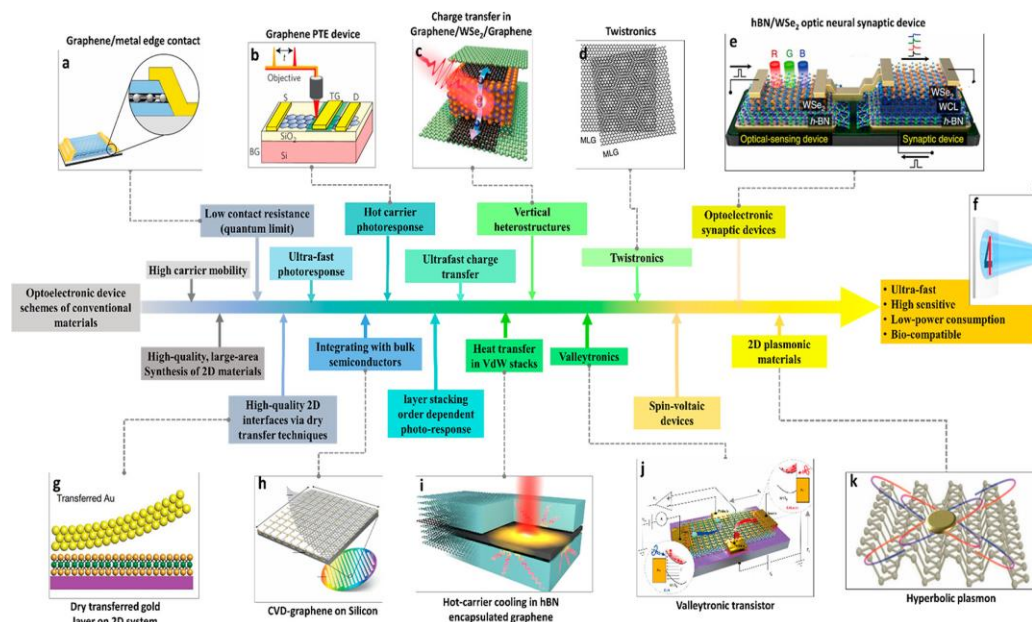


Figure 1.5. Evolution of 2D heterostructure-based devices/systems with the features of being ultrafast and weakly light sensitive and having low power consumption and biocompatibility. The insets include: (a) 2D material/metal edge contact based on the hBN/graphene/hBN heterostructure (b) Graphene photothermal electric (PTE) device (c) Charge transfer in a graphene/WSe₂/graphene heterostructure (d) Twistronics based on twisted bilayer graphene. (e) hBN/WSe₂ heterostructure-based optic neural synaptic device. (f) Schematic of the human optic nerve system (g) Dry transferred Au layer on the 2D MoS₂ system (h) CVD graphene on silicon (i) Hot-carrier cooling in an hBN-encapsulated graphene heterostructure (j) Valleytronic transistor based on the Au NPs/MoS₂ heterostructure (k) Hyperbolic plasmon based on anisotropic 2D materials. Reprinted with permission from reference³⁶.

1.2 Properties of 2D TMDCs semiconductors: MoS₂ and WS₂, WSe₂ and WS_{2-x}Se_x

Molybdenum disulfide (MoS₂)

The MoS₂ has emerged as a promising low-dimensional semiconductor material due to its exceptional electrical, optical, and mechanical properties. It has been the first and most investigated member owing to its excellent properties; tunable band gap from an indirect bandgap of 1.2 eV (bulk) to a direct bandgap of 1.9 eV (monolayer) in addition to the ambient stability, valley Hall effect, high carrier mobility $\sim 200 \text{ cm}^2 \text{ V}^{-1} \text{ s}^{-1}$ and the on-off ratio of $\sim 10^8$ that makes it suitable for a wide range of electronic applications^{37,38}. A band structure of MoS₂ in bulk, multilayer, and monolayer are shown in Figure 1.6.

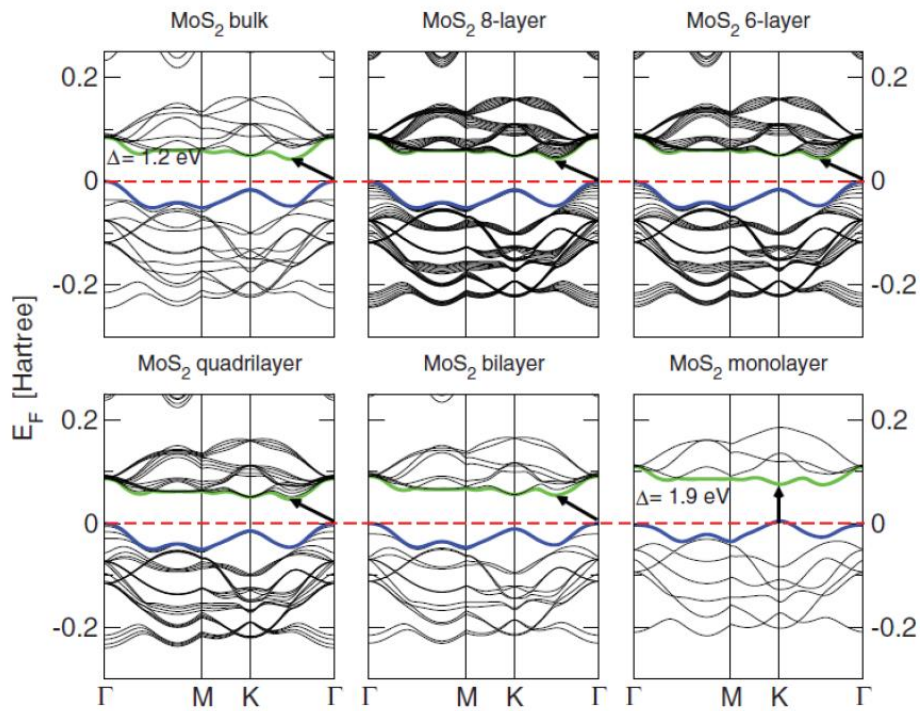


Figure 1.6. Band structure of MoS₂ in bulk, multilayer, and monolayer (obtained from GGA, PBE). The arrow highlights the fundamental band gap. Reprinted with permission from references^{39,40}.

Bulk MoS₂ is composed of weakly bonded by van der Waals force (vdW) MoS₂ monolayers. Each monolayer of MoS₂ consists of a hexagonally packed S-Mo-S unit. MoS₂ exists in three polytypes: (a) 1T (octahedral coordination of Mo atom), (b) 2H (trigonal prismatic) and (c) 3R (trigonal prismatic). 2H and 3R are thermodynamically stable polytypes while 1T polytype is metastable and changes at 300. 2H and 3R

polytypes share trigonal prismatic coordination of Mo atom but differ in stacking order of monolayers in bulk structure. The present research is focused on the 2H polytype which is the most abundant in Earth's crust⁴¹. Figure 1.7 shows the hexagonal structure of MoS₂ (2H-MoS₂) as a whole hexagonal symmetry in which, the Mo atom has trigonal prismatic coordination. There are six S atoms bonded to each Mo atom with a distance of 2.42 Å and with internal displacement $z=1.2$ Å. This phase has two layers per unit therefore it is named 2H. In the 2H phase, the S atoms below the Mo atom are positioned exactly below the three S atoms which are bonded above the Mo atom because of this orientation. Bulk MoS₂ exists in this 2H phase and it behaves as a semiconductor since the d orbitals are fully occupied⁴².

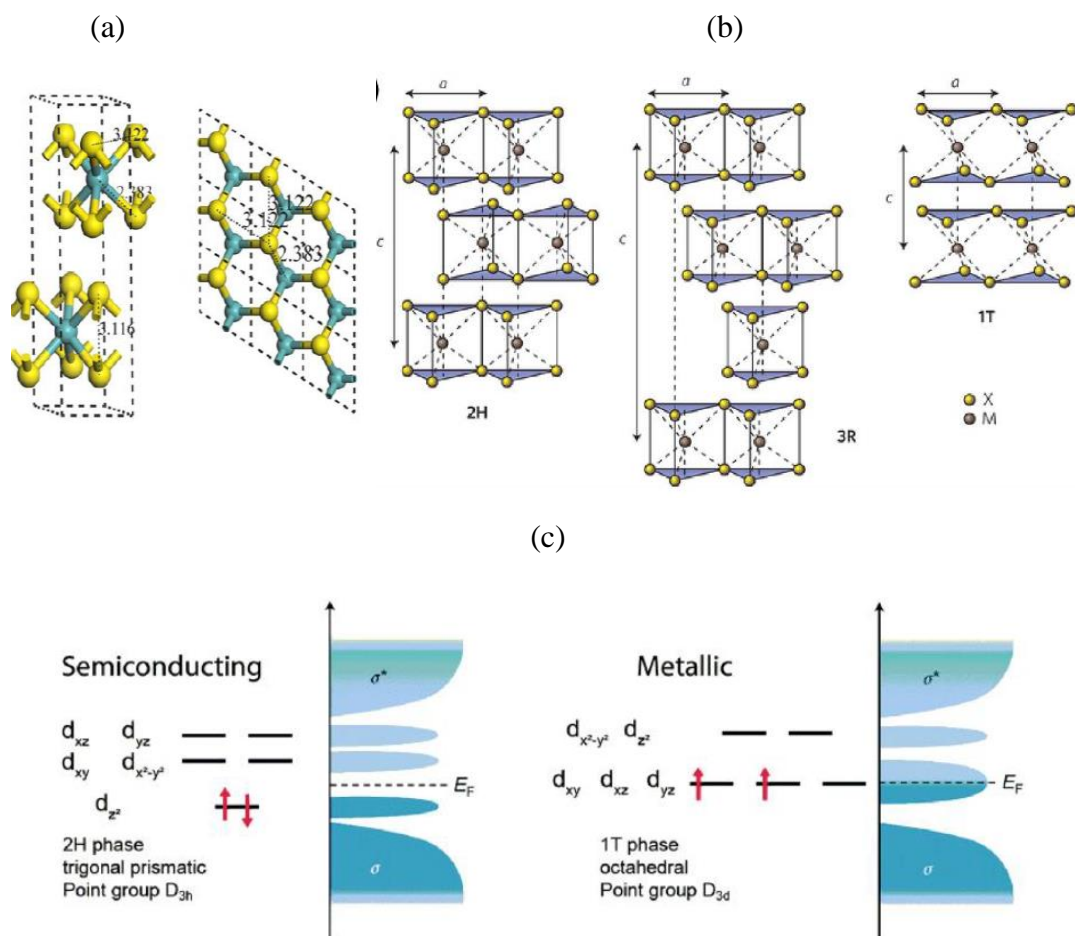


Figure 1.7. (a) Bulk 2H-MoS₂ side view and top view of single MoS₂ monolayer (3×3-unit cells). (b) Polytypes of TMDs: 2H, 3R, and 1T lattice (c) The graphical depiction of d-orbitals in TMDs. 2H TMD shows a primarily semiconducting nature because of the filled d_{z^2} and empty d_{xy} and $d_{x^2-y^2}$ orbitals; the 1T form is metallic because of the partially filled t_{2g} band (d_{xy} , d_{xz} , d_{yz}). Reprinted with from references^{40,43}.

Tungsten disulfide (WS₂)

WS₂ is notable one of the TMD materials that have superior properties like relatively high carrier mobility, large spin-orbit splitting, large exciton binding energy, and strong photoluminescence (PL). These properties make it idle for a wide range of applications such as photodetectors, transistors, light-emitting devices (LEDs), etc.⁴⁴. The reported articles demonstrated the transition from indirect to direct semiconductor with the transition from bulk down to monolayer. The band gap value is greater for monolayer than for bulk form of material. Figure 1.8 represents the band structures of WS₂. For bulk and monolayer of WS₂, the indirect band gap is 1.3 eV and the direct band gaps are 2.1 eV respectively are observed⁴⁵.

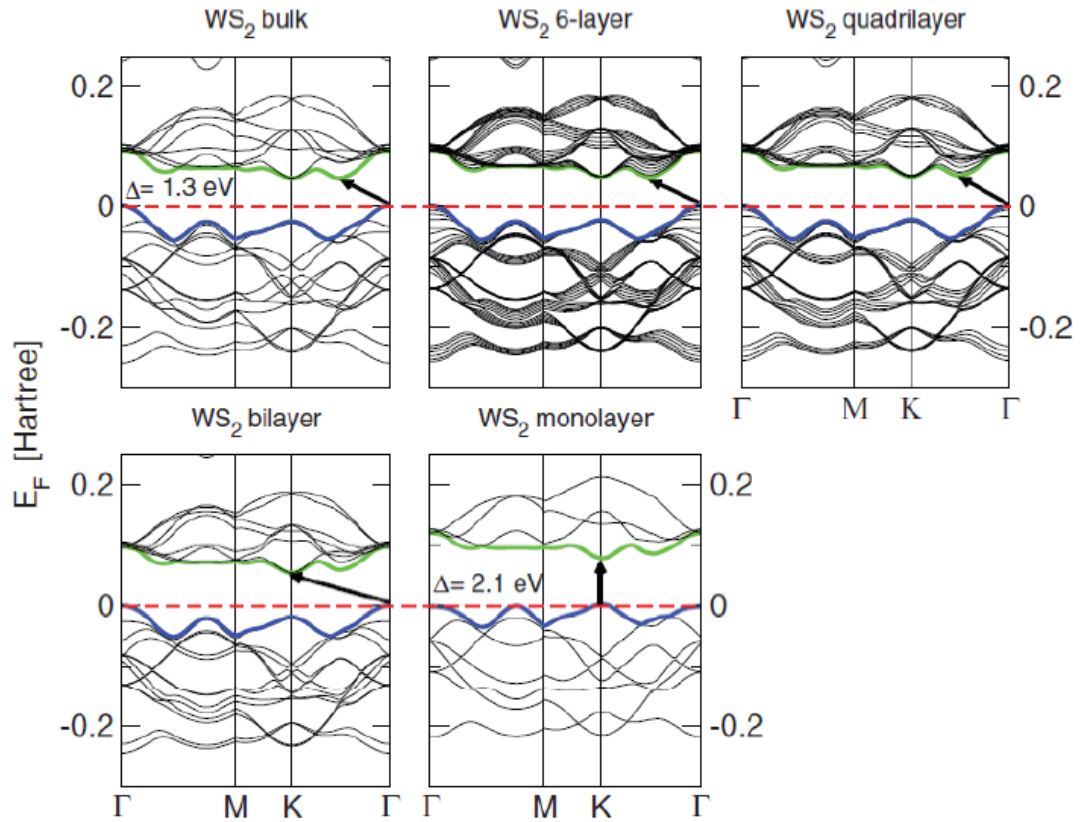


Figure 1.8. Band structure of WS₂ in bulk, multilayer, and monolayer. The arrow highlights the fundamental band gap. Reprinted with permission from references^{39,40}.

WS₂ has a layered crystal structure in which each layer consists of three atomic planes with each of the atomic planes having the hexagonally packed atoms⁴⁶. The W metal atom plane is sandwiched between two planes of S atoms, forming the S-W-S structure. The distance between each layer is about 0.65 nm and absence the dangling bonds but exists van der Waals interaction between the surfaces of each layer, which makes

the WS₂ surface very stable and nonreactive. the WS₂ crystal can be mechanically exfoliated by scotch tape owing to the weak interlayer van der Waal interaction. Figure 1.9 shows the stable coordination of W is trigonal prismatic, which is the case for 2H phase WS₂ (1H for phase single layer) and the octahedral coordination, which can be seen in the meta-stable 1T phase WS₂. Detailed discussion about the polymorphs due to the stacking difference and lattice distortion can be found elsewhere⁴⁷. The crystal lattice of 2H WS₂ belongs to the non-symmorphic hexagonal space group $P6_3/mmc$ (D^4_{6h}) that has space inversion symmetry. The crystal lattice of monolayer WS₂ belongs to $P6_m2(D^1_{3h})$ ⁴⁸. The even layer-number WS₂ has the space inversion symmetry while the odd layer-number WS₂ lacks the space inversion symmetry from the crystal structure.

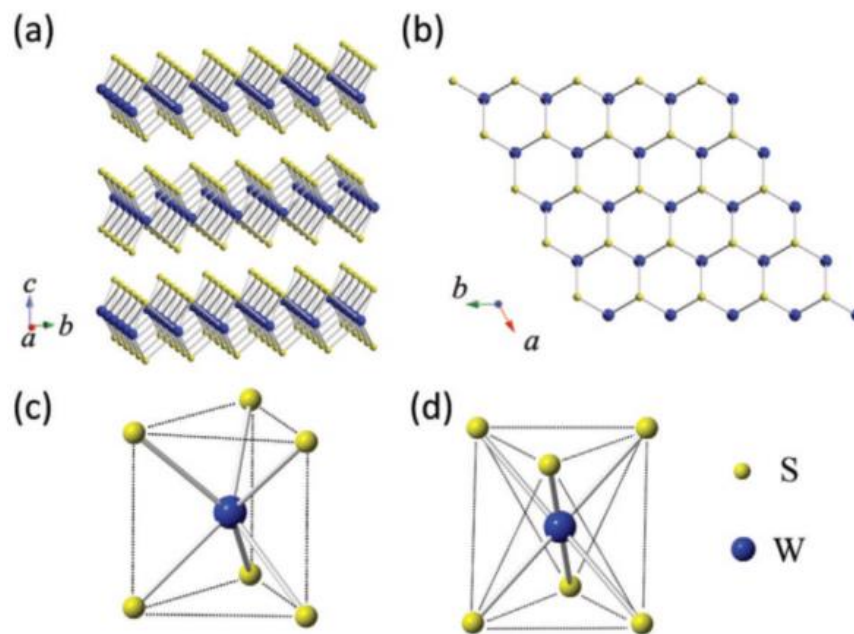


Figure 1.9. Crystal structure of WS₂: a) Schematic view of the layered structure, b) Schematic view from the c-axis, c) Unit cell of the trigonal prismatic structure, d) Unit cell of the octahedral structure. Reprinted with permission from reference⁴⁴.

Tungsten diselenide (WSe₂)

Tungsten diselenide (WSe₂) is the emerging candidate in the family of TMDC and is successfully utilized for various applications like in photodetectors, field-effect transistors (FETs), photocatalysts, etc.^{49,50}. It has a typical group six TMDC lattice structure, where W atoms are confined in a trigonal prismatic coordination sphere near Se atoms. The crystal structure of single-layer tungsten diselenide (WSe₂) is shown in

Figure 1.10. The WSe₂ possesses unique properties such small band gap of 1.0 eV (indirect) and 1.7 eV (direct) with large adjacent layer spacing of 0.648 nm (2 times larger than that of graphite) with a higher density of 9.32 g cm⁻³. Therefore, WSe₂ has a high volumetric capacity, and these properties help manifest this material for prospective electronic device applications⁵¹.

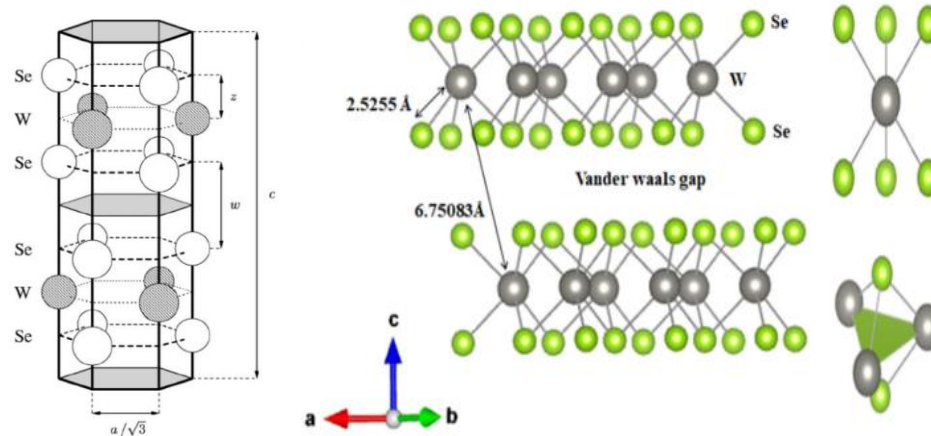


Figure 1.10. The crystal structure of single-layer tungsten diselenide (WSe₂) and its stacking layered structure. Reprinted with permission from references^{52,53}.

An important point in the band structure is the Σ point, the conduction band minimum of the bulk crystal. Going from the bulk crystal to the monolayer, the minimum at Σ shifts upwards and in the monolayer, the K-valley becomes the conduction band minimum. Consequently, the monolayer exhibits a direct band gap, and thus a different optical behavior⁵⁴. An electronic band structure of bulk and monolayer WSe₂ is shown in Figure 1.11.

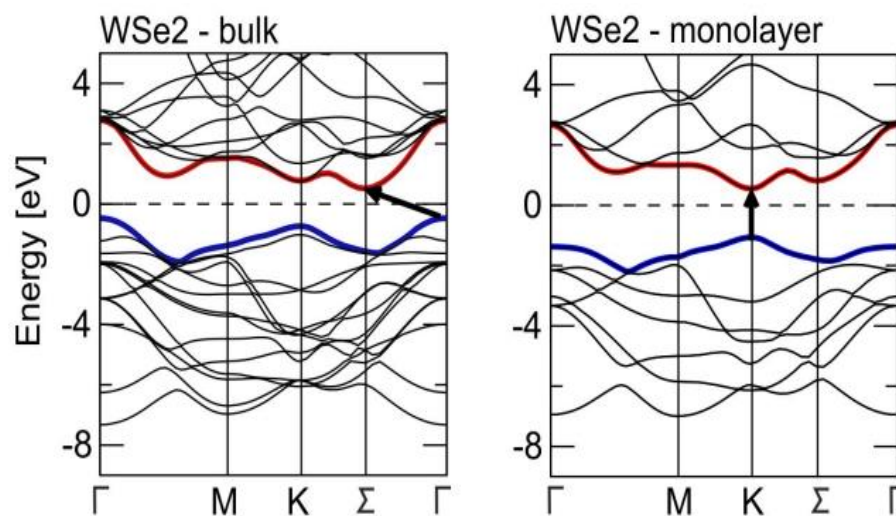


Figure 1.11. Electronic band structure of bulk and monolayer WSe₂. The valence band maximum and the conduction band minimum are highlighted in blue and red, respectively. Reprinted from reference⁵⁴.

A typical experimental and theoretical values of lattice constant for bulk and single-layer TMD materials are shown in [Table 1.1](#) and [Table 1.2](#).

Table 1.1. Experimental and theoretical lattice constants of bulk TMDs. Lattice constants are provided in Å. Reprinted with permission from reference⁴⁰.

TMD bulk	Symmetry	Theory	Experiment
MoS ₂	hexagonal	a = 3.173 c = 12.696 [PBE] a = 3.122 c = 11.986	a = 3.160 c = 12.295
MoSe ₂	hexagonal	a = 3.309 c = 13.323 [PBE]	a = 3.288 c = 12.900
MoTe ₂	hexagonal	-	a = 3.530 c = 13.882
WS ₂	hexagonal	a = 3.164 c = 12.473 [PBE]	a = 3.154 c = 12.362
WSe ₂	hexagonal	a = 3.319 c = 13.729 [PBE]	a = 3.280 c = 12.950
WTe ₂	orthorhombic	a = 6.34 b = 3.54 c = 14.44	a = 6.282 b = 3.496 c = 14.07

PBE: Perdew-Burke-Ernzerhof functional

Table 1.2. Theoretical in-plane lattice constants of monolayer TMDs with hexagonal symmetry obtained from different numerical calculations of PBE, LDA, and HSE. Lattice constants are provided in Å. Reprinted with permission from reference⁴⁰.

TMD 1L	Ref. ⁵⁵	Ref. ⁵⁶	Ref. ⁵⁷	Ref. ⁵⁸
MoS ₂	3.19 [PBE]	3.18 [PBE]	3.19 [PBE]	3.18 [PBE]
	3.12 [LDA]		3.13 [LDA]	3.16 [HSE06]
MoSe ₂	3.33 [PBE]	3.32 [PBE]	3.33 [PBE]	3.32 [PBE]
	3.25 [LDA]		3.25 [LDA]	3.29 [HSE06]
MoTe ₂	3.56 [PBE]	3.55 [PBE]	3.56 [PBE]	3.55 [PBE]
	3.47 [LDA]		3.47 [LDA]	3.52 [HSE06]
WS ₂	3.19 [PBE]	3.19 [PBE]	3.19 [PBE]	3.18 [PBE]
	3.13 [LDA]		3.13 [LDA]	3.16 [HSE06]
WSe ₂	3.32 [PBE]	3.32 [PBE]	3.32 [PBE]	3.32 [PBE]
	3.25 [LDA]		3.25 [LDA]	3.29 [HSE06]
WTe ₂	3.56 [PBE]	-	3.56 [PBE]	3.55 [PBE]
	3.48 [LDA]		3.47 [LDA]	3.52 [HSE06]

PBE: Perdew-Burke-Ernzerhof functional, LDA: Local density approximation

HSE: Heyd-Scuseria-Ernzerhof functional

Tungsten sulfoselenide (WS_{2-x}Se_x)

Alloy structures and heterostructures are two effective ways to realize precise modulation of the electronic structures of TMDs. So far, lots of TMD alloys with homogeneous compositions have been synthesized, and the preparation of TMDs heterostructures has also got great progress that brought big innovations in the field of nanoelectronics, optoelectronics, and photonics⁵⁹. Two-dimensional (2D) transition-metal dichalcogenides (TMDs) with tunable bandgaps are highly significant for the applications in nanophotonic, electronic, and optoelectronic due to their efficient modulation of the physical and chemical properties. As is known, the application of semiconductor materials is closely related to their bandgaps (composition). It reported that the spectrally tunable and robust electroluminescent devices are possible to fabricate with the change of the alloy content and the thickness uncovering the indirect to direct gap crossover as a function of the number of layers and tunable content of sulfur and selenium elements^{33,61}. The evolution of the valence band structure for different layer thicknesses is shown in [Table 1.3](#).

Table 1.3. Spin-orbit splitting at K and VBM at Γ and K was obtained from the experimental ARPES data for mono, bi-, and tri-layer W_{2(1-x)}Se_{2x} (x= 0.8). Reprinted from reference⁶².

$WS_{2(1-x)}Se_{2x}$ ($x = 0.8$)	1 ML	2 ML	3 ML
VBM at Γ (eV)	-1.66	-1.16	-1.27
		-1.78	-1.60
		-	-2.10
VBM at K (eV)	-1.16	-1.10	-1.75
	-1.66	-1.52	-2.13
SO splitting at K (eV)	0.5	0.42	0.38

1.3 Techniques for the synthesis of 2D transition metal dichalcogenides TMDCs and benefits of Mist-CVD

Transition metal dichalcogenides are recognized as lubricants and tribological materials historically owing to their layered structures. Richard P. Feynman proposed the possibility of the use of two-dimensional thin layers instead of their bulk form in 1959⁶³. After that, several efforts have attempted and executed to produce an atomically thin TMD layer using adhesive tape and Li-intercalation in 1966 and 1986 respectively^{64,65}, but, a successful realization of 2D materials was demonstrated by the Manchester group using mechanically exfoliated graphene flakes for modern optoelectronic applications^{66,67}. There are two commonly used exfoliation techniques (a) mechanical exfoliation using the “Scotch-tape” method and (b) liquid exfoliation. In mechanical exfoliation methods use adhesive tape to transfer TMD layers from the bulk crystal to the desired substrate revealing well crystallinity and quality^{66,68}. However, these exfoliation methods are not practical for scalable manufacturing due to poor control of size, layer thickness, and yield. On the other hand, the bottom-up approaches using vapor phase techniques have appeared as a promising method for the controllable and scalable synthesis of TMDs⁶⁹. So far, vapor-based methods, especially chemical vapor deposition (CVD) is found as the most efficacious method to deposit both large-area graphene and TMDs, whereas vapor phase TMD constituent elements (metal and sulfur/selenium) are deposited on the substrate surface through carrier gases at a specified temperature⁷⁰. A list of functional thin-film fabrication methods is shown in [Figure 1.12](#).

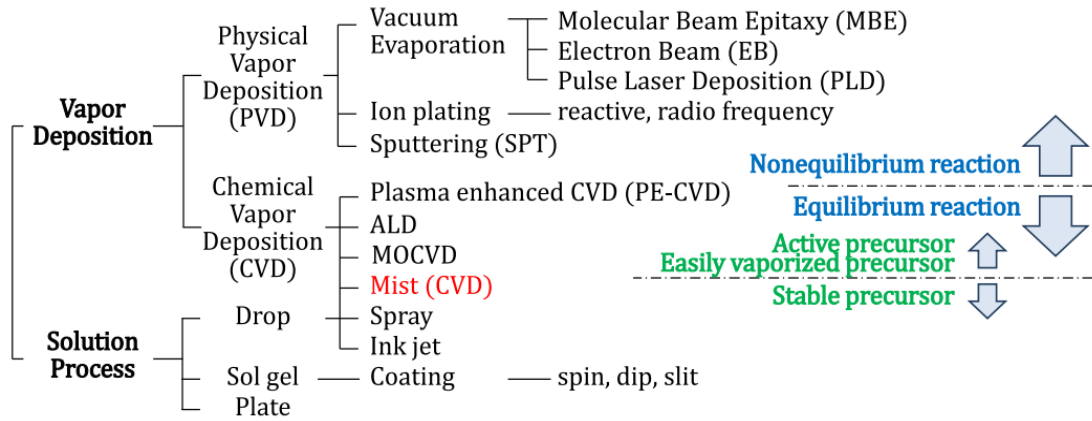


Figure 1.12. Classification diagram of functional thin-film fabrication method. Reprinted with permission from reference⁷¹.

Growth techniques of thin films are classified into three categories based on development scheme, reaction scheme, and reaction condition. The development scheme refers to two ways (a) top-down and (b) bottom-up methods and the reaction scheme includes two processes; (a) gas phase or (b) solution process, whereas the reaction condition includes; (a) non-equilibrium and (b) equilibrium condition⁷¹⁻⁷³. The non-equilibrium process combines all of the physical vapor deposition (PVD): Vacuum evaporation, Pulsed Laser Deposition (PLD), Molecular Beam Epitaxy (MBE), Sputtering, Plasma Enhanced Chemical Vapor Deposition (PECVD), etc., in which the development of a uniform, even, strain-free large area film is challenging. On the other side, an equilibrium condition includes some of the CVD like thermal CVD, Metal-Organic CVD (MOCVD), Atmospheric-pressure CVD (APCVD), Atomic Layer Deposition (ALD), together with sol-gel methods: spin coat, dip coat, and thermal electrode deposition, etc. A schematic of the development of the vapor-phase synthesis of 2D WS₂ with the single domain size corresponds to various methods as depicted in [Figure 1.13](#). So far, a highly active and high vapor pressure material is kept under a vacuum or in an inactive gas environment, or the atmospheric condition in equilibrium method, resulting in chemical reactions to form thin films at the substrate surface. Thus, the solution process at atmospheric pressure is found as a promising method for the synthesis of 2D TMDs, though there is a possibility of remaining inert ingredients in the precursor solution and the formation of cracks during synthesis⁷³.

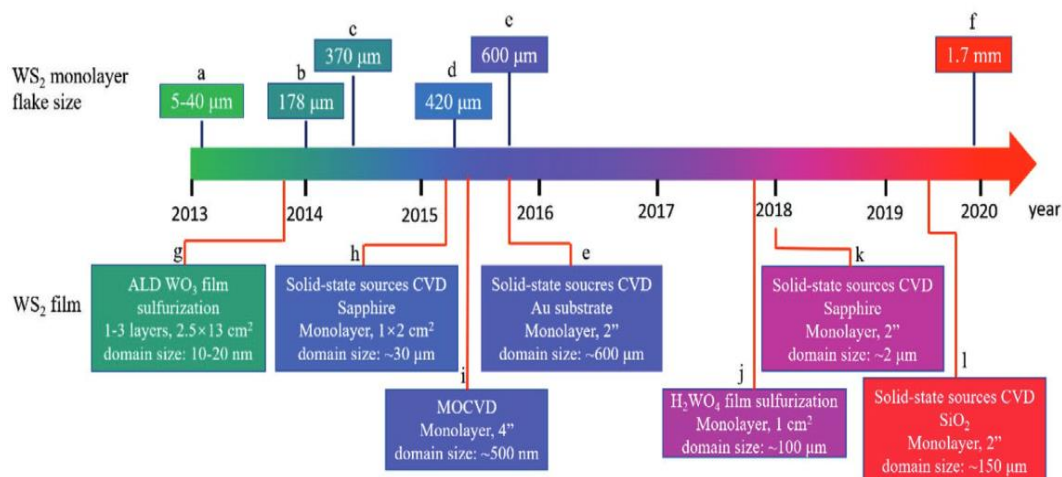
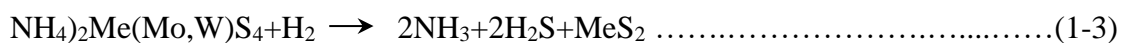


Figure 1.13. Schematic of the development of the vapor-phase synthesis of WS₂. The upper side indicates the development of single domain size, the lower side indicates the development of the growth of large-area WS₂ film by various methods. Reprinted with permission from reference³⁶.

Mist chemical vapor deposition (mist-CVD) is classified as a solution-based equilibrium process with vapor phase reaction at atmospheric pressure^{74,75}. This method combines the benefits of CVD and the solution processes, facilitating the synthesis of controllable atomic layer films. This solution-based vapor phase reaction method is capable to deposit a large area of atomic layer film from the liquid precursor without the inherent limitations observed in other solution-based techniques like spin coating, dip coating, electrode deposition, etc. In a mist deposition system, the mist droplet of the precursor experiences no initial external force, therefore, precursor mist is supplied into the hot-wall reaction chamber from the generation unit at a favorable carrier gas flow rate and furnace temperature, which facilitates uniformly sticking and coalesces of mist droplets on the substrate surface and consequently the formation of uniform large-area films. Thus, mist-CVD is found as independent of the type and shape of the substrate with promising thickness controllability. In addition, the film deposition rates and film properties are determined by the deposition parameters of the mist-CVD system; solution concentration, generation, and carrier gas flow rate, tabular furnace temperature, mist supply time, mist storage time in the reaction chamber, number of repetitions of mist supply for sequential deposition, mesh bias supply, and atomizer power and frequency. Generation of fine mist droplets to obtain a smooth and uniform film with varieties of precursor and respective solvents is still a challenge of this newly introduced deposition approach. Moreover, the optimization of the deposition

parameters to obtain fine mist particles and choice of the effective precursor as well as respective solvents offer a new pathway for the well-controlled formation of 2D-TMDCs atomic layer films using the simple and economical method at atmospheric condition^{73,76}. Additionally, mist-CVD can be employed to synthesize TMDCs alloys thin films; $\text{MoS}_{2-x}\text{Se}_x$, $\text{WS}_{2-x}\text{Se}_x$, $\text{Mo}_{1-x}\text{W}_x\text{Se}_y$, $\text{Mo}_{1-x}\text{W}_x\text{S}_y$, etc. with a chemical combination of precursor constituents and the use of favorable annealing environment, which are economical, chemically stable with low-vapor-pressure and environmentally benign. The thermal decomposition of Mo-containing substances of $(\text{NH}_4)_2\text{MeS}_4$ (Me = Mo, W) for the synthesis of MeS_2 and their ternaries are studied extensively⁷⁷. In the decomposition mechanism of $(\text{NH}_4)_2\text{MeS}_4$ found that Mo_2S_5 or MoS_3 formed upon heating at $<400\text{ }^\circ\text{C}$, whereas MoS_2 or WS_2 formation occurred upon heating up at $\geq 600\text{ }^\circ\text{C}$. The represented transformation processes of $(\text{NH}_4)_2\text{MeS}_4$ to MeS_2 are shown in Equations⁷⁸⁻⁸⁰:



The thermolysis of ammonium thiomolybdates in high vacuum conditions proceeds through the formation of the vertically aligned orientation of MeS_2 structures in a layer-by-layer mode at a temperature of $400\text{ }^\circ\text{C}$ and thereafter, in a horizontal orientation with improved crystallinity along with the merging of adjacent flakes when heating up at a temperature of $T \geq 700\text{ }^\circ\text{C}$ as observed for the formation of few layers MeS_2 on Mo foil upon heating at $500\text{ }^\circ\text{C}$ in Ar ⁸¹. The reaction process shown above is sensitive to the presence of oxygen. $(\text{NH}_4)_2\text{MeS}_4$ is partially changed to MeO_3 if there is oxygen, thus, the reducing atmosphere (H_2 gas) is needed to avoid oxidation during the annealing process. On the other hand, the carbon contamination from the residual solvent may cause a sulfur deficit in the composition or often amorphous film or low crystallinity. Therefore, to prevent sulfur deficiencies in the film and to obtain high-quality MeS_2 . A sulfur atmosphere is found fruitful during the crystallization annealing process even though sulfur atoms are emitted from the film according to the reaction shown in Eq 1-3. N-Methyl-2-Pyrrolidone (NMP) was chosen as a solvent owing to the high stability of the solution, small solvent contamination effect and film uniformity¹⁸. The chemical structure of precursors $(\text{NH}_4)_2\text{MeS}_4$ and some of the favorable solvents used are shown in [Figure 1.14](#).

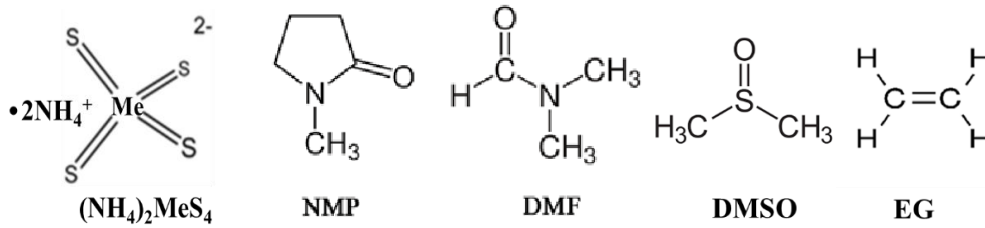


Figure 1.14. Chemical structure of $(\text{NH}_4)_2\text{MeS}_4$ precursor and different solvents of N-Methyl-2-Pyrrolidone (NMP), Dimethylformamide (DMF), Dimethyl sulfoxide (DMSO), and Ethylene glycol (EG).

1.4 Metal oxide field-effect transistors (MOSFETs), complementary MOS, and their electrical parameters

Two-dimensional materials reveal the great potential for future nanoelectronics since the conventional semiconductor technologies face serious limitations in performance as well as power dissipation. The highly scaled field-effect transistors (FETs) based on atomic layer 2D materials enable reduced short-channel effects together with high carrier mobility, which is very essential for the operation of low-voltage, high-performance devices⁸². The richness of the electronic band structure of 2D TMDCs opens up the possibility of use in novel electronic and optoelectronic devices. Thus, proper extraction of important properties is very essential to understanding the degree of quality of 2D FETs. Figure 1.15 illustrates the representative parameters that can be extracted by various electrical characterization methods.

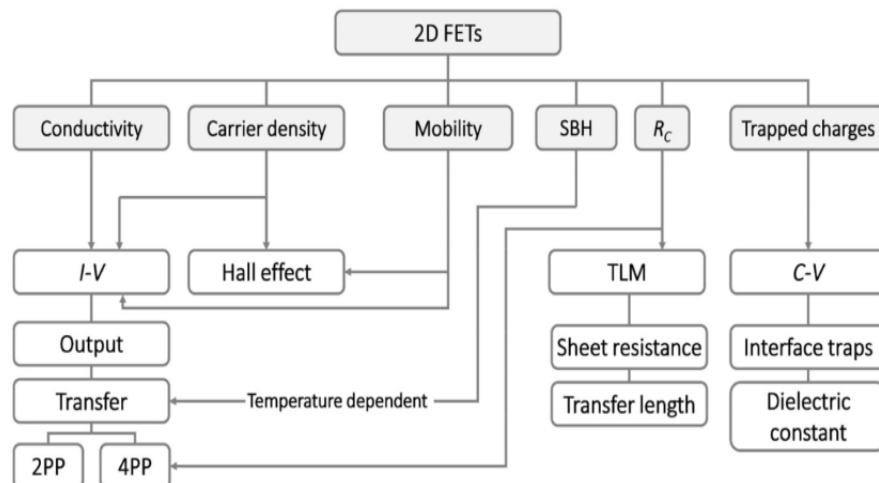


Figure 1.15. Key parameters of 2D FETs and corresponding electrical characterization methods. Reprint from reference⁸³.

The metal contact for achieving alignment of Schottky or ohmic behavior is an important issue for fabricating the MOSFETs device. The behavior of selective TMDCs channel FETs can be tuned by using favorable metal contact. Band alignment of various 2D materials and elemental contact metals. The schematic of bandgap, electron affinity, ionization potential, and charge neutrality level (CNL) values for multilayer 2D materials and the work functions Φ_M of common contact metals is depicted in Figure 1.16.

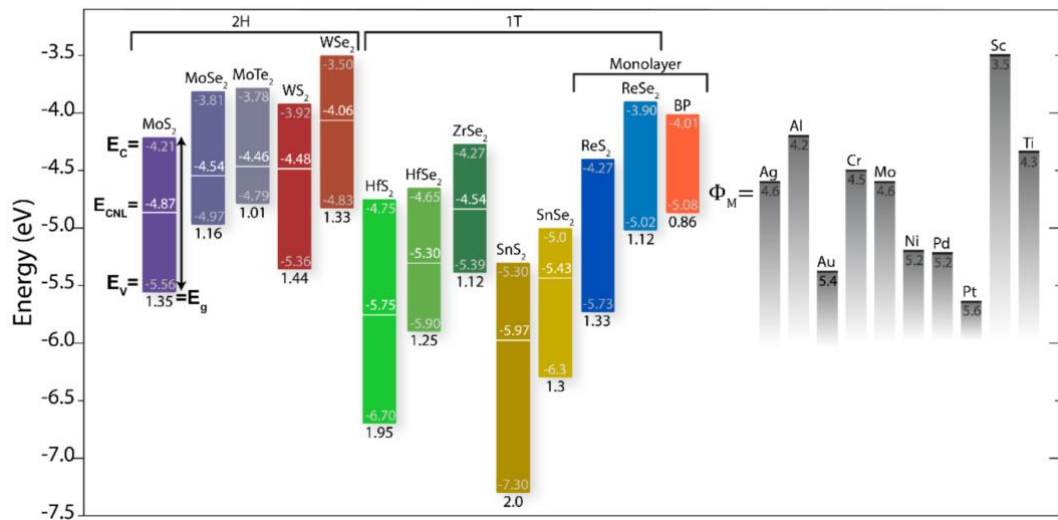


Figure 1.16. Band alignment of various 2D materials and elemental contact metals. Schematic of bandgap, electron affinity, ionization potential, and charge neutrality level (CNL) values for multilayer 2D materials along with the work functions Φ_M of common contact metals. Reprinted with permission from reference⁸².

The I-V measurement is the key electrical characterization technique for understanding the working principle of FETs with a qualitative and quantitative understanding of intrinsic semiconductor properties such as mobility and carrier density, along with external properties like interface states and contact resistance. The performance of the FETs is characterized primarily by measuring the output characteristics (I_D as a function of V_{DS}) along with the transfer (I_D as a function of V_{GS}) characteristics. The linearity of the output characteristics can be used to determine the effect of contact resistance on FET performance. Moreover, the linear behavior does not provide any information regarding the mechanism behind the Ohmic nature of

contacts as doped (gated) Schottky contacts can resemble Ohmic characteristics due to enhancement of the source junction tunneling component. At a small V_{DS} , the output characteristics allow the extraction of important FET parameters as the device acts as a linear resistor in this region. Considering the channel-dominated behavior, the drain current I_D for an n-type 2D FET in the linear regime can be expressed as-

$$I_D = \frac{\mu_n W C_{ox}}{L} [(V_{GS} - V_{TH}) V_{DS}] \dots\dots\dots(1-4)$$

where L , W , μ_n , C_{ox} , and V_{TH} are the channel length, channel width, channel electron mobility oxide capacitance, and the threshold voltage, respectively. But, in the presence of contact resistance R_C for the source and drain junction at small V_{DS} , V_{DS} needs to be replaced as-

$$I_D = \frac{\mu_n W C_{ox}}{L} [(V_{GS} - V_{TH}) (V_{DS} - I_D \cdot 2R_C)] \dots\dots\dots(1-5)$$

On the other hand, The other way to assess the electrical performance of a FET is by utilizing the transfer characteristics that can be obtained by measuring I_D as a function of V_{GS} at constant V_{DS} . This characteristic is used to extract the important parameters; transconductance (g_m), threshold voltage (V_{th}), subthreshold swing (SS), and mobility (μ_{FE})⁸³.

$$g_m = \frac{\partial I_D}{\partial V_G} |_{V_D=const.} = \frac{W}{L} \mu C_{OX} V_D \dots\dots\dots(1-6)$$

$$\mu = \frac{L}{W C_{OX} V_D} g_m \dots\dots\dots(1-7)$$

$$SS = \frac{dV_{GS}}{d(\log I_D)} = \ln(10) \frac{k_B T}{q} \left(1 + \frac{C_{CH}}{C_{ox}} \right) \dots\dots\dots(1-8)$$

The V_T of a MOSFET is defined as the V_G where an inversion layer forms at the interface between the insulating layer and the substrate of the transistor providing a low resistance conducting path and device starts the conduction. Subthreshold swing (SS in V/dec.) is a type parameter to describe the control ability of the gate toward the channel and is defined as the amount of V_G required to increase/decrease I_D by one order of magnitude. However, the SS might increase with drain voltage due to short-channel effects such as charge sharing, avalanche multiplication, and punch through-like effect⁸⁴. On the other hand, the on-current I_D represents the transistor's on-state, while

the off-current transistor is the off-state. The large on/off current ratio reveals negligible leakage current in the device. The V_{th} and SS in shown in Figure 1.17.

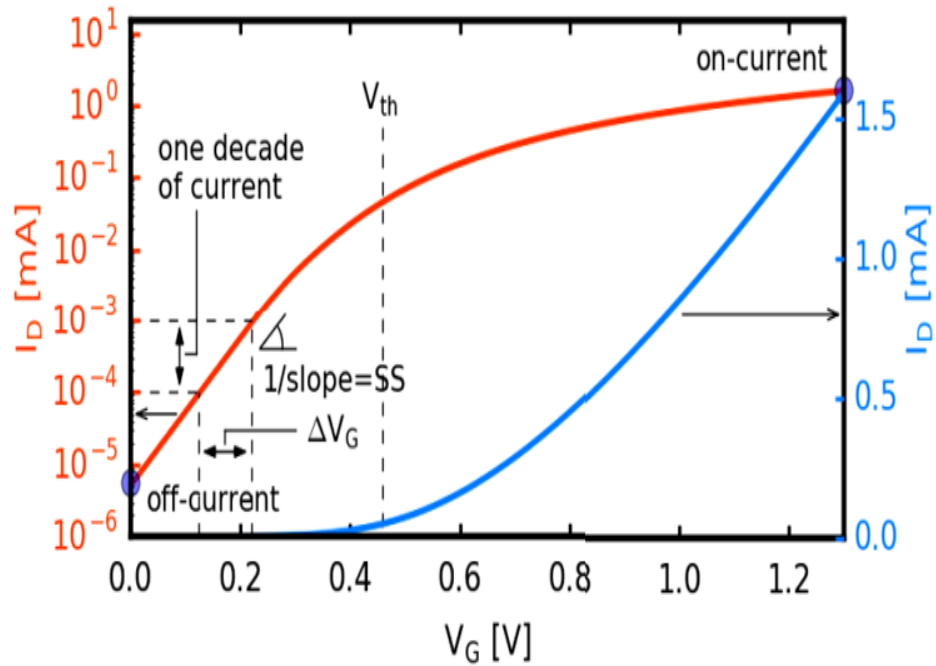


Figure 1.17. Typical I_d – V_g characteristics of an n-MOSFET: Drain current I_d plotted against gate voltage V_g on a log–lin. (red, left scale) and lin.–lin. (blue, right scale) scale. Off-current (current flowing when MOSFET is switched off), subthreshold slope (slope of the subthreshold region in a log–lin. plot), threshold voltage (V_g where inversion layer is formed), and on-current (current flowing in the on-state) are the most important parameters characterizing the I_d – V_g curve. Reprinted from reference⁸⁵.

So far, the cascading of complementary and symmetrical pairs of n-channel and p-channel devices constructs complementary MOSFETs which is a major class of integrated circuits. Two important characteristics of CMOS devices are (a) high voltage gain and (b) low static power consumption. The CMOS technology is used widely in microprocessors, microcontrollers, static RAM, and other digital logic circuits. The inverter circuit and standard symbol are shown in Figures 1.18a, b, and c. The important parameter of a CMOS inverter is gain (gain = $-dV_{out}/dV_{in}$), which refers to the ability of a circuit (often an amplifier) to increase the power or amplitude of an input signal to its output^{84,86}.

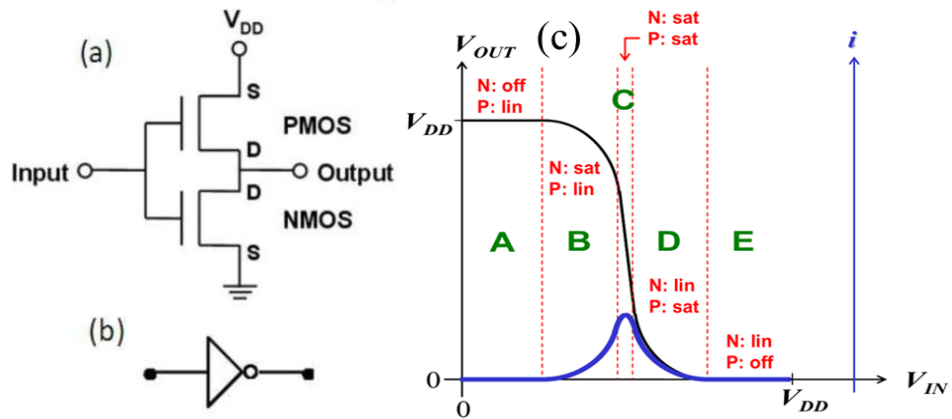


Figure 1.18. (a) Schematic of CMOS inverter circuit; (b) standard symbol; (c) different operating regions of CMOS circuit. Reprinted from references ^{84,86}.

1.5 Motivation and objective of this study

2D semiconductors like MoS₂, WS₂, MoSe₂, WSe₂, and MoTe₂ have a layered structure with single-layer thickness and attracted attention owing to their excellent electrical and optical properties. High-performance TMDCs channel devices are mostly built from flakes produced by mechanical exfoliation of bulk MX₂ crystal using the dry-exfoliation (scotch-tape) technique. Though this technique leads to devices with good performances, the synthesized flakes are of limited size, and difficult to control flakes' size and thickness, which limited their application to large area atomic-scale devices. In addition, the conventional preparation techniques are high temperature and/or vacuum-based techniques such as chemical vapor deposition (CVD), atomic layer deposition (ALD), pulse laser deposition (PLD), spin coating, dip coating, sputtering, etc. Considering the controllability of layer thickness, growth temperature and growth rate, and stoichiometry composition, these processes are not compliant fully to date. Therefore, the scalable and controllable methods are required to prepare large-area atomically thin TMDCs at a low temperature and atmospheric pressure with the stoichiometry composition. In this perspective, Mist chemical vapor deposition (mist-CVD) is one of the competitive methods for preparing both the TMDCs and metal oxide thin films from chemically stable and low-vapor-pressure materials with gas-phase reactions.

The objective of this research is to the development of large-area atomic layer stoichiometry TMDCs films, specifically MoS₂, WS₂, and WS_{2-x}Se_x through a solution-processed vapor phase reaction; mist chemical vapor deposition (mist-CVD) on high-κ thin Al_{0.76}Ti_{0.26}O_y dielectric layer coated p⁺-Si substrate and their applications in different electronic and optical devices such as MOSFETs, CMOS, photodetector and solar cells. So far, motivated by the importance in the realizing wide ranges of applications of 2D TMDCs, and dielectric layers, this study mainly focuses on the following issues:

- Direct synthesis of large-size, atomic layer 2D TMDCs films: MoS₂, WS₂, and WS_{2-x}Se_x by mist-CVD.
- Application of synthesized MoS₂, WS₂, and WS_{0.3}Se_{1.7} films on high-κ, thin, mist-CVD Al_{0.76}Ti_{0.26}O_y dielectric layers in electronic and optical devices such as MOSFETs, CMOS, photodetectors Solar cells etc.
- Fabrication of WS_{0.3}Se_{1.7}/WO_x lateral p⁺-n junction-based multiple stacks solar cells for obtaining higher V_{oc} with least photogenerated carrier loss.

1.6 Structure of this dissertation

In this work, mist-CVD deposition of MoS₂, WS₂, and WS_{2-x}Se_x thin films was systematically investigated. The synthesized MoS₂, WS₂, and WS_{2-x}Se_x were applied to the MOSFETs, complementary MOS circuits, and photovoltaic devices. The structure of this dissertation is as follows:

Chapter 1, is an introduction, mentioning a brief description of the background of this study, properties of extensively studied 2D-TMDCs materials, and their applications. The TMDCs thin film growth techniques along with their pros and cons including benefit of mist CVD are deliberated. A short description of TMDCs channel devices like MOSFETs, CMOS, and solar cells including their important electrical parameters are also deduced. Finally, the objective and motivation of this research has been discussed.

In **chapter 2**, the significance and characteristics of the mist-CVD system for the synthesis of atomic layer TMDCs and high-k dielectric films. A short description on

the different functioning units of mist CVD system, growth steps of MoS₂, WS₂, and WS_{2-x}Se_x films, and the fabrication procedure of MOSFETs, CMOS, and solar cells are demonstrated in this chapter. The working principle of several instrumentations used throughout this study including the criteria of sample preparation has been discussed at in this chapter.

In **Chapter 3**, the experimental results of the synthesis of submillimeter-size few-layer Molybdenum disulfide (MoS₂), tungsten disulfide (WS₂), and tungsten sulfoselenide (WS_{0.3}Se_{1.7}) flake grown on *th*-SiO₂ and Al_{0.74}T_{0.26}O_y dielectric layers coated p⁺-Si substrates by mist CVD have been described. In addition, the performance of MoS₂, WS₂, and WS_{0.3}Se_{1.7} channel MOSFETs, n-WS₂, and p-WS_{0.3}Se_{1.7} channel FETs-based CMOS logic circuit and WS_{0.3}Se_{1.7}/WO_x-based FETs structure lateral p⁺-n junction solar cells have been described.

In **chapter 4**, the findings of this study have been concluded including some promising ideas for future work.

References

1. Bardeen, J. & Brattain, W. H. Physical Principles Involved in Transistor Action. *Bell Syst. Tech. J.* **28**, 239–277 (1949).
2. Bardeen, J. & Brattain, W. H. Transistor, a semiconductor triode. *Proc. IEEE* **86**, 29–30 (1998).
3. Saraiva, E. F. & Milan, L. A. Clustering Gene Expression Data using a Posterior Split-Merge-Birth Procedure. *Scand. J. Stat.* **39**, 399–415 (2012).
4. Mollick, E. Establishing Moore’s law. *IEEE Ann. Hist. Comput.* **28**, 62–75 (2006).
5. Rupp, K. 42 Years of Microprocessor Trend Data. Online access, May, (2022).
6. Radamson, H. H. *et al.* Miniaturization of CMOS. *Micromachines* **10**, (2019).
7. Khanna, V. K. Short-Channel Effects in MOSFETs. In: Integrated Nanoelectronics. NanoScience and Technology, *Springer*, New Delhi (2017).
8. Scott E. T. and Srivatsan P., Moore’s law:the future of Si microelectronics, **9**, 6, 20–25 (2006).
9. Carey, P., Jose, S. & News, M. Silicon Valley marks 50 years of Moore ’ s Law. 24–26 (2015).
10. Scully, S. R. & McGehee, M. D. *Physics and Materials Issues of Organic Photovoltaics.* (2009).
11. Stoppa, M. & Chiolerio, A. Wearable electronics and smart textiles: A critical review. *Sensors (Switzerland)* **14**, 11957–11992 (2014).
12. Ryder, C. R., Wood, J. D., Wells, S. A. & Hersam, M. C. Chemically Tailoring Semiconducting Two-Dimensional Transition Metal Dichalcogenides and Black Phosphorus. *ACS Nano* **10**, 3900–3917 (2016).
13. Mir, S. H., Yadav, V. K., Singh, J. K. & Singh, J. K. Recent Advances in the Carrier Mobility of Two-Dimensional Materials: A Theoretical Perspective. *ACS Omega* **5**, 14203–14211 (2020).
14. Ye, M., Zhang, Z., Zhao, Y. & Qu, L. Graphene Platforms for Smart Energy Generation and Storage. *Joule* **2**, 245–268 (2018).
15. Randviir, E. P., Brownson, D. A. C. & Banks, C. E. A decade of graphene research: Production, applications and outlook. *Mater. Today* **17**, 426–432 (2014).
16. Schwierz, F. Graphene transistors. *Nat. Nanotechnol.* **5**, 487–496 (2010).
17. Wu, P. *et al.* Complementary Black Phosphorus Tunneling Field-Effect Transistors. *ACS Nano* **13**, 377–385 (2019).
18. Kim Jonam. Investigation of solution process of molybdenum disulfide for thin film transistor applications, thesis desertation. *JAIST Repository, Japan* (2017).

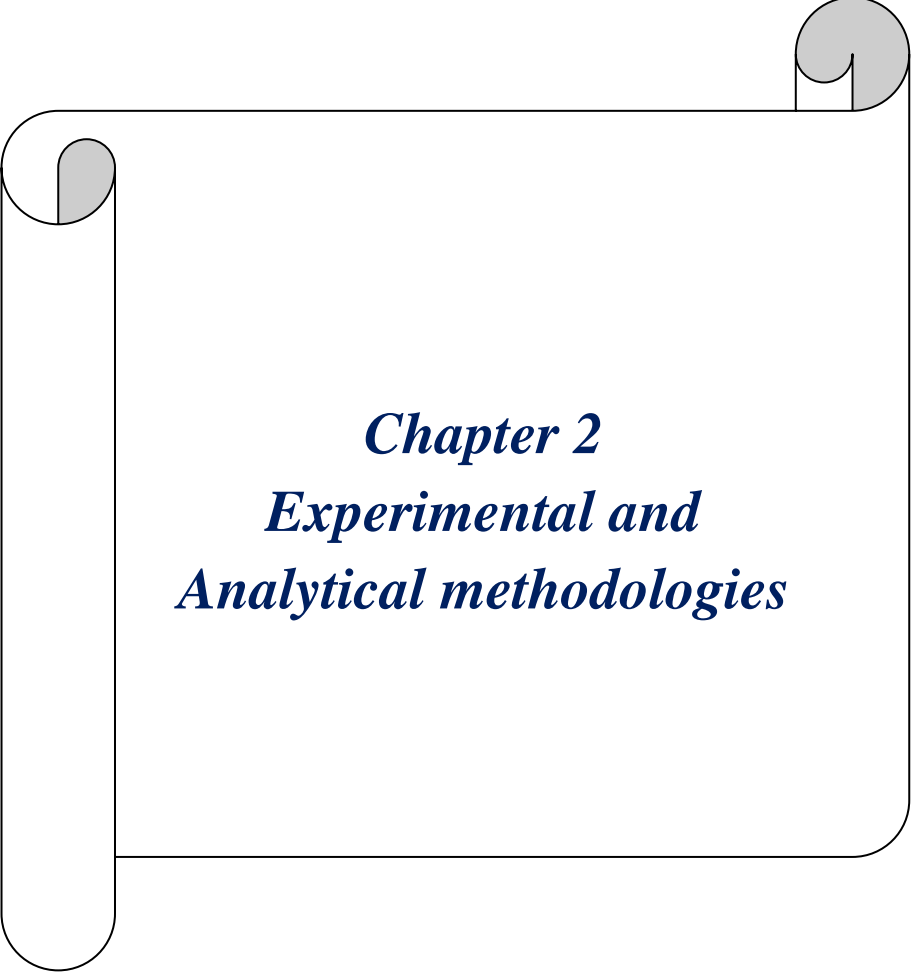
19. Cao, J. Tunnel field effect transistors based on two-dimensional materials tunnel field effect transistors based on two-dimensional materials Micro and nanotechnologies/Microelectronics. *Université Grenoble Alpes*, (2017)
20. Udayabagya, H. Electronic A Study of the Transition Metal Dichalcogenide and its Direct Organic Intercalation Chemistry. Theses and Dissertations. *University of california* (2017).
21. Nathan, A. *et al.* Flexible electronics: The next ubiquitous platform. *Proc. IEEE* **100**, 1486–1517 (2012).
22. Rogers, J. A., Someya, T. & Huang, Y. Materials and mechanics for stretchable electronics. *Science (80-.)*. **327**, 1603–1607 (2010).
23. Kim, D. H., Ghaffari, R., Lu, N. & Rogers, J. A. Flexible and stretchable electronics for biointegrated devices. *Annu. Rev. Biomed. Eng.* **14**, 113–128 (2012).
24. Zeng, H., Dai, J., Yao, W., Xiao, D. & Cui, X. Valley polarization in MoS₂ monolayers by optical pumping. *Nat. Nanotechnol.* **7**, 490–493 (2012).
25. Chhowalla, M., Liu, Z. & Zhang, H. Two-dimensional transition metal dichalcogenide (TMD) nanosheets. *Chem. Soc. Rev.* **44**, 2584–2586 (2015).
26. Radisavljevic, B., Radenovic, A., Brivio, J., Giacometti, V. & Kis, A. Single-layer MoS₂ transistors. *Nat. Nanotechnol.* **6**, 147–150 (2011).
27. Rycerz, A., Tworzydło, J. & Beenakker, C. W. J. Valley filter and valley valve in graphene. *Nat. Phys.* **3**, 172–175 (2007).
28. Zeng, X. Solution Processed 2D Transition Metal Dichalcogenides and Electrical Properties of TMD Thin Film Transistors. Thesis dissertation, *Jacobs University Bremen* (2017).
29. Lin, Y. F. *et al.* Ambipolar MoTe₂ transistors and their applications in logic circuits. *Adv. Mater.* **26**, 3263–3269 (2014).
30. Tsai, M. L. *et al.* Monolayer MoS₂ heterojunction solar cells. *ACS Nano* **8**, 8317–8322 (2014).
31. Jeon, P. J. *et al.* Low Power Consumption Complementary Inverters with n-MoS₂ and p-WSe₂ Dichalcogenide Nanosheets on Glass for Logic and Light-Emitting Diode Circuits. *ACS Appl. Mater. Interfaces* **7**, 22333–22340 (2015).
32. Shunfeng, W. *et al.* Efficient Carrier-to-Exciton Conversion in Field Emission Tunnel Diodes Based on MIS-Type van der Waals Heterostack. *Nano Lett.* **17**, 5156–5262 (2017).
33. Duan, X. *et al.* Synthesis of WS_{2-x}Se_{2-2x} Alloy Nanosheets with Composition-Tunable Electronic Properties. *Nano Lett.* **16**, 264–269 (2016).
34. Yu, D. *et al.* Vertical Few-Layer WSe₂ Nanosheets for NO₂ Sensing. *ACS Appl. Nano Mater.* **4**, 12043–12050 (2021).

35. Yu, H. *et al.* Spatially Graded Millimeter Sized $\text{Mo}_{1-x}\text{W}_x\text{S}_2$ Monolayer Alloys: Synthesis and Memory Effect. *ACS Appl. Mater. Interfaces* **13**,37, 44693–44702 (2021).
36. Pham, P. V. *et al.* 2D Heterostructures for Ubiquitous Electronics and Optoelectronics: Principles, Opportunities, and Challenges. *Chem. Rev.* **122**, 6514–6613 (2022).
37. Mun, J. *et al.* Low-temperature growth of layered molybdenum disulphide with controlled clusters. *Sci. Rep.* **6**, 1–7 (2016).
38. Kim, T., Fan, S., Lee, S., Joo, M. K. & Lee, Y. H. High-mobility junction field-effect transistor via graphene/MoS₂ heterointerface. *Sci. Rep.* **10**, 1–8 (2020).
39. Kuc, A., Zibouche, N. & Heine, T. Influence of quantum confinement on the electronic structure of the transition metal sulfide TS_2 . *Phys. Rev. B - Condens. Matter Mater. Phys.* **83**, 1–4 (2011).
40. Gusakova, J. 2D transition metal dichalcogenides: first principles study School of Electrical and Electronic Engineering. (2018).
41. Song, I., Park, C. & Choi, H. C. Synthesis and properties of molybdenum disulphide: From bulk to atomic layers. *RSC Adv.* **5**, 7495–7514 (2015).
42. Thomas, N. *et al.* 2D MoS₂: structure, mechanisms, and photocatalytic applications. *Mater. Today Sustain.* **13**, 100073 (2021).
43. Tsai, M. Y. Materials Challenges of Two-Dimensional Materials for Flexible Sensing Applications. *Georgia Institute of Technology* (2017).
44. Lan, C., Li, C., Ho, J. C. & Liu, Y. 2D WS₂: From Vapor Phase Synthesis to Device Applications. *Adv. Electron. Mater.* **7**, 1–36 (2021).
45. Abbas, O. A. *et al.* Solution-Based Synthesis of Few-Layer WS₂ Large Area Continuous Films for Electronic Applications. *Sci. Rep.* **10**, 1–10 (2020).
46. Schutte, W. J., De Boer, J. L. & Jellinek, F. Crystal structures of tungsten disulfide and diselenide. *J. Solid State Chem.* **70**, 207–209 (1987).
47. Kuc, A. Low-dimensional transition-metal dichalcogenides. *Chemical Modelling* vol. 11 (2015).
48. Pettenkofer, C., Klein, A., Jaegermann, W., Tiefenbacher, S. & Eyert, V. Electronic band structure of single-crystal and single-layer (formula presented) Influence of interlayer van der Waals interactions. *Phys. Rev. B - Condens. Matter Mater. Phys.* **64**, 1–14 (2001).
49. Nguyen, D. A. *et al.* Highly Enhanced Photoresponsivity of a Monolayer WSe₂ Photodetector with Nitrogen-Doped Graphene Quantum Dots. *ACS Appl. Mater. Interfaces* **10**, 10322–10329 (2018).
50. Sujoy, G. *et al.* Low temperature photoconductivity of few layer p-type tungsten diselenide (WSe_2) field-effect transistors (FETs) *Nanotechnology.* **29**, 484002 (2018).

51. Konar, R. *et al.* Scalable Synthesis of Few-Layered 2D Tungsten Diselenide (2H-WSe₂) Nanosheets Directly Grown on Tungsten (W) Foil Using Ambient-Pressure Chemical Vapor Deposition for Reversible Li-Ion Storage. *ACS Omega* **5**, 19409–19421 (2020).
52. Voß, D., Krüger, P., Mazur, A. & Pollmann, J. Atomic and electronic structure of (formula presented) from ab initio theory: bulk crystal and thin film systems. *Phys. Rev. B - Condens. Matter Mater. Phys.* **60**, 14311–14317 (1999).
53. Jamil, S., Farooq, F., Khan, S. R. & Janjua, M. R. S. A. Synthesis of WSe₂ Nanorods by Selenium Powder Precursor for Photocatalytic Application and Fuel Additive. *J. Clust. Sci.* **32**, 1061–1073 (2021).
54. Zahn, D. Structural dynamics of transition metal dichalcogenide heterostructures studied by ultrafast high-energy electron diffraction. Thesis dissertation, *Freie Universität, Berlin, German*, online access (2022)
55. Gong, C. *et al.* Erratum: Band alignment of two-dimensional transition metal dichalcogenides: Application in tunnel field effect transistors (Applied Physics Letters (2013) 103 (053513)). *Appl. Phys. Lett.* **107**, 102–103 (2015).
56. Rasmussen, F. A. & Thygesen, K. S. Computational 2D Materials Database: Electronic Structure of Transition-Metal Dichalcogenides and Oxides. *J. Phys. Chem. C* **119**, 13169–13183 (2015).
57. Ding, Y. *et al.* First principles study of structural, vibrational and electronic properties of graphene-like MX₂ (M = Mo, Nb, W, Ta; X=S, Se, Te) monolayers. *Phys. B Condens. Matter* **406**, 2254–2260 (2011).
58. Komsa, H. P. & Krasheninnikov, A. V. Effects of confinement and environment on the electronic structure and exciton binding energy of MoS₂ from first principles. *Phys. Rev. B - Condens. Matter Mater. Phys.* **86**, 1–6 (2012).
59. Wu, X. *et al.* Spatially composition-modulated two-dimensional WS₂_xSe_{2(1-x)} nanosheets. *Nanoscale* **9**, 4707–4712 (2017).
60. Chauhan, P. *et al.* Investigation of transient photoresponse of WSSe ternary alloy crystals. *AIP Conf. Proc.* **1961**, (2018).
61. Peng, J. *et al.* Electronic Properties and Carrier Dynamics at the Alloy Interfaces of WS₂_xSe_{2-2x} Spiral Nanosheets. *Adv. Mater.* **34**, 2107738 (2022).
62. Ernandes, C. *et al.* Indirect to direct band gap crossover in two-dimensional WS_{2(1-x)}Se_{2x} alloys. *npj 2D Mater. Appl.* **5**, 1–7 (2021).
63. Richard, P. F. Size Really Does Matter; The Nanotechnology Revolution. *World Scientific* 19–33 (2019).
64. Joensen, P., Frindt, R. F. & Morrison, S. R. Single-layer MoS₂. *Mater. Res. Bull.* **21**, 457–461 (1986).

65. Frindt, R. F. Single crystals of MoS₂ several molecular layers thick. *J. Appl. Phys.* **37**, 1928–1929 (1966).
66. Novoselov, K. S. *et al.* Two-dimensional atomic crystals. *Proc. Natl. Acad. Sci. U. S. A.* **102**, 10451–10453 (2005).
67. K. S. Novoselov *et al.* Electric Field Effect in Atomically Thin Carbon Films. **306**, 666–669 (2016).
68. Benameur, M. M. *et al.* Visibility of dichalcogenide nanolayers. *Nanotechnology* **22**, (2011).
69. Bosi, M. Growth and synthesis of mono and few-layers transition metal dichalcogenides by vapour techniques: A review. *RSC Adv.* **5**, 75500–75518 (2015).
70. Li, X. *et al.* Large-area synthesis of high-quality and uniform graphene films on copper foils. *Science (80-.)*. **324**, 1312–1314 (2009).
71. Kawaharamura, T. Physics on development of open-air atmospheric pressure thin film fabrication technique using mist droplets: Control of precursor flow. *Jpn. J. Appl. Phys.* **53**, (2014).
72. Rajib, A. *et al.* Synthesis of AlO_x thin films by atmospheric-pressure mist chemical vapor deposition for surface passivation and electrical insulator layers . *J. Vac. Sci. Technol. A* **38**, 033413 (2020).
73. Kuddus, A. *et al.* Mist chemical vapor deposition of crystalline MoS₂ atomic layer films using sequential mist supply mode and its application in field-effect transistors. *Nanotechnology* **33**, (2022).
74. Rajib, A. *et al.* Mist chemical vapor deposition of Al_{1-x}Ti_xO_y thin films and their application to a high dielectric material . *J. Appl. Phys.* **131**, 105301 (2022).
75. Dang, G. T., Allen, M. W., Furuta, M. & Kawaharamura, T. Electronic devices fabricated on mist-CVD-grown oxide semiconductors and their applications. *Jpn. J. Appl. Phys.* **58**, (2019).
76. Sato, S., Sakamoto, M. & Kawaharamura, T. Fabrication of molybdenum disulfide (MoS₂) layered thin films by atmospheric-pressure solution based mist CVD. *Zair. Soc. Mater. Sci. Japan* **68**, 155–161 (2019).
77. Sygellou, L. An in-situ photoelectron spectroscopy study of the thermal processing of ammonium tetrathiomolybdate, (NH₄)₂MoS₄, precursor. *Appl. Surf. Sci.* **476**, 1079–1085 (2019).
78. Kim, J., Higashimine, K., Haga, K. I. & Tokumitsu, E. Fabrication of MoS₂ thin films on oxide-dielectric-covered substrates by chemical solution process. *Phys. Status Solidi Basic Res.* **254**, (2017).
79. Müller, A., Prasad, T. P. & Menge, R. Thermal decomposition of (NH₄)₂MoS₄ and (NH₄)₂WS₄ heat of formation of (NH₄)₂MoS₄. *ZAAC - J. Inorg. Gen. Chem.* **391**, 107–112 (1972).

80. Hunyadi, D., Vieira Machado Ramos, A. L. & Szilágyi, I. M. Thermal decomposition of ammonium tetrathiotungstate. *J. Therm. Anal. Calorim.* **120**, 209–215 (2015).
81. Ponomarev, E. A., Neumann-Spallart, M., Hodes, G. & Lévy-Clément, C. Electrochemical deposition of MoS₂ thin films by reduction of tetrathiomolybdate. *Thin Solid Films* **280**, 86–89 (1996).
82. Schulman, D. S., Arnold, A. J. & Das, S. Contact engineering for 2D materials and devices. *Chem. Soc. Rev.* **47**, 3037–3058 (2018).
83. Mitta, S. B. *et al.* Electrical characterization of 2D materials-based field-effect transistors. *2D Mater.* **8**, (2021).
84. Yi-Hsing, C. High Performance Amorphous InGaZnO₄/Organic Ambipolar Thin Film Transistors. Thesis desertation, *National Chiao Tung University, China* (2008).
85. Ullmann, B. & Grasser, T. Transformation: Nanotechnologie – Herausforderungen beim Design von Transistoren und Technologien der Zukunft. *Elektrotechnik und Informationstechnik* **134**, 349–354 (2017).
86. Das, S., Dubey, M. & Roelofs, A. High gain, low noise, fully complementary logic inverter based on bi-layer WSe₂ field effect transistors. *Appl. Phys. Lett.* **105**, 1–6 (2014).



Chapter 2
Experimental and
Analytical methodologies

Chapter 2: Experimental and Analytical Methodologies

A brief discussion of the mist-CVD system including each part is demonstrated first. Second, the steps of direct fabrication of few-layer MoS₂, WS₂, and WS_{0.3}Se_{1.7} films using intermittent mist CVD are discussed. In the latter, the fabrication of MoS₂, WS₂, and WS_{2-x}Se_x channel MOSFETs, CMOS, and WS_{0.3}Se_{1.7}/WO_x based lateral p⁺-n junction solar cells on high-κ mist CVD Al_{0.76}Ti_{0.24}O_y dielectric layer is elucidated in detail. Finally, the working principles and steps of different measurements of analytical methods are also included. The MOS-FET and solar cell parameters and their extracted phenomenon are also considered at the end of this chapter.

2.1 Experimental

2.1.1 Hot-wall Mist-CVD system

Recently, solution-processed mist chemical vapor deposition (mist CVD) has emerged as a promising deposition technique compare to high and ultra-high vacuum-based techniques like molecular beam epitaxy (MBE), pulse laser deposition (PLD), atomic layer deposition (ALD), metalorganic chemical vapor deposition (MOCVD), sputtering, etc. Since mist CVD operated at atmospheric pressure is an energy-saving and environment-friendly technique for a future world¹. The mist CVD concept and its mechanism were explored first by prof. Kawaharamura and his research team in the first decade of 2021. K. Shanmugasundaram et al. utilized the mist deposition technique for patterning liquid precursors to thin films². H. Shirai et. al. also used the chemical mist deposition (CMD) method for transparent conductive polymers; poly (3,4-ethylene dioxythiophene): poly (styrene sulfonate) (PEDOT: PSS) on textured n-type crystalline Si as photovoltaics where improved light absorption was observed^{3,4}. Mist-CVD is the advanced prototype of the CMD system by adding a furnace in the reaction unit. A combination of mist supply unit, reaction unit, and vent unit represents a complete mist-CVD system. In [Figure 2.1](#), the basic units of the mist-CVD system are shown.

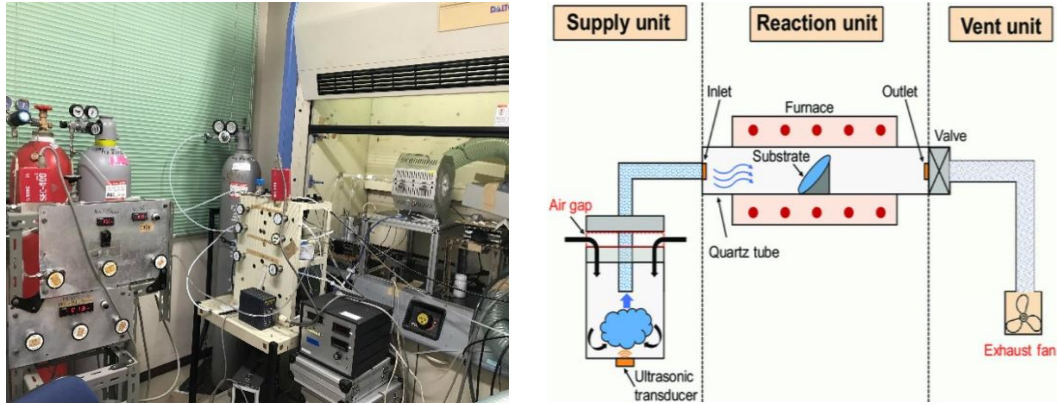


Figure 2.1. Camera image of mist CVD system and a schematic with different units⁵.

2.1.1.1 Mist generation unit

An ultrasonic atomizer to generate mist particles is the key element of this unit. A schematic of the mist generation unit is shown in Figure 2.2. The generation of fine mist particles is the most important task to obtain a good quality thin film. The ultrasonic mist generator consists of a compact mist maker device equipped with ultrasonic transducers with a steady water level, where the water atomization process is properly controlled. The ultrasonic transducer is composed of a piezo-electric crystal, which is capable of transforming high-frequency electronic signals, typically up to several MHz frequencies, into high-frequency mechanical oscillations. When the solution tank is set onto the disc connected with a piezo-electric crystal, the solution is detached from the disc on the negative oscillations and produces a transitory vacuum, where the solution cavitates and changes into steam. Then, on the positive oscillation, the steam solution is driven by the high-pressure wave through the water surface. In this adiabatic process, a fine water mist is formed, with droplet diameters on the scale of several nanometers to a few tens of microns, which are easy can be transported by the gas flow. Rayleigh attributed this instability to a statistical distribution of capillary disturbance of amplitude α and wavelength λ as $\lambda > 2\pi R$. Two major hypotheses; the capillary wave hypothesis and cavitation hypothesis have been proposed to explain the mechanism of liquid disintegration during ultrasonic atomization. According to Taylor's instability criteria, the capillary wave hypothesis refers to a strong correlation between mean droplet size and capillary wavelength⁶. On the other hand, the cavitation hypothesis is generally applied to high frequency (16 kHz–5 MHz) and high-energy intensity (W/m^2) systems. During the liquid film is sonication, cavitation bubbles are

formed. During the implosive collapse of these cavities, especially cavities near the surface of the liquid, high-intensity hydraulic shocks have generated that initiate the disintegration of the liquid film and ejection of the droplets.

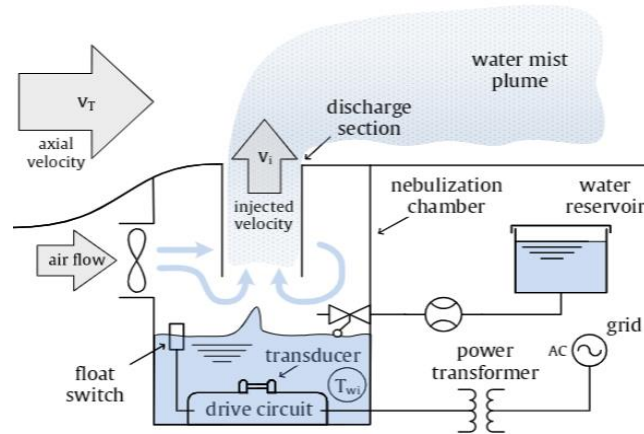


Figure 2.2. Schematic of an ultrasonic mist generator and its principal components⁷.

According to Lang's findings, the mist droplet size depends on the frequency of the surface standing wave at the liquid interface, which is due to the piezoelectric element known as Lang equation⁸, which is;

$$d_p = 0.34 \left(\frac{8\pi\sigma}{\rho f^2} \right)^{1/3} \dots\dots\dots(2.3)$$

where d_p is denoted by the droplet size, σ is the surface tension in the liquid surface, f is the excitation frequency, ρ is the density of the liquid.

2.1.1.2 Reaction unit

The reaction unit of the mist-CVD system consists of a hot wall reaction chamber in which films are deposited. The furnace heater is associated with a reaction chamber to carry thermal energy for decomposing the precursors and facilitating the diffusivity of the mist droplets on the substrate surface. A substrate holder placed at a higher temperature zone is another important part of the reaction unit. A schematic of a reaction unit with a different reaction scheme is shown in [Figure 2.3](#). During the transportation of mist precursors in the reaction chamber, the average size of the mist droplets decreased from 40-500 nm to a few nanometers under the influence of heat, evapotranspiration, and burst. Additionally, the rate of carrier gas flow also determines

the residence time of mist precursors, therefore the diffusivity of mist precursors. In addition, a higher flow of carrier gas decreases the mist droplet size.

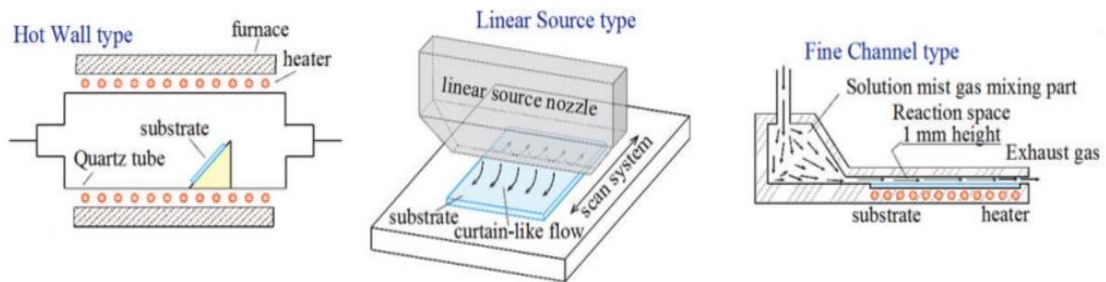


Figure 2.3. Schematic diagram of different types of reaction units of mist CVD system⁹.

The Hot wall type mist CVD system is the same as the general CVD system. The source material is transferred to the reactor like a furnace and film is grown on the substrate surface. The object of this system is the growth of high-quality crystals at high temperatures. Linear source type mist CVD system, where a curtain-like mist flows from the novel nozzle to the substrate surface. This system is suitable for large-scale substrate and continuous deposition of thin films in a few minutes. And another is a Fine channel type mist CVD system. In this system, a substrate needs to be set in the fine channel of the novel nozzle, which gives driving force to the substrate for depositing uniform thin films. The uniform distribution of temperature offers a uniform reaction, therefore smooth films. In this system, same the reaction rate can be obtained in all reaction areas if enough precursor was supplied so-called "reaction limited". Moreover, uniform, smooth and crystalline films are obtained in a Hot wall type mist CVD reaction system.

2.1.1.3 Ventilation unit

The removal of excessive mist is performed by the vent unit. In the vent unit, the outlet valve is usually used to adjust the velocity of the flow. An arrangement with a certain power fan with a vacuum pump is added with a pipe having a certain diameter in the ventilation lines, thereby a controlled pressure at the outlet is usually obtained. So far, the mist is transferred into the reaction tube by pulling the air from the air gap in the solution tank (Figure 2.1).

2.1.1.4 Sulfurization/Selenization system

The sulfur or selenium vapor exposure of as-deposited mist CVD films usually is used to enrich the film's crystallinity and obtain the stoichiometry composition. The thermolysis steps of a TMDCs precursor and the properties of as-deposited films are highly sensitive to the presence of oxygen during growth. In addition, the formation of vacancies by removal of chalcogenides elements of S or Se to the film requires a further exposure of S or Se vapor in an H_2 gas atmosphere at high temperature (> 500 °C) to obtain the stoichiometry film composition¹⁰. A typical schematic of three-zone sulfur or selenium exposure system is shown in Figure 2.4.

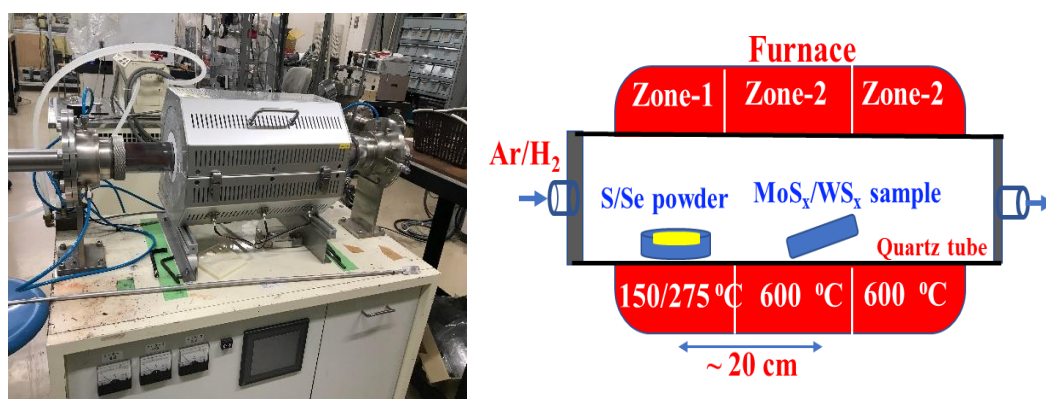


Figure 2.4. Camera image and schematic diagram of sulfurization/selenization setup.

2.1.2 Synthesis of MoS_2 , WS_2 , and $WS_{2-x}Se_x$ films by mist-CVD

Molybdenum disulfide (MoS_2) with atomic mono/bilayer thickness was synthesized from $(NH_4)_2MoS_4$ dissolved in N-methyl-2-pyrrolidone (NMP) while tungsten disulfide (WS_2) and tungsten sulphoselenide ($WS_{2-x}Se_x$) from $(NH_4)_2WS_4$ precursor using mist-CVD. Deposition of MoS_2 , WS_2 , and $WS_{0.3}Se_{1.7}$ atomic mono/bilayer thin films was performed on *th*- SiO_2 and mist-CVD grown $Al_{0.76}Ti_{0.24}O_y$ (ATO) layers coated p^+ -Si substrates by alternating mist supply in the closed chamber at different furnace temperatures, storage times of precursor mist in the chamber, repetition cycles of mist supply, and followed by sulfurization or selenization. Direct synthesis of atomic mono/bilayer MoS_2 , with an average size of 120 μm and WS_2 , and $WS_{2-x}Se_x$ with an average grain size over 700 μm by adjusting the deposition condition without using mechanical exfoliation and assistance of an alkali metal salt or seed layer (Figure 2.5). Detail of deposition of the atomic monolayer to few-layer MoS_2 , WS_2 , and $WS_{0.3}Se_{1.7}$

and their application in MOSFETs are described in sections 3.1 and 3.2 of the “Results and discussions” chapter.

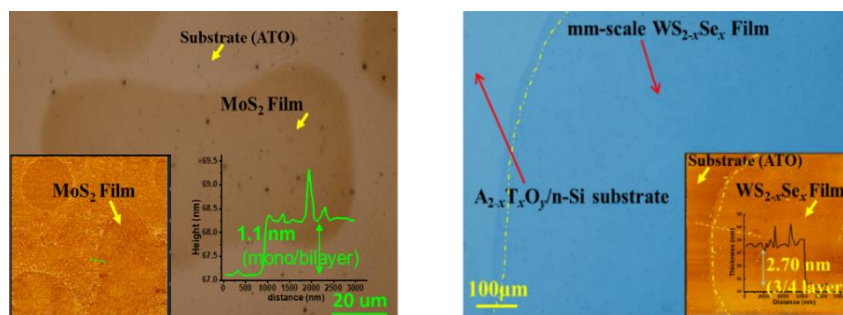


Figure 2.5. AFM and microscopic images of mist CVD MoS₂, and WS_{2-x}Se_x flakes synthesized by mist-CVD.

2.1.3 Fabrication of MoS₂, WS₂, and WS_{2-x}Se_x channel MOSFETs and design of CMOS logic circuit

MX₂ (M= Mo, W; X= S, Se, Te) crystals were grown at a temperature of >1000 °C by the chemical vapor transport (CVT) method introduced by Al-Hilli and Evans¹¹ and Agarwal et al.¹²⁻¹⁴ in 1972 and 1977 respectively. In the latter, CVD, ALD, PLD, intercalation using Li-ion, sputtering, spin and dip coat, and mist-CVD were found promising methods. Although CVD has shown potential but yet to meet industrial criteria considering the growth temperature, growth rate, controllability of layer thickness, and stoichiometry composition. Mist-CVD is found to be one of the competitive and promising consistent methods for preparing TMDCs and metal oxide thin films from chemically stable and low-vapor-pressure materials with gas-phase reactions.

Atomic mono/bilayer MoS₂, WS₂, and WS_{0.3}Se_{1.7} flakes directly synthesized by mist CVD on high-k A_{0.76}T_{0.24}O_y (ATO) dielectric layers were used to fabricate the MOSFETs. The schematic and microscopic images of MoS₂, WS₂, and WS_{2-x}Se_x-channel MOSFETs on a ~45 nm thick ATO dielectric layer are shown in Figure 2.6. The source/drain electrodes of gold or Pt were formed through the UV-photolithography and followed by a lift-off process using a positive photoresist (AZ5214E). The photoresist was spun on the TMDCs films at 2500 rpm for 30 s and then heated at 110 °C for 90 s. After that, photolithographic pattern using UV-exposure,

development of the exposed area (pattern) with tetramethylammonium hydroxide (NMD-3) and followed by rinsed with deionized (DI) water. Source and drain (Au or Pt) metal electrodes with a thickness of ~ 50 nm were sputtered after pattern development. Finally, an ultrasonic standard lift-off is executed using hot acetone in a beaker and wired with golden wire and golden/silver paste.

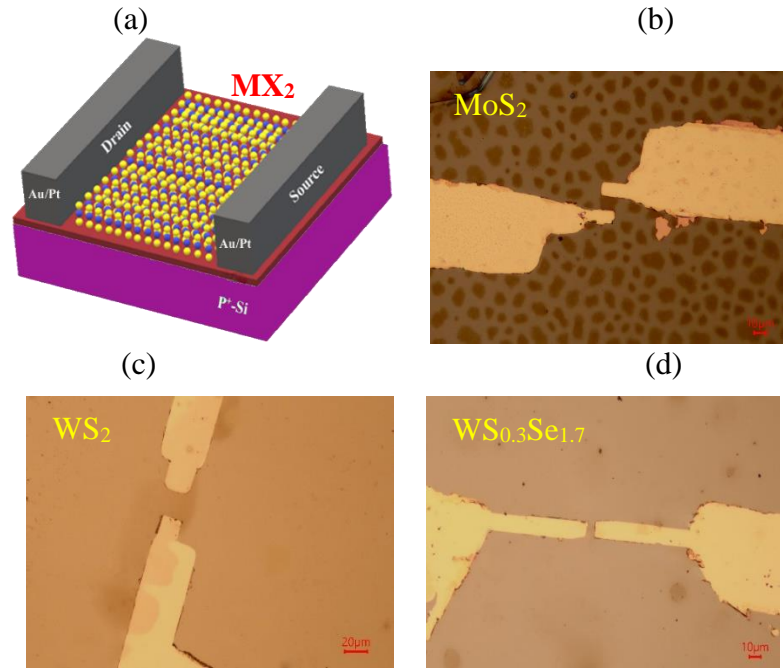


Figure 2.6. (a) 3D Schematic of MX₂ channel FETs; and microscopic images of mist CVD: (a) MoS₂, (b) WS₂, and (c) WS_{2-x}Se_x channel MOSFETs. The MoS₂ and WS₂ channel n-FETs with Au as S/D electrodes and WS_{2-x}Se_x channel p-FET with Pt S/D electrodes were used.

The inverting performance of the CMOS circuit designed by cascading p-WS_{0.3}Se_{1.7} and n-WS₂ channel FETs with a common gate as the input voltage V_{IN} and the common source as the output voltage (V_{OUT}) at V_{dd} (Figure 2.7). The transition between the two logic states 1 and 0 corresponds to the ON state of p-WS_{0.3}Se_{1.7} and n-WS₂ channel FETs respectively, which is characterized by the voltage gain = $\Delta V_{OUT}/\Delta V_{IN}$.

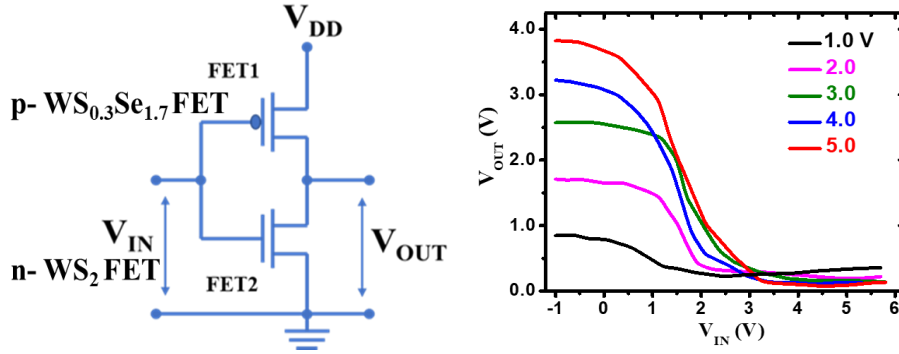


Figure 2.7. (a) Circuit designed for complementary inverter circuit comprising p- $\text{WS}_{0.3}\text{Se}_{1.7}$ channel MOSFET with n- WS_2 channel MOSFETs with a common gate as the input voltage, V_{IN} , and common source as the output, V_{OUT} , and (b) Inverter characteristics at different $+V_{\text{DD}}$.

2.1.4 Fabrication of $\text{WS}_{0.3}\text{Se}_{1.7}/\text{WO}_x$ based lateral p⁺-n junction solar cells

Figure 2.8. shows the images of 10 kV, 10 kHz He/ O_2 exposure system, laser of different oscillation wavelengths of 420, 532, and 650 nm, the I-V measurement set-up including the schematic of $\text{WS}_{0.3}\text{Se}_{1.7}/\text{WO}_x$ lateral p⁺-n junction device. Few-layers $\text{WS}_{0.3}\text{Se}_{1.7}$ was oxidized by He/ O_2 plasma for 60 s and laser irradiation using a metal mask to form a lateral p⁺-n junction to form $\text{WS}_{0.3}\text{Se}_{1.7}/\text{WO}_x$ lateral p⁺-n junction by high electron affinity WO_x after synthesis. The $\text{WS}_{0.3}\text{Se}_{1.7}$ film was synthesized from ammonium tetrathiotungstate $(\text{NH}_4)_2\text{WS}_4$ precursor by spin coating at 4000 rpm for 60 s on thermally-grown SiO_2 (285 nm)/P⁺-Si substrate and subsequent selenization at 600 °C for 60 minutes under low pressure. The laser irradiation was performed with a different oscillation wavelength of 420, 532, and 650 nm for 0 to 60 s. Finally, S/D electrodes of Au/Pt were formed by a combination of photolithography and sputtering. The detail is described in section 3.3 of the “Results and discussions” chapter.

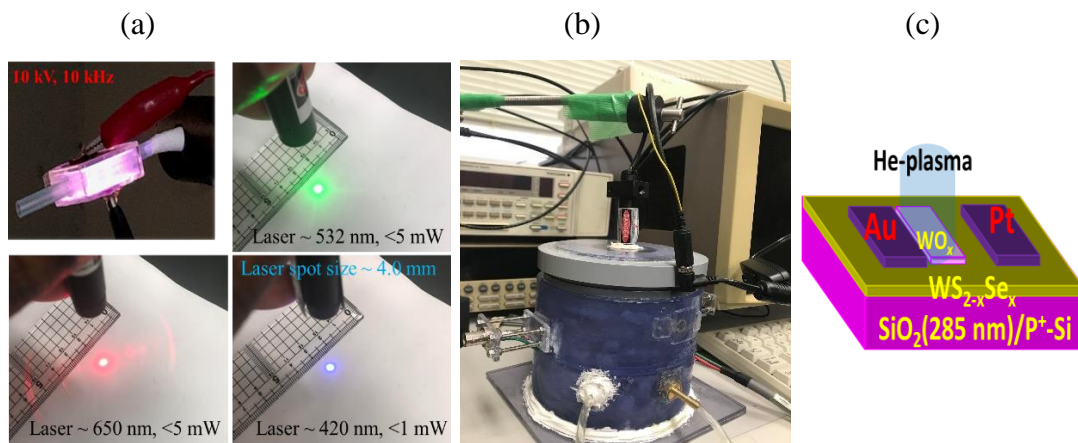


Figure 2.8. Camera images of (a) 10 kV, 10 kHz He/O₂ exposure system and laser of different oscillation wavelengths of 420, 532, and 650 nm; (b) Laser irradiation and I-V measurement setup; (c) schematic of WS_{2-x}Se_x/WO_x lateral p⁺-n junction solar cells.

2.2 Analytical methodologies

2.2.1 Optical microscopy

Optical imaging is a rapid and non-destructive way to characterize 2D materials with an optical microscope deposited on thermally grown SiO₂ or other high-k dielectric layers coated p⁺-Si substrates¹⁵. This method is based on achieving the contrast between reflected light from material/dielectric and blank substrate, which strongly depends on the wavelength of incident light and the thickness of the SiO₂ dielectric layer. Optical microscopy can visualize 2D TMDCs film even a few layers to a single layer¹⁶. A schematic of optical reflection and transmission phenomena and a microscopic image of MoS₂ flakes on SiO₂(285 nm)/Si are shown in Figure 2.9. The visualization of electrode patterning after photolithography, device structure, flake's shape, and determination of the TMDCs flake's size and density were studied by optical microscopy.

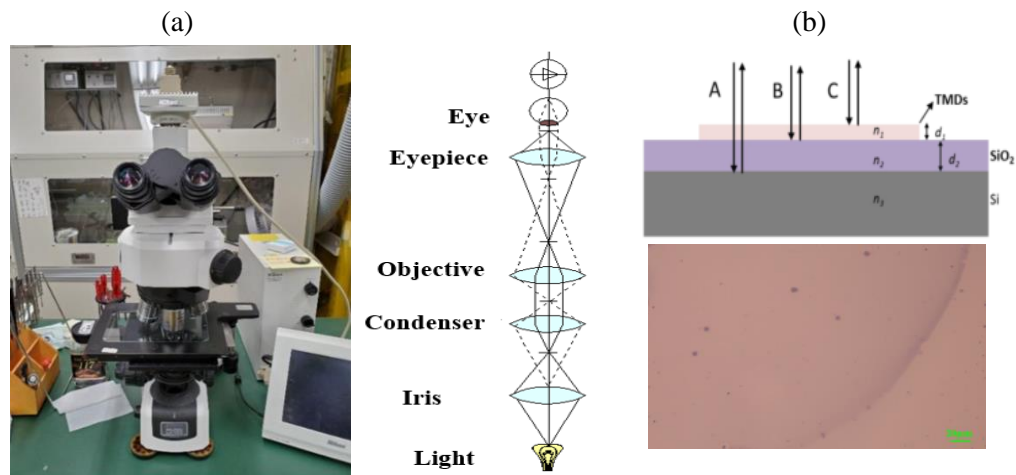


Figure 2.9. (a) Optical microscopy (OM), (b) internal diagram of OM, and (c) Schematic of optical reflection and transmission for a TMDCs film with thickness d_1 and index of refraction n_1 on SiO₂/Si substrate, the thickness, and index of refraction of SiO₂ are d_2 and n_2 , and index of refraction of Si is n_3 and optical image of mono/bilayer of WS_{0.3}S_{1.7} flake on ATO substrate¹⁷.

The bottom Si layer, which is much thicker than the SiO₂ layer, can be considered an infinite film (Figure 2.9). Therefore, the reflected intensity of the system can be written as¹⁷:

$$I(n_1) = \frac{\left| r_1 e^{i(\phi_1 + \phi_2)} + r_2 e^{-i(\phi_1 - \phi_2)} + r_3 e^{-i(\phi_1 + \phi_2)} + r_1 r_2 r_3 e^{i(\phi_1 - \phi_2)} \right|^2}{\left| e^{i(\phi_1 + \phi_2)} + r_1 r_2 e^{-i(\phi_1 - \phi_2)} + r_1 r_3 e^{-i(\phi_1 + \phi_2)} + r_2 r_3 e^{i(\phi_1 - \phi_2)} \right|^2} \dots\dots\dots(2-1)$$

with amplitude reflection coefficients:

$$r_1 = \frac{n_0 - n_1}{n_0 + n_1}, r_2 = \frac{n_1 - n_2}{n_1 + n_2}, r_3 = \frac{n_2 - n_3}{n_2 + n_3} \dots\dots\dots(2-2)$$

$$\phi_i = \frac{2\pi d_i n_i}{\lambda} \dots\dots\dots(2-3)$$

i = 1, 2 are the phase shifts due to the changes in the optical path length and λ is the wavelength of incident light. The contrast between the reflected light in TMDCs/SiO₂/Si system (n₁ ≠ 1) and bare SiO₂/Si substrate (n₁=n₀=1) is:

$$Contrast = \frac{I(n_1 = n_0 = 1) - I(n_1)}{I(n_1)} \dots\dots\dots(2-4)$$

The relationship between contrast and the thickness of the dielectric layer as well as the wavelength of light can be calculated from Eq.2-4. If the contrast is zero, the material is invisible. By changing the thickness of the substrate and wavelength of the incident light, the film contrast can be optimized.

The function to illuminate a specimen consists of three basic functions; (a) supplying light, (b) collecting light, and (c) changing light intensity. The major parts of an optical microscope include the eyepiece, objective, and stage for both reflective and transmitted light microscopes. Eyepieces are used for magnification. Microscopes either are monocular, meaning that it has only one, two, or three eyepieces respectively. A reflecting light microscope has a lower resolving power than a transmitted light microscope. However, a reflecting microscope has a better depth of field and is ideal for dissecting/looking at larger objects. In transmitting light microscopes, the illumination system is very important. The system includes the light source, condenser, and iris. A condenser is usually a combination of lenses that gathers and concentrates light in a specified direction, under the stage. An iris controls the intensity of the light that goes into the condenser. So far, the transmitted light microscope also needs to consider illumination which aids in seeing the object.

2.2.2 Atomic Force Microscope (AFM)

Atomic force microscopy (AFM), is used for characterizing a material's surface topography, thickness profile, phase, and surface roughness by sensing the force between a sample and a probing tip. A schematic representation of the AFM measurement system is shown in Figure 2.10. In AFM, typically a silicon or silicon nitride cantilever is used which has a downward-facing sharp tip at the end with a few nanometer radiuses.

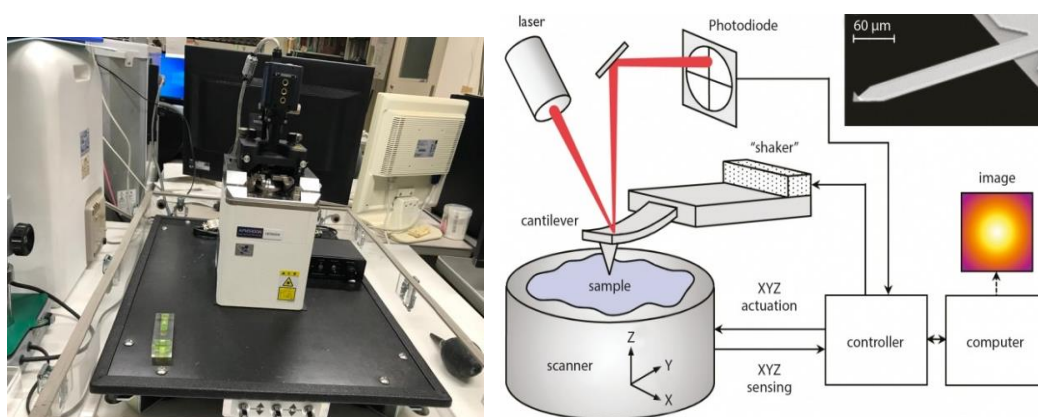


Figure 2.10. Camera image of AFM5100N & schematic of atomic force microscope¹⁸.

The van der Waals force between the tip and the sample surface is increased when the tip is close to the surface. The force curve depends on the distance between the tip and the sample. There are two measuring modes; contact and non-contact (Figure 2.11). The repulsive force is used in the contact mode because the cantilever is closed less than a few angstroms to the sample surface and the attractive force in the non-contact mode is generated by long-range van der Waals interactions. In non-contact mode, the cantilever maintains the space of ten to a hundred Å from the sample surface. The cantilever moves back and forwards to scan the surface. The force on the cantilever varies depending on the surface height profile. An integrated circuit with a piezoelectric crystal sustains a constant height difference, therefore a constant force. A laser is attached to the back of the cantilever and the photodetector checks the position changing of the reflected laser. In 3D, the piezoelectric ceramics are used to move either the sample or the tip with high precision. The scanning is done in a feedback loop when moving during the scan the bending of the cantilever remains constant to remain at a constant force. Afterward, the up-and-down motion is recorded as the sample topography.

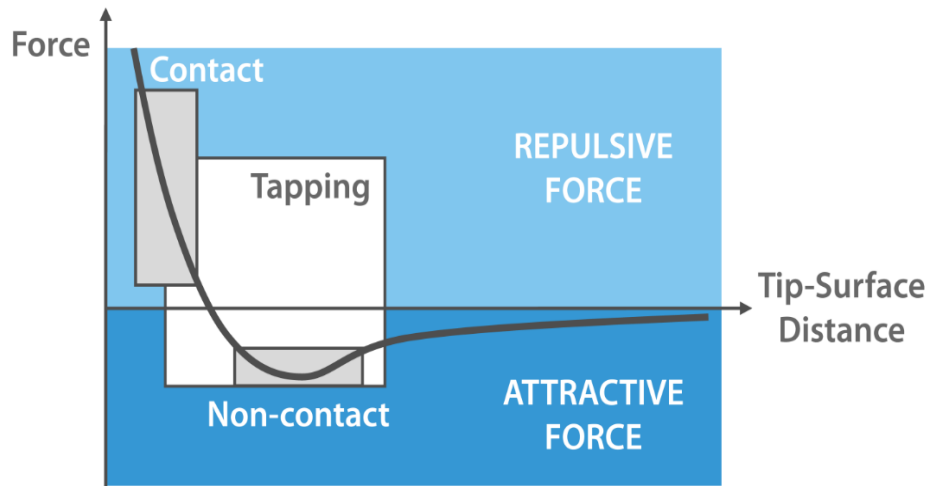


Figure 2.11. Force curve of atomic force microscopy; contact and non-contact scanning mode¹⁸.

2.2.3 Scanning Electron Microscopy (SEM)

A scanning electron microscope (SEM) is a valuable utility for imaging beyond the visible light diffraction limit, where a high-energy electron beam is used (typically 0.1 to 50 keV) to scan the surface to generate an image profile. The incident high-energy electrons can eject the electrons in the outer shell of the sample atom. With an additional scattering within the sample, a fraction of these low-energy electrons leaves the sample surface with energies less than 50 eV. The SEM produces the whole sample image detecting the secondary electrons. In a typical SEM, an electron beam is thermionically emitted from an electron gun which is fitted with a tungsten filament cathode. Tungsten is normally used in thermionic electron guns as an electron source because of its higher melting point and lower vapor pressure, thereby electrons emitted by the electrically heating. The electron beam having an energy ranging from 0.2 keV to 40 keV, is focused by one or two condenser lenses to make a spot with a diameter of ~ 0.4- 5 nm. The e-beam passes through pairs of deflector plates in the electron column, which deflect the beam in the x and y axes so that it scans in a raster fashion over the sample surface with a rectangular area (Figure 2.12). The energy exchange between the electron beam and the sample results in the reflection of high-energy electrons by elastic scattering and emission of secondary electrons by inelastic scattering including the emission of electromagnetic radiation, each of these electrons can be detected by specialized detectors. For imaging purposes, secondary electrons are most valuable for showing morphology and topography on samples and backscattered electrons are most

valuable for illustrating contrasts in composition in multiphase samples. In addition, X-ray can be used for identifying elemental analysis. Therefore, SEM usually is used to obtain surface morphology and chemical compositions of samples.

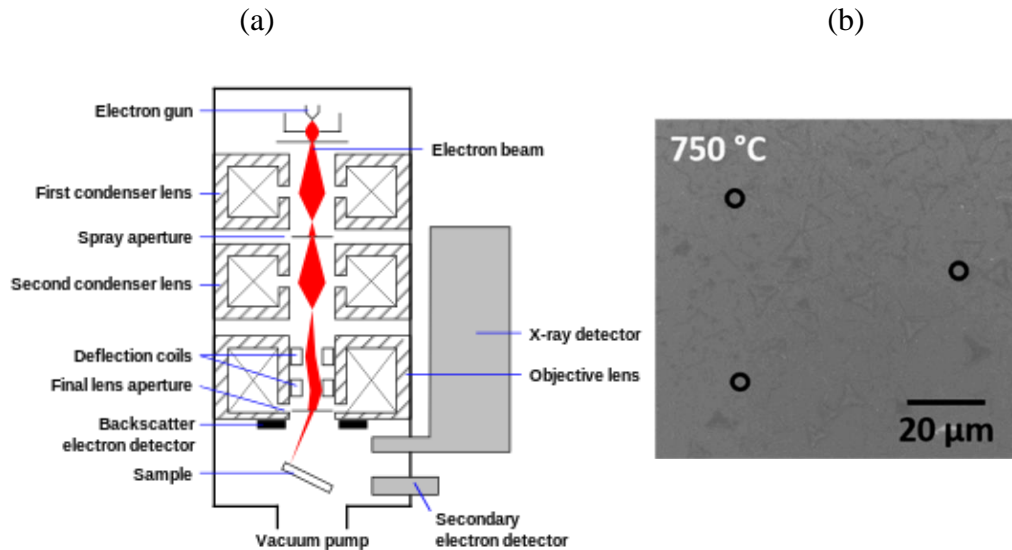


Figure 2.12. (a) Schematic of an internal diagram of scanning electron microscopy (SEM) system and (b) SEM image of MoS₂ film. Reprinted from References^{19,20}.

2.2.4 Transmission Electron Spectroscopy (TEM)

Transmission electron microscopy (TEM) is a microscopy technique where an image is formed from the interaction of the electrons with the sample as the beam is transmitted through the specimen. TEM is used to analyze crystal quality, shape, size, etc. of ultrathin samples. The specimen is most often ultrathin with a thickness of < 100 nm. The image is magnified and focused onto an imaging device, such as a fluorescent screen, a layer of photographic film, or a sensor such as a scintillator attached to a charge-coupled device after the image formation. Transmission electron microscopes are capable of imaging at a significantly higher resolution than light microscopes, owing to the smaller de Broglie wavelength of electrons. It has three essential systems: (a) an electron gun, which produces the electron beam, and the condenser system, and focuses the beam onto the desired object, (b) the image-producing system, movable specimen stage, consisting of the objective lens, and intermediate and projector lenses, that focuses the electrons passing through the specimen to form a real, magnified image, and (3) the image-recording system, which converts the electron image into some form perceptible to the human eye. The image-recording system consists of a fluorescent

screen for detecting and focusing the image with a digital camera. The electron beam follows a vertical path through the microscope, which requires a high vacuum environment for avoiding a collision of an electron with molecules in the ambient atmosphere. After accelerated by the anode voltage, the electron beam travels through electromagnetic fields and lenses, which focus the beam down towards the sample. Electrons including Auger electrons, backscattered electrons, and secondary electrons, as well as X-rays and light, are ejected after the high-energy incident electron beam interacted with the specimen. Transmitted electrons that depend on the thickness and transparency of the specimen are focused by the objective lens usually on a charge-coupled device (CCD) camera forming the image. The image can be enlarged by projector lenses. A schematic of the transmission electron microscope system and TEM image of crystalline MoS₂ is shown in Figure 2.13.

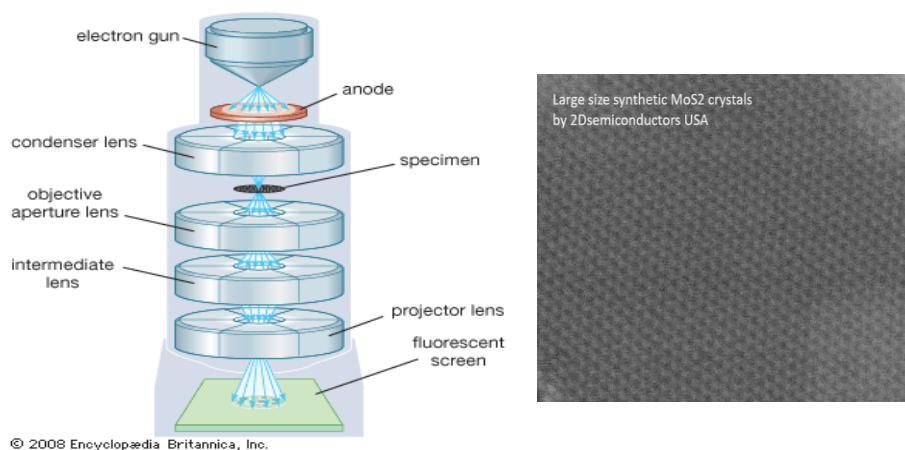


Figure 2.13. (a) Schematic of a TEM measurement system, and (b) TEM image of single-crystal 2H-phase MoS₂ crystals¹⁹.

2.2.5 Raman and photoluminescence (PL) Spectroscopy

Raman Spectroscopy is one of the most popular methods to detect modes of molecular motions, vibrations et al. It can be used to identify substances, chemical structure, crystal phase, crystalline symmetries, etc. Each molecule has a different set of vibrational energy levels, and the photons emitted have unique wavelength shifts. When a monochromatic light normally produced by a laser, is incidents on the sample, two types of light scattering processes will happen: elastic (Rayleigh) scattering and inelastic (Raman)^{17,21}. Raman scattering was first experimentally observed by Raman; therefore, this inelastic scattering is named after him. At a short wavelength, it is more

effective and it is proportional to the fourth power of the frequency²². Different materials have different chemical compositions and molecular vibrations, which leads to different characteristic spectral patterns (fingerprints). However, a small fraction of the incident photons (about $1/10^7$) is scattered due to the interaction of molecules owing to different optical frequencies. In Figure 2.14, a laser beam is directed and focused onto the sample after passing a beam splitter and microscope system. The scattered light is collected by the microscope and passes through a beam splitter. After passing the focusing lens, the scattered light goes towards the spectrometer's entrance slit, then goes through a notch filter, which removes most of the Rayleigh scattering light. The rest light goes into the spectrometer where it gets diffracted by a grating and splitted into its spectral components. A CCD detector collects the signal and represents the data of the Raman spectra. The common practice for plotting Raman spectra is intensity, or "Count Rate", on the y-axis and the frequency of the "Raman Shift" along the x-axis. Raman shift is the difference in frequency between the laser light and the scattered light. This difference is unrelated to the laser's wavelength and expressed as wavenumbers. Count Rate is the number of events the spectrometer detects for the particular Raman shift per second and is relative to the strength of light detected. Raman spectroscopy was extensively studied to obtain information on chemical structure and identity, Phase and polymorphism, intrinsic stress/strain and contamination and impurity.

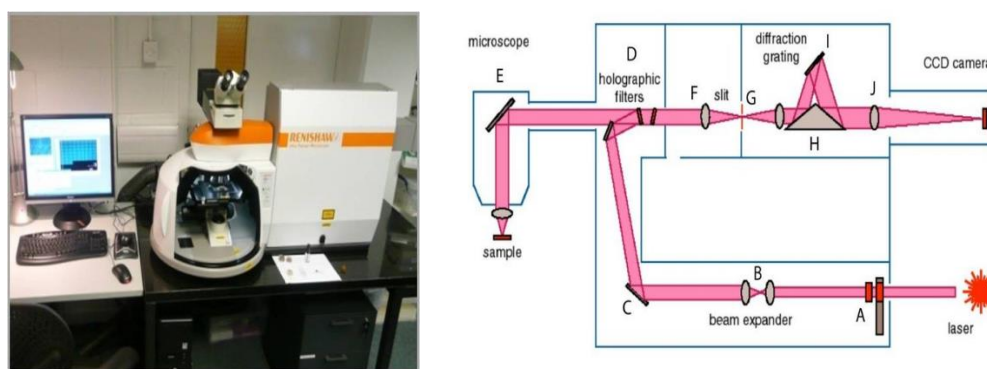
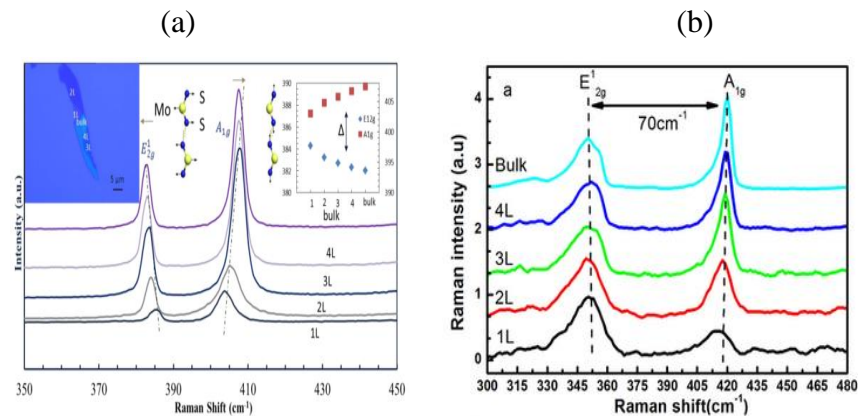


Figure 2.14. Camera image of Renishaw InVia microscope Raman system and schematic of internal diagram with laser wavelength 532 nm.

Layered TMDCs unit cell consists of two X-M-X units with 6 atoms except for monolayer MX_2 (where each unit cell comprises one X-M-X unit with 3 atoms). Thus, there are 18 phonon modes (15 optical modes and 3 acoustic) and 9 phonon modes (6 optical modes and 3 acoustic) for bulk and monolayer MX_2 , respectively. The lattice

vibration of bulk hexagonal MX_2 (D_{6h} point group symmetry) at Γ point can be expressed by the irreducible representations of D_{6h} , $\Gamma = A_{1g} + 2A_{2u} + 2B_{2g} + B_{1u} + E_{1g} + 2E_{1u} + 2E_{2g} + E_{2u}$, one A_{2u} , and one E_{1u} are acoustic modes, while another A_{2u} and one E_{1u} are infrared (IR) active modes, A_{1g} , E_{1g} , and E_{2g} are Raman (R) active modes, B_{2g} , B_{1u} , and E_{2u} are optically inactive (silent) modes. Thin MX_2 with few layers has a different symmetry compared to the bulk, because of the lack of translational symmetry along the z axis, and different symmetry is also observed between even and an odd number of layers. ML MX_2 has D_{3h} point group symmetry, the vibration modes at Γ point are $\Gamma = 2A_2'' + A_1' + 2E' + 2E''$, where one A_2'' and one E' are acoustic modes. Another A_2'' is IR active mode, another E' is both R and IR active mode, A_1' and E'' are R active modes [44]. For bulk MoS_2 , there are 4 Raman active modes A_{1g} , E_{1g} , and $2E_{2g}$. E_{1g} is undetected under back-scattering Raman configuration, while the frequency of E_{2g}^2 is relatively low, with Raman peak being around $\sim 33 \text{ cm}^{-1}$ [23]. Therefore, two Raman modes in-plane E_{2g}^2 ($\sim 383 \text{ cm}^{-1}$ of MoS_2 and $\sim 365 \text{ cm}^{-1}$ of WS_2) and out-of-plane A_{1g} ($\sim 408 \text{ cm}^{-1}$ of MoS_2 and $\sim 415 \text{ cm}^{-1}$ of WS_2) are generally inspected. It has been found and approved that the peak position and width of E_{2g}^2 and A_{1g} depend on the number of layers of MX_2 . Both modes shift in opposite directions due to the influence of the van der Waals interlayer coupling, interlayer stacking, and Coulombic interactions. As a result, Raman Spectroscopy is also used widely to identify the number of stacks of atomic layers of TMDCs. The evolution of the Raman spectra of MoS_2 , WS_2 , WSe_2 , and $\text{WS}_{2(1-x)}\text{Se}_{2x}$ is depicted in Figure 2.15. The quantitative wavenumber differences of the two peaks of MoS_2 and WS_2 are tabulated in Table 2.1.



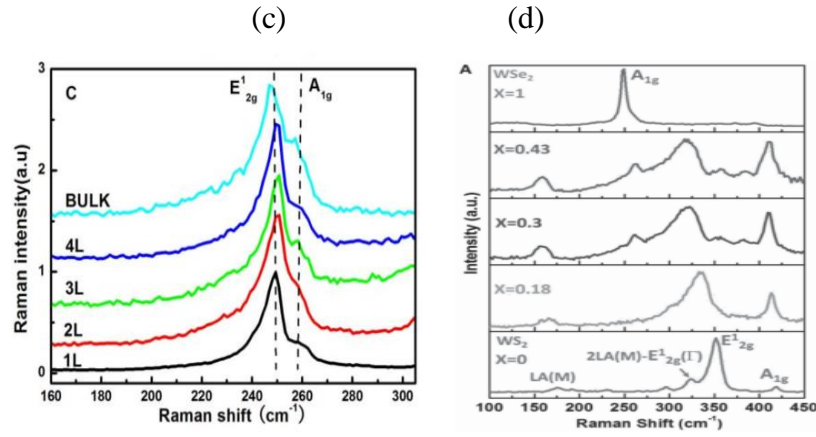


Figure 2.15. Raman spectra of (a) MoS₂; (b) WS₂; (c) WSe₂ at different number of layers; (d) WS_{2(1-x)}Se_{2x} at different Se composition. Re printed with permission from references^{17,24,25}.

Table 2.1. Wavenumber differences ($\Delta\omega$) between in-plane E^1_{2g} and out-of-plane A_{1g} modes of MoS₂ and WS₂.

Layer		1L	2L	3L	4L	bulk
$\Delta\omega$ (cm ⁻¹)	MoS ₂	18.7	21.6	23.1	24.4	25.5
	WS ₂	65.5	68.3	69.2	70.0	>70.0

In Photoluminescence (PL) spectroscopy, light is directed onto a sample, resulting in the generation of photoexcitation by the absorption and the emission of PL in the relaxation process. Room and low temperature spatially resolved micro-PL is done with a focused laser beam of He- Ne, Ar⁺, etc., providing a diffraction-limited spot diameter of the order 1 μm . A CCD camera collects the spectrum for each examined point while scanning over the sample and develops human perceptible spectra. In addition, photoluminescence mapping is an extremely fast spatially resolved characterization technique. The spatial variation of the effective lifetime of minority carriers is measured without being affected by minority carrier trapping or by excess carriers in space charge regions, both of which lead to experimental artifacts in other techniques. The layer-dependent PL of MoS₂, WS₂, and WSe₂ are depicted in Figure 2.16. The PL intensity gradually goes down with the increase of the number of stacks of atomic layer for every MoX₂ sample and disappears when more than a quadrilayer or bulk.

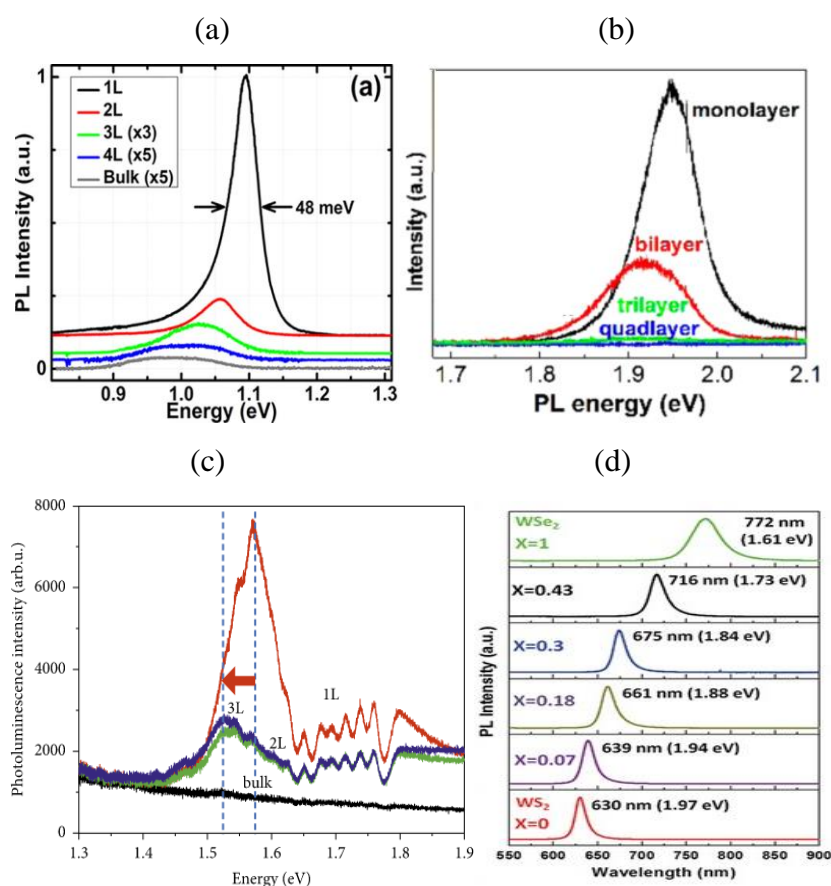


Figure 2.16. PL spectra of (a) MoS₂; (b) WS₂; (c) WSe₂ at different number of layers and (d) WS₂(1-x)Se_{2x} at different Se-composition. Reprinted with permission from references²⁵⁻²⁸.

2.2.6 X-ray photoelectron spectroscopy (XPS)

X-ray photoelectron spectroscopy (XPS) is a surface characterization technique that can analyze a sample having a depth of 2 to 5 nm. Chemical elements are present at the surface except for hydrogen and helium and the nature of the chemical bond that exists between elements can be investigated by the XPS study. In the 1960s, Kai Siegbahn developed XPS, which won the Nobel Prize in physics in 1981. XPS is conducted usually in ultrahigh vacuum (UHV) conditions, $P \sim 10^{-9}$ millibar. At a pressure of 10^{-6} mbar, background gas constituents (O₂, H₂O, etc.) can react with the surface of a sample in several seconds though this time is more trivial than reaction time. However, it takes hours before a sample significantly degrades at UHV pressures, thus enabling accurate surface interrogation using XPS. In a typical XPS, sufficient energy is exposed to break the photoelectron away from the nuclear attraction force of an element. Two key

features are derived from XPS data: (a) even photo-ejected electrons from core levels have slight shifts depending on the outer valence configuration of the material examined and (b) the specific energy of an elemental core level transition occurs at specific binding energy that can uniquely identify the element^{21,29}. Figure 2.17 shows the schematic AXIS Nova, Kratos Axis Ultra XPS system, and the internal diagram.

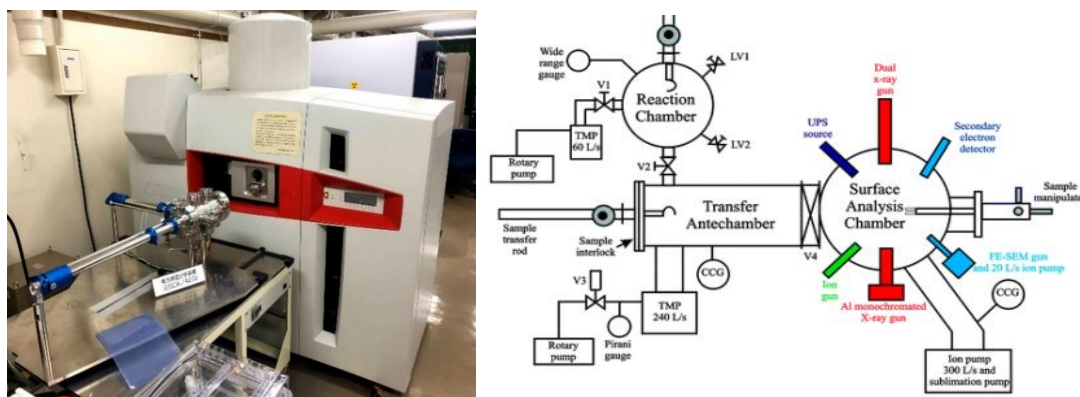


Figure 2.17. Camera image of AXIS Nova, Kratos Axis Ultra XPS system, and its internal diagram²⁹.

In an XPS spectrum, a few of the photo-ejected electrons inelastically scatter through the sample en route to the surface, while others undergo emission and suffer no energy loss in escaping the surface and into the surrounding vacuum. Once these photo-ejected electrons are in the vacuum, they are collected by an electron analyzer which measures their kinetic energy. An electron energy analyzer produces an energy spectrum of intensity (number of photo-ejected electrons versus time) versus binding energy. Each prominent energy peak on the spectrum corresponds to a specific element. The photon radiated by monochromatic source normally used X-Ray is absorbed in material then, ionization and the emission of a core (inner shell) electrons are occurred with following equation (Eq. 2-5).

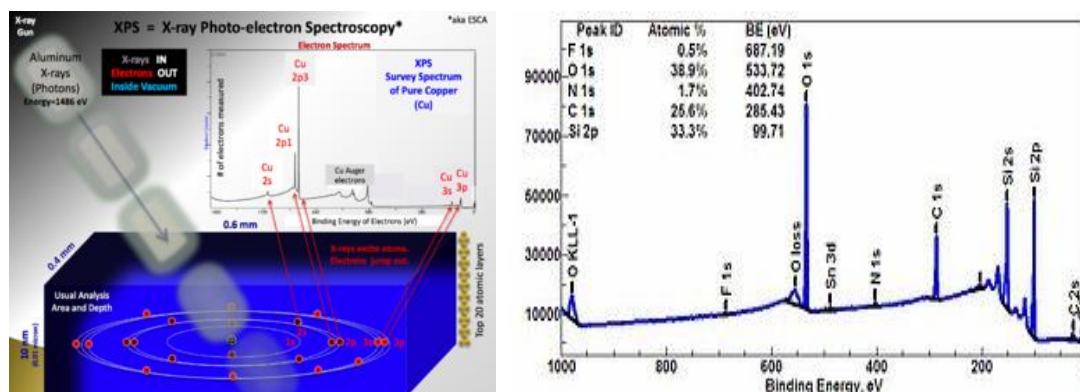


Figure 2.18. Schematic of photoemission excitation and survey spectra obtained from XPS observation.

Since the energy of an X-ray is known with a particular wavelength (for Al K_{α} X-rays, $E_{\text{photon}} = 1486.7$ eV), and the emitted electrons' kinetic energies are measured, the electron binding energy of each of the emitted electrons can be determined by using the photoelectric effect equation, (eq. 2-6);

$$M + h\nu = M^+ + e^- \dots\dots\dots (2-5)$$

$$E_{\text{binding}} = E_{\text{photon}} - (E_{\text{kinetic}} + \phi) \dots\dots\dots (2-6)$$

$$KE = h\nu - [E(M^+) - E(M)] = h\nu - BE \dots\dots\dots (2-7)$$

Where, E_{binding} is the binding energy (BE) of the electron measured relative to the chemical potential, E_{photon} is the energy of the X-ray photons being used, E_{kinetic} is the kinetic energy of the electron as measured by the instrument and ϕ is a work function-like term for the specific surface of the material, includes a small correction by the instrument's work function in real measurements because of the contact potential. The indicated brackets in Eq.2-7 represent the energy difference between the ionized and neutral atoms so-called the binding energy (BE) of the electron. For every element, there is specific binding energy due to each core atomic orbital i. e. detected electrons provide a specific fingerprint of the atomic species. A typical XPS spectrum is a plot of the number of electrons detected at a specific binding energy (Figure 2.18). Each peak area is proportional to the number of atoms present in each element. By applying relative sensitivity factors (RSF) and appropriately integrating peak areas, a number of atomic percent of each element can be determined.

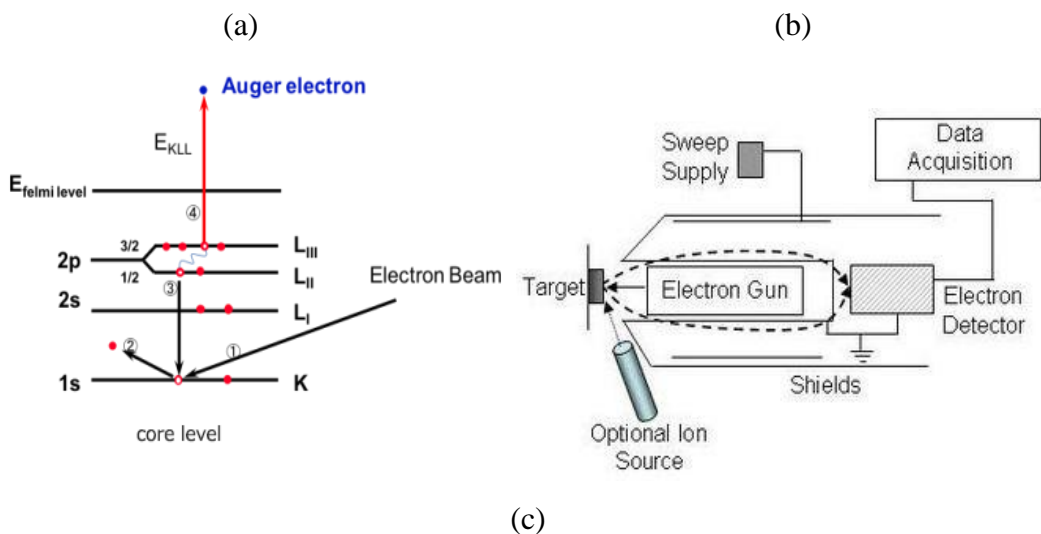
2.2.7 Auger electron spectroscopy (AES)

Auger electron spectroscopy (AES) is an analytical technique used specifically in the study of surfaces in the area of materials science. It is a form of electron spectroscopy based on the Auger effect, where the analysis of energetic electrons emitted from an excited atom after a series of internal relaxation events. In the 1920s, the Auger effect was discovered independently by Lise Meitner and Pierre Auger. The element on the sample surface can be identified by measuring the electron energy since the Auger electron energy emitted from the sample with a specific value. The Auger electrons lose

energy as they pass through a sample, the analysis target for Auger spectroscopy is limited to several nanometers from the sample surface. An emitted electron will have kinetic energy:

$$E_{\text{kin}} = E_{\text{Core State}} - E_B - E'_C \dots\dots\dots(2-8)$$

Where, $E_{\text{core state}}$, E_B and E'_C are the core levels, first outer shell, and second outer shell electron binding energies respectively. Moreover, the irradiated electron beam can be focused to 5 nm or less, allowing for an ultra-microscopic area of the sample to be analyzed³⁰. Because of the low energy of Auger electrons, most AES setups are run under ultra-high vacuum (UHV) conditions, resulting in the prevention of electron scattering of residual gas atoms as well as the formation of a thin gas layer on the surface of the sample. The internal diagram of the Auger spectroscopic system, AES setup, and a typical AES spectrum of MoS₂ is shown in Figure 2.19. This system consists of three major parts: (a) an electron gun; Field Emission (FE) electron source used for SEM focuses the electron beam diameter on the sample to 5 nm or less, enabling high current density, (b) a Detection system; a cylindrical Mirror Analyzer (CMA) electron analyzer used as the Auger electron energy analyzer that is equipped with an electron gun along its central axis where the emitted Auger electrons can be detected from 360 degrees around the sample, enabling measurement of samples with uneven and complex shapes. In the detection unit, Auger electrons are multiplied and the signal is sent to data processing electronics. Collected Auger electrons are plotted as a function of energy against the broad secondary electron background spectrum and (c) Shields; Auger spectrometers measuring microscopic areas are equipped with enclosures that shut out vibrations from external sounds and temperature changes.



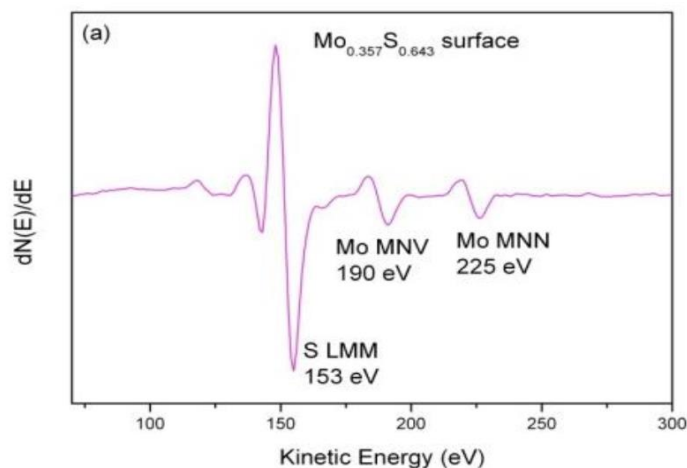


Figure 2.19. (a) The internal diagram of the AES system, (b) AES experimental setup with a cylindrical mirror analyzer (CMA), and (c) a typical AES spectrum of MoS_2 ^{30,31}.

2.2.8 Ultraviolet photoelectron spectroscopy (UPS)

Ultraviolet photoelectron spectroscopy (UPS) is the measurement of kinetic energy spectra of photoelectrons emitted by molecules employing absorption of ultraviolet photons to determine molecular orbital energies in the valence band region. The ultraviolet photoelectron spectroscopy (UPS) was discovered by physicist Feodor I. Vilesov, at St. Petersburg (Leningrad) State University in Russia (USSR) in 1961. As compared to XPS, UPS is limited to energy levels of valence electrons, but measures more accurately. Ultraviolet photoelectron spectroscopy operates on the same principles as XPS, the only difference being that ionizing radiation at energies of 10s of 1 eV is used to induce the photoelectric effect while greater than 1 keV in XPS. The full width of the photoelectron spectrum with the ranges from the highest kinetic energy (lowest binding energy) cutoff to the lowest kinetic energy cutoff is measured and subtracted from the photon energy of the exciting radiation, and this difference indicates the work function of the measured material (Figure 2.20). Usually, the sample is biased negatively to separate the low energy cutoff from the spectrometer response. In the laboratory setting ultraviolet photons are produced using a gas discharge lamp, typically filled with helium having energies of 21.2 eV (He I) and 40.8 eV (He II), although other gases such as argon and neon can also be used³².

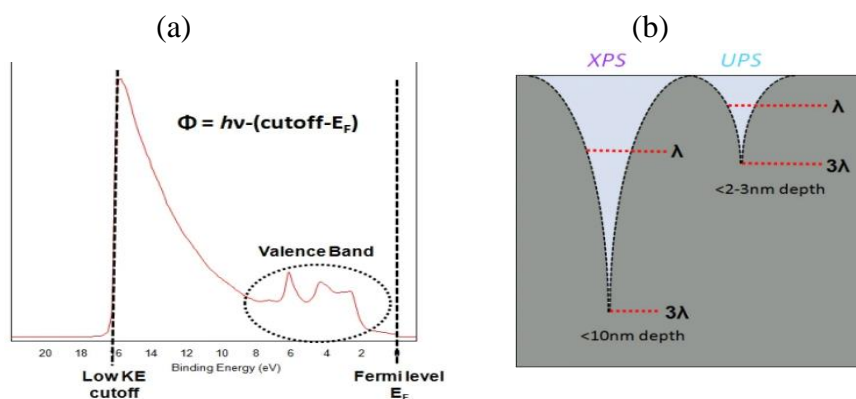


Figure 2.20. (a) Work function spectrum of a chemical element obtained from UPS observation, and (b) information depth for UPS compare with XPS³³.

There are two modes in ultraviolet photoelectron spectroscopy: valence band acquisition and thereafter an electronic work function measurement. In valence band acquisition, many of the molecular orbitals from which valence band photoelectron signal originates possess a high degree of hybridization, consequently the shifts in peak binding energy are far more varied and subtle than those observed for core-level photoemission peaks. Therefore, a valence band spectrum is predominantly used for material characterization through spectral fingerprinting, and individual peak assignment. In electronic work function measurement, the difference between the Fermi level and Vacuum level is referred to as the electronic work function. The electronic work function is acquired spectroscopically by measuring the difference between the Fermi Level and cutoff of the ‘tail’ at the low kinetic energy end of the spectrum and subtracting this value from the incident photon energy.

2.2.9 Kelvin Probe Force Measurement (KPFM)

Kelvin probe force microscopy (KPFM), also known as surface potential microscopy, is a non-contact variant of atomic force microscopy. By raster scanning in the x, and y plane, the work function of the sample can be locally mapped for correlation with sample features with a small or no magnification. The probe and sample are set parallel to each other and electrically connected to form a parallel plate capacitor. The different material probe shows a distinct Fermi level. An electron flow between the probe and the sample in the direction of the lower to the higher Fermi level at an applied electric field. This electron flow causes the equilibration of the probe and sample Fermi levels. Furthermore, a surface charge develops on the probe and the sample, with a

related potential difference known as the contact potential (V_c). The probe is vibrated along a perpendicular to the plane of the sample and causes a change in the probe to sample distance, which in turn results in the flow of current forming an ac sine wave. The resulting ac sine wave is demodulated to a dc signal through the use of a lock-in amplifier. Once the dc potential has been determined, an external potential, known as the backing potential (V_b) can be applied to null the charge between the probe and the sample, consequently, the Fermi level of the sample returns to its original position. This means that V_b is equal to V_c , which is the work function difference between the probe and the sample measured. The schematic diagram of the KPFM measurement system and a scanned spectrum for the surface potential of He^+ oxidized/pristine WSe_2 homojunction is shown in Figure 2.21³⁴.

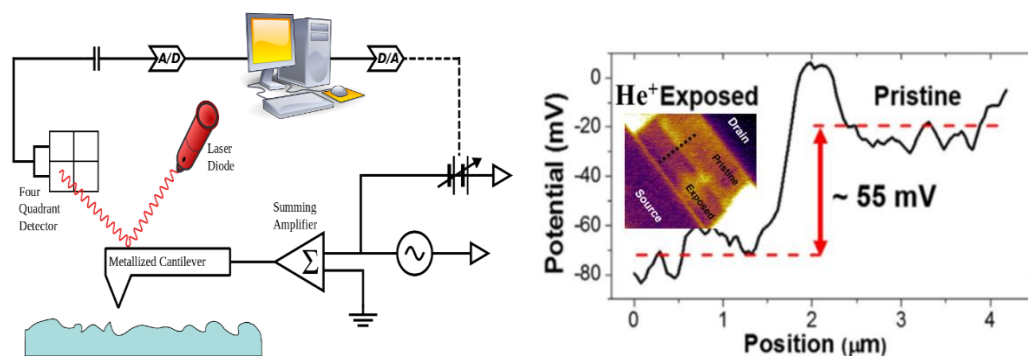


Figure 2.21. The schematic of the KPFM system; scanning a WSe_2 film surface retaining at a constant height and corresponding KPFM profile spectra. Reprinted from references^{34,35}.

2.2.10 Time-of-Flight Secondary Ion Mass Spectrometry (TOF-SIMS)

Time-of-Flight Secondary Ion Mass Spectrometry (TOF-SIMS) provides about surface layers or thin-film structures is important for many industrial and research applications where surface or thin-film composition plays a critical role in performance including nanomaterials, catalysis, corrosion, photovoltaics, polymer surface modification, adhesion, magnetic media, display technology, semiconductor devices and packaging, thin-film coatings, and medical materials with average analysis depth is approximately 1 nm. Physical Electronics spatial distribution information is obtained by scanning a micro-focused ion beam across the sample surface with a spatial resolution of down to 0.1 μm . Depth distribution information is obtained by combining TOF-SIMS measurements with ion milling (sputtering) to characterize a thin film structure. In

addition, the Physical Electronics TOF-SIMS instrument provides a unique 3D analysis capability that combines in-situ focused ion beam sectioning with high mass resolution and high spatial resolution imaging to provide 3D chemical characterization. TOF-SIMS is executed by exciting the surface of a sample with a sharply focused ion beam that causes secondary ions and ion clusters emitted from the sample's surface. the exact mass of both of the emitted ions and clusters is measured by a TOF analyzer. From the exact mass and intensity of the SIMS peak, the identity of an element or molecular fragments is determined. The principle of TOF-SIMS measurement and depth profile profiles spectra of S^- , MoS_2^- , and MoO^- ions is shown in [Figure 2.22](#).

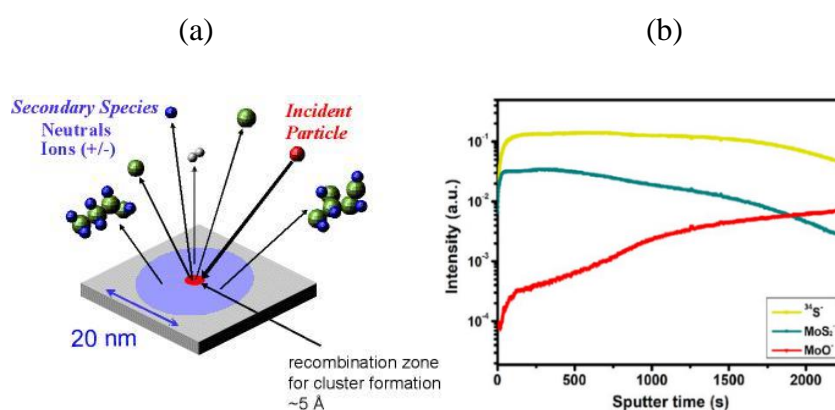


Figure 2.22. (a) A particle beam interaction in TOF-SIMS liberating single ions (+/-) and molecular compounds, and (b) a TOF-SIMS depth profiles spectra of S^- , MoS_2^- , and MoO^- ions³⁶⁻³⁸.

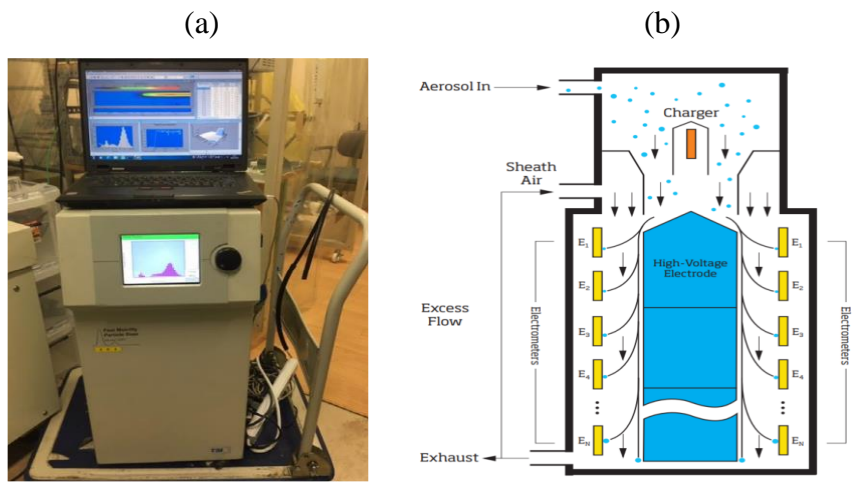
2.2.11 Fast Mobility Particle Sizer (FMPS-3091)

The Fast Mobility Particle Sizer™ (FMPS™) Model 3091 spectrometer measures aerosol particles in the range from 5.6 to 560 nanometers, offering a total of 32 channels of resolution (16 channels per decade). It uses an electrical mobility technique similar to the TSI Scanning Mobility Particle Sizer™ (SMPS™) spectrometer. However, instead of a Condensation Particle Counter (CPC), it uses low-noise multiple electrometers for particle detection resulting in particle size distribution measurements with one-second resolution, letting users visualize particle events and changes in particle size distribution in real-time. The instrument draws an aerosol sample into the inlet continuously. Particles are charged positively to a predictable level using a corona charger. Charged particles are then introduced to the measurement region near the center of a high-voltage electrode column and transported down the column via HEPA-

filtered sheath air. A positive voltage applied to the electrode creates an electric field that repels the particles outward according to their electrical mobility. Charged particles strike the respective electrometers and transfer their charge. A particle with high electrical mobility strikes an electrometer near the top, whereas a particle with lower electrical mobility strikes an electrometer lower in the stack. This arrangement with the highly sensitive electrometers allows for concentration measurements of multiple particle sizes simultaneously. A Fast-Scanning Mobility Particle Sizer FMPS-3091, aerosol flow diagram, and data presentation are shown in Figure 2.23. The basic four components of particle counter are (a) Impactor (aerosol conditioner), (b) Neutralizer (charge conditioner), (c) dynamic mobility analyzer DMA and (d) Condensation particle counter CPC. The cut-off diameter for a round jet impactor is dependent on the orifice diameter and flow rate according to the following equation (Baron and Willeke)^{39,40}:

$$d_{50} = \sqrt{\frac{9\eta\pi W^3}{4ppCcQ}} \sqrt{Stk_{50}} \dots\dots\dots (2-9)$$

Where Stk_{50} is the stokes number is expressed as $Stk_{50} \approx 0.24$, η is the air viscosity, W is the nozzle diameter, Cc is the Cunningham slip factor, pp is the particle density, and U is the average flow velocity in the nozzle. Impactors are devices that separate particles based on inertia and remove particles of a given size range from the sample flow, either collecting them for later analysis or removing them to avoid problems of instrument contamination. The next part of the particle counter is the neutralizer which is carried out to neutralize the charged particles so that they cannot radiate energy in the later sections.



(c)

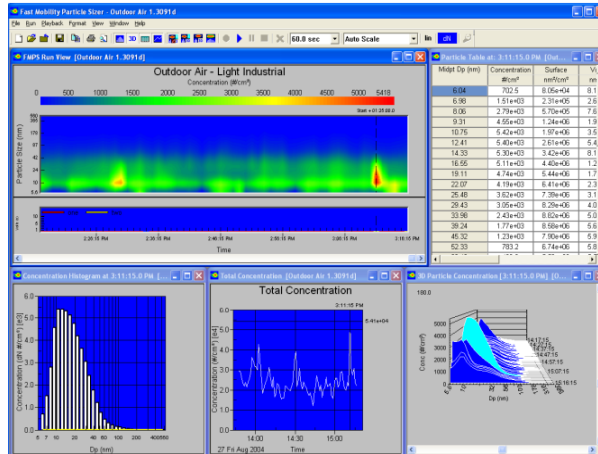


Figure 2.23. (a) Fast Scanning Mobility Particle Sizer (FMPS), Model-3091 image; (b) Schematic of aerosol flow diagram; (c) data representation by FMPS -3091^{40,41}.

In the DMA, particles having different electrical mobility are selected and measured in their concentration by setting different voltages. The DMA consists of two electrodes with the inner electrode at a negative voltage, while the outer electrode is electrically grounded. Before entering the DMA, the aerosol particles are charged by passing through the charger, where positive and negative ions are produced. The charged aerosols are introduced through an annular slit closed to the outer electrode into the top of the DMA and then, merged with the particle-free airflow. The electrical particle mobility is a function of the particle charge, particle diameter, flow rate, and dimensions of the DMA. In CPC, particle growth is achieved by passing the aerosol through a saturated vapor of the working fluid such as n-butanol followed by cooling in a condenser. The temperatures of the saturator condenser and properties of the working fluid determine the lower detectable size, typically in the ranges of 3-10 nm. A schematic of the cascade impactor, differential mobility analyzer, condensation particle counter (CPC), and limits of FMPS 3091 with RMS noise level that varies with averaging time are depicted in Figure 2.24.

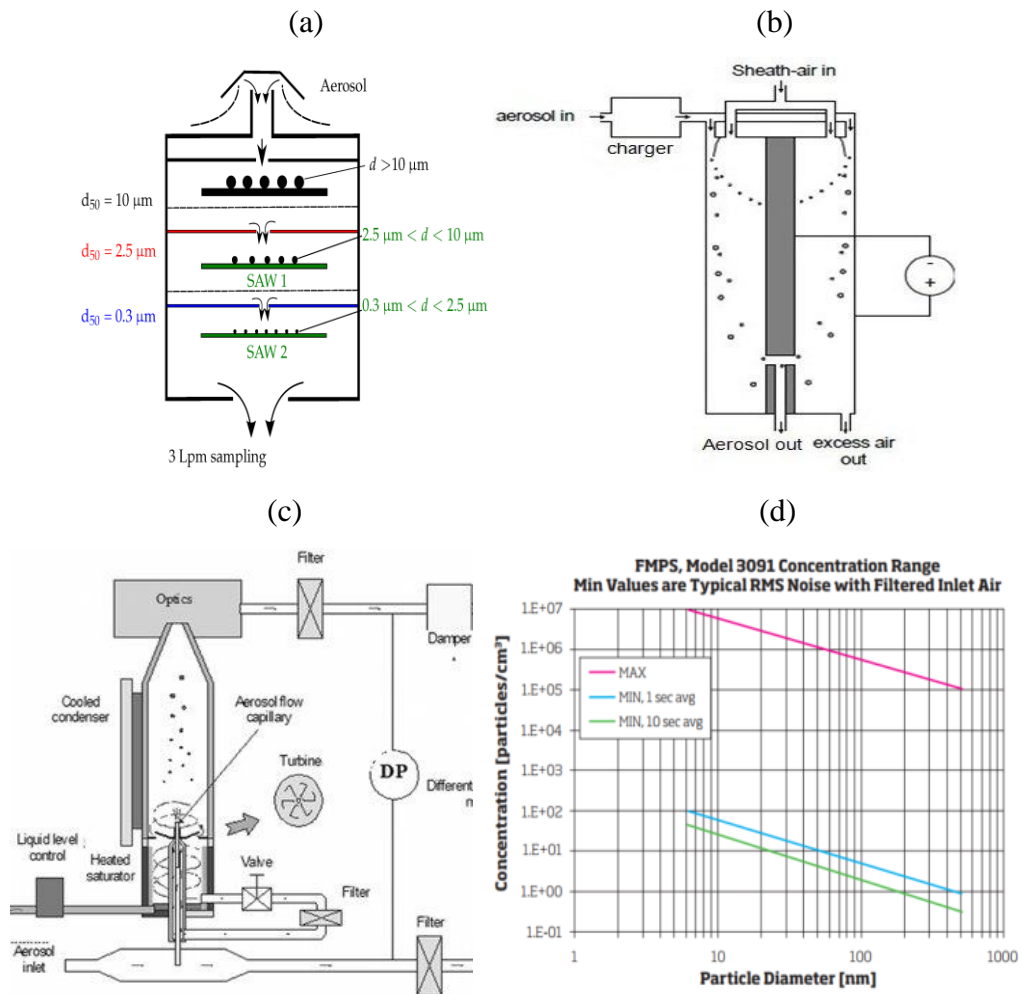


Figure 2.24. Schematic of (a) a cascade impactor; (b) differential mobility analyzer, (c) continuous flow condensation particle counter (CPC), and (d) measurable ranges of solution concentration by FMPS 3091: the maximum (red) and the minimum RMS noise level⁴¹⁻⁴⁷.

2.2.12 Spectroscopic Ellipsometry (SE)

Spectroscopic ellipsometry is an indirect optical characterization method for determining film thickness and optical constants (n , k) of thin-film structure, where the measured values ψ_{exp} and Δ_{exp} are compared to the values calculated from the standard model. Electromagnetic radiation is emitted by a light source linearly polarized by a polarizer. Two parameters, amplitude ratio, ψ_{exp} and phase shift Δ_{exp} , are defined by using the Fresnel reflection coefficients for light polarized parallel to the incident plane p - (r_p) and perpendicular to the plane s - (r_s) polarized light and express the change of the polarization state. Ellipsometry measures the complex reflectance ratio, ρ , of a system, which may be parameterized by the thickness and refraction coefficient. So far,

assigning normalization values of the amplitude of S and P is denoted by r_s and r_p , the complex reflectance ratio, ρ (a complex quantity) can be calculated from Fresnel equations as:

$$\rho = \frac{r_p}{r_s} = \tan(\psi) \exp(i\Delta) \dots \dots \dots (2-10)$$

, Optical parameters were measured by laser ellipsometry (SE: Jobin Yvon, UVISEL) in the photon energy range from 0.5 eV to 5 eV, the spot size of about 1 nm, angle of incidence 70° , sampling time 20 ms as well as measured 10 times at the same location. Note that, the accuracy of the measurement is ± 0.005 for refractive index and ± 0.3 nm for thickness. Spectroscopic data are obtained in the spectral range between 1.5eV (830 nm) and 5.0 eV (250 nm) with constant wavelength steps of 0.1 eV. The quality of the fit is expressed by mean square error (MSE). An optical beam geometry and corresponding electric field in shown in [Figure 2.25](#).

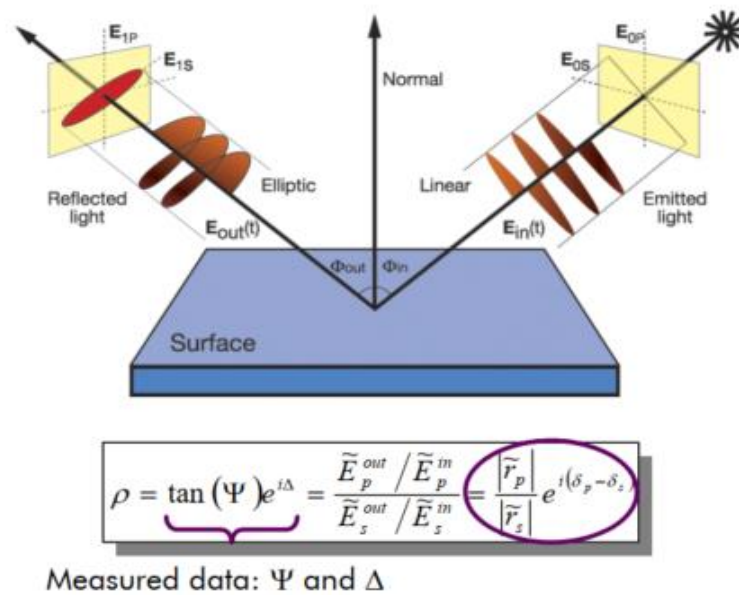


Figure 2.25. Beam geometry for light with its electric field in spectroscopic ellipsometry.

The amplitude ratio of Ψ and phase shift Δ in terms of Fourier coefficients and azimuthal angle,

$$\tan \Psi = \sqrt{\frac{1+\alpha}{1-\alpha}} \tan P, \dots \dots \dots (2-11)$$

$$\cos \Delta = \frac{\beta}{\sqrt{1-\alpha^2}} * \frac{\tan P}{|\tan P|}, \dots\dots\dots(2.12)$$

where α and β are the Fourier coefficients and P is the azimuthal angle. The fitting of the experimental optical spectra and standard Model offers values of sample parameters of interest; thickness, optical constants, refractive index, extinction coefficient, etc. This procedure may be divided into the steps: (a) measure of sample response and (b) analysis with standard models. A model from which reveals unknown interested parameters value based on best fitting with model known values for a specific wavelength of the incident light, polarization state, and the angle of incidence. The single classical oscillator model was used in this study. The single extensively used classical model with single Lorentz and Drude oscillators is expressed as;

$$\tilde{\epsilon}(\omega) = \epsilon_{\infty} + \frac{(\epsilon_s - \epsilon_{\infty}) \cdot \omega_t^2}{\omega_t^2 - \omega^2 + i \cdot \Gamma_0 \cdot \omega} + \frac{\omega_p^2}{-\omega^2 + i \cdot \Gamma_d \cdot \omega} + \sum_{j=1}^2 \frac{f_j \cdot \omega_{0j}^2}{\omega_{0j}^2 - \omega^2 + i \cdot \gamma_j \cdot \omega} \dots\dots(2-13)$$

Where the constant ϵ_{∞} is the high-frequency dielectric constant. Generally, $\epsilon_{\infty} = 1$ or >1 when the oscillators are in higher energies. The constant ϵ_s ($\epsilon_s > \epsilon_{\infty}$) is a static dielectric function at a zero frequency, $\epsilon_s - \epsilon_{\infty}$ is the strength of the single oscillator, ω_t (eV) is the resonant frequency of the oscillator, Γ_0 (in eV) is the broadening of each oscillator or damping factor, which is due to the absorption process involving transitions between two states.

2.2.13 Van der Pauw method for Hall measurement

The Van der Pauw measurement method, named after its inventor Leo J. van der Pauw, is extensively used for determining the sheet resistance and the Hall coefficient of materials with a 4-point measurement system. This technique is used to determine an average resistivity and Hall coefficient, carrier concentration, and mobility, including the semiconductor type either thin films or bulk. This method involves applying a current and measuring voltage using four small contacts on the circumference of a flat, arbitrarily shaped sample with a uniform thickness and traditional structures. However, a well-proportioned shape and a uniform thickness that is much smaller than the contact distance are desirable to obtain precise results. A setup

measuring system with small electrodes attached to the four corners of a uniform and flat square-shaped film is shown in [Figure 2.26](#).

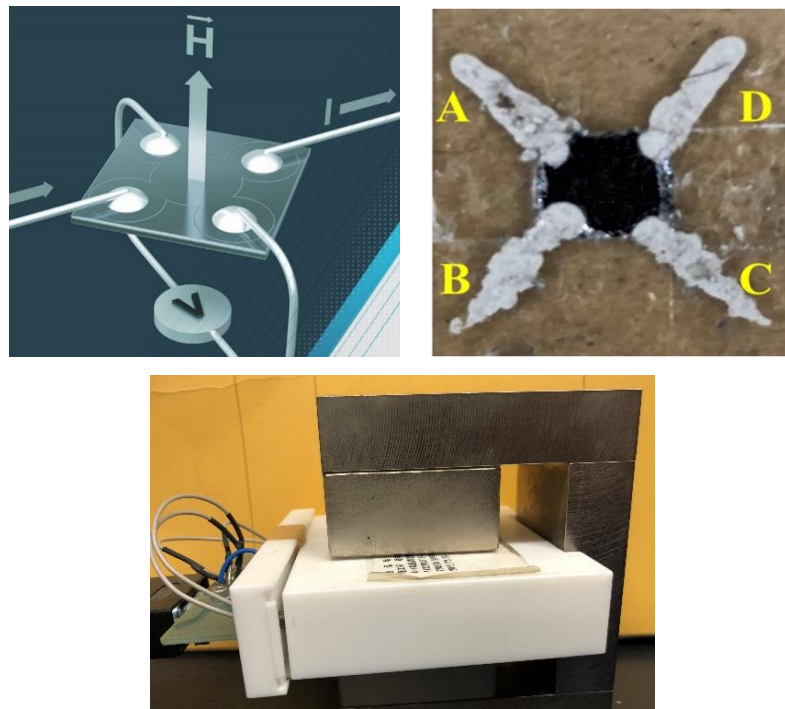


Figure 2.26. A configuration of the Van der Pauw measurement system for the Hall coefficient measurement without and with the magnetic field (0.5 T) is applied perpendicular to the sample surface and the experimental set-up.

Assuming the contacts electrodes as A, B, C, and D, when the current I_{AB} is passed between the electrodes A, and B in absence of a magnetic field, and the voltage V_{CD} between the electrodes C, D, the resistors $R_{AB, CD}$ can be defined as follows:

$$R_{(AB, CD)} = \frac{V_C - V_D}{I_{AB}} \dots\dots\dots(2-14)$$

Similarly, the resistance $R_{BC, DA}$ is:

$$R_{(BC, DA)} = \frac{V_D - V_A}{I_{BC}} \dots\dots\dots(2-15)$$

Therefore, $R_{vertical}$ and $R_{horizontal}$ can be written as:

$$R_{vertical} = \frac{R_{AB, CD} + R_{CD, AB}}{2} \dots\dots\dots(2-16)$$

$$R_{horizontal} = \frac{R_{BC, DA} + R_{DA, BC}}{2} \dots\dots\dots(2-17)$$

Based upon the measured R_{vertical} and $R_{\text{horizontal}}$ values, along with their corresponding reverse values, the average resistance R can be measured assuming $R_{\text{vertical}} = R = R_{\text{horizontal}}$. Then, the sheet resistance, $R_S = \pi R / \ln 2$, where $\pi / \ln 2 \sim 4.53236$ is the van der Pauw constant.

At applied external magnetic field B (0.5 T) perpendicular to the direction of current flow, the resulting Lorentz force will cause the electrons to accumulate at one edge of the sample and therefore, results in a formula for the Lorentz force experienced by the electrons:

$$F_L = \frac{IB}{nA} \dots\dots\dots(2-18)$$

Where n is the electron density, A is the cross-sectional area of the material, and q is the elementary charge (1.602×10^{-19} coulombs). Since the force on an electron from an electric field ϵ is $q\epsilon$, the strength of the electric field is therefore

$$\epsilon = \frac{IB}{qnA} \dots\dots\dots(2-19)$$

$$\epsilon = \frac{IB}{qnA} \dots\dots\dots(2-20)$$

Finally, the magnitude of the Hall voltage is simply the strength of the electric field multiplied by the width of the material, that is:

$$V_H = d\epsilon \dots\dots\dots(2-21)$$

$$V_H = \frac{IB}{qnt} \dots\dots\dots(2-22)$$

where d and t are the width and thickness of the material film respectively. Now, the resistivity, carrier density, and mobility of a semiconductor material based on the aforementioned measurement can be written as:

$$\rho = \frac{\pi d}{\ln 2} \frac{(R_{AB,CD} + R_{BC,DA})}{2} f\left(\frac{R_{AB,CD}}{R_{BC,DA}}\right) \dots\dots\dots(2-23)$$

$$n = \frac{B}{e \cdot 2d \cdot \Delta R_{AC,BD}} \dots\dots\dots(2-24)$$

$$\mu = \frac{t}{B} \cdot \frac{\Delta R_{AC,BD}}{\rho} \dots\dots\dots(2-25)$$

Where e is the charge of the electron and t is the thickness of the epitaxial layer, f is a coefficient for correcting non-uniformity caused by the shape of the sample, the position of the electrodes, etc.

2.2.14 Electrical characterization: MOSFETs, CMOS, and solar cells

The invention of the MOSFET has brought a huge change in the domain of switching electronics and in the amplification of electronic signals. A MOSFET is either a core or integrated circuit where it is designed and fabricated in a single chip with portable small size. It is a four-terminal device having source (S), gate (G), drain (D), and body (B) terminals. In general, the body of the MOSFET is in connection with the source terminal thus forming a three-terminal device such as a field-effect transistor. In this study, characteristics of MOSFETs were performed using Keithley 2100. A schematic of MOSFETs with their terminals, different terminals, and FET measurement system with Keithley 2100 is depicted in Figure 2.27.

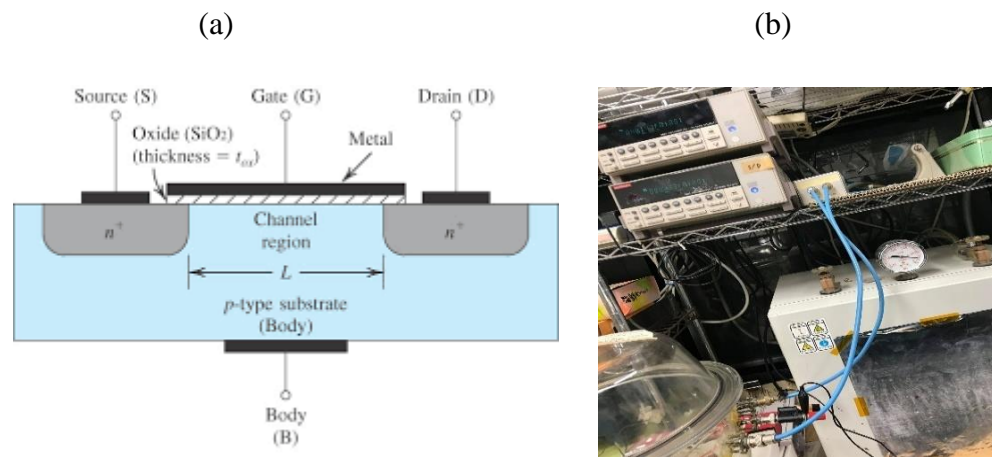


Figure 2.27. Schematic of (a) MOSFET structure with different terminals and (b) device measurement system with Keithley 2100⁴⁸.

Conventionally, the MOSFETs channel shows maximum conductance in depletion mode at no gate voltage and biased conditions. At gate voltage either positive or negative, the channel conductivity decreases in depletion mode. On the other hand, when there is no voltage across the gate terminal, then the device does not conduct and the device shows enhanced conductivity at the maximum voltage across the gate terminal in enhanced mode. So far, the P-channel MOSFET has a p-type channel region located in between the source and drain terminals while the drain and source are heavily doped p⁺ region and the body or substrate is of n-type. The flow of current is in the direction of positively charged holes. Reverse doping and carrier with n-channel behavior for n-type MOSFETs. Three different regions of the cut-off region, linear region, and saturation region are assigned based on conduction behavior in both n-and

p-type MOSFETs. The regions below the threshold voltage are called cut-off regions. The magnitude of current flowing through MOS in cut-off conditions is as small as the channel is absent. At a gate voltage higher than the threshold voltage, the channel is formed between the source and drain terminals. The drain current will flow when there is a voltage difference between the source to drain. A transfer characteristic of n-channel MOSFETs assigning different electrical parameters is shown in Figure 2.28. Where, the drain current increases linearly with the increase of drain to source voltage, this region is called the linear region, and the corresponding mobility is assigned as linear mobility.

$$\mu_{lin} = (dI_{DS}/dV_G) \times (L/(W \cdot C_i \cdot V_D)) \dots\dots\dots(2-26)$$

Further, with an increase of drain to source voltage beyond the linear condition, increasing voltage seems to have no effect on the drain to source current, which is referred to as the saturation region, and the saturation mobility is expressed as,

$$\mu_{sat} = (d\sqrt{I_{DS}}/dV_G)^2 \times (2L/W \cdot C_i) \dots\dots\dots(2-27)$$

where L is a channel length, W is channel width, C_i is the capacitance between the MoSe₂ channel and back gate, and V_D is the voltage drop through the channel.

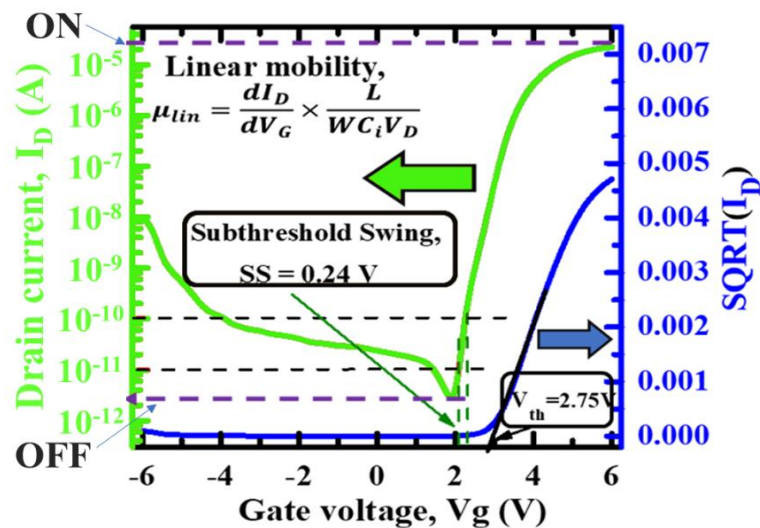


Figure 2.28. A typical transfer characteristic of MOSFET and its respective electrical parameters.

The threshold voltage (V_{th}) has been extracted from a plot of the square root of I_D versus V_g. In particular, V_{th} can be estimated from the intersection of the tangent of the

linear part of the plot of the square root of I_D with the axis of gate voltages. Generally, the variation of threshold voltage in MOSFETs is directly related to the trapped charge density in the insulator/semiconductor interface. The trapped charge density at the interface, subthreshold swing, related to the sharpness between the off and on stat, can be determined by the following relation:

$$N_{trap.charge} = \frac{\Delta V_{th} C_i}{q} \dots\dots\dots(2-28)$$

$$SS = \left[\frac{d \log(I_D)}{dV_g} \right]^{-1} \dots\dots\dots(2-29)$$

Where C_i is the insulator capacitance per unit area, ΔV_{th} is the measured shift in the threshold voltage, q is the electronic charge, V_g is the gate voltage and I_d is the drain current.

So far, the two FETs were connected in series and n-FET drain-by-p-FET drain as output and connected two gates as input, with a metal line to have them work together as a logic MOS inverter. Four probes were used to obtain inverting characteristics of the CMOS circuit. Voltage transfer characteristics and gain curve of an n- WS_2 and p- $WS_{0.3}Se_{1.7}$ FETs based complementary inverter at a V_{DD} of 1-5 V. The transition between two logic 1 and 0 is characterized by voltage gain = $\Delta V_{OUT} / \Delta V_{IN}$. The detailed description and analysis are demonstrated in section 3.2 of the “Result and discussion” chapter.

In general, solar cells are treated as diodes and are been designed for absorbing a wide range of light with a low dark current. [Figure 2.29](#) shows the typical carrier conduction model of $WS_{0.3}Se_{1.7}/WO_x$ lateral p⁺-n junction solar cell and basic parameters of a PV device respectively. The photoconversion efficiency (PCE) is a parameter to understand a solar cell's performance. But several factors affect the PCE of a cell, including its reflectance, thermodynamics, charge carrier separation efficiency, and conduction behavior. To avoid the difficulties of a direct measure of these parameters, primary parameters including short-circuit current density (J_{sc}), open-circuit voltage (V_{oc}), and fill factor (FF) are measured under different monochromatic laser light and AM1.5G of 100 mW/cm² illumination solar simulator.

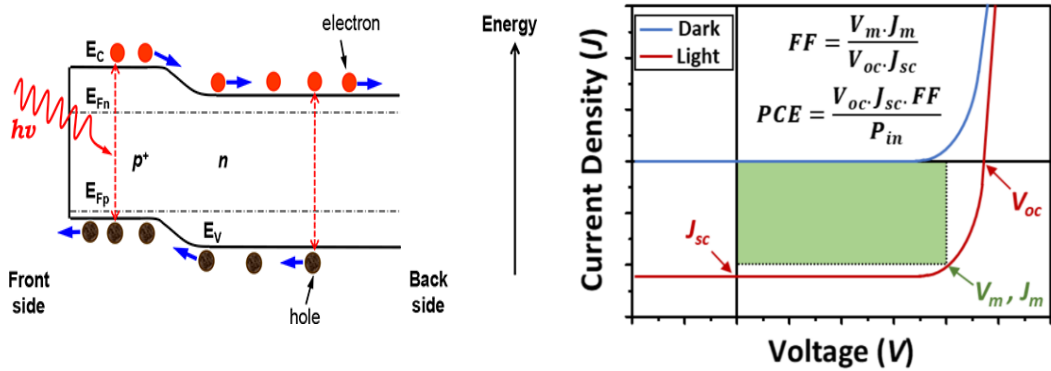


Figure 2.29. Photogenerated carrier transport in a typical p-n junction, and J-V characteristics and different parameters of a solar cell device.

Ideally, each absorbed photon generates an electron-hole pair and is separated by an internal electric field. So, the maximum photocurrent could be calculated for a given wavelength as:

$$J(V) = J_0 \left(e^{\frac{qV}{nkT}} - 1 \right) - J_{sc} \tag{2-30}$$

Here, J_{sc} is the short circuit current, n is the ideality factor, J_0 is the diffusion current of minority carriers in an absorber, q is the electron charge, k is the Boltzmann constant and T is the operating temperature.

The voltage in which the external circuit current becomes zero is called the open-circuit voltage. The V_{oc} depends on the J_{sc} as:

$$V_{oc} = \frac{kT}{q} \ln \left(\frac{J_{sc}}{J_0} + 1 \right) \approx \frac{kT}{q} \ln \left(\frac{J_{sc}}{J_0} \right) \tag{2-31}$$

Due to making a light window for the solar cells, usually only ~10% top surface area is covered by the electrode. As a result, the photogenerated carriers need to travel a large lateral distance to the nearby electrode before they recombined. FF is greatly influenced by the series resistance of the solar cell device. The Fill factor is determined by the ratio of maximum power ($J_m V_m$) generated by a solar cell to the product of V_{oc} and J_{sc} as:

$$FF = \frac{J_m V_m}{J_{sc} V_{oc}} \tag{2-32}$$

Therefore, the resulting efficiency for a p-n junction solar cell is:

$$\eta = \frac{V_{oc} J_{sc} FF}{P_{in}} \tag{2-33}$$

External Quantum Efficiency is the ratio of the number of charge carriers collected by the solar cell to the number of photon irradiation of given energy on the solar cell is another significant parameter of the solar cell. This is a wavelength-dependent measurement of photocurrent by illuminating monochromatic light of wavelength λ . Since the I_{sc} depends on the bias voltage, the bias voltage must be fixed during measurement. The recombination losses throughout the bulk semiconductor of a solar cell can be understood from the EQE spectra.

References

1. Dang, G. T., Allen, M. W., Furuta, M. & Kawaharamura, T. Electronic devices fabricated on mist-CVD-grown oxide semiconductors and their applications. *Jpn. J. Appl. Phys.* **58**, (2019).
2. Hossain, J. *et al.* Investigating the chemical mist deposition technique for poly(3,4-ethylenedioxythiophene):poly(styrene sulfonate) on textured crystalline-silicon for organic/crystalline-silicon heterojunction solar cells. *Jpn. J. Appl. Phys.* **55**, (2016).
3. Ohki, T. *et al.* Effect of substrate bias on mist deposition of conjugated polymer on textured crystalline-Si for efficient c-Si/organic heterojunction solar cells. *Phys. Status Solidi Appl. Mater. Sci.* **213**, 1922–1925 (2016).
4. Islam, A. T. M. S. *et al.* Chemical mist deposition of organic for efficient front- and back-PEDOT:PSS/crystalline Si heterojunction solar cells. *Appl. Phys. Lett.* **114**, (2019).
5. Burlingame, P. J. & Dowhower, A. L. The Pennsylvania State University. *New Dir. Student Serv.* **2009**, 79–86 (2009).
6. The instability of liquid surfaces when accelerated in a direction perpendicular to their planes. II. *Proc. R. Soc. London. Ser. A. Math. Phys. Sci.* **202**, 81–96 (1950).
7. Ruiz, J., Martínez, P., Martín, Í. & Lucas, M. Numerical characterization of an ultrasonic mist generator as an evaporative cooler. *Energies* **13**, 2971 (2020).
8. Avvaru, B., Patil, M. N., Gogate, P. R. & Pandit, A. B. Ultrasonic atomization: Effect of liquid phase properties. *Ultrasonics* **44**, 146–158 (2006).
9. Kawaharamura, T. Physics on development of open-air atmospheric pressure thin film fabrication technique using mist droplets: Control of precursor flow. *Jpn. J. Appl. Phys.* **53**, 05FF08 (2014).
10. Young, J. R. *et al.* Uniform large-area growth of nanotemplated high-quality monolayer MoS₂. *Appl. Phys. Lett.* **110**, 263103 (2017).
11. Al-Hilli, A. A. & Evans, B. L. The preparation and properties of transition metal dichalcogenide single crystals. *J. Cryst. Growth* **15**, 93–101 (1972).
12. Agarwal, M. K., Patel, H. B. & Nagireddy, K. Growth of single crystals of WSe₂ by sublimation method. *J. Cryst. Growth* **41**, 84–86 (1977).

13. Agarwal, m. K., reddy, k. N. & patel, h. B. Letter to the editors growth of tungstenite single crystals by direct vapour transport method m.k. agarwal, k. Nag! Reddy and h.b. patel. *J. Crystak Growth* **46**, 139–142 (1979).
14. Growth, C., Company, N. P., Pate, S. & Vidyanagar, V. Vapour growth and characterization of mo0 5w0 5se2 single crystals m.k. Agarwal, p.a. Wan! And p.d. Patel. **49**, 693–695 (1980).
15. Blake, P. *et al.* Making graphene visible. *Appl. Phys. Lett.* **91**, 063124 (2007).
16. Benameur, M. M. *et al.* Visibility of dichalcogenide nanolayers. *Nanotechnology* **22**, 125706 (2011).
17. Zeng, X. Solution Processed 2D Transition Metal Dichalcogenides and Electrical Properties of TMD Thin Film Transistors. Thesis sessertation, IRC-Library, *Information Resource Center der Jacobs University Bremen* (2017).
18. Improved Surface Characterization with AFM Imaging. *Tech Briefs: Engineering solutions for Design and Manufacturing*. online access, May (2022).
19. Scanning electron microscope -*wikipedia* -online access, May (2022).
20. Tummala, P. *et al.* Application-oriented growth of a molybdenum disulfide (MoS₂) single layer by means of parametrically optimized chemical vapor deposition. *Materials*, **13**(12), 2786 (2020).
21. Kim, J. Investigation of solution process of molybdenum disulfide for thin film transistor applications, thesis desertation. *JAIST Repository, Japan* (2017).
22. Jones, R. R., Hooper, D. C., Zhang, L., Wolverson, D. & Valev, V. K. Raman Techniques: Fundamentals and Frontiers. *Nanoscale Res. Lett.* **14**, 231 (2019).
23. Liang, F. *et al.* Raman spectroscopy characterization of two-dimensional materials. *Chinese Phys. B* **27**, 037802 (2018).
24. Zeng, H. *et al.* Optical signature of symmetry variations and spin-valley coupling in atomically thin tungsten dichalcogenides. *Sci. Rep.* **3**, 1608 (2013).
25. Fu, Q. *et al.* Synthesis and Enhanced Electrochemical Catalytic Performance of Monolayer WS₂(1-x)Se_{2x} with a Tunable Band Gap. *Adv. Mater.* **27**, 4732–4738 (2015).
26. Aslan, O. B. *et al.* Probing the Optical Properties and Strain-Tuning of Ultrathin Mo_{1-x}W_xTe₂. *Nano Lett.* **18**, 2485–2491 (2018).
27. Han, B. *et al.* Correlatively Dependent Lattice and Electronic Structural Evolutions in Compressed Monolayer Tungsten Disulfide. *J. Phys. Chem. Lett.* **8**, 941–947 (2017).

28. Zhang, X. & Li, X. B. Characterization of Layer Number of Two-Dimensional Transition Metal Diselenide Semiconducting Devices Using Si-Peak Analysis. *Adv. Mater. Sci. Eng.* **2019**, 7865698 (2019).
29. Xray Photoemission Spectroscopy, Los Almos National Laboratory, *University of California*, online access, May (2022).
30. Surface analysis technique; AES. *ULVAC-PHI, Inc.* online access, May (2022).
31. Krawczyk, M., Pisarek, M., Szoszkiewicz, R. & Jablonski, A. Surface characterization of MoS₂ atomic layers mechanically exfoliated on a si substrate. *Materials*. **13**, 3595, 1–12 (2020).
32. Jonathan, N. Ultraviolet photoelectron spectroscopy. *Nature* **268**, 774–774 (1977).
33. Material Science; Ultraviolet Photoelectron Spectroscopy, *ThermoFisher Scientific*, online access, May (2022).
34. Kelvin Probe Force Microscope. *Wikipedia*, online access, May (2022).
35. Stanford, M. G. *et al.* Focused helium-ion beam irradiation effects on electrical transport properties of few-layer WSe₂: Enabling nanoscale direct write homo-junctions. *Sci. Rep.* **6**, (2016).
36. TOF-SIMS. *ULVAC-PHI, Inc.* online access, May (2022).
37. Mogk, D.W. Time-of-Flight Secondary Ion Mass Spectrometry (TOF-SIMS). Teaching Activities and Resources, *Monash state university*, online access, May (2022).
38. Jeong, Y. *et al.* Structural characterization and transistor properties of thickness-controllable MoS₂ thin films. *J. Mater. Sci.* **54**, 7758–7767 (2019).
39. Marple, V. A. & Willeke, K. Impactor design. *Atmos. Environ.* **10**, 891–896 (1976).
40. Hering, S. V. Impactors, cyclones, and other inertial and gravitational collectors. *Air sampling instruments for evaluation of atmospheric contaminants* Book chapter: **4**, 279–289 (1995).
41. Fast mobility particle sizer™ (fmps™) spectrometer model 3091. *TSI Inc.* online access, May (2022).
42. Jeong, C. H. & Evans, G. J. Inter-comparison of a fast mobility particle sizer and a scanning mobility particle sizer incorporating an ultrafine water-based condensation particle counter. *Aerosol Sci. Technol.* **43**, 364–373 (2009).

43. M. Obaidullah, S. B. and J. D. R. An overview of PM formation mechanisms from residential biomass combustion and instruments using in PM measurements. *International Journal of Energy and environment*, **12**, 41–50 (2018).
44. Giechaskiel, B. *et al.* Calibration of condensation particle counters for legislated vehicle number emission measurements. *Aerosol Sci. Technol.* **43**, 1164–1173 (2009).
45. Agarwal, J. K. and SEM, J. G. Continuous flow, Single particle-counting condensation nucleus counter. *J. Aerosol Sci.* **11** 343-357 (1980).
46. Wang, X., Caldow, R., Sem, G. J., Hama, N. & Sakurai, H. Evaluation of a condensation particle counter for vehicle emission measurement: Experimental procedure and effects of calibration aerosol material. *J. Aerosol Sci.* **41**, 306–318 (2010).
47. Hering, S. V. & Stolzenburg, M. R. A method for particle size amplification by water condensation in a laminar, thermally diffusive flow. *Aerosol Sci. Technol.* **39**, 428–436 (2005).
48. What is a MOSFET: Working and its Applications, *Electronic Project Focus*, *elprocus*, online access, May (2022).



Chapter 3
Results and Discussions

Chapter 3: Results and Discussions

This chapter describes the overall results obtained in this study. In particular, the first part of this chapter explores the effects of deposition parameters of sequential mist CVD such as tubular furnace temperature (T_f), storage time of mist precursor within the closed chamber (t_2), number of repetition cycles of alternate mist supply (N), and sulfurization conditions. An obtained atomic mono/bilayers MoS_2 with an average flakes size of $120\ \mu\text{m}$ under adjusted conditions was applied to fabricate the metal-oxide field-effect transistors (MOSFETs) on *th*- SiO_2 and mist-CVD grown amorphous aluminum titanium oxide $\text{a-Al}_{0.74}\text{Ti}_{0.26}\text{O}_y$ (ATO) substrate. As a second topic, we investigated the synthesis of millimeter-size few-layer tungsten disulfide (WS_2) and tungsten sulphoselenide ($\text{WS}_{2-x}\text{Se}_x$) by intermittent mist- CVD from $(\text{NH}_4)_2\text{WS}_4$ precursor dissolved in N-methyl-2-pyrrolidone (NMP) in the same analogy as the previous MoS_2 study from $(\text{NH}_4)_2\text{MoS}_4$. The synthesized WS_2 and $\text{WS}_{0.3}\text{Se}_{1.7}$ was applied in FETs fabrication to obtain n- and p-channel behaviors using gold and platinum source/drain electrodes, respectively. Furthermore, a prototype of CMOS logic circuits using n- WS_2 and p- $\text{WS}_{0.3}\text{Se}_{1.7}$ FETs was designed. As a third topic, the photovoltaic effect of few-layer $\text{WS}_{0.3}\text{Se}_{1.7}$ based lateral $\text{p}^+\text{-n}$ junctions formed by the He/O_2 plasma, followed by the laser irradiations using MOSFET structure has been studied. The impact of a gold mirror layer inserted between the dielectric layer and the c-Si substrate was also investigated for further improvement of photocurrent.

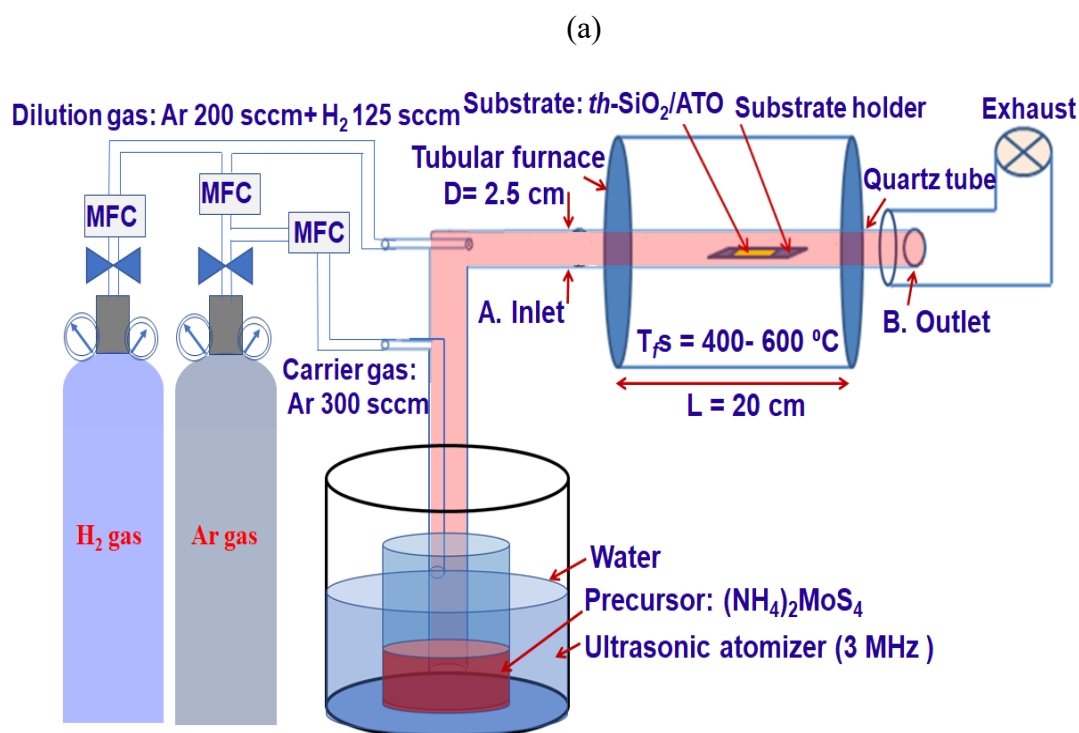
3.1 Mist chemical vapor deposition of crystalline MoS_2 atomic layer films using sequential mist supply mode and its application in field-effect transistors

In this section, we first diagnose the size distribution of mist particles by the fast-scanning mobility particle analyzer (Tokyo Dylec Co., Ltd. FMPS model-3091). Then, the effects of deposition parameters of mist CVD such as tubular furnace temperature (T_f), storage time of mist precursor within the closed chamber (t_2), number of repetition cycles of alternate mist supply (N), and sulfurization conditions on the growth of atomic mono/bilayers MoS_2 using the sequential precursor mist supply mode is examined. Finally, the synthesized mono/bilayer MoS_2 was applied as a channel layer of metal–

oxide–semiconductor field-effect transistors (MOSFETs) on th -SiO₂ and mist-CVD grown amorphous Al_{0.74}Ti_{0.26}O_y dielectric layer.

3.1.1 Growth of MoS₂ thin films under sequential mist supply mode

Figure 3.1.1a shows the schematic of the mist-CVD system consisting of a 3 MHz atomizer, quartz tube, tubular furnace, and substrate holder. A 90-nm-thick th -SiO₂ and 50-nm-thick ATO by mist-CVD on p⁺-Si substrates were placed at the position of a maximum temperature zone of 12 cm- from the inlet. (NH₄)₂MoS₄ dissolved in *N*-Methyl-2-pyrrolidone (NMP) (0.05 M/L) was used as a precursor and H₂/Ar mixture as mist generation and carrier gas. The flow chart of the sequential supply of mist precursor is shown in Figure 3.1.1b. After flowing Ar/H₂ (95/5 sccm) for 10 min in the chamber to remove air, the chamber is closed. Then, the mist precursor generated by the ultrasonic atomizer was transported through the glass tube using Ar/H₂ as a carrier gas for 50 s and it was stored within the closed chamber at different storage times (t_2) after each supply of mist precursor. Subsequently, the stored mist is exhausted for 30 s using a vacuum pump and the cycle was repeated for different cycles (N). The growth condition of MoS₂ is summarized in Table 3.1.1. All the samples were sulfurized after film deposition using an Ar/H₂ (95/5 sccm) gas mixture at a T_f of 600 °C for 1200 s to obtain the stoichiometric composition of MoS₂ (Figure 3.1.1c).



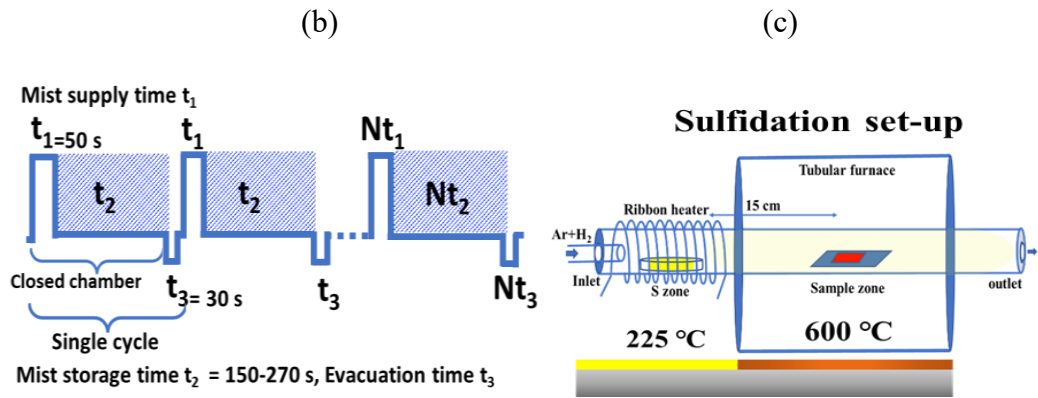


Figure 3.1.1. (a) Schematic representation of the mist CVD system, (b) The sequential MoS₂ precursor mist supply mode, and (c) sulfurization setup.

Table 3.1.1. MoS₂ deposition and sulfurization conditions

MoS ₂ deposition conditions	
Solute	(NH ₄) ₂ MoS ₄ (ATTM)
Solvent	C ₅ H ₉ NO (NMP)
Substrate	SiO ₂ (90 nm)/p ⁺ -Si Mist-CVD Al _{0.74} Ti _{0.26} O _y /p ⁺ -Si
Carrier gas, flow rate, F _d	Ar: 500 sccm + H ₂ : 125 sccm
Solution concentration	0.05, 0.01 M/L
Tabular furnace temperature, T _f	400- 600 °C
Mist supply time, t ₁	30-75 s
Mist storage time, t ₂	150- 270 s
Number of repetition cycles, N	3- 9 cycles
Sulfurization condition	600 °C, 1200 s Ar 95 sccm + H ₂ 5 sccm

Figure 3.1.2a shows the size distribution of mist particles at the inlet and outlet positions of the tubular furnace, A and B for a different flow rate of N₂ for a T_f of 850 °C and different furnaces temperature from 700 to 900 °C. No significant changes in the size distributions of mist particles were observed at the inlet and outlet, A and B

positions when N₂ was used as carrier gas having the mist particle size of 100-130 nm. The reaction formula for the synthesis of MoS₂ from (NH₄)₂MoS₄ is shown with the reaction temperature range in equations 3-1,2. According to thermodynamics of (NH₄)₂MoS₄ in a vacuum environment resulted in the conversion of (NH₄)₂MoS₄ to MoS₃ at 120- 360 °C as shown in eq. (3-1), and the conversion of MoS₃ to MoS₂ [eq. (3-2)] required the annealing at a temperature of > 800 °C. It is also suggested that the conversion of (NH₄)₂MoS₄ to MoS₂ was further lowered to ~ 425 °C in the presence of H₂ gas as described in eq. (3-3)¹:



Figure 3.1.2b shows the size distribution of mist particles at the inlet and outlet positions of the tubular furnace, A and B for different H₂/Ar mixing ratios for a T_f of 850 °C. The average size of mist particle showed a maximum at ~75 nm with a shoulder peak at ~40 nm. The tail distribution toward the larger mist size and its number density increased with increasing H₂ flow rate for the inlet position A. On the other hand, the use of solely Ar as a carrier gas showed broad bands having a maximum at 50 and 130 nm with a sharp intense peak at 20 nm at the outlet position B. This suggests that the use of solely Ar (or N₂) as a dilution gas accelerate the promotion of the mist aggregation by T_f in the gas phase. However, when H₂ flow was increased, the number density of mist particles with a size of ~50 nm increased markedly together with a slight increase and/or no marked changes in those at 20- 30 nm at the outlet position B. Thus, an H₂ addition in Ar promote the reduction of the number density of mist particle of 130- 140 nm together with a marked increase of those of ~50 nm. Moreover, additional H₂ flow shortens the residence time of the mist precursor by decreasing its number density by one order of magnitude at the outlet position B compared to position A, which suggests that the mist precursor generated by the primary reaction in the furnace contributes preferentially to the film formation. The broadband peaks containing three to four components were observed in the region of 30- 250 nm in the size distribution of mist particles at different T_fs of 200 to 850 °C under an H₂/Ar mixture gas of 150/200 sccm. The broadband peak at 140 nm was almost independent of T_f up to 800 °C but it disappeared at a T_f of 850 °C. These results suggest that the main peak observed at 50

nm generated by the thermal decomposition and chemical reaction with H₂ mainly contributes to the formation of MoS₂ by promoting the decomposition of a mist of 140–150 nm, which is attributed to MoS_x at a T_f of 850 °C. Addition of H₂ with Ar as carrier gas reduces the precursor decomposition temperature markedly as was expected from the equation 3-3 leads to the synthesis of MoS₂ at a T_f ≤ 500 °C.

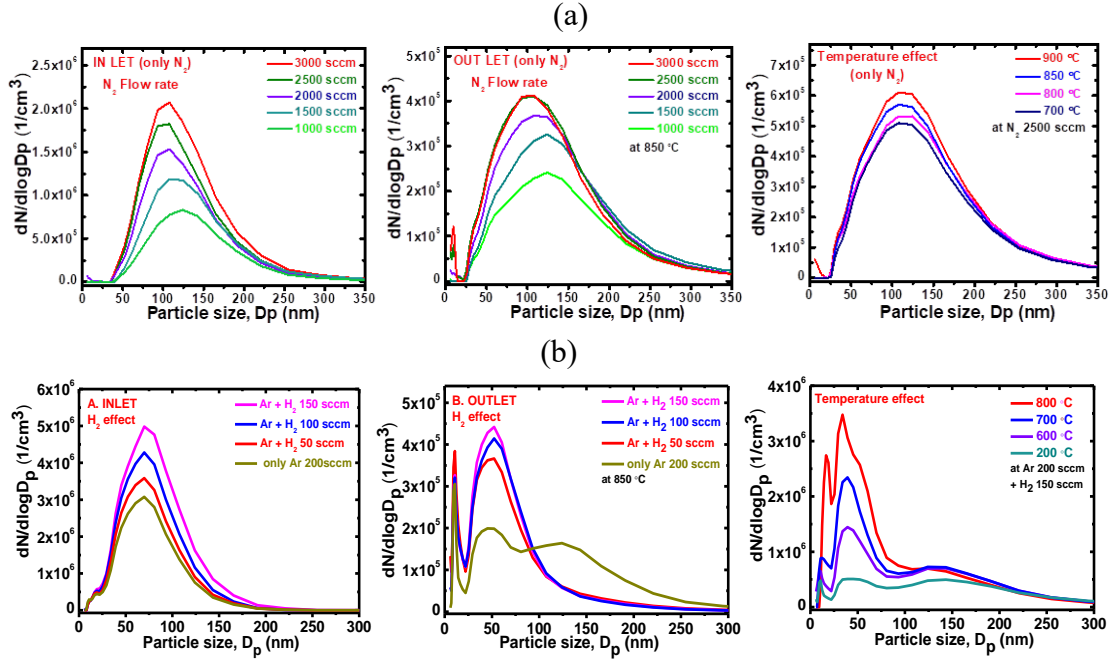


Figure 3.1.2. (a) Size distribution of mist particle monitored at the inlet and outlet positions of the tubular furnace for different N₂ flow rates for a T_f of 850 °C and different T_fs of 700 to 900 °C under an N₂ gas flow of 2500 sccm, (b) Size distribution of mist particle monitored at the inlet and outlet positions for different H₂/Ar mixing ratios at a T_f of 850 °C, and at different T_fs of 200 to 850 under an H₂/Ar mixture gas of 150/200 sccm.

Figure 3.1.3 shows an optical microscope image and Raman spectra of as-deposited MoS_x layers synthesized at different furnace temperature T_fs of 400–600 °C with a mist supply time of 300 s. The metallic phase peaks of J₁, J₂, and semiconducting phase peaks of A, and B are observed in each of the samples synthesized at 400–600 °C. A broad Raman peak observed at 200–350 cm⁻¹ corresponds to the composed of metallic phase J₂ of 1T mode (J₁ is at 150 cm⁻¹ also 1T), single layer chalcogen mode E_g¹ (of 1H) including crystalline Si peaks². In addition, a semiconducting 2H phase in-plane vibration mode of E_g¹ (A) and out-of-plane mode of A_{1g} (B) with multiple 1st and 2nd order LO and TO phonon modes have appeared. No significant change is observed with

increasing furnace temperature. Every as-deposited sample for different furnace temperatures requires further sulfurization for obtaining semiconducting trigonal phase MoS₂ as revealed by Raman observations. Therefore, all the samples were sulfurized after film deposition using an Ar/H₂ (95/5 sccm) gas mixture at a T_f of 600 °C for 1200 s, resulting in the stoichiometric compositional MoS₂ as stated the below.

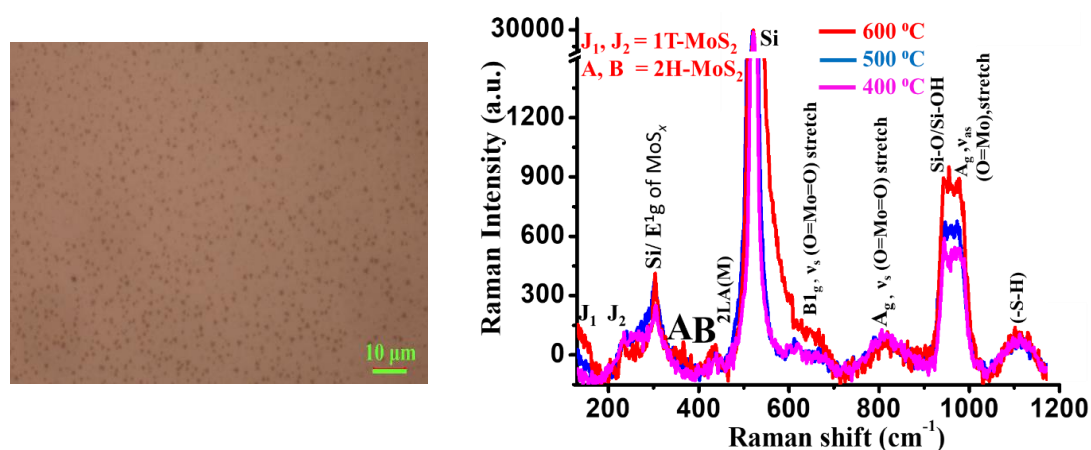


Figure 3.1.3. Optical Microscope image (500 °C, supply t of 150 s) and Raman spectra of as-deposited MoS_x (without sulfurization) synthesized at different T_fs of 400– 600 °C, mist supply time of 300 s.

Figure 3.1.4 shows an optical microscope image of MoS₂ flake synthesized at different mist supply times t₁s under the t₂ = 150 s, N = 7 cycles at a T_f = 500 °C. The average size of the MoS₂ flake was increased up to 28 μm at a t₁ = 75 s with multilayers thickness. Bilayer uniform flake with an average size of ~10 μm was obtained at a t₁ = 50 s. Therefore, the precursor mist supply time t₁ was constant at 50 s for further study considering the tradeoff among flakes size, uniformity, and the number of stacks of MoS₂ atomic layers.

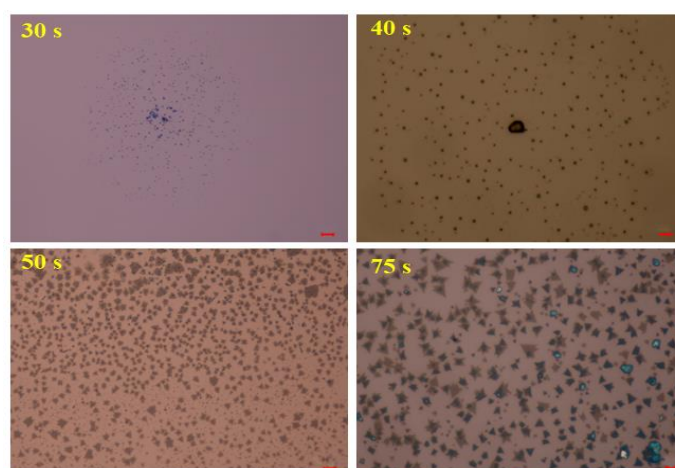
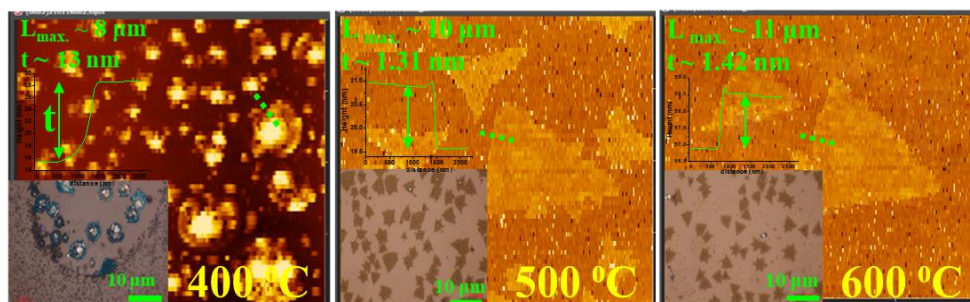


Figure 3.1.4. Optical microscope images of MoS₂ flake synthesized at different mist supply times t_1 = 30- 75 s under the t_2 = 150 s, N = 7 cycles at a T_f = 500 °C followed by sulfurization at 600 °C for 1200 s. The scale bar is 25 μ m.

Figure 3.1.5a shows the AFM image of MoS₂ layers synthesized at different T_f s for t_1 = 50 s, t_2 = 150 s, N = 7, and a precursor concentration of 0.05 M/L. The inset shows the height profile obtained by the line scans and optical microscope images of the corresponding samples. Figure 3.1.5b shows the variations in layer thickness, and the average size of the MoS₂ flake within a $270 \times 180 \mu\text{m}^2$ area are summarized as a function of T_f . At a T_f of 400 °C, a large number of bulk particles was dominant with an average size of several micrometers. However, a triangular MoS₂ flake with an average side of $\geq 10 \mu\text{m}$ was observed at T_f of 500 and 600 °C. The layer thickness was decreased markedly from 13 to 1.42 nm at a T_f of 500 °C and no significant changes in the average size and shape of MoS₂ flakes were observed at 600 °C. Further higher T_f over 600 °C increased the sublimation of S vapor. The optical microscope image also revealed that the area ratio of MoS₂ flake in the $270 \times 180 \mu\text{m}^2$ was also decreased from 65 to 44%, while the average size of MoS₂ flake increases from 8 to 11 μm when T_f s is increased from 400 to 600 °C. In addition, Raman and PL spectra of corresponding samples are shown in Figure 3.1.5c. The frequency difference $\Delta\omega$ of the Raman peak at ~ 385 and $\sim 405 \text{ cm}^{-1}$ related to the number of atomic layers decreases from ~ 24.4 to 21.2 cm^{-1} , which is almost consistent with the result in the AFM images^{3,4}. Further, the PL intensity increases with an increase in the T_f as the number of layers decreases. These results suggest that film deposition at T_f s of 500–600 °C improves the layer crystallinity. Thus, the number density and size distribution of triangular MoS₂ flakes are determined during the 150 s in the closed chamber, i.e., the thermal equilibrium state between the sticking of incoming mist precursors and sublimation of S vapor at the layer surface.

(a)



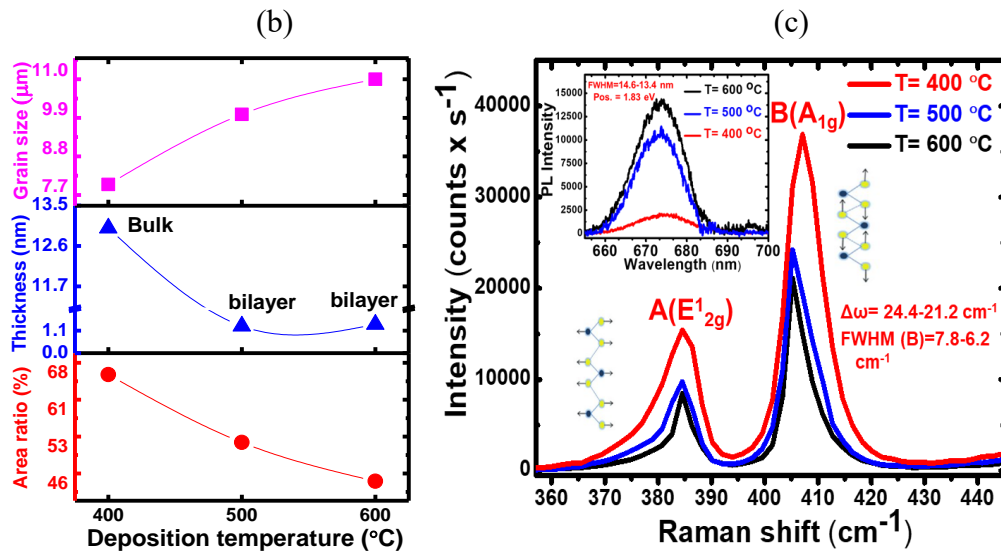


Figure 3.1.5. (a) AFM images of MoS₂ layers synthesized at different T_s of 400–600 °C for $t_1 = 50$ s, $t_2 = 150$ s, and $N = 7$ cycles (the insets show the optical microscope image and height profile of the corresponding samples); (b) Variations of the layer thickness, the average size of the MoS₂ flake, and area ratio of the MoS₂ flake with T_s ; (c) Raman and PL spectra of the corresponding samples.

Figure 3.1.6a shows the AFM images of MoS₂ flakes synthesized at different t_s for $t_1 = 50$ s, $N = 7$ cycles, $T_f = 500$ °C, and precursor concentration of 0.05 M/L. The insets show the height profile of the flake and optical microscope images of the corresponding samples. In Figure 3.1.6b, the layer thickness, grain size, and area ratio of MoS₂ flakes are depicted as functions of t_s . The layer thickness and the area ratio of MoS₂ flakes decrease from 1.41 to 0.93 nm (from bilayer to monolayer thickness) and 45 to 22%, respectively, while the average size of the MoS₂ flakes increases from 12 to 27 μm. This may be attributed to the enhanced sublimation of S with an increase in t_2 , which promotes thinning of the MoS₂ flake layers with an increase in the grain size noticeably together with smaller surface roughness. The Raman and PL spectra of the corresponding MoS₂ films are shown in Figure 3.1.6c. The $\Delta\omega$ decreases from 21.3 to 20.2 nm (bilayer to monolayer) with an increase in t_2 , and the PL intensity increases despite thinning of the layers.

Here, t_2 corresponds to the transition of the thermal equilibrium state between the sticking of incoming mist precursors and the sublimation of S vapor at the layer surface. The average size of the flake is enlarged with longer t_2 and the growth of crystalline

flake proceeds from the edge and side corners equivalently. As a result, the circular-shaped MoS₂ flake is dominant at a t_2 of 210 s and a further increase in t_2 promotes the surface roughness due to the increased sublimation of sulfur vapor. These results imply that there exists an appropriate t_2 for enlarging the average size of crystalline MoS₂ flakes.

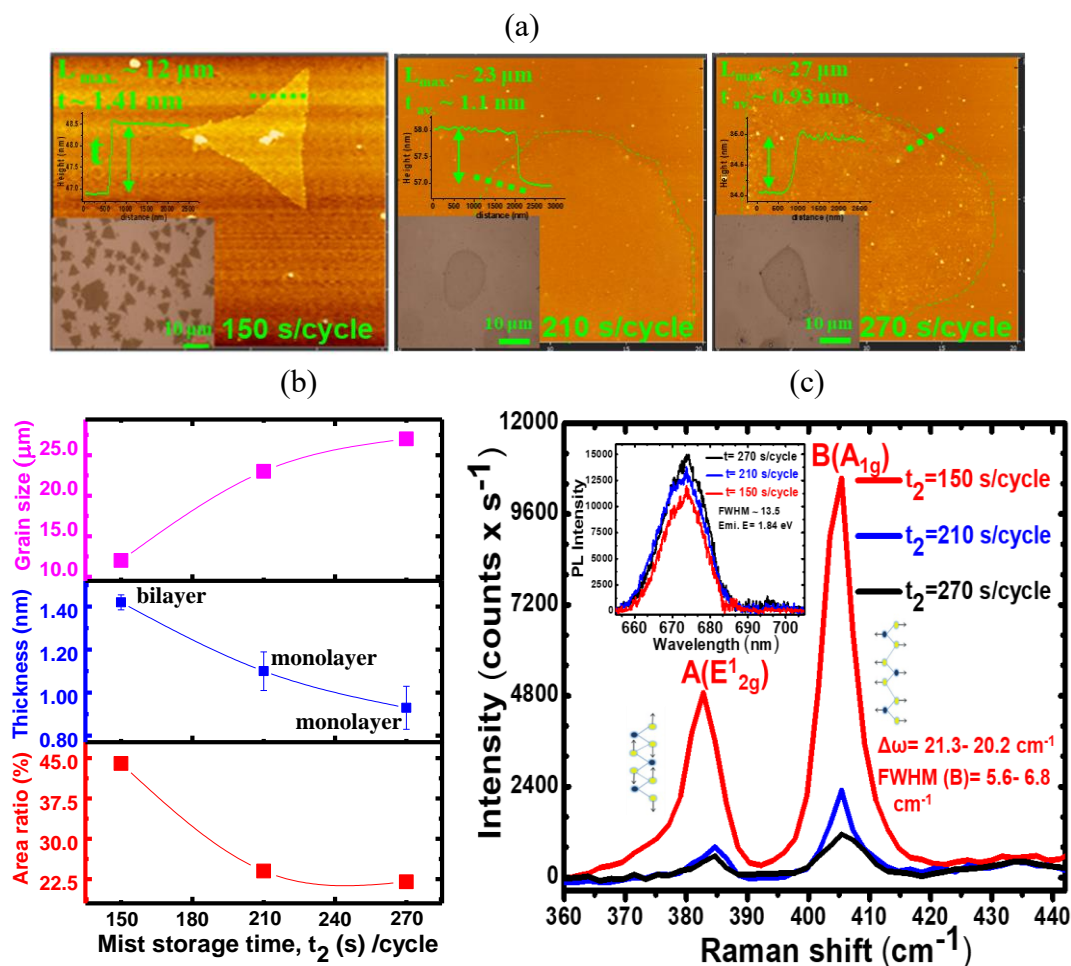


Figure 3.1.6 (a) AFM images of MoS₂ flakes synthesized at different t_2 for $t_1 = 50$ s, $N = 7$ cycles, and $T_f = 500$ °C; (b) Variations of layer thickness, area ratio, and an average size of the MoS₂ flakes with t_2 ; (c) Raman and PL spectra of the corresponding samples.

Figure 3.1.7a shows the AFM images of MoS₂ flakes synthesized by varying N for a $t_1 = 50$ s, $t_2 = 150$ s, $T_f = 500$ °C, and solution precursor concentration of 0.05 M/L. The inset shows the height profile of the flake and optical microscope images of the corresponding samples. The variations in the area ratio of the MoS₂ flake, layer thickness, and the grain size of the MoS₂ layers calculated from the AFM and optical microscope images are shown in Figure 3.1.7b. Both the grain size and the layer thickness of MoS₂ flakes increased from 2.0 to 23 μm and 0.68 to 2.51 nm, respectively,

with an increase in N , while the area ratio of the MoS₂ flakes decreased from 75 to 39%. The Raman spectra of corresponding MoS₂ layers also revealed that the $\Delta\omega$ increases from ~ 20.3 to 23.8 cm^{-1} , which indicated the increase in the number of layers from monolayer to multilayer as observed in AFM studies (Figure 3.1.7c). On the other hand, no significant changes were observed in the full width at half maximum (FWHM) of the Raman and PL peaks. These results suggest that the alternate supply of mist precursor mode may contribute to the increase in the number of stacks of atomic layer together with the sublimation of weakly adhered particles. Herein, repetition cycles of the mist precursor offer controlled deposition of mono/bilayer to multilayer (3– 5 layer) MoS₂ film. The mono/bilayer flakes were observed for 7 repetition cycles and a further increase in the repetition cycles caused the vertical growth rather than lateral.

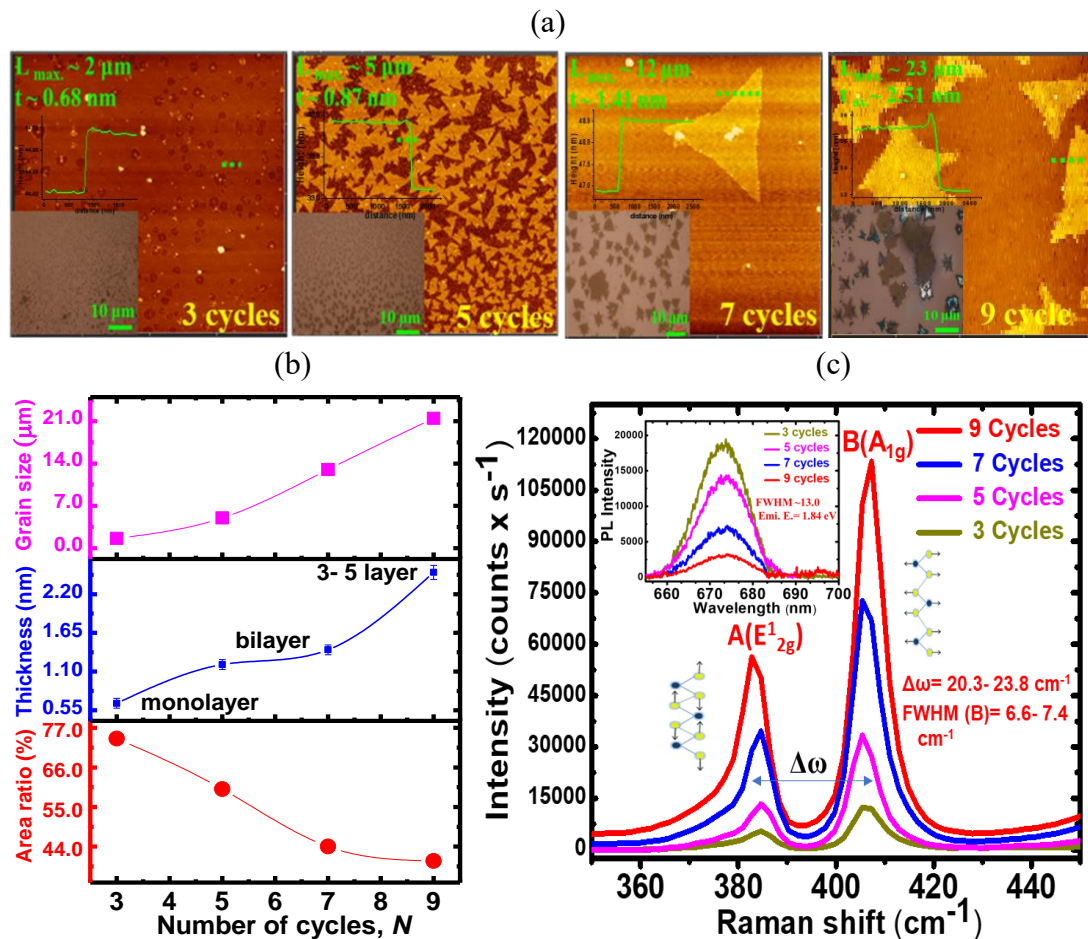


Figure 3.1.7. (a) AFM images of MoS₂ flakes fabricated at different N for $t_1 = 50$ s, $t_2 = 150$ s, and $T_f = 500$ °C (the inset shows the optical microscope image and height profile of the corresponding samples); (b) Variations of the layer thickness, area ratio, and average size of the MoS₂ flakes with N ; (c) Raman and PL spectra of the corresponding samples.

3.1.2 Role of sulfurization of MoS₂ films

Figure 3.1.8a depicts the AFM and optical microscope images of MoS₂ samples exposed to sulfur vapor using H₂/Ar (5/95 sccm) gases at different sulfidation temperatures $T_s = 600\text{--}650\text{ }^\circ\text{C}$ for 20 minutes synthesized at a $t_1 = 50\text{ s}$, $t_2 = 150\text{ s}$, $N = 7$ cycles, $T_f = 500\text{ }^\circ\text{C}$. The area ratio of MoS₂ flakes, layer thickness, and grain size of the corresponding MoS₂ layers calculated from the AFM and optical microscope images are summarized in Figure 3.1.8b. The MoS₂ film uniformity decreases with an increase in the selenization temperature beyond 625 °C with increasing flakes thickness. The higher sulfurization temperature increases the aggregation of the MoS₂ flakes together with the sublimation of S elements. No noticeable change was observed in Raman and PL peaks intensity with increasing the sulfurization temperature rather small increase of peaks intensity (Figure 3.1.8c). Thus, crystalline MoS₂ flakes with a relatively uniform surface are observed at a temperature of 600- 625 °C.

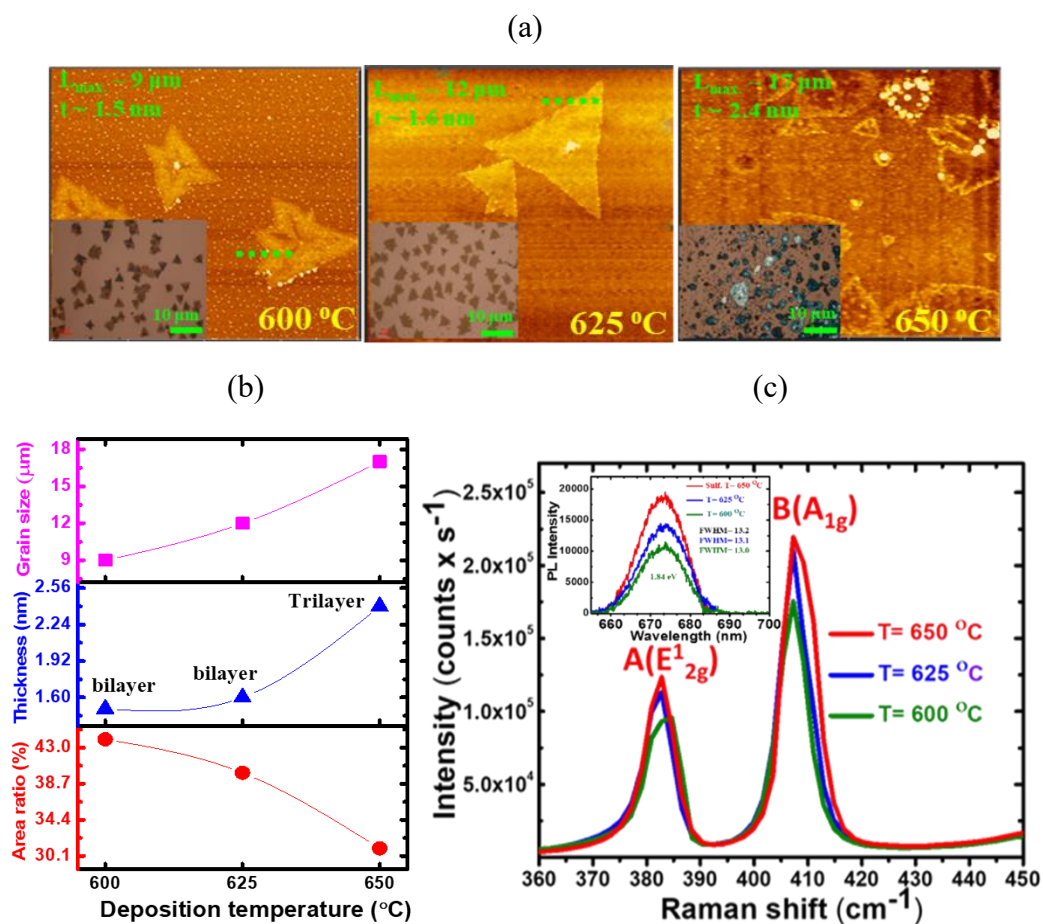
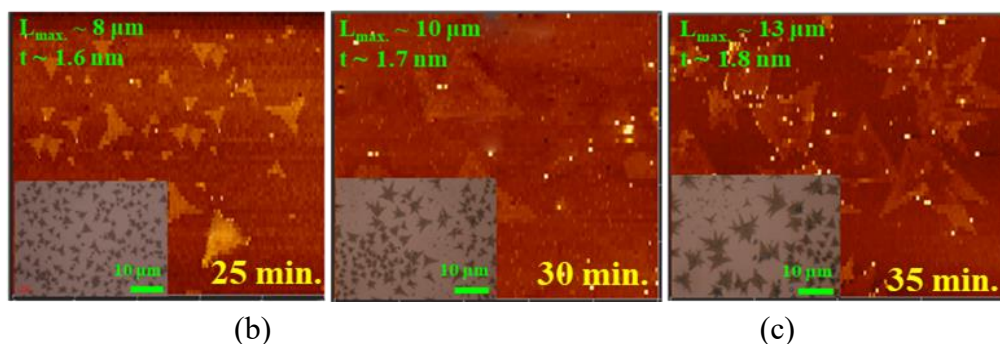


Figure 3.1.8. (a) AFM image of MoS₂ samples exposed to sulfur vapor using H₂/Ar (5/95 sccm) gases at different sulfidation temperatures $T_s = 600\text{--}650\text{ }^\circ\text{C}$ for 20 min. synthesized for a $t_1 = 50\text{ s}$, $t_2 = 150\text{ s}$, $N = 7$ cycles, $T_f = 500\text{ }^\circ\text{C}$. (b) The area ratio of

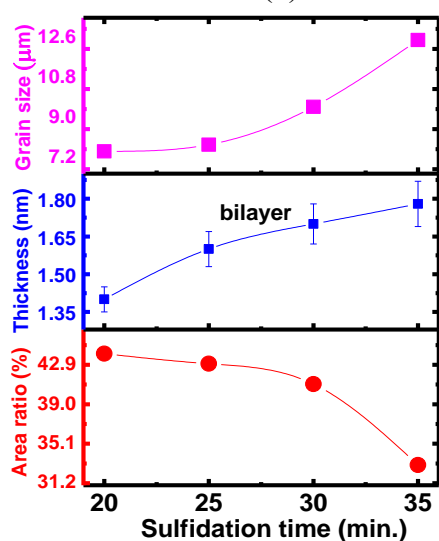
MoS₂ flake to the observation area of 270 × 180 μm², layer thickness, and grain size determined from the optical microscope and AFM observations, (c) Raman and PL spectra of the corresponding samples. Higher sulfidation temperature increases the aggregation of the MoS₂ flakes together with the sublimation of S and Mo.

Figure 3.1.9a shows the AFM and optical microscope images of MoS₂ flake exposed to sulfur vapor using H₂/Ar (5/95 sccm) for different times at a T_f of 600 °C synthesized at a t₁ = 50 s, t₂ = 150 s, N = 7 cycles, T_f = 500 °C. The area ratio of MoS₂ flake, layer thickness, and grain size of corresponding MoS₂ layers calculated from the AFM and optical microscope images are summarized in Figure 3.1.9b. Apparently, the number density of MoS₂ flake decreased with enlarging the grain size of MoS₂ flake. However, Raman and PL measurements revealed no significant changes except the slight increase in the A_{1g} Raman intensity and PL intensity (Figure 3.1.9c). These findings suggest that the chemical reactivity of the corner of the triangle shape MoS₂ flake is higher, which contributes to the promotion of lateral grain growth.

(a)



(b)



(c)

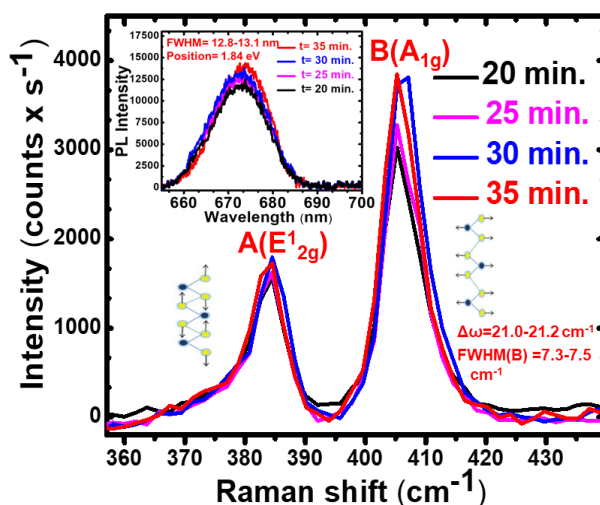


Figure 3.1.9. (a) AFM images of MoS₂ flakes exposed to sulfur vapor using H₂/Ar (5/95 sccm) mixture for different times at T_f = 600 °C synthesized at for a t₁ = 50 s, t₂ =

150 s, $N=7$ cycles, $T_f = 500$ °C, (b) Variations of the area ratio, layer thickness, and grain size of MoS₂ flakes with sulfurization time; (c) Raman and PL spectra of the corresponding samples.

Figure 3.1.10 shows the XPS survey spectra in addition to the high-resolution spectra of Mo 3d, and S 2p of MoS_x films synthesized at a $t_1 = 50$ s, $t_2 = 150$ s, $N=7$ cycles, $T_f = 500$ °C before and after sulfurization at a 600 °C for 1200 s. The atomic ratio of Mo: S is found of 1.4 for as-deposited MoS_x films, which is far from the stoichiometry of (1:2) MoS₂. However, the sulfur vapor exposure on as-deposited MoS_x films is required to obtain the stoichiometry MoS₂. So far, the stoichiometry MoS₂ with an atomic ratio of 1:2.06 is obtained after sulfurization at 600 °C for 1200 s (Table 3.1.2). The lower energy shift of ~0.2 eV of Mo 3d doublet and higher energy shift of ~0.5 eV of S 2P doublet indicate the promotion of sulfurization, this result is consistent with the Raman observation.

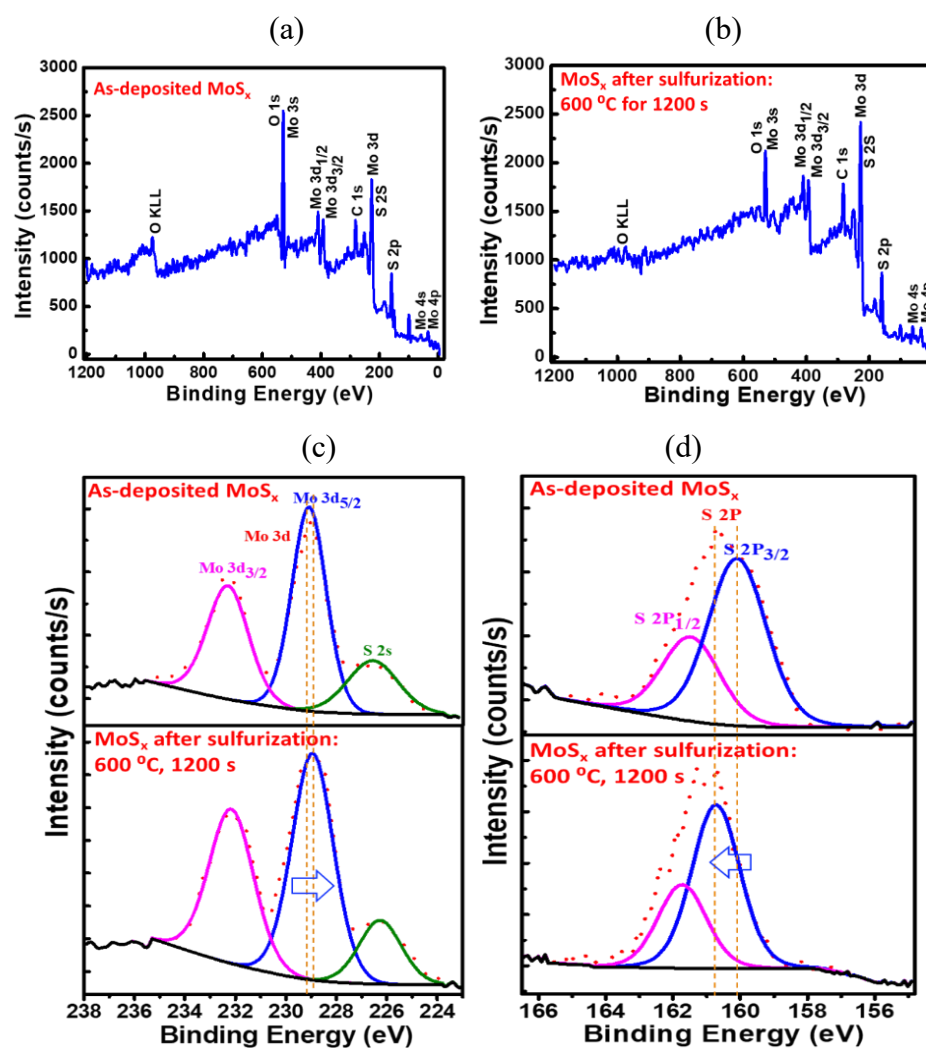


Figure 3.1.10. XPS survey spectra (a) as-deposited, (b) sulfurized MoS_x films at a T_f= 600 °C for 1200 s and high-resolution spectra of (c) Mo 3d and (d) S 2p doublet of corresponding samples synthesized at a t₁ = 50 s, t₂ = 150 s, N= 7 cycles, T_f= 500 °C.

Table 3.1.2. Summary of XPS Analysis: atomic ratio S/M and position of Mo and S.

Name	line	B.E (eV)	Mo:S
As-deposited MoS _x	Mo 3d5/2	229.1	1:1.42
	Mo 3d3/2	232.3	
	S 2p3/2	160.1	
	S 2p1/2	161.4	
Sulfurized MoS _x	Mo 3d5/2	229.3	1:2.06 (stoichiometry)
	Mo 3d3/2	232.5	
	S 2p3/2	160.7	
	S 2p1/2	161.8	

3.1.3 Synthesis of MoS₂ by intermittent and continuous mode

Figure 3.1.11a shows the AFM and optical images of MoS₂ layers fabricated by the intermittent and continuous precursor supply modes under the optimized condition at a precursor concentration of 0.05 M/L and a t₁ = 50 s, t₂ = 150 s, N= 7 cycles, T_f= 500 °C. In sequential and continuous cases, the total deposition time of 350 s for continuous or 50 s × 7 cycles (350 s) for sequential mode and followed by sulfur vapor exposure temperature of 600 °C and time of 1200 s were kept equal. MoS₂ flakes with 4- 5 stacking layers were dominant with an average flake size of 70 μm for the continuous mode, whereas atomic mono/bilayer was preferentially formed with an average flake size of 15- 25 μm for sequential mode. Raman and PL measurements also revealed that the frequency difference of Δω value of 23.4 and 21.2 nm corresponding to 4- 5 layers and bilayer MoS₂ with a uniform distribution for continuous and sequential mode respectively (Figure 3.1.11b). The higher intense PL peak also revealed crystalline MoS₂ formation with emission energy of 1.84 eV for sequential mode (Figure 3.1.11c). These results suggest the storage time of mist in the closed chamber during t₂ in the sequential mode promotes the etching of 1- 2 monolayers and smoothing of the roughened MoS₂ flakes.

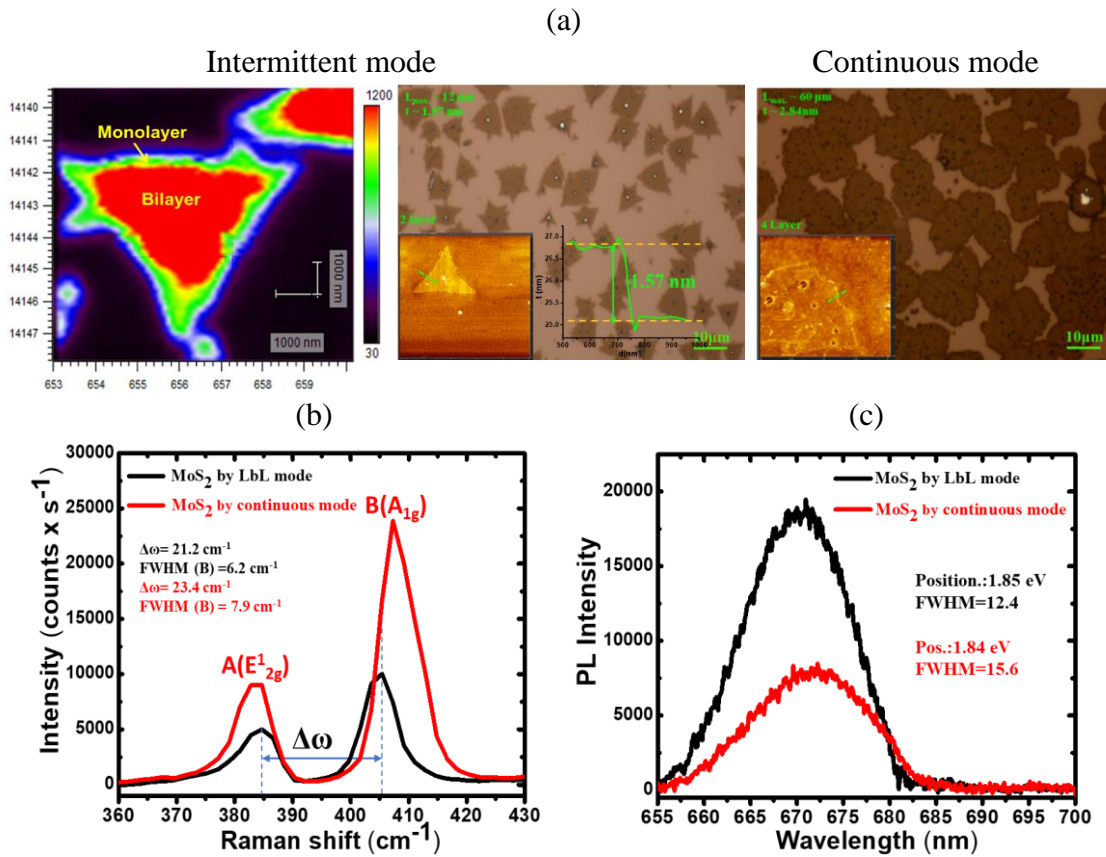


Figure 3.1.11. (a) AFM and optical microscope images of MoS₂ layers synthesized by the intermittent and continuous mist supply modes under the optimized condition at a precursor concentration of 0.05 M/L and a T_f of 500 °C followed by the sulfurization at 600 °C for 1200 s.

Figure 3.1.12a presents the optical microscope and AMF images of the MoS₂ atomic layer for different precursor solutions of 0.05 and 0.01 M/L using continuous supply mode on *th*-SiO₂/p⁺-Si substrate. The number of stacks of an atomic layer is larger with the wide distribution of flake size for the MoS₂ layer for 0.05 M/L solution. The analysis of the AFM image reveals that the layer thickness corresponds to 3 to 4 monolayers. However, significant changes were observed by decreasing the concentration of precursor solution to 0.01 M/L. Atomic MoS₂ monolayer with a layer thickness of 0.87 nm and an average flake size of 65 μm was observed with a relatively uniform distribution. The PL mapping of a synthesized flake at a concentration of 0.01 M/L revealed a uniform distributed compositional MoS₂. The Raman frequency difference of $\Delta\omega = 20.2 \text{ cm}^{-1}$ also revealed the formation of trigonal phase monolayer MoS₂ (Figure 3.1.12b). Layer thickness, maximum flake size, $\Delta\omega$ value, and the E_{12g}/A_{1g} intensity ratio of A/B and PL emission energy are summarized in Table 3.1.3. These values are

almost the same as those of the MoS₂ atomic monolayer reported elsewhere⁴.

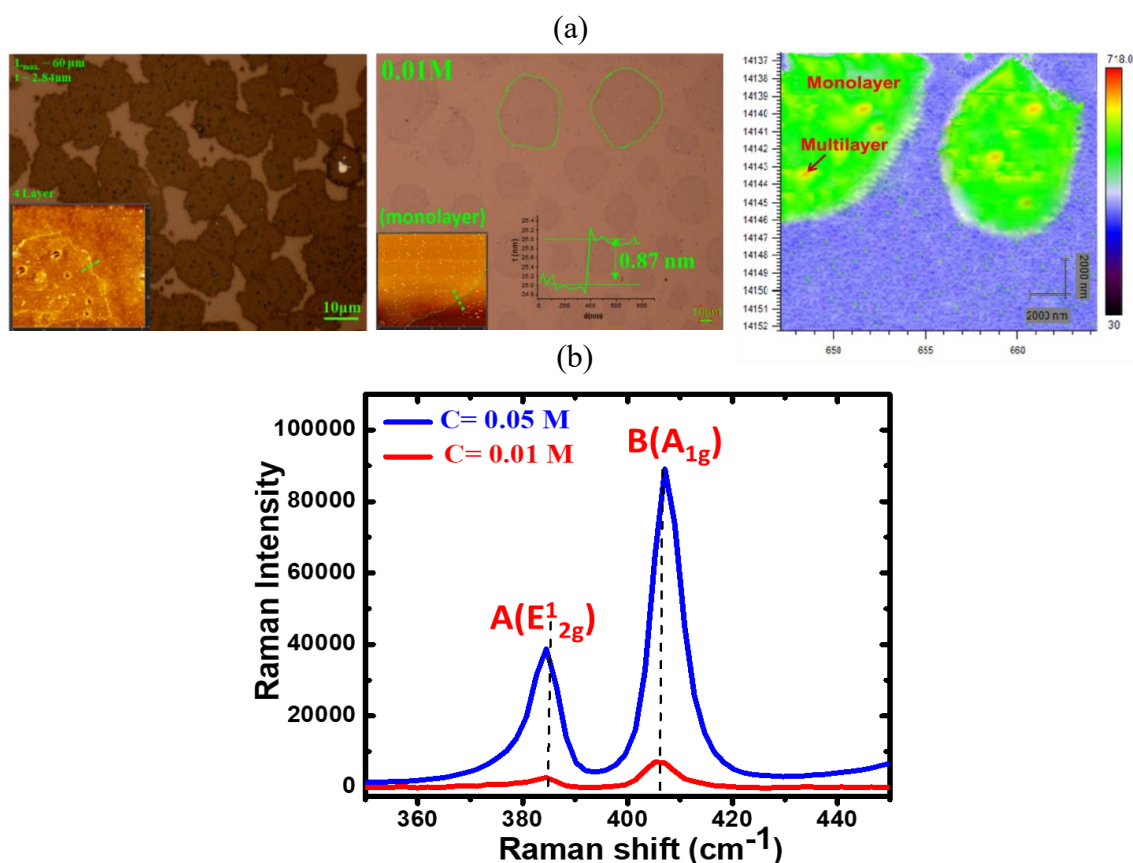


Figure 3.1.12. (a) AFM and optical microscope images of MoS₂ flake fabricated from 0.05 and 0.01 M/L precursor solutions on *th*-SiO₂/p⁺-Si substrate followed by exposure to sulfur vapor using H₂/Ar (5/95 sccm) at a T_f of 600 °C for 1200 s and PL mapping for a sample of 0.01 M/L and (b) Raman spectra of corresponding samples.

Table 3.1.3. Summary of layer thickness, maximum flake size, frequency difference $\Delta\omega$ value, intensity ratio A/B, A/B, and PL emission energy.

Parameters/ Sol. concen.	AFM	Optical microscope	Raman		PL
	t _{av.} (nm)	L _{max.} (μm)	$\Delta\omega$	P _A /P _B	Emi.E. (eV)
0.05 M/L	2.8	65	22.8	2.2	1.84
0.01 M/L	0.9	75	20.2	2.1	1.90

3.1.4 Synthesis of atomic mono/bilayer MoS₂ on mist CVD Al_{0.74}Ti_{0.26}O_y

Figure 3.1.13a shows the optical microscope and AFM images of atomic MoS₂ monolayers fabricated under sequential mist supply and continuous modes on *th*-SiO₂

and $\text{Al}_{0.74}\text{Ti}_{0.26}\text{O}_y$ (ATO) with and without atmospheric-pressure plasma exposure pretreatment. MoS_2 monolayer flakes fabricated by the sequential mist supply mode with atmospheric plasma exposure pretreatment exhibit better crystallinity and increased flake size. The flake size of the atomic MoS_2 monolayer increases to 110 - 120 μm with an increased area coverage ratio of $\sim 49\%$. The enlargement of MoS_2 mono/bilayer flakes originates from the enhanced wettability of the mist precursor; the surface energy of the mist CVD grown ATO layer is higher than that of *th*- SiO_2 . Raman spectra of corresponding samples revealed the formation of crystalline trigonal phase MoS_2 formation (Figure 3.1.13b). A comparative study of flake size with the corresponding covered area ratio is shown in Figure 3.1.13c. Thus, the sequential mist supply mode offers enlarged atomic mono/bilayer MoS_2 deposition with better uniformity than the continuous mode. This is also confirmed by the AFM thickness profile of MoS_2 flakes.

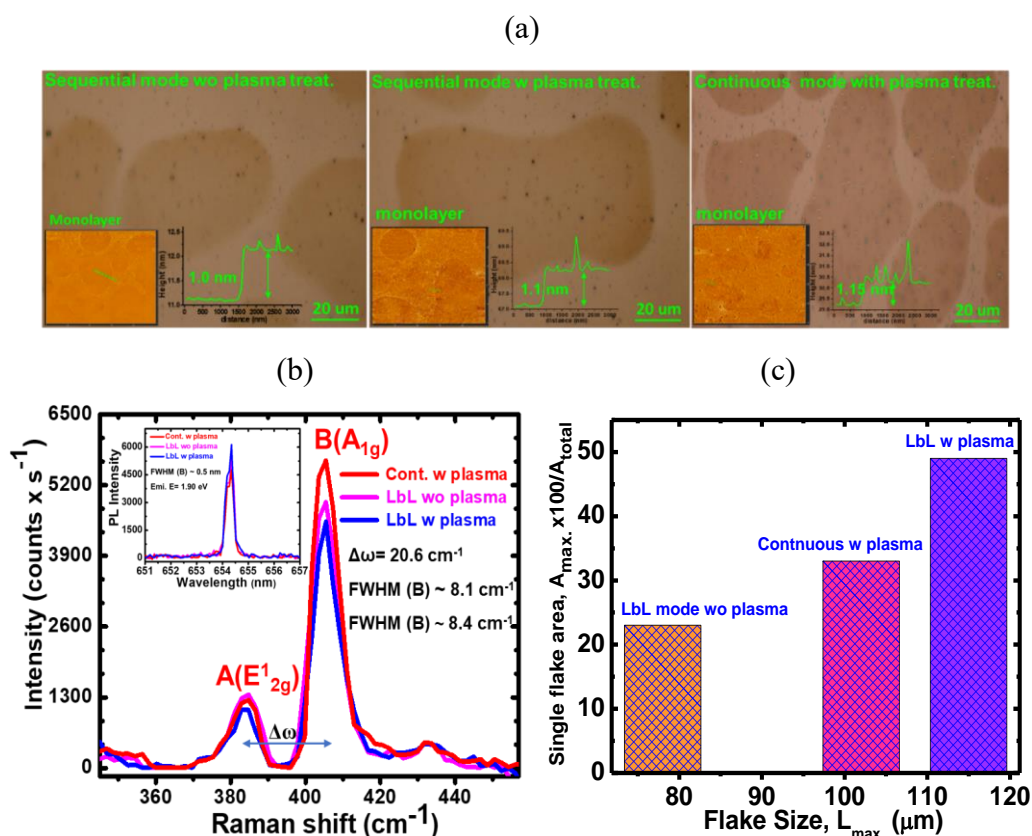


Figure 3.1.13. AFM and optical microscope images of MoS_2 flakes fabricated from 0.01 M/L precursor solutions on (a) ATO substrate without plasma treatment, plasma-treated (30 s) ATO using sequential mist supply mode, and plasma-treated (30 s) ATO using continuous mode followed by exposure to sulfur vapor using H_2/Ar (5/95 sccm)

mixture at a T_f of 600 °C for 1200 s; (b) Raman and PL spectra of the corresponding samples; (c) Plot of an area of a single MoS₂ flake vs. corresponding flake size.

Figure 3.1.14 show the contact angle measurement of (NH₄)₂MoS₄ precursor dissolved in n-Methyl-2-pyrrolidone (NMP) solution dropped on ~45 nm mist-CVD ATO coated p⁺-Si substrate, AFM images of corresponding substrates and PL mapping of atomic mono/bilayer MoS₂ flakes. The contact angle θ_c of ~29 ° without plasma treatment and ~21 ° after plasma treatment of ATO substrate with RMS values of 0.5 and 0.61 nm respectively were observed. No significant change in RMS value before and after 30 s He/O₂ plasma exposure was observed. These results revealed the surface energy of ATO improved with He/O₂ treatment, which promotes the higher wettability of precursors mist. Thus, the MoS₂ monolayer flake with an average size of ~120 μm was obtained on a high-κ dielectric ATO substrate.

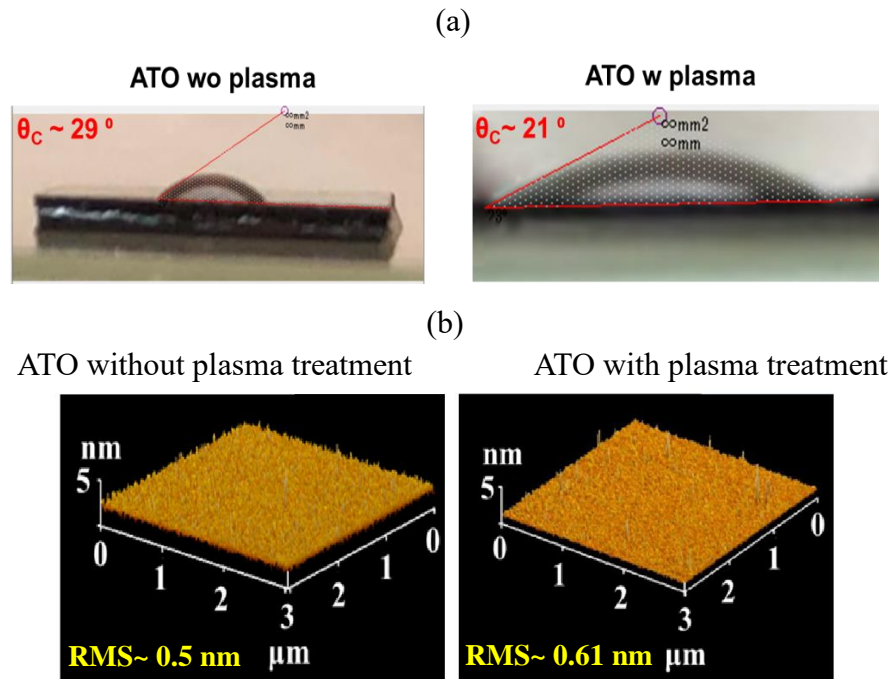


Figure 3.1.14. Contact angle (wettability) of (NH₄)₂MoS₄ precursor solution (2μL) dropped on (a) ATO substrate before and after plasma treatment, and (b) AFM image of corresponding substrates.

3.1.5 Fabrication of atomic mono/bilayer MoS₂ channel MOSFETs

Figure 3.1.15 shows the transfer characteristics of bottom-gate MIS-FETs fabricated by depositing atomic MoS₂ monolayer (channel layer) on *th*-SiO₂ (90 nm)/p⁺-Si and

mist CVD grown ATO (~ 45 nm)/p⁺-Si substrates⁵. The field-effect mobility μ_{FET} is calculated by the equation:

$$\mu_{FET} = \left(\frac{L}{WC_g V_{sd}} \right) \left(\frac{dI_{ds}}{dV_g} \right)$$

where $\frac{dI_{ds}}{dV_g}$ is the slope, L and W are the channel length and width, respectively, and C_g is the capacitance per unit area between the channel and the back gate. The $\sqrt{I_{ds}}-V_{gs}$ plots for *th*-SiO₂ and ATO gate insulators are also shown in Figure 3.1.15. Au gold S – D electrode was formed on top of MoS₂ flakes using standard wet-lithography, and sputtering, followed by a standard lift-off process. The FET parameters determined from the $\sqrt{I_{ds}}-V_{gs}$ plot are summarized in Table 3.1.4. The V_{th} value is negative with a relatively larger SS value and smaller on/off current ratio for FETs on *th*-SiO₂ despite their smaller RMS value (< 0.01 nm) than that of mist CVD grown ATO layer (~ 0.5 nm). These results suggest that surface defects are generated on *th*-SiO₂ during the growth of the MoS₂ layer and/or subsequent sulfurization. On the other hand, marked improvements in the FET performance are observed in the case of ATO, suggesting that surface defects formed on ATO were lower than those on *th*-SiO₂. The output characteristics of FETs ATO substrate is also showing improved output performance depicted on the right. The FET parameters of ATO are comparable to those reported previously for CVD and ALD grown MoS₂ atomic mono/bilayers. A comparative study of the device performance in the present study with those reported in the literature is presented in Table 3.1.5. These findings imply that mist- CVD has a great potential for the fabrication of 2D MoS₂ atomic mono/bilayer crystal-based MOS-FETs without mechanical exfoliation.

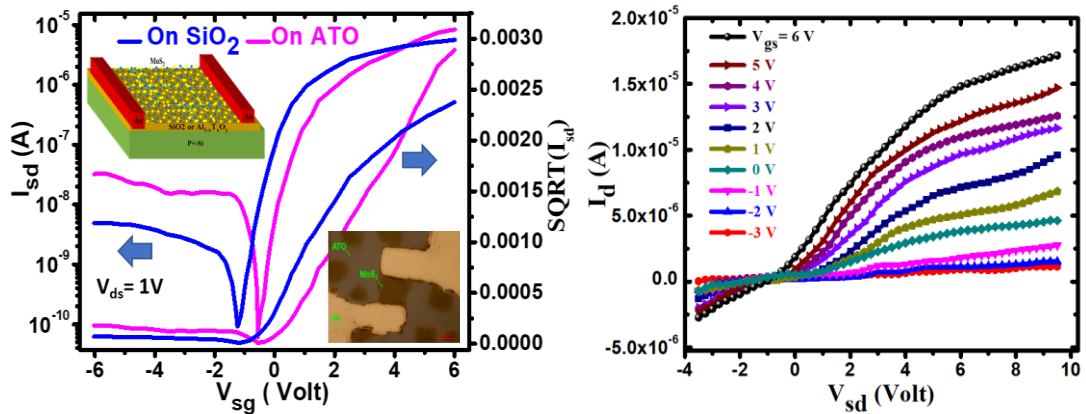


Figure 3.1.15. Transfer and output characteristics and $\sqrt{I_{SD}}-V_{gs}$ curves of atomic MoS₂ mono/bilayer-based FET devices on mist- CVD grown ATO dielectric layers (L/W= 16/12 μm) including transfer characteristics on *th*-SiO₂/p⁺-Si substrate.

Table 3.1.4. FET parameters are determined from the transfer characteristics.

Dielectric layers	V _{th} (V)	SS(V/dec.)	I _{ON} /I _{OFF}	μ (cm ² V ⁻¹ s ⁻¹)
On <i>th</i> -SiO ₂	-1.6	~ 0.80	~3.0×10 ⁴	31- 40
On ATO	-0.5	~ 0.11	~3.5×10 ⁵	43-55

Table 3.1.5. FET parameters for different deposition techniques of atomic layer mono/bilayer MoS₂.

Name	Dielectric layers	V _{th} (V)	SS (V/dec.)	I _{ON} /I _{OFF}	μ (cm ² V ⁻¹ s ⁻¹)	Ref.
Mist-CVD	On <i>th</i> -SiO ₂	-1.6	~ 0.80	~ 3.0×10 ⁴	31-40	This work
	On Al _{1-x} Ti _x O _y	-0.5	~ 0.110	~ 3.5×10 ⁵	43-55	
CVD	SiO ₂	7.4	0.66	1.0×10 ⁶	28	6
		1.0	~1.3	1.0×10 ⁴	38-75	7
	Al ₂ O ₃	2.0	0.22	1.0×10 ⁴	~ 5.0	8
	Al ₂ O ₃ /SiO ₂	-10	0.23	2.0×10 ⁶	22-49	9

The investigation of the synthesis of MoS₂ atomic mono/bilayers using the sequential mist supply mode by mist CVD reveals the following outcomes¹⁰:

1. The number of stacking layers of MoS₂ flakes under the sequential mist supply mode was varied from atomic monolayer to 4–5 layers by varying t_2 , repetition cycles of precursor mist supply N , and solution precursors concentration.
2. The average size of atomic MoS₂ monolayer flakes deposited using sequential mist supply mode on atmospheric-pressure He plasma exposed *th*-SiO₂ and ATO dielectric layers increased to ~70 and >100 μm , respectively with relatively uniform size distribution.
3. Atomic MoS₂ monolayer-based FETs exhibited a mobility of 31- 40 (43- 55) cm²/Vs with a V_{th} of -1.6 (-0.5 V), an on/off ratio of 3.2×10^4 (3.6×10^5), and SS of 0.80 (0.11) V/dec. for *th*-SiO₂ (ATO) gate insulator layers without mechanical exfoliation.
4. These findings imply that mist CVD has a great potential for the fabrication of 2D MoS₂ atomic mono/bilayer crystal-based MOSFETs.

3.2 Direct Synthesis of Submillimeter-Size Few-layers WS₂ and WS_{0.3}Se_{1.7} by Mist Chemical Vapor Deposition and Its Application to Complementary MOS Inverter

In this part, the synthesis of millimeter-size few-layer tungsten disulfide (WS₂) and tungsten sulphoselenide (WS_{2-x}Se_x) by intermittent mist- CVD from (NH₄)₂WS₄ precursor dissolved in N-methyl-2-pyrrolidone (NMP) in the same analogy as the previous MoS₂ study from (NH₄)₂MoS₄ has been investigated. The synthesized few-layer WS₂ and WS_{0.3}Se_{1.7} were applied in FETs fabrication to obtain n- and p-channel behaviors using gold and platinum source/drain electrodes, respectively. Furthermore, a prototype of CMOS circuits using n-WS₂ and p-WS_{0.3}Se_{1.7} FETs was designed and employed in a perspective of the cascaded logic application.

3.2.1 Synthesis of few-layer WS_{2-x}Se_x flake under intermittent mist CVD mode

Figure 3.2.1a shows the mist-CVD system used in this study, which has been described in detail elsewhere¹⁰. Tungsten disulfide (WS₂) and tungsten sulphoselenide (WS_{2-x}Se_x) was synthesized by intermittent mist- CVD from (NH₄)₂WS₄ precursor dissolved in N-methyl-2-pyrrolidone (NMP) in the same analogy as the previous MoS₂ study. The p⁺-Si substrates with and without 285-nm-thick *th*-SiO₂ were precleaned with acetone, isopropyl alcohol (IPA) and distilled (DI) water every 10 minutes and subsequently, exposed He/O₂ plasma for 30 s to remove residual organics absorbed on the substrate surface. An aqueous solution of (NH₄)₂WS₄ dissolved in NMP (24 hrs. stirred) was used as a precursor, with Ar/H₂ mixture as the mist generation and carrier gas. The flowchart of sequential mist supply is shown in Figure 3.2.1b. After allowing the flow of Ar/H₂ (95/5 sccm) for 10 min in the chamber to eliminate air, the chamber was closed. After that, the mist precursor generated by the ultrasonic atomizer (3 MHz) was transported through the glass tube using an Ar/H₂ carrier gas. Mist supply time per one cycle t_1 , mist storage time t_2 , furnace temperature T_f , precursor concentration, and sulfurization/selenization conditions were investigated as variables. The growth and sulfurization/selenization conditions for the atomic/bilayer WS_{1.2} and WS_{2-x}Se_x are listed in Table 3.2.1. All the samples were sulfurized/selenized after the film deposition using sulfur/selenium vapor and an Ar/H₂ (95/5 sccm) gas mixture at $T_f = 600$ °C for different periods using a three-zones furnace as shown in Figure 3.2.1c. At the initial stage, selenization of the as-deposited WS_x layer is executed to obtain p-type WS_{2-x}Se_x

for the fabrication of p-channel FETs and thereafter sulfurization for n-channel FETs for designing the CMOS logic circuit.

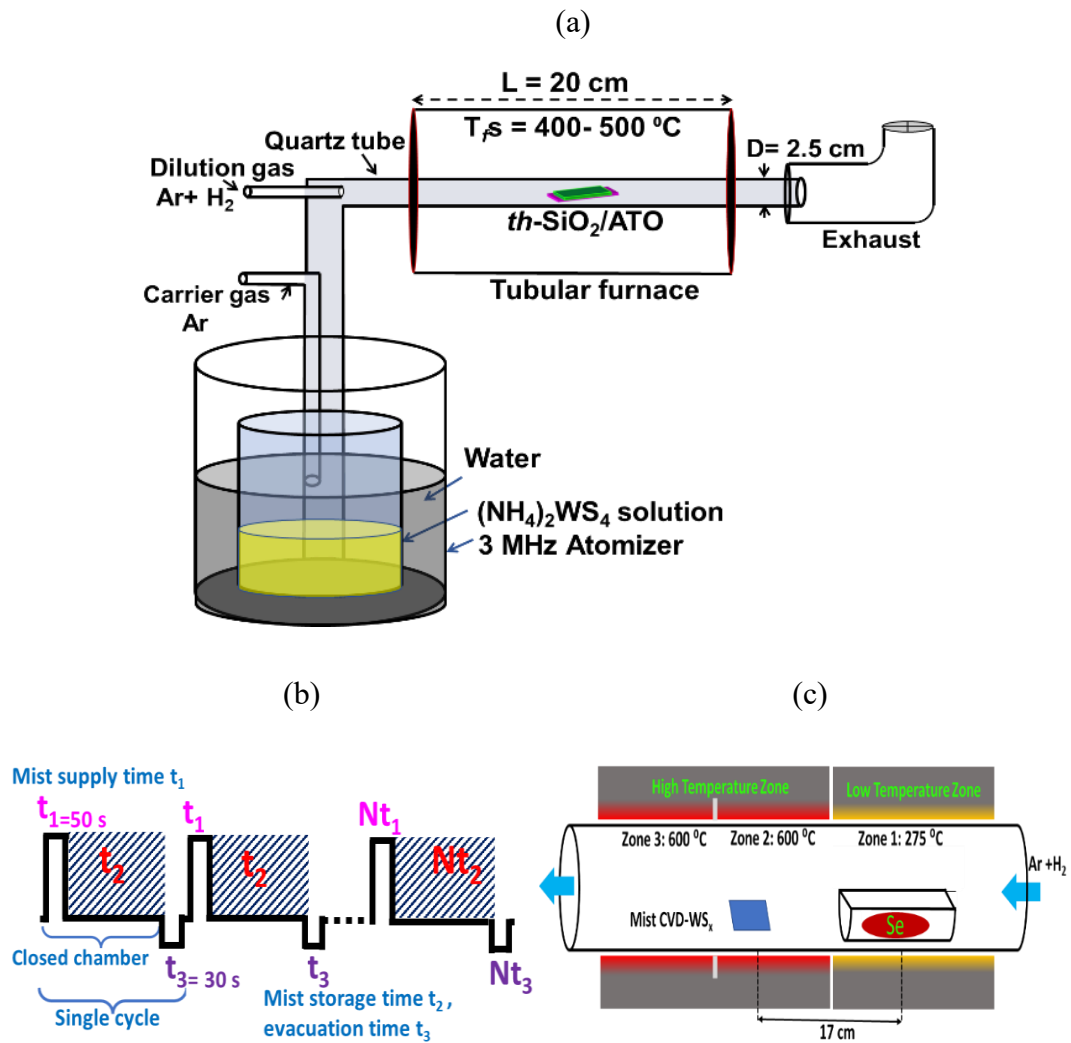


Figure 3.2.1. (a) Schematic diagram of the mist-CVD system, (b) Flow chart of sequential mist precursor supply, (c) Schematic of sulfurization/selenization set-up.

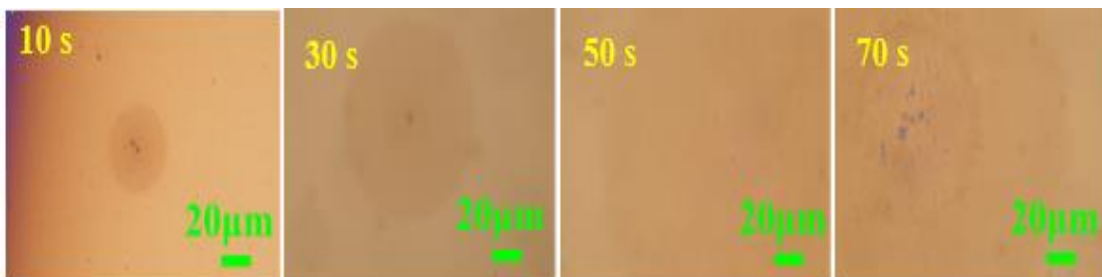
Table 3.2.1. The deposition conditions of WS_2 and $WS_{2-x}Se_x$ films.

WS _x and WS _{2-x} Se _x deposition conditions	
Solute	(NH ₄) ₂ WS ₄ (ATT)
Solvent	C ₅ H ₉ NO (NMP)
Substrate	<i>th</i> -SiO ₂ (285 nm)/p ⁺ -Si, mist-CVD Al _{0.74} Ti _{0.26} O _y
Carrier gas, flow rate, F _d	Ar: 500 sccm + H ₂ : 125 sccm

Solution concentration	0.01, 0.025 M/L
t_1	50 s
t_2	150- 270 s
Tabular furnace temperature, T_f	400- 500 °C
Sulfurization and selenization conditions	600 °C, 1200 ~ 3600 s Ar 95 sccm + H ₂ 5 sccm

Figure 3.2.2a depicts Optical microscope images of WS_{2-x}Se_x flakes synthesized at different mist supply times t_1 = 10- 70 s per one cycle under the t_2 = 210 s, N = 7 cycles at a T_f = 475 °C followed by selenization at 600 °C for 1200 s. The average size of WS_{2-x}Se_x flakes was increased up to ~257 μ m at a t_1 = 70 s with 3-5 stacks of atomic layers. Thus, mono/bilayer uniform flakes with the size of ~250 μ m were obtained at t_1 = 50 s. In addition, an extrapolated plot of flake size variation to deposition times (t_1+t_2) indicates an estimated incubation time $t_{incu.}$ of ~ 15 s of WS_{2-x}Se_x synthesized at a T_f = 475 °C (Figure 3.2.2b).

(a)



(b)

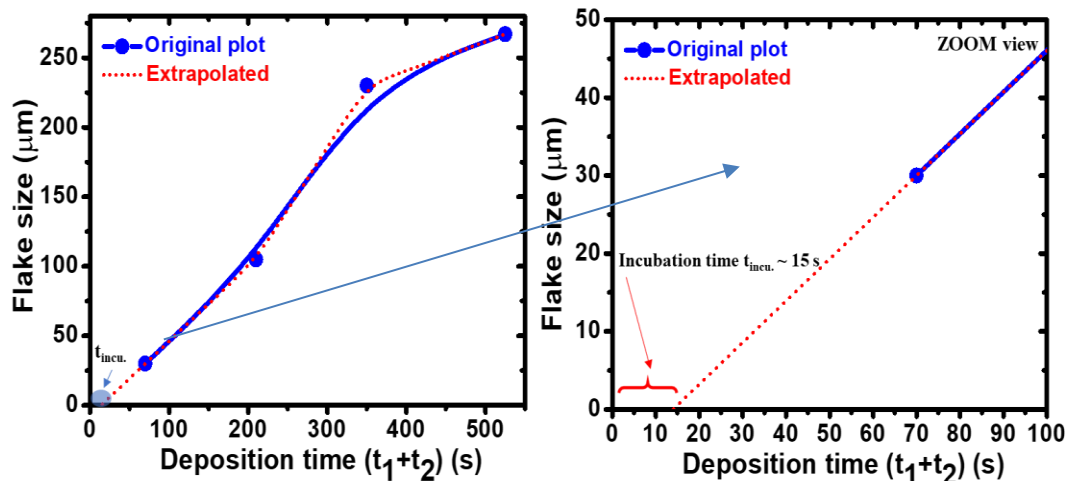


Figure 3.2.2. (a) Optical microscope images of $WS_{2-x}Se_x$ flakes synthesized at different mist supply times $t_1 = 10-70$ s per one cycle under the $t_2 = 210$ s, $N = 7$ cycles at a $T_f = 475$ °C, followed by selenization at 600 °C for 1200 s and (b) An estimated incubation time of $WS_{2-x}Se_x$ determined by the extrapolation from flake size to deposition times (t_1+t_2) plot.

Figure 3.2.3a shows the AFM images of few-layers $WS_{2-x}Se_x$ synthesized at different T_f s at a $t_1 = 50$ s, a $t_2 = 150$ s, and $N = 7$ cycles followed by the selenization at 600 °C for 1200 s on *th*-SiO₂(285 nm)/p⁺-Si substrate. The inset shows the optical microscope images of the corresponding samples and their height profiles. The layer thickness and the average size of the $WS_{2-x}Se_x$ flake analyzed by the AFM (270×180 μm² area) and optical microscope images are also shown. The layer thickness decreased notably from 3.2 to 1.9 ± 0.4 nm corresponding to a bilayer with increasing T_f from 450 to 500 °C. The median of the integrated area ratio of $WS_{2-x}Se_x$ flakes increased from 47 to 60 ± 6%, and the average size of flakes increased from 215 to 260 ± 8 μm, while the films became inhomogeneous at a $T_f = 500$ °C. As a result, bilayer-thick $WS_{2-x}Se_x$ flakes with an RMS of 0.86 nm were obtained at $T_f = 475$ °C.

Figure 3.2.3b also shows the AFM images of $WS_{2-x}Se_x$ flakes synthesized on *th*-SiO₂/p⁺-Si substrate by varying t_2 for a $t_1 = 50$ s, $T_f = 475$ °C, and $N = 7$ cycles. The layer thickness, grain size, and area ratio of $WS_{2-x}Se_x$ flakes are also shown at the bottom for different t_2 . The layer thickness and the integrated area ratio of $WS_{2-x}Se_x$ flakes decreased from 2.0 to 1.05 ± 0.07 nm (correspond from bilayer to monolayer thickness) and 53 to 66 ± 6%, respectively, while the average size of the $WS_{2-x}Se_x$ flakes increased from 230 to 270 ± 7 μm. However, the surface roughness increased for a further increase in t_2 of 270 s, which may be attributed to the enhanced removal of the S-element with an increase in t_2 . Thus, an atomic mono/bilayer $WS_{2-x}Se_x$ flakes with an enlarged size of ~265 μm were obtained at a T_f of 475 °C for t_2 of 210 s.

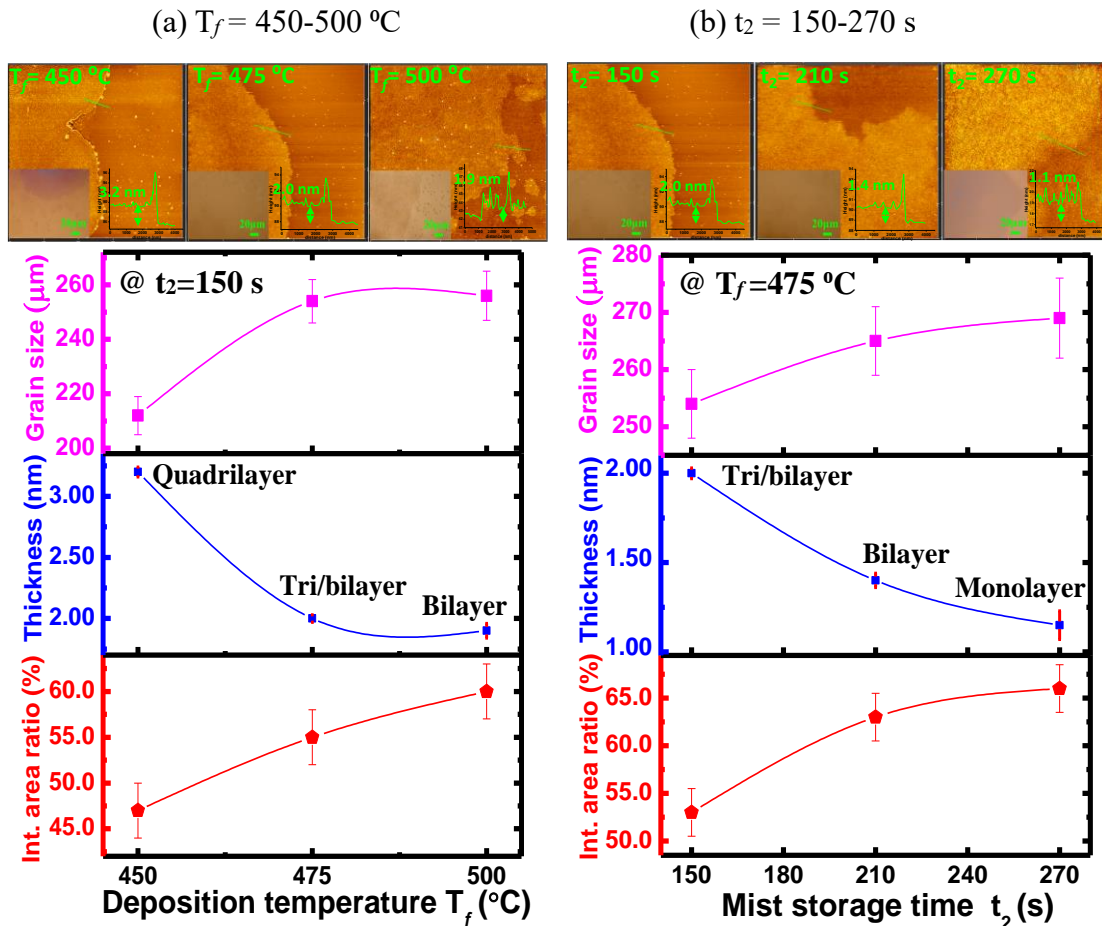


Figure 3.2.3. AFM image, average layer thickness, median of integrated area ratio, and average size of $\text{WS}_{2-x}\text{Se}_x$ flakes synthesized at different (a) T_f for $t_2 = 150\text{ s}$, and (b) t_2 at a $T_f = 475\text{ }^\circ\text{C}$, $t_1 = 50\text{ s}$, and $N = 7$ cycles. The inset shows the optical microscope images and height profiles for corresponding samples.

Figure 3.2.4a shows the Raman and PL spectra of $\text{WS}_{2-x}\text{Se}_x$ flakes synthesized at different T_{fS} at a $t_1 = 50\text{ s}$, a $t_2 = 150\text{ s}$, and $N = 7$ cycles followed by the selenization at $600\text{ }^\circ\text{C}$ for 1200 s . A broad Raman peak is observed at $200\text{--}350\text{ cm}^{-1}$ attributed to the in-plane peak of E_{2g}^1 and out-of-plane peak A_{1g} including multiple 1st and 2nd order LO and TO phonon modes and active peaks of the S-W-Se complex and the 2nd order WS_2 related peak at 298 cm^{-1} . An increase of peak intensity in Raman and PL spectra with increasing the furnace temperature refers to an improvement of film crystallinity while broadening FWHM indicate defect inclusion into the film simultaneously. Thus, the temperature T_f of $475\text{ }^\circ\text{C}$ is chosen for further investigation. On the other hand, a similar result is observed in Raman observation of $\text{WS}_{2-x}\text{Se}_x$ synthesized by varying t_2 for a $t_1 = 50\text{ s}$, $T_f = 475\text{ }^\circ\text{C}$, and $N = 7$ cycles. In Figure 3.2.4b, a broad-band at $200\text{--}350$

cm^{-1} appeared with 2nd order WS_2 related peak at 298 cm^{-1} , whereas PL intensity shows a maximum at a t_2 of 210 s and it decreased for longer t_2 with increasing surface roughness. These results may be caused by the sublimation of Se vapor. Thus, mist storage time t_2 of 210 s is found as an optimized value at a furnace temperature of $475 \text{ }^\circ\text{C}$.

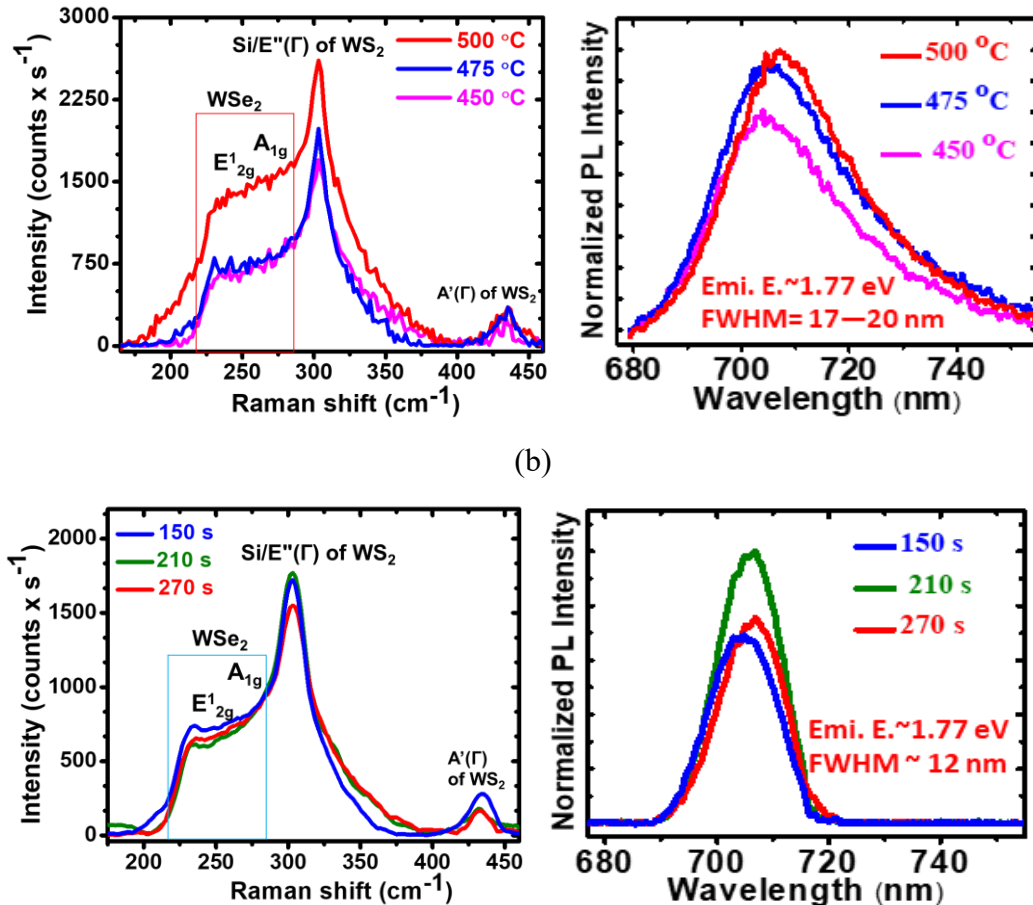


Figure 3.2.4. (a) Raman and PL spectra of $\text{WS}_{2-x}\text{Se}_x$ layers synthesized at different (b) T_f s for $t_2 = 150$ and (b) t_2 for $T_f = 475 \text{ }^\circ\text{C}$, with $t_1 = 50 \text{ s}$, $N = 7$ cycles, precursor concentration of 0.01 M/L and followed by selenization at $600 \text{ }^\circ\text{C}$ for 1200 s .

Figure 3.2.5 shows a histogram of the integrated area ratio for t_2 of 210 and 270 s. The integrated area ratio refers to an area covered by $\text{WS}_{2-x}\text{Se}_x$ flakes to the total area of the optical microscope image. The median value was obtained from the integral of the covered area by $\text{WS}_{2-x}\text{Se}_x$ flakes in optical microscopic images (10–12 images) of each sample in the total area of $270 \times 180 \text{ } \mu\text{m}^2$, considering the possibility of the variation of $\text{WS}_{2-x}\text{Se}_x$ flakes density on the entire substrate surface. Thus, the median of an integrated area ratio for mist storage time $t_2 = 210$ and 270 s was found of 62 and 62% respectively.

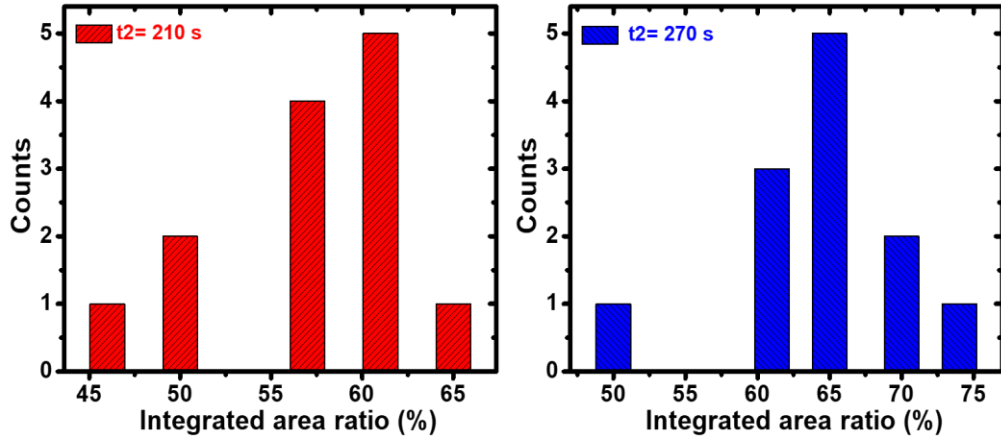


Figure 3.2.5. Histogram of integrated area ratio for mist storage time, $t_2 = 210$ and 270 s of $WS_{2-x}Se_x$ flakes synthesized at different t_2 for $t_1 = 50$ s, $N = 7$ cycles, $T_f = 475$ °C, and precursor concentration of 0.01 M/L, selenization at 600 °C for 1200 s.

Figure 3.2.6a shows the AFM images of $WS_{2-x}Se_x$ flakes synthesized by varying N for a $t_1 = 50$ s, $t_2 = 210$ s, $T_f = 475$ °C, and a precursor solution concentration of 0.01 M/L. The inset shows the optical microscope images and height profiles of the corresponding samples. The variations in the area ratio of the $WS_{2-x}Se_x$ flake, layer thickness, and the grain size of the $WS_{2-x}Se_x$ layers calculated from the AFM and optical microscope images are shown in Figure 3.2.6b. Both the grain size and the layer thickness of $WS_{2-x}Se_x$ flakes increased from 62 to 264 ± 11 μm and 1.7 to 3.60 ± 0.06 nm, respectively with an increase in N , while the integrated area ratio of the $WS_{2-x}Se_x$ flakes decreases from 27 to $65 \pm 7\%$. The Raman and PL spectra of the corresponding $WS_{2-x}Se_x$ layers are shown in Figure 3.2.6c. The WSe_2 - and $WS_{2-x}Se_x$ - related Raman bands at 240 - 290 cm^{-1} were prominent at $N = 7$ cycles, while the PL spectra shifted to a lower wavelength with an FWHM of ~ 22 nm. These results suggest that the sequential mist supply and exhaust of mist precursor may contribute to an increase in the number of stacks of the atomic layer as well as the sublimation of weakly adhered particles. Herein, the repetition cycles of the mist precursor controlled the deposition of mono/bilayer to multilayer (3–5 layer) WS_2 and $WS_{2-x}Se_x$ films. Mono/bilayer flakes were observed for 7 repetition cycles and a further increase in the repetitions resulted in vertical growth rather than lateral one and the surface being inhomogeneous. Thus, atomic mono/bilayer $WS_{2-x}Se_x$ flakes with an average size of ~ 250 μm were obtained at an $N = 7$ cycles with $t_2 = 210$ s at $T = 475$ °C. However, the broad WSe_2 - related Raman peak requires a further selenization of as-deposited $WS_{2-x}Se_x$.

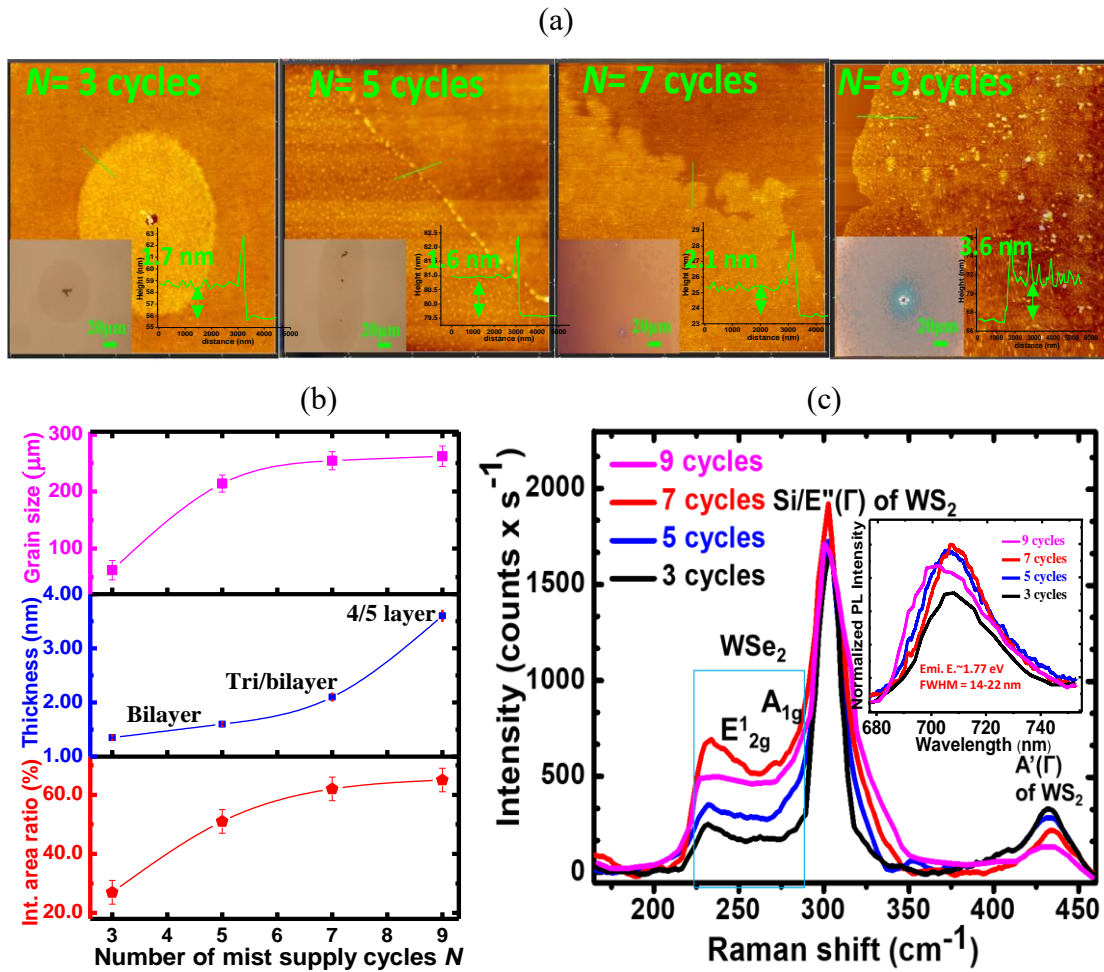


Figure 3.2.6. (a) AFM images of $\text{WS}_{2-x}\text{Se}_x$ flakes fabricated at different N for $t_1 = 50$ s, $t_2 = 210$ s, and $T_f = 475$ °C (the inset shows optical microscope images of the corresponding samples); (b) the variations of the layer thickness, median of integrated area ratio, and an average size of the $\text{WS}_{2-x}\text{Se}_x$ flakes with N ; (c) Raman and PL spectra of the corresponding $\text{WS}_{2-x}\text{Se}_x$ samples.

3.2.2 Effect of selenization and sulfurization of WS_x films

Figure 3.2.7a shows the AFM images of $\text{WS}_{2-x}\text{Se}_x$ flakes synthesized on $th\text{-SiO}_2/\text{p}^+\text{-Si}$ substrate exposed to selenium vapor using an H_2/Ar (5/95 sccm) mixture gas for further longer exposed times at a $T_f = 600$ °C. The area ratio of $\text{WS}_{2-x}\text{Se}_x$ flakes, layer thickness, and average grain size of flake for the corresponding samples are shown in Figure 3.2.7b. The area ratio and grain size of $\text{WS}_{2-x}\text{Se}_x$ flakes increased, whereas the thickness of the flakes decreased with an increase in Se-vapor exposure time under a steady flow of H_2/Ar mixture gas. These results suggest that the chemical reactivity of the outer edge of the $\text{WS}_{2-x}\text{Se}_x$ flakes is higher, which promotes lateral grain growth. However, a

significant improvement in the crystallinity in $WS_{2-x}Se_x$ flakes was observed with an increasing incorporation ratio of Se element when the selenization period was increased from 1200 to 2400 s. The prominent feature is that Raman active bands corresponding to E'_{2g} and A_{1g} at approximately 250 cm^{-1} for WSe_2 are observed with the WS_2 related second-order weak peak at 298 cm^{-1} as depicted in Figure 3.2.7c. The PL also revealed the peak energy shift from 1.77 to 1.64 eV with an increase in the exposure time of Se vapor from 1200 to 2400 s, suggesting the promotion of selenization. However, for further longer exposure of 3600 s, the surface roughness increased.

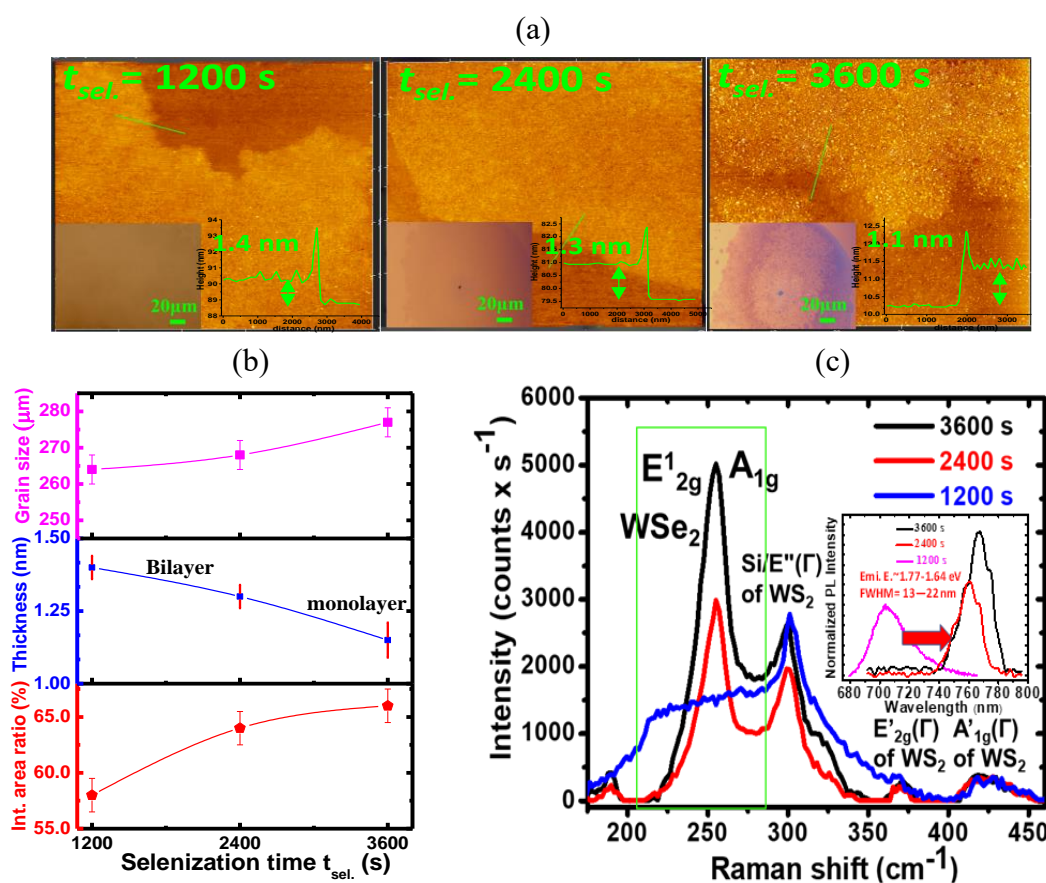


Figure 3.2.7. (a) AFM images of $WS_{0.3}Se_{1.7}$ flakes exposed to selenium (Se) vapor for different times at a $T_f = 600\text{ }^\circ\text{C}$ under the steady flow of H_2/Ar (5/95 sccm) mixture gas with 0.01 M/L $(NH_4)_2WS_4$; (b) The variations of an integrated area ratio, layer thickness, and grain size of $WS_{2-x}Se_x$ flakes for different exposure time; (c) Raman and PL spectra of the corresponding samples.

Figure 3.2.8 shows a high-resolution core-spectra of W 4f and Se 3d doublets of $WS_{2-x}Se_x$ samples with selenium vapor exposure for 1200 and 2400 s at $600\text{ }^\circ\text{C}$. WS_x samples synthesized under optimized condition; a $T_f = 475\text{ }^\circ\text{C}$, for $t_1 = 50\text{ s}$, $t_2 = 210\text{ s}$ and $N = 7$ cycles. The XPS revealed that an atomic concentration ratio of W: Se was 1:1.13 in

1200 s selenized sample and it is increased to 1:1.7 (near the stoichiometric composition) for further increased Se-vaporization period from 1200 to 2400 s as shown in Table 3.2.2. In addition, a lower energy shift of W 4*f* doublet and a ~0.5 eV of Se 3*d* doublet also revealed the promotion of selenization. Thus, atomic mono/bilayer WS_{0.3}Se_{1.7} with an average flake size of ~280 μm with near stoichiometric composition was obtained on *th*-SiO₂ (285 nm)/p⁺-Si substrate by adjusting the deposition condition of the intermittent mist supply.

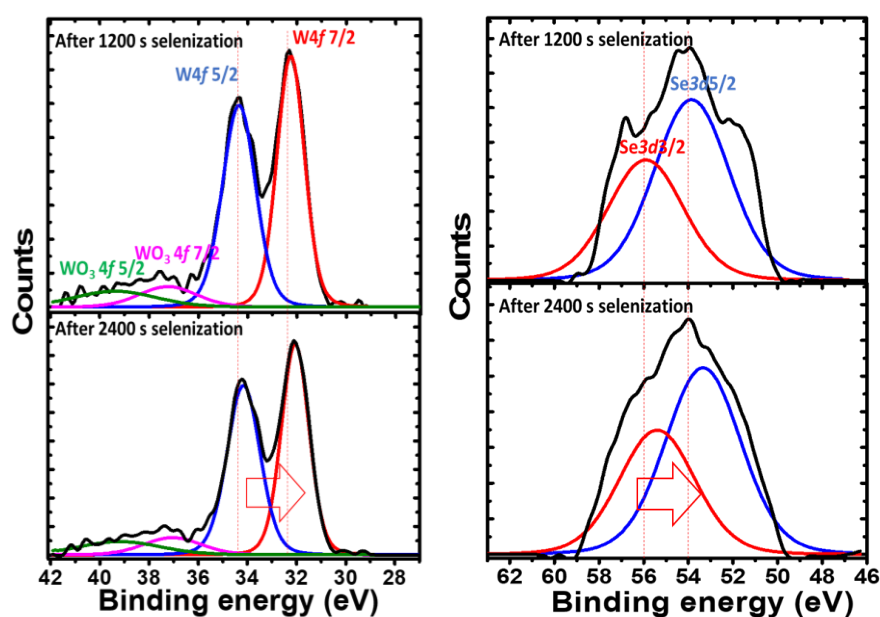


Figure 3.2.8. XPS observation: a high-resolution core-spectra of W 4*f* and Se 3*d* doublets of WS_{2-x}Se_x samples with selenium vapor exposure for 1200 s and 2400 s at 600 °C; WS_x synthesized at a T_f= 475 °C, for t₁ = 50 s, t₂ = 210 s and N = 7 cycles.

Table 3.2.2. Summary of XPS observation of WS_{2-x}Se_x for Se-exposure time t= 1200 and 2400 s.

Selenization time	line	B.E (eV)	A (%)	ratio (W: Se)
1200 s	W 4f7/2	32.30	47.05	1:1.13
	W 4f5/2	34.42		
	Se 3d5/2	53.81	52.95	
	Se 3d3/2	55.90		
2400 s	W 4f7/2	32.08	37.24	1:1.7
	W 4f5/2	34.18		
	Se 3d5/2	53.30	62.76	
	Se 3d3/2	55.35		

3.2.3 Growth of submillimeter-size few-layer $WS_{0.3}Se_{1.7}$ flakes by mist CVD on $\alpha-Al_{0.74}Ti_{0.26}O_y$

Figure 3.2.9 shows optical microscope and AFM images of $WS_{0.3}Se_{1.7}$ flakes for precursor concentration of 0.01 and 0.035 on $Al_{0.76}Ti_{0.24}O_y/p^+$ -Si substrate under the optimized condition which we obtained on th - SiO_2/p^+ -Si substrate; $t_1 = 50$ s, $t_2 = 210$ s, $T_f = 475$ °C with selenization at 600 °C for 2400 s. The $WS_{0.3}Se_{1.7}$ flakes with an average size of ~ 450 μm , a thickness of 1.1 nm (mono/bilayers), and RMS of 1.2 nm were obtained for a precursor concentration of 0.01 M/L, while ~ 1460 μm , with a thickness of 3.4 nm (4-5 monolayers) and high RMS of 3.83 nm at a concentration of 0.035 M/L. Thus, an adjusted precursor concentration of 0.025 was used to obtain large-size, uniform few-layer $WS_{0.3}Se_{1.7}$ and WS_2 film as described underneath.

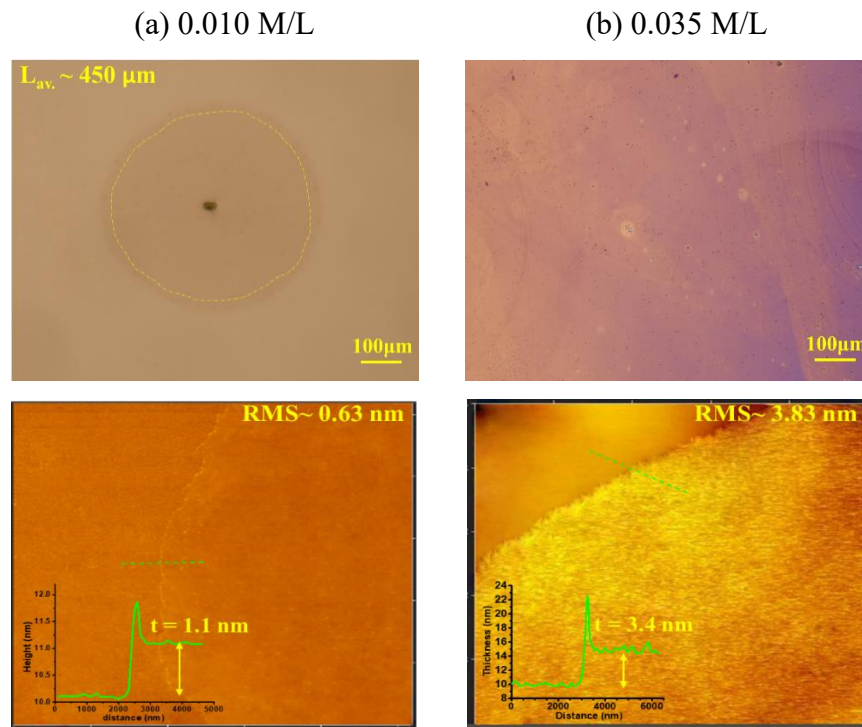


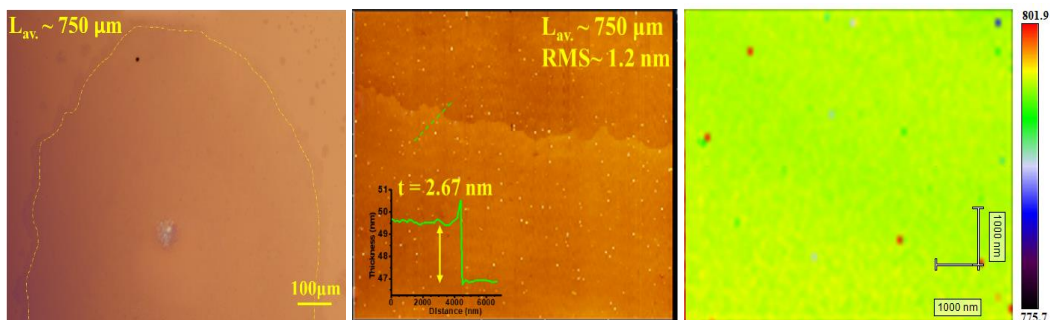
Figure 3.2.9. (a) Optical microscope and AFM images of $WS_{0.3}Se_{1.7}$ flakes for different precursor concentration of (a) 0.01 and (b) 0.035 M/L on $Al_{0.76}Ti_{0.24}O_y/p^+$ -Si substrate at mist supply times $t_{1s} = 50$ s, $t_2 = 210$ s, $N = 7$ cycles at a $T_f = 475$ °C followed by selenization at 600 °C for 2400 s.

Figure 3.2.10a shows the AFM and optical images of $WS_{0.3}Se_{1.7}$ synthesized from a precursor concentration of 0.025 M/L on $Al_{0.74}Ti_{0.26}O_y/p^+$ -Si under the optimized condition which we obtained on th - SiO_2/p^+ -Si substrate; $t_1 = 50$ s, $t_2 = 210$ s,

$T_f = 475\text{ }^\circ\text{C}$ with selenization at $600\text{ }^\circ\text{C}$ for 2400 s. The detail of mist CVD $\text{Al}_{0.74}\text{Ti}_{0.26}\text{O}_y$ growth was recently reported elsewhere^{5,11}. The inset shows the thickness profiles of the corresponding sample. The $\text{WS}_{0.3}\text{Se}_{1.7}$ flakes with an average size of $\sim 750\text{ }\mu\text{m}$, a thickness of $\sim 2.67\text{ nm}$ (3- 4 monolayers), and RMS of 1.2 nm were obtained for a precursor concentration of 0.025 M/L , while it was $\sim 450\text{ }\mu\text{m}$ with a thickness of 1.57 nm (mono/bilayers) at a concentration of 0.01 M/L . The PL mapping shows a uniform compositional distributed film. The Raman spectra also show a peak at around 249 cm^{-1} corresponding to coexisted E_{2g}^1 and A_{1g} modes of WSe_2 , which revealed the formation of trigonal phase $\text{WS}_{0.3}\text{Se}_{1.7}$ (Figure 3.2.10b). In addition, the PL emission energy of 1.57 eV (791 nm) with FWHM of 14 nm for 2400 s Se-vapor exposure, also confirmed the film crystallinity.

Figure 3.2.10c shows the contact angle measurement of $(\text{NH}_4)_2\text{WS}_4$ precursor solution dropped on mist-CVD $\text{Al}_{0.74}\text{Ti}_{0.26}\text{O}_3$ ($\sim 45\text{ nm}$) and *th*- SiO_2 (285 nm) coated p^+ -Si substrate. The contact angle θ_C for $(\text{NH}_4)_2\text{WS}_4$ precursor solution dissolved in NMP was found of $\theta_C \leq 14.7^\circ$ on ATO/p^+ -Si, whereas the θ_C was $> 49^\circ$ on *th*- SiO_2/p^+ -Si substrate. These results reveal the surface energy of $\text{Al}_{0.74}\text{Ti}_{0.26}\text{O}_3$ is higher, which promotes the higher wettability of precursors mist. Additionally, Raman spectra (inset) indicate 2D 1T- TiSe_2 related modes, which also may act as nucleation sites and accordingly promote the large grain growth as is a similar analogy to the metal-assisted growth of TMDCs films¹². Thus, submillimeter size few-layers $\text{WS}_{0.3}\text{Se}_{1.7}$ was obtained on a high- κ dielectric $a\text{-Al}_{0.74}\text{Ti}_{0.26}\text{O}_y$ layer at adjusted intermittent mist supply mode.

(a)



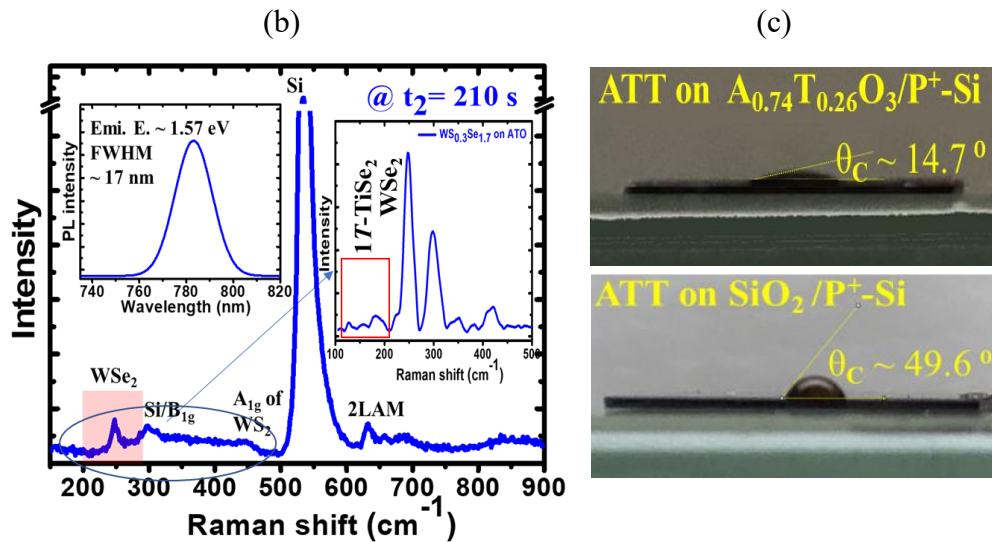


Figure 3.2.10. (a) Optical microscope and AFM images of few-layer $\text{WS}_{0.3}\text{Se}_{1.7}$ on $\text{Al}_{0.74}\text{Ti}_{0.26}\text{O}_3/\text{P}^+\text{-Si}$ substrate synthesized for $t_2=210$ s, at $T_f=475$ °C, $t_1=50$ s, $N=7$, and $C=0.025$ M/L; (inset AFM height profile) and PL mapping of corresponding samples (b) Raman and PL spectra of the corresponding samples; (c) Contact angle of $(\text{NH}_4)_2\text{WS}_4$ precursor dissolved in NMP dropped ($2\mu\text{L}$) on mist CVD $\text{Al}_{0.74}\text{Ti}_{0.26}\text{O}_3$ and thermally grown *th*- SiO_2 (285 nm) coated $\text{p}^+\text{-Si}$ substrates.

Figure 3.2.11 shows optical microscope and AFM images of $\text{WS}_{0.3}\text{Se}_{1.7}$ film synthesized using continuous mist supply mode for equal mist supply time of (50×7 cycles) 350 s at a $T_f=475$ °C, 0.025 M/L on $\text{Al}_{0.76}\text{Ti}_{0.24}\text{O}_3/\text{p}^+\text{-Si}$ substrate followed by selenization at 600 °C for 2400 s. $\text{WS}_{0.3}\text{Se}_{1.7}$ synthesized using continuous mist supply mode is found as a continuous film on the entire surface with a severe rough surface showing RMS of ~ 11.0 nm. The intermittent mist supply mode develops of an equilibrium condition between the sticking of incoming mist precursors and the sublimation of sulfur S element at the layer surface, consequently enhancing lateral growth, unlike vertical one. Thus, a uniform distributed submillimeter size few-layers $\text{WS}_{0.3}\text{Se}_{1.7}$ was obtained on a high- κ dielectric a- $\text{Al}_{0.74}\text{Ti}_{0.26}\text{O}_y$ layer at adjusted intermittent mist supply mode instead of continuous supply mode.

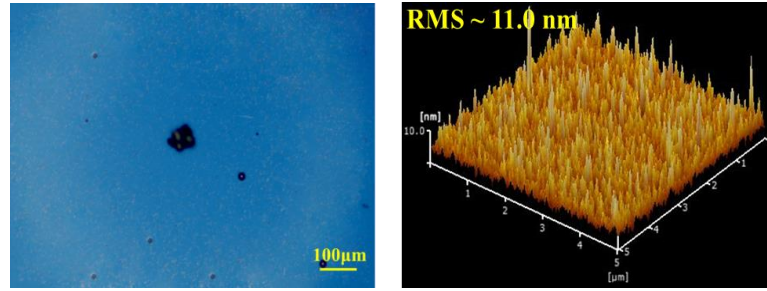
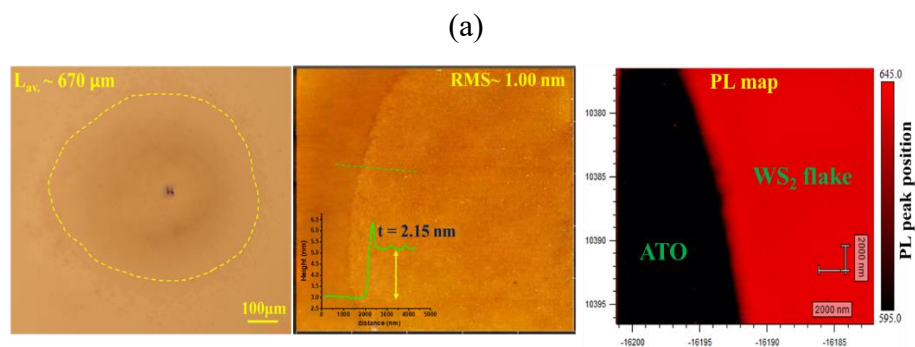


Figure 3.2.11. Optical microscope and AFM images of $\text{WS}_{0.3}\text{Se}_{1.7}$ film synthesized using continuous mist supply mode for equal mist supply time of $(50 \times 7 \text{ cycles})$ 350 s at a $T_f = 475 \text{ }^\circ\text{C}$, 0.025 M/L on $\text{a-Al}_{0.76}\text{Ti}_{0.24}\text{O}_y/\text{p}^+\text{-Si}$ substrate followed by selenization at $600 \text{ }^\circ\text{C}$ for 2400 s.

3.2.4 Growth of submillimeter size few-layer WS_2 flakes on $\text{a-Al}_{0.74}\text{Ti}_{0.26}\text{O}_y$

Figure 3.2.12a shows the AFM and optical images of WS_2 synthesized from a precursor concentration of 0.025 M/L on $\text{Al}_{0.74}\text{Ti}_{0.26}\text{O}_y/\text{p}^+\text{-Si}$ under the optimized condition which we obtained on $\text{th-SiO}_2/\text{p}^+\text{-Si}$ substrate; $t_1 = 50 \text{ s}$, $t_2 = 210 \text{ s}$, $T_f = 475 \text{ }^\circ\text{C}$ with selenization at $600 \text{ }^\circ\text{C}$ for 2400 s. Average size of $\sim 670 \text{ } \mu\text{m}$ with a thickness of $\sim 2.15 \text{ nm}$ (2- 3 monolayers) and RMS of $\sim 1.0 \text{ nm}$ was obtained. The PL mapping shows a uniform distributed compositional WS_2 film, while Raman spectra show two peaks at around $\sim 353.4 \text{ cm}^{-1}$ and ~ 417.6 corresponding to the in-plane mode of E_{2g}^1 and out-off plane mode of A_{1g} of WS_2 , which confirmed the formation of trigonal prismatic phase crystalline WS_2 and the PL emission energy of 1.94 eV with FWHM of $\sim 1.0 \text{ nm}$ also revealed the formation of crystalline WS_2 (Figure 3.2.12b). Thus, a uniform distributed submillimeter size few-layers WS_2 was obtained on a high- κ dielectric $\text{a-Al}_{0.74}\text{Ti}_{0.26}\text{O}_y$ layer as was observed in $\text{WS}_{0.3}\text{Se}_{1.7}$ at adjusted intermittent mist supply mode.



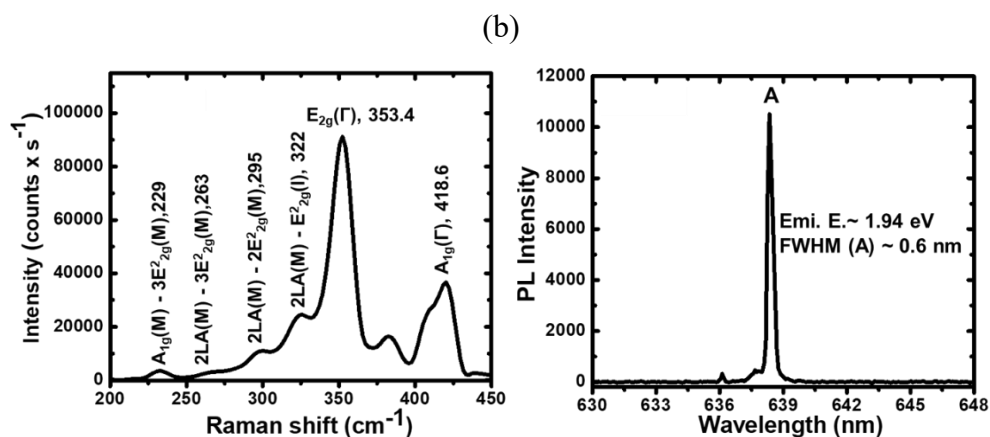


Figure 3.2.12. (a) Optical microscope and AFM images of few-layer WS₂ on Al_{0.74}Ti_{0.26}O_y/p⁺-Si substrate synthesized for t₂= 210 s, at T_f = 475 °C, t₁ = 50 s, N = 7, and C = 0.025 M/L; (inset AFM height profile) and PL mapping of corresponding samples; (b) Raman and PL spectra of the corresponding samples.

Figure 3.2.13 shows high-resolution core-spectra of (a) W 4*f* and (b) S 2*p* doublets of as-deposited and Sulfur (S) vapor exposed WS_x films at 600 °C for 1200 s. The WS_x films was synthesized at a T_f = 475 °C, for t₁ = 50 s, t₂ = 210 s and N = 7 cycles. The higher energy shift of W 4*f* doublet of ~0.42 eV and S 3*p* doublet of ~2.09 eV to their definite position indicate the promotion of sulfurization. A stoichiometry WS₂ was found with an S-exposure period of 1200 s. Moreover, the formation of stoichiometry WS₂ was observed for the sulfurization period of 1200 s at 600 °C, which is shorter than the Se-exposure time as was for WS_{0.3}Se_{1.7} film owing to the S-containing precursor as revealed by the XPS study.

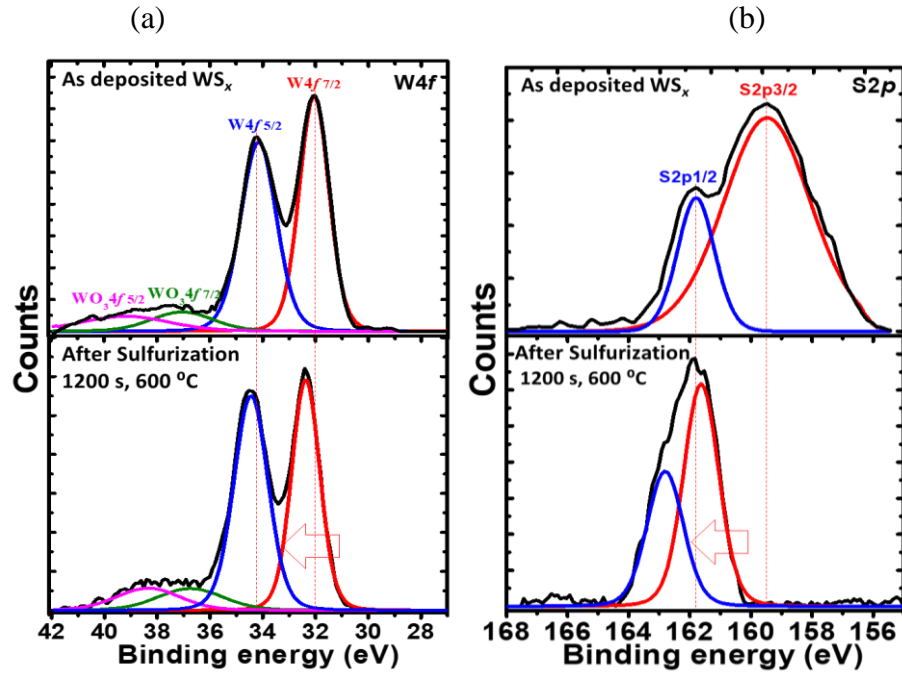


Figure 3.2.13. XPS observation; a high-resolution core-spectra of (a) W $4f$ and (b) S $2p$ doublets of as-deposited and S- vapor exposed WS_x films for 1200 s at 600 °C; the WS_x films was synthesized at a $T_f = 475$ °C, $t_1 = 50$ s, $t_2 = 210$ s, $N = 7$ cycles and 0.025 M/L.

Table 3.2.3. Summary of XPS results of as-deposited and 1200s sulfurized WS_x films.

Conditions	line	B.E (eV)	A (%)	ratio (W: S)
As-deposited WS_x	S $2p_{3/2}$	159.65	55.03	1: 1.2
	S $2p_{1/2}$	161.93		
	W $4f_{7/2}$	32.07	44.97	
	W $4f_{5/2}$	34.24		
Sulfurized $t = 1200$ s	S $2p_{3/2}$	161.74	68.92	1: 2.2 (stoichiometry)
	S $2p_{1/2}$	163.15		
	W $4f_{7/2}$	32.49	31.08	
	W $4f_{5/2}$	34.64		

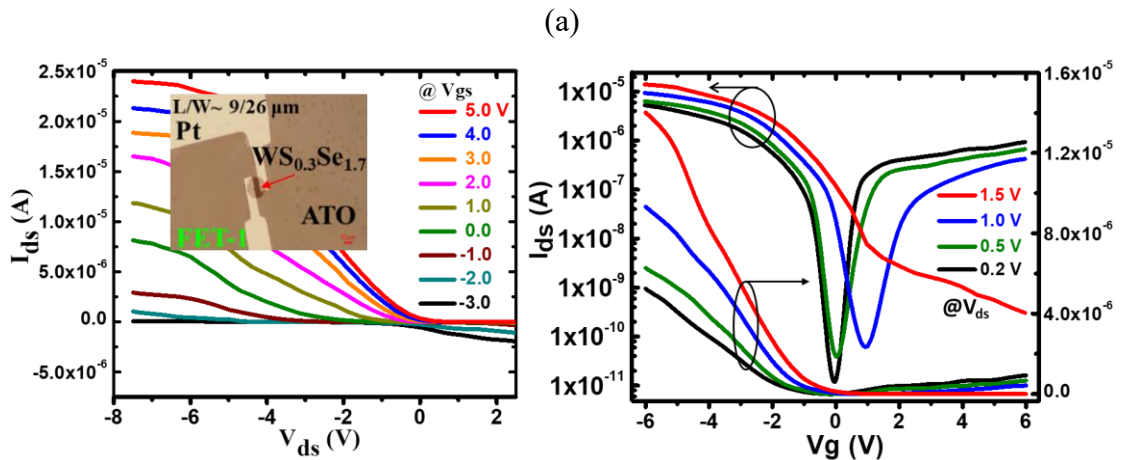
3.2.5 Fabrication of FETs and CMOS using mist CVD WS_2 and $WS_{0.3}Se_{1.7}$ on $a-Al_{0.74}Ti_{0.26}O_y$

Figure 3.2.14a shows the output and transfer characteristics of $WS_{0.3}Se_{1.7}$ channel bottom gate MOSFETs on mist-CVD grown a 45 nm thin- $Al_{0.74}Ti_{0.26}O_3/p^+$ -Si substrates with Pt S/D electrodes with a linear and a logarithmic scale in the positive

and negative V_{ds} regimes. A p-type characteristics was obtained in $WS_{0.3}Se_{1.7}$ channel bottom gate MOSFETs, which was further improved by forming sulfur-related defects with high electron affinity WO_x by He/O_2 plasma exposure for 60 s on the channel region. A p-type behavior of $WS_{0.3}Se_{1.7}$ with carrier concentration of $6.3 \times 10^{-17} \text{ cm}^{-3}$ was also observed by Hall measurement. Figure 3.2.14b depicts the output and transfer characteristics of WS_2 channel MOSFETs with S/D gold electrodes. The inset shows the optical microscope images of the corresponding devices. Herein, the stoichiometric WS_2 was used to fabricate n-channel FETs obtained through the post-sulfurization at $600 \text{ }^\circ\text{C}$ for 1200 s in sulfur vapor under the flow of an Ar/H_2 gases, which was confirmed by the XPS study. The field-effect mobility μ_{FET} is calculated by the equation:

$$\mu_{FET} = \left(\frac{L}{WC_g V_{ds}} \right) \left(\frac{dI_{ds}}{dV_{gs}} \right),$$

where $\frac{dI_{ds}}{dV_{gs}}$ is the slope, L and W are the channel length and width, respectively, and C_g is the capacitance per unit area between the channel and the back gate. The FET parameters determined from the $\sqrt{I_{ds}}-V_{gs}$ plot are summarized in Table 3.3.4. These FET parameters were also consistent with previous reports, implying the existence of low contact resistance in WS_2 and $WS_{0.3}Se_{1.7}$ channel FETs owing to the well-suited work function of metals (gold and platinum) used as the S/D electrodes. A comparative study of the performance of the devices fabricated using different techniques is presented in Table 3.3.5. These observations imply that mist-CVD has a great potential for the fabrication of a few layers n- WS_2 and p- $WS_{0.3}Se_{1.7}$ based MOSFETs without mechanical exfoliation and transfer process.



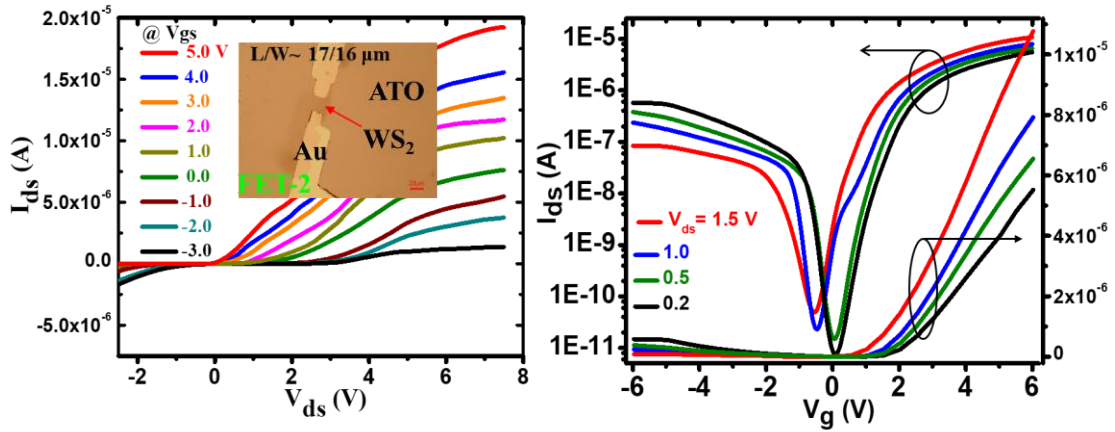


Figure 3.2.14. (a) Output and transfer characteristics of an atomic tri/bilayer p-channel $WS_{0.3}Se_{1.7}$ transistor on a linear and logarithmic scale in the positive and negative V_{ds} regimes; (b) Output and transfer characteristics of an atomic bi/monolayer WS_2 channel FETs with S/D gold electrodes on a linear and logarithmic scale; Inset shows the optical images of WS_2 and $WS_{0.3}Se_{1.7}$ MOSFETs with S/D gold and platinum electrodes, respectively, on ~ 45 -nm-thick $Al_{0.74}Ti_{0.26}O_y$ gate dielectric layer.

Table 3.2.4. The electrical characteristics of WS_2 and $WS_{2-x}Se_x$ atomic bi/monolayers-based MOSFETs with mist-CVD $Al_{0.74}Ti_{0.26}O_y$ as a dielectric layer.

FETs parameters / at $V_{ds} = 0.2$ V	V_{th} (V)	SS (V/dec.)	I_{ON}/I_{OFF}	$\mu_{lin.}$ ($cm^2V^{-1}s^{-1}$)
$WS_{0.3}Se_{1.7}$ - FETs	-0.20	0.20	7.5×10^5	~ 41
WS_2 - FETs	0.28	0.25	1.1×10^6	~ 52

Table 3.2.5. A comparative study on electrical parameters of atomic mono/bilayer WS_2 - and WSe_2 - channel FETs for different deposition methods. (*Sulf. = sulfurization, Sel. = selenization)

Name	Dielectric layers	V_{th} (V)	SS (V/dec.)	I_{ON}/I_{OFF}	μ ($cm^2V^{-1}s^{-1}$)	Ref.
Sulf. of WO_3	Al_2O_3/SiO_2	-1.0	~ 1	$\sim 1.0 \times 10^6$	2-17	6,13
PVD	Si/ SiO_2	-20.0	~ 15	$\sim 1.0 \times 10^8$	51	14
Exfoliation	Si/ SiO_2	10.0	~ 11	$> 1.0 \times 10^5$	20-150	15
Sel. of WO_3	Si/ SiO_2	~ 0.1	1.5-4	$< 1.0 \times 10^5$	< 1	16
Mist-CVD	$Al_{0.74}Ti_{0.26}O_y$	~ 0.2	~ 0.25	$\sim 1.0 \times 10^6$	32-62	This Work ¹⁷

Figure 3.2.15 depicts the histogram of the electrical characteristics of V_{th} , SS, I_{ON}/I_{OFF} , and μ_{lin} of several (6-7) FETs, the median value was obtained. The median threshold voltage, V_{th} of -0.2 (0.3) V with a standard deviation σ of 0.05 (0.11) V, an on-off ratio, I_{ON}/I_{OFF} of 6.2×10^5 (1.1×10^6) with σ of 5.9×10^5 (1.6×10^6), an SS of 0.2 (0.25) V/dec. with σ of 0.05 (0.05) V, and a linear mobility, μ_{lin} , of ~ 41 (~ 52) $\text{cm}^2 \text{V}^{-1} \text{s}^{-1}$ with σ of 7.03 (4.68) $\text{cm}^2 \text{V}^{-1} \text{s}^{-1}$ for $\text{WS}_{2-x}\text{Se}_x$ (WS_2) channel FETs. These reproduced electrical parameters values of $\text{WS}_{0.3}\text{Se}_{1.7}$ and WS_2 channel FETs revealed the potential of mist-CVD for the synthesis of large-area TMDCs films for the application in MOSFETs.

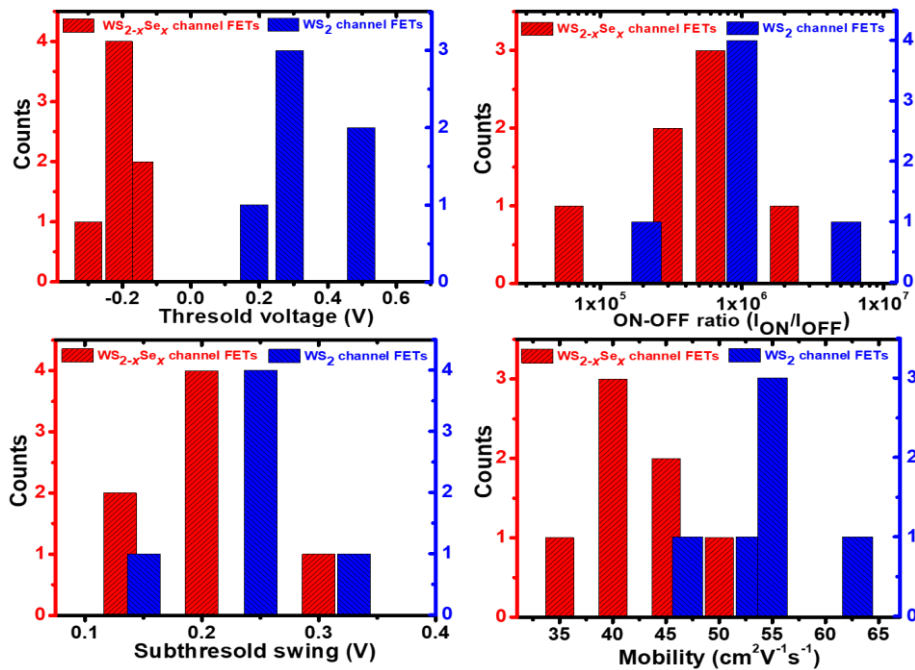


Figure 3.2.15. The histogram of threshold voltage V_{th} , on-off ratio I_{ON}/I_{OFF} , subthreshold swing SS, and mobility μ_{lin} calculated at V_g sweeping range of 0.5 V at a fixed V_{ds} of 0.2 V for $\text{WS}_{0.3}\text{Se}_{1.7}$ channel (red curve) and WS_2 channel (blue curve) bottom-gate FETs on mist- CVD grown $\text{a-A}_{0.74}\text{T}_{0.26}\text{O}_y$ (~ 45 nm)/ p^+ -Si substrates with platinum (Pt) and gold (Au) S-D electrodes, respectively.

Figure 3.2.16 shows an energy band diagram for meta/TMDCs contact (Au/ WS_2 and Pt/ $\text{WS}_{0.4}\text{Se}_{0.6}$) at thermal equilibrium. The Schottky barrier height at conduction ($q\phi_{SB,CBM}$) and valence band ($q\phi_{SB,VBM}$) to metal-work function ($q\phi_M$), are determined using the value of metal; Au, Pt work function from previous report and UPS, KPFM results of WS_2 and $\text{WS}_{0.3}\text{Se}_{1.7}$ ¹⁸⁻²⁰. Au (Pt) and TMDCs junctions exhibit ambipolar behavior with n-(p-) type carrier domination^{15, 21-25}. The Schottky barrier heights

between Au and WS₂ conduction band are lower ($\Delta q\phi \sim 1.21$ eV) than those of the Pt/WS_{0.3}Se_{1.7} interface. Therefore, the electrons can be transported, with no significant barrier height, from WS₂ to Au, in contrast to that from WS_{0.3}Se_{1.7} to the Pt electrode. On the other hand, the Schottky barrier heights between the Au and WS₂ valence band are higher ($\Delta q\phi \sim 1.51$ eV) than those of the Pt/WS_{0.3}Se_{1.7} interface, resulting in more facile transport of holes from WS_{0.3}Se_{1.7} to Pt than from WS₂ to the Au electrode. Consequently, electrons and holes were dominant in the WS₂- and WS_{0.3}Se_{1.7}- based FETs, respectively.

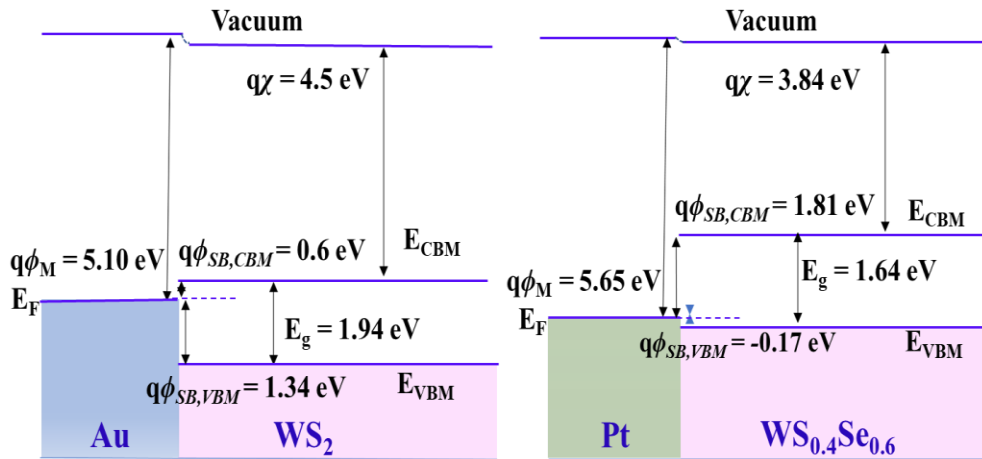


Figure 3.2.16. A typical energy band diagram for metal/TMDCs contact (Au/WS₂ and Pt/WS_{0.4}Se_{0.6}) at thermal equilibrium.

Figure 3.2.17a shows the inverting performance of designed complementary circuit by cascading p- WS_{0.3}Se_{1.7} channel MOSFET with n-WS₂ channel MOSFETs with a common gate as the input voltage V_{IN} under V_{dd} of 1 to 5 V and output voltage (V_{OUT}) is at the common source of the n-FET and p-FETs. Full logic swings with the symmetrical shape with a smaller static current are observed. When a small voltage is applied at V_{IN} , the p-FET is in ON (closed switch) and n-FET is in OFF (open switch); therefore, V_{OUT} is connected to V_{DD} , consequently, V_{OUT} is pulled up to logic 1, and pulled down to logic 0 at high input voltages with the p-FET is OFF and the n-FET is ON. The transition between the two logic states is characterized by the voltage gain $A_v = dV_{OUT}/dV_{IN}$. In Figure 3.2.17b, the gain of ~ 5 observed at half of V_{dd} region at V_{dd} of 5 V was found in similar gain values as observed in previous reports²⁵⁻²⁹. Thus, these findings imply that mist CVD synthesized submillimeter size few-layers WS₂ and WS_{0.3}Se_{1.7} and high- κ Al_{0.74}Ti_{0.26}O_y are promising as a channel and gate dielectric layers,

respectively, for the application in the MOSFETs and the complementary MOS logic circuit.

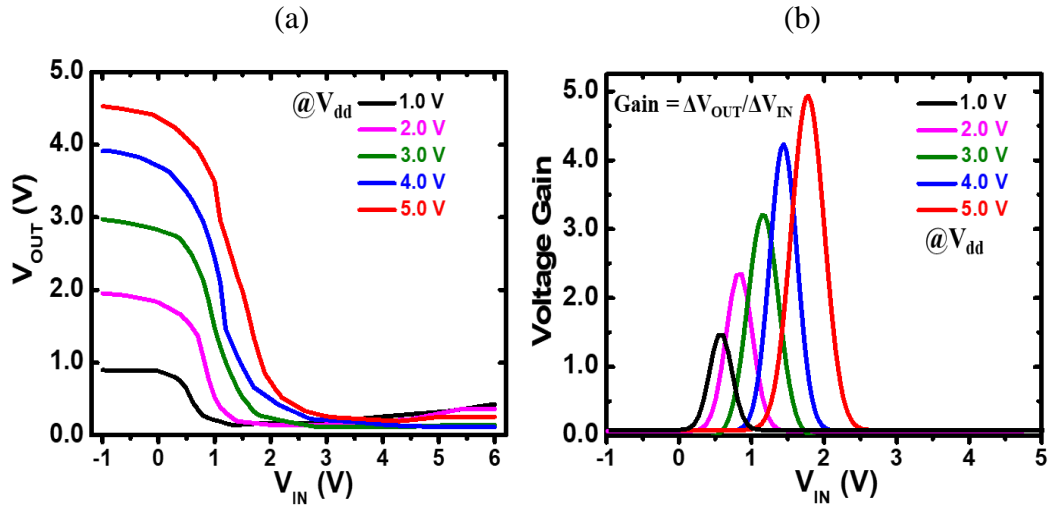


Figure 3.2.17. (a) Complementary MOS characteristics where V_{IN} and V_{DD} were both positively biased (inset schematic of a complementary inverter circuit comprising p- $WS_{0.3}Se_{1.7}$ and n- WS_2 -channel FETs), and (b) the corresponding voltage gain ($\Delta V_{OUT} / \Delta V_{IN}$) at V_{dd} of 1 to 5 V.

3.3 Improved photovoltaic properties of few-layers $WS_{0.3}Se_{1.7}/WO_x$ lateral p-n junctions using silver mirror layer

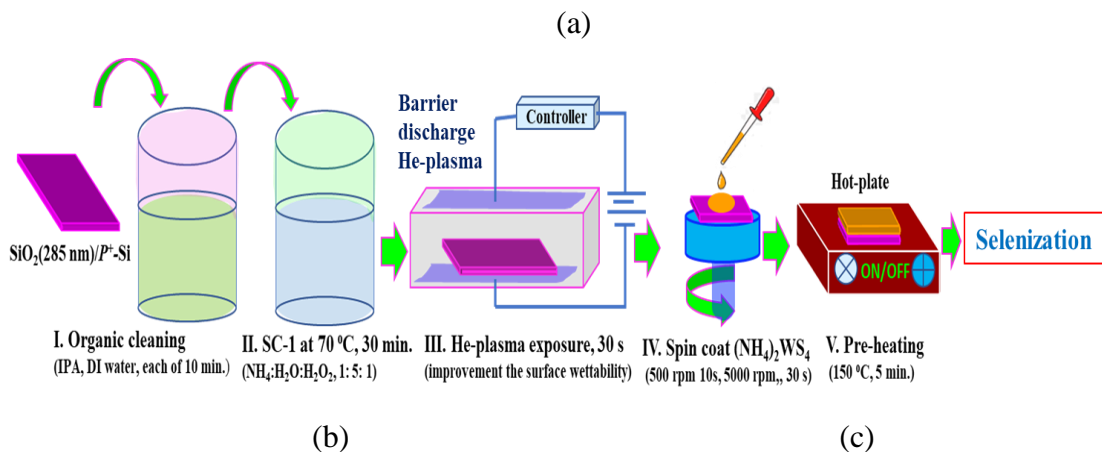
In this study, the photovoltaic effect of few-layer $WS_{0.3}Se_{1.7}$ based lateral p^+n junctions using MOSFET structure. The carrier transport properties for the lateral p-n junctions composed of the field-effect transistor under different monochromatic oscillation wavelength and simulated 100 mW/cm^2 solar light illumination has been demonstrated. In addition, the impact of the silver and gold mirror to enhance photocurrent is also investigated.

3.3.1 Fabrication of $WS_{0.3}Se_{1.7}/WO_x$ lateral p^+n junction device with a FET structure

Figure 3.3.1 shows the fabrication procedure of the lateral $WS_{2-x}Se_x/WO_x$ p^+n junction. First, a few-layers WS_x with a thickness of 3-5 nm were fabricated by spin-coat at 500 rpm for 10s followed by 4000 rpm for 60 s on thermally grown (*th*-) SiO_2 (285 nm)/ p^+ -Si substrate ($1 \times 1 \text{ cm}^2$) from 0.01 M/L $(NH_4)_2WS_4$ dissolved in a complex

solvent of N-methyl-2-Pyrrolidone (NMP) (55wt%), methylamine (30wt%), and 2-aminoethanol (5wt%). After the removal of the residual solvent by preheating at 140 °C for 5 minutes, the selenium vapor exposure was performed at 600 °C for 60 minutes at low pressure. Thereafter, the plasma treatment of few-layers $WS_{0.3}Se_{1.7}$ was carried out at half of the channel region and one electrode (Platinum) side using atmospheric-pressure He/O₂ barrier discharge excited by 10 kHz and 10 kV for 60 s using a shadow metal mask to form the oxidized layer at the top few-layers of $WS_{0.3}Se_{1.7}$. For several $WS_{0.3}Se_{1.7}$ samples, additional laser irradiation with different oscillation wavelengths of 420, 532, and 650 nm (<1 mW) was performed for 60 s after the He/O₂ plasma exposure with a similar metal mask configuration. Finally, gold (Au) and platinum (Pt) electrodes were formed to straddle the p-n junction interface. The gold and platinum electrodes with a length of 0.5 mm and a width of 0.2 mm were formed on $WS_{0.3}Se_{1.7}$ and WO_x region, respectively, as source and drain (S/D) electrodes, with a channel length of ~0.56 mm using sputtering. The FET devices with S/D electrodes of gold and platinum alone were also fabricated for comparative study.

The current-voltage characteristics for the $WS_{0.3}Se_{1.7}/WO_x$ lateral p-n junctions in the dark and under monochromatic light illumination were measured by varying the light intensity with a neutral density filter. In addition, photocurrent-voltage (I_p -V) curves were also measured using a Bunkoukeiki (CEP-25BX) system under simulated 100 mW/cm² solar light AM1.5G exposure. An external quantum efficiency (EQE) was also studied with and without applying forward and reverse bias to understand the change of the depletion width. The impact of a gold mirror layer inserted between the 40-nm-thick $Al_{0.74}Ti_{0.26}O_y$ dielectric and *th*-SiO₂/Si substrate to enhance the optical absorption and the carrier generation due to multiple reflections in the Fabry-Perot cavity was also studied.



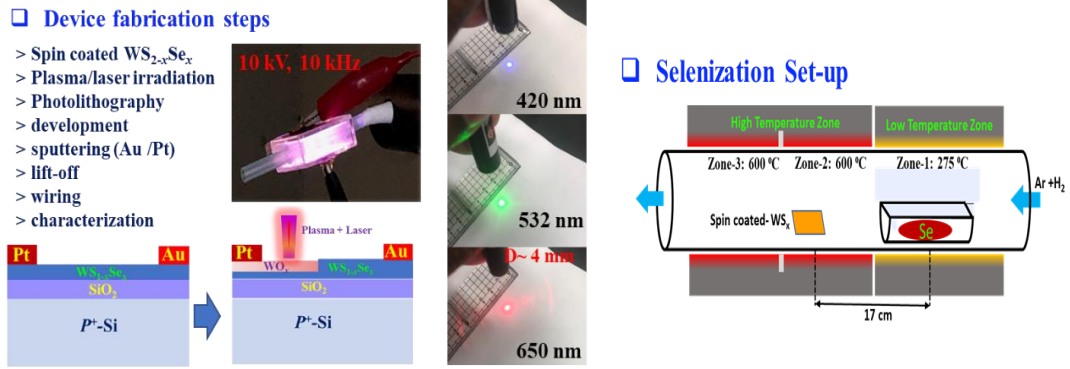


Figure 3.3.1. (a) Flowchart of the $WS_{2-x}Se_x$ synthesis steps, (b) $WS_{2-x}Se_x/WO_x$ lateral p⁺-n junction device fabrication, O₂/He plasma exposure system, 0.1 mW Laser of 420, 532, and 650 oscillation wavelengths with ~4 mm spot diameter, and a FET structure.

Table 3.3.1. $WS_{2-x}Se_x$ deposition and sulfurization conditions

WS _{2-x} Se _x deposition conditions	
Solute	(NH ₄) ₂ WS ₄
Solvent	N-methyl-2-pyrrolidone (NMP) (55 wt.%) Methylamine (30 wt.%) 2-aminoethanol (15 wt.%)
Substrate	SiO ₂ (285 nm)/P ⁺ -Si
Solution concentration	0.01 M
Spinning speed	500 rpm, warm speed, 10 s 4000 rpm, spinning speed, 30 s
Selenization condition	275 °C (Se Zone-1) 600 °C (WS _x Film Zone 2 and 3), 60 min., Ar + H ₂ (5%)
Plasma and Laser exposure	He/O ₂ -plasma exposure, 0-90 s Laser exposure, 0- 60 s $\lambda = 420, 532, 650$ nm

Figure 3.3.2a shows AFM and TEM images of $WS_{2-x}Se_x$ film synthesized at 4000 rpm for 30s and subsequent Se-exposure at 600 °C for 60 minutes (the inset shows AFM thickness profile, optical microscope, and SEM images). A uniform film distribution on the entire surface was observed in AFM observation. The height profile of the AFM

image shows a thickness of ~ 4 nm corresponding to 4-5 monolayers. The cross-sectional TEM image for the corresponding synthesized film also reveals the 4-5 monolayer stacked of $WS_{2-x}Se_x$ on th - SiO_2/p^+ -Si substrate. A sharp Raman peak at 250 - 255 cm^{-1} is attributed to the in-plane and out-of-plane vibrations of trigonal phase WSe_2 with the 2nd order WS_2 related signals at 298 and 530 cm^{-1} , and defect-related signals at 620 cm^{-1} (Figure 3.3.2b). The inset shows PL emission energy of $WS_{2-x}Se_x$ is 1.54 eV with FWHM of ~ 19 nm confirming the film crystallinity and uniform compositional distribution of $WS_{2-x}Se_x$ is observed in PL map (Figure 3.3.2c).

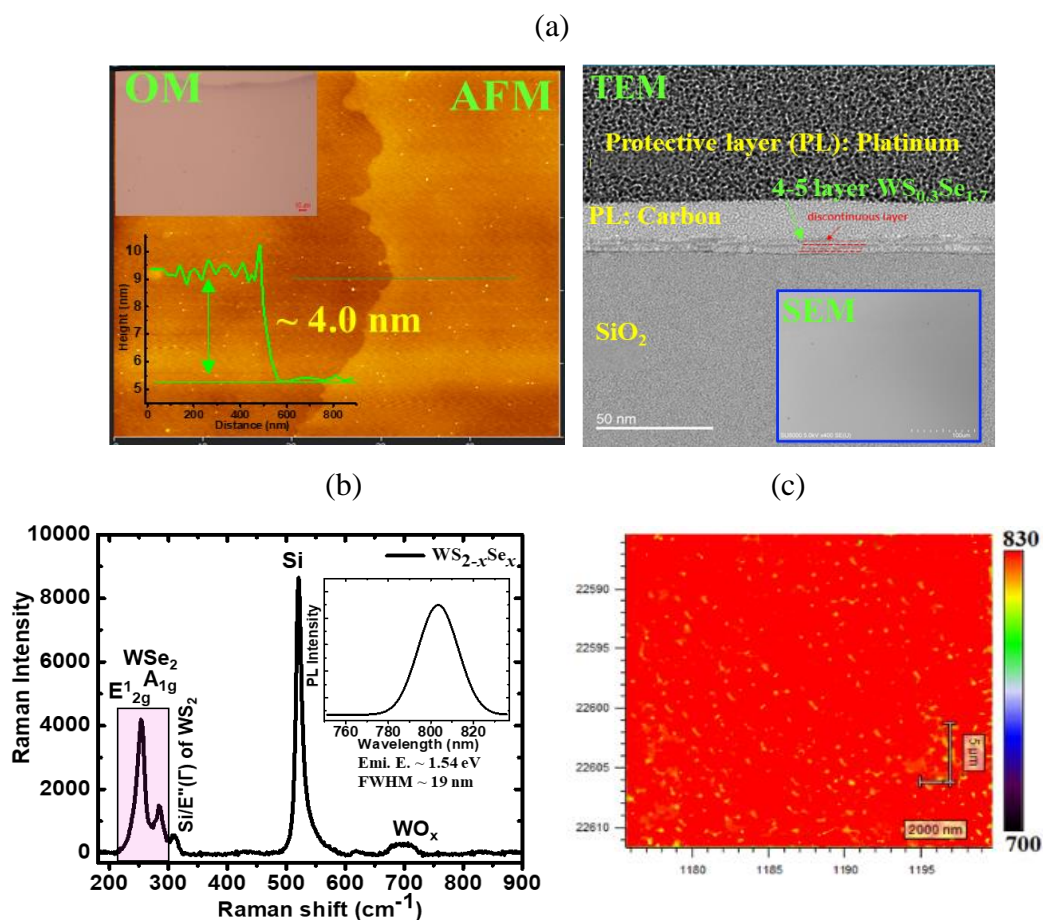


Figure 3.3.2. (a) AFM, and TEM images of synthesized $WS_{2-x}Se_x$ (the inset shows the line profile, optical microscope, and SEM images) and (b) Raman spectra (the inset shows the PL spectra), and (c) PL map of the corresponding $WS_{2-x}Se_x$ sample.

Figure 3.3.3 shows the XPS core energy spectra of Se(3d) and W(4f) of synthesized $WS_{0.3}Se_{1.7}$ film with Se-exposure at 600 $^{\circ}C$ for 60 minutes. The composition ratio of Se to W element is $\sim 85\%$ ($WS_{0.3}Se_{1.7}$) is obtained as revealed by the XPS observation. A summary of the XPS study is summarized in Table 3.3.2.

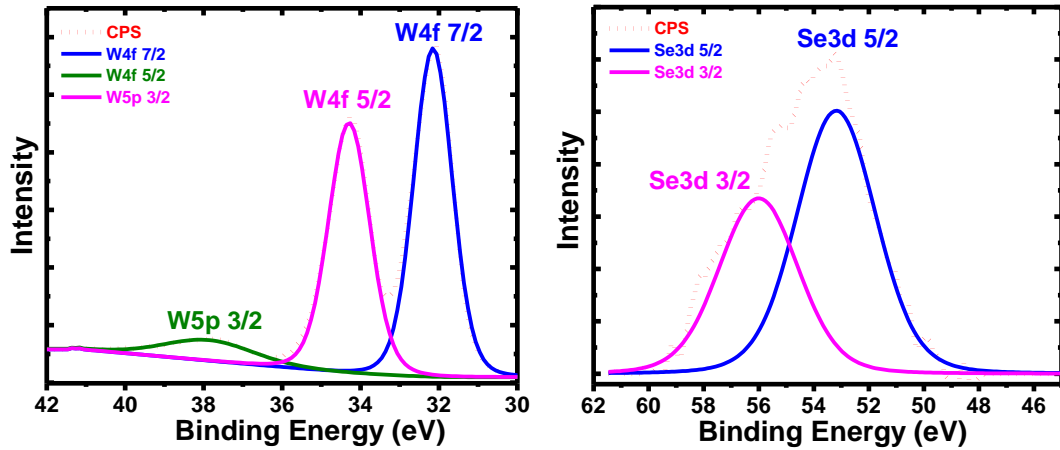


Figure 3.3.3. XPS observation; a core energy spectrum of Se W 4f and 3d of synthesized $WS_{0.3}Se_{1.7}$ film with Se-exposure at 600 °C for 60 minutes.

Table 3.3.2. Summary of XPS observation of synthesized $WS_{0.3}Se_{1.7}$ film with Se-exposure at 600 °C for 60 minutes.

ine	B.E. (eV)	At (%)	ratio (W: Se)
W 4f7/2	32.14	36.77	1.72
W 4f5/2	34.29		
Se 3d5/2	53.19	63.23	
Se 3d3/2	55.87		

Figure 3.3.4 shows the Raman and PL spectra of few-layers $WS_{0.3}Se_{1.7}$ normalized by the transverse optical (TO) phonon peak intensity at 520 cm^{-1} of a c-Si at different laser irradiation time of $t = 0\text{-}120\text{ s}$ for the with a wavelength of 420 nm. The as-deposited few-layers $WS_{0.3}Se_{1.7}$ show the prominent WSe_2 related phonon mode attributed to the in-plane E_{2g} and out-off plane A_{1g} vibrations of WSe_2 with the 2nd order WS_2 related signals at 298 cm^{-1} . The WSe_2 -related peak intensity was systematically reduced, while the WO_4 and WO_6 complex-related defects at $650\text{-}900\text{ cm}^{-1}$ increased, i.e., oxidation with increasing the irradiation time. The lower wavelength shifts from 810 to 650 nm with gradually decreased peak intensity with laser irradiation time also reveals the improvement of the degree of oxidation. Since the $WS_{0.3}Se_{1.7}$ semiconducting layers are required beneath oxidized WO_x few-layer, the laser irradiation time of 60 s, was chosen for further study.

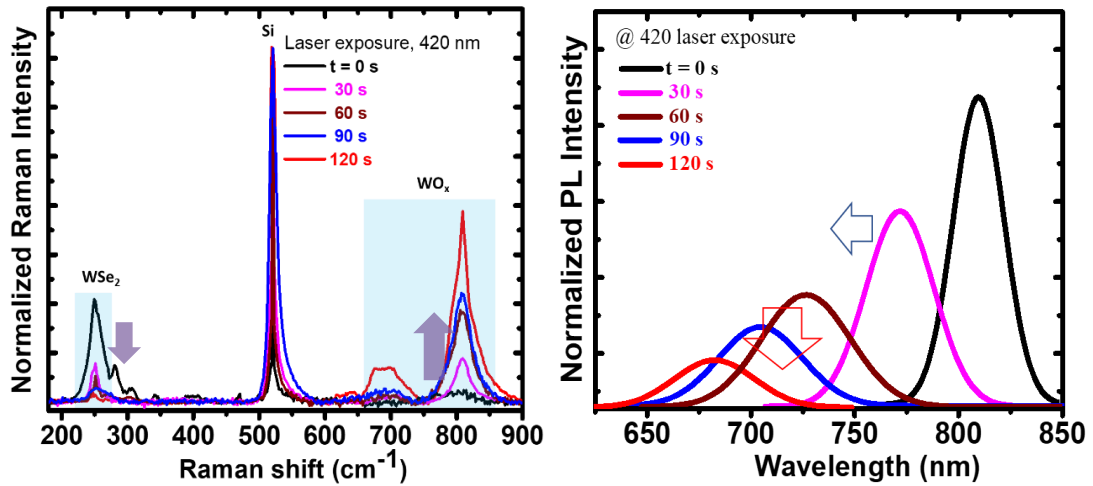


Figure 3.3.4. Micro-Raman spectra of few-layers $\text{WS}_{0.3}\text{Se}_{1.7}$ normalized by the TO phonon mode intensity at 520 cm^{-1} of a c-Si at different 420 nm laser irradiation time $t = 0\text{-}120\text{ s}$ and PL spectra of corresponding samples.

Figure 3.3.5a shows the Raman spectra of few-layers $\text{WS}_{0.3}\text{Se}_{1.7}$ normalized by the transverse optical (TO) phonon peak intensity at 520 cm^{-1} of a c-Si before and after the He/ O_2 plasma exposure for 30 and 60 s. The as-deposited few-layers $\text{WS}_{0.3}\text{Se}_{1.7}$ show the prominent WSe_2 related phonon mode attributed to the in-plane E_{2g} (246 cm^{-1}) and out-of-plane A_{1g} (251.1 cm^{-1}) vibrations of WSe_2 with the 2nd order WS_2 related signals at 298 and 530 cm^{-1} , and defect-related signals at 620 cm^{-1} . The He/ O_2 plasma exposure for 60 s reduced the WSe_2 related peak intensity with a slight increase in the WO_4 and WO_6 complex related defects at $800\text{-}900\text{ cm}^{-1}$, i.e., oxidation. Additional laser irradiation with an excitation wavelength of 420 nm for 60 s to the plasma-treated few-layers $\text{WS}_{0.3}\text{Se}_{1.7}$, further promoted the oxidation with disappearance of second-order and defect-related bands at 540 and 620 cm^{-1} (Figure 3.3.5b). PL spectra for exposure time of $t = 0\text{-}60$ and the combined plasma/laser irradiation for 60 s also shows increased oxidation with a higher energy shift of $\sim 0.45\text{ eV}$ (from $\sim 810\text{ nm}$ to $\sim 640\text{ nm}$). The degree of oxidation promoted efficiently for the use of a shorter laser wavelength of 420 nm after plasma exposure.

Figure 3.3.5d also shows the Raman and PL map images for the corresponding $\text{WS}_{0.3}\text{Se}_{1.7}/\text{WO}_x$ interface region together with the AFM image. Apparently, two different zones attributed to the as-deposited $\text{WS}_{0.3}\text{Se}_{1.7}$ and plasma/laser-irradiated regions were observed. These results suggest that the degree of the oxidation of few-layers $\text{WS}_{0.3}\text{Se}_{1.7}$ could be adjusted by the laser excitation wavelength and the

irradiation times, which promoted efficiently for the laser irradiation with a wavelength of 420 nm. In Raman spectra for the oxidized $WS_{2-x}Se_x$ layer, the WSe_2 related band at 250 cm^{-1} regions was observed even the 420 nm laser exposure for 60 s. The TEM observation also revealed the layered structure remained even after the laser irradiation for 60 s (Figure 3.3.5e). These findings imply that the oxidized layer is formed with atomic tri/bilayer level. Thus, the $WS_{0.3}Se_{1.7}$ layer remained at the bottom surface and the hole doping developed by the top plasma-oxidized high electron affinity WO_x to the underneath $WS_{0.3}Se_{1.7}$ layer.

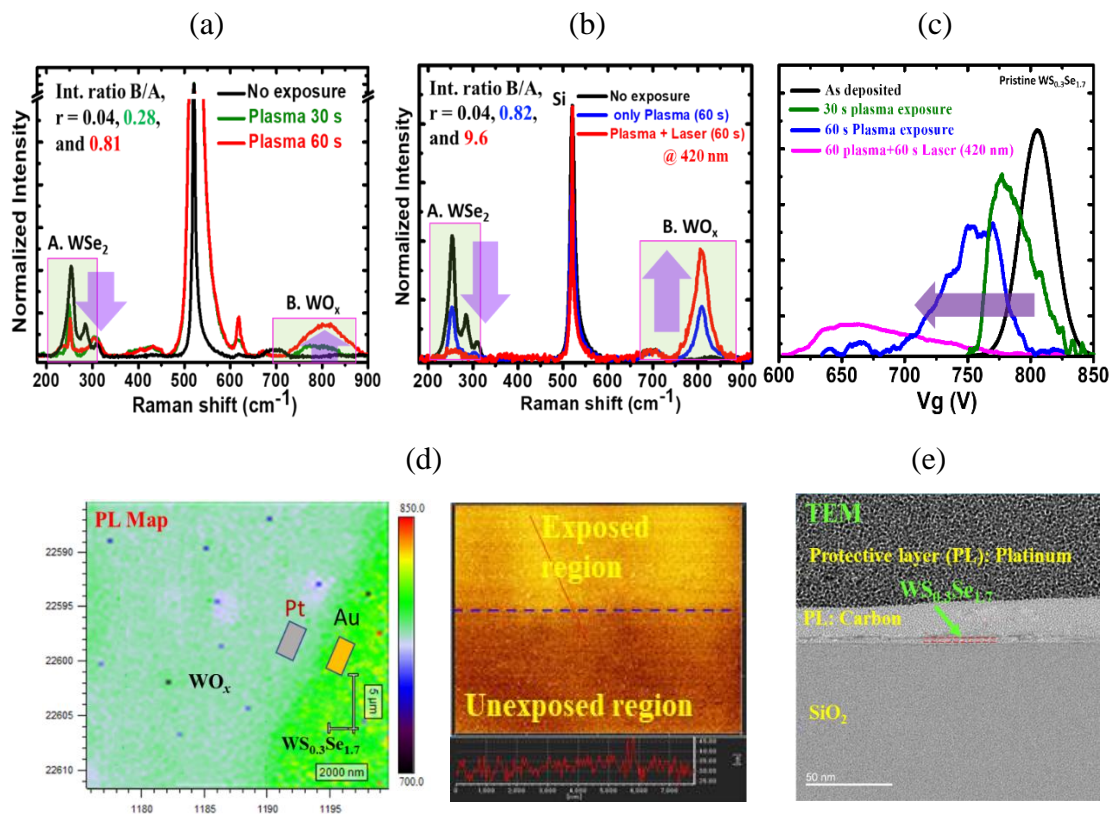


Figure 3.3.5. Micro-Raman spectra of few-layers $WS_{0.3}Se_{1.7}$ normalized by the TO phonon mode intensity at 520 cm^{-1} of a c-Si (a) before and after the He/ O_2 plasma exposure for 30 and 60s; (b) before and after laser exposure for 60 s after the He/ O_2 plasma exposure; and (c) PL spectra; (d) PL map and AFM images of the corresponding $WS_{0.3}Se_{1.7}/WO_x$ lateral p^+-n junction area (the inset shows the line profile of the $WS_{0.3}Se_{1.7}$ layer); (e) TEM observation of plasma (60 s) and 420 nm laser (60 s) irradiated $WS_{0.3}Se_{1.7}$ film.

Figure 3.3.6 shows the degree of oxidation of few-layers $WS_{0.3}Se_{1.7}$ before and after the He/ O_2 plasma exposure for 30 and 60s added with further 420 nm laser irradiation (60

s) through Time-of-Flight Secondary Ion Mass Spectrometry (TOF-SIMS), Auger Electron Spectroscopy (AES) and X-ray photoelectron spectroscopy (XPS) observation. In the TOF-SIMS, the intensity of oxygen spectra systematically increased with increasing the plasma exposure and subsequent laser irradiation, consequently increasing the formation of WO_3 in the film as observed in the TOF-SIMS WO_3 spectra. A higher energy shift of O 1S doublet from atomic concentration from 29 to 65% with increasing plasma exposure time and subsequent laser irradiation also revealed the promotion of oxidation. A similar consequence of oxygen increment in the $\text{WS}_{0.3}\text{Se}_{1.7}$ is found in AES spectra and its corresponding AES map (inset shows AES map for oxygen “O”). Thus, a level of oxidation with plasma exposure and subsequently laser irradiation could be obtained for controllable hole doping in a few-layer $\text{WS}_{0.3}\text{Se}_{1.7}$ film.

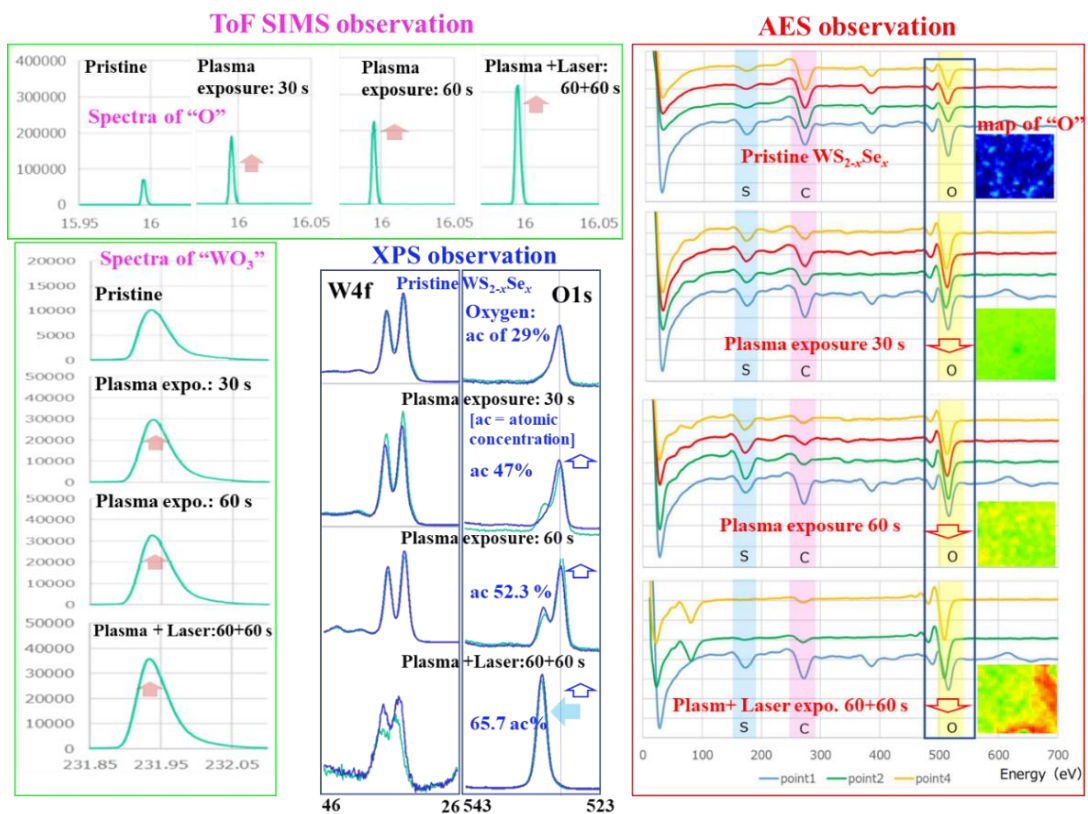
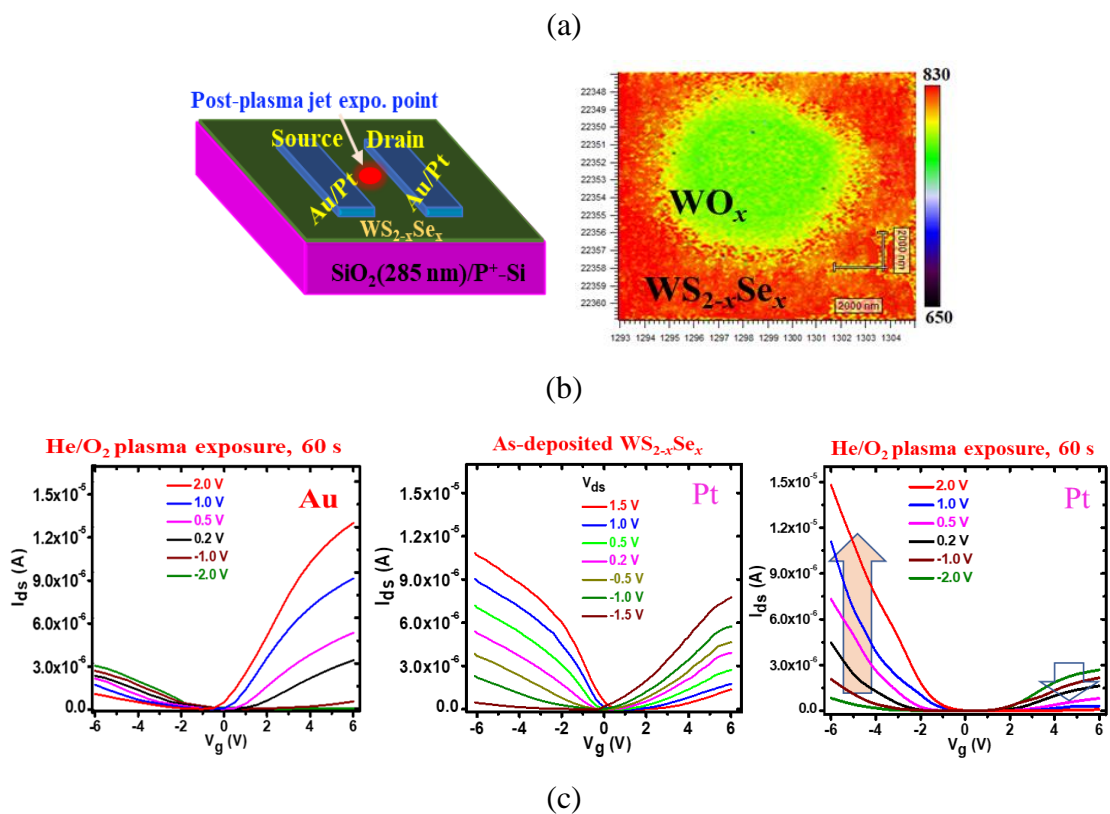


Figure 3.3.6. The degree of oxidation; TOF-SIMS, XPS, and AES (inset AES map for oxygen “O”) observation of few-layers $\text{WS}_{0.3}\text{Se}_{1.7}$ before and after the He/O_2 plasma exposure for 30 and 60s and subsequent 420 nm laser irradiation for 60 s.

3.3.2 Carrier transport properties in the FETs with lateral $\text{WS}_{0.3}\text{Se}_{1.7}/\text{WO}_x$ ($\text{WS}_{0.3}\text{Se}_{1.7}$) p^+-n junction

Figure 3.3.7a shows the schematic of FETs with a channel of few-layer $WS_{0.3}Se_{1.7}$ with He/O_2 plasma jet exposed region in the channel and PL map of the oxidized region. Figures 3.3.7b, c depict the transfer and output characteristics of FETs for gold and platinum (S/D) electrodes, respectively with a channel of few-layers $WS_{0.3}Se_{1.7}$ having an oxidized region between source and drain (S/D) electrodes generated by the He/O_2 plasma exposure for 60 s. The FET mainly acts as an n-channel drive for the gold electrode, whereas it shows an ambipolar behavior for the platinum. However, the hole current increased 1.5-fold at the negative V_g region by the He/O_2 plasma oxidation, although the electron current is not negligible in the positive V_g apply. The output current I_{ds} were also found of 1.4-fold compared with no exposure device. The high electron affinity WO_x few-layer on top of $WS_{0.3}Se_{1.7}$ causes electron transfer to WO_x from beneath $WS_{0.3}Se_{1.7}$ layers, which origins induced hole doping, therefore an improved I_{ds} .



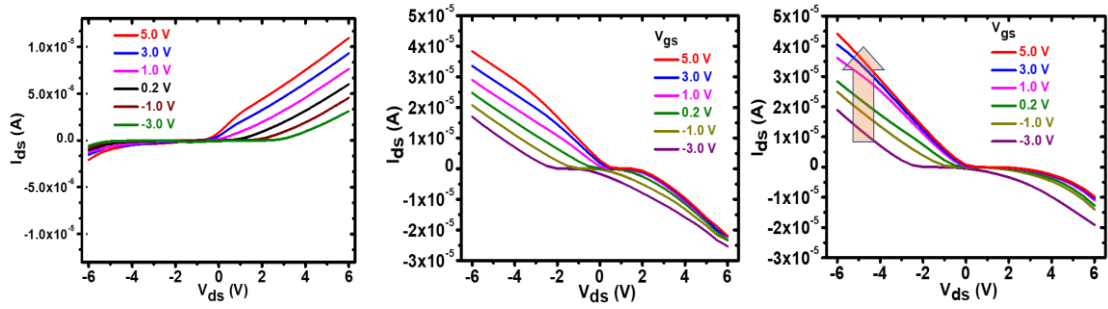


Figure 3.3.7. (a) Schematic of FETs with a channel of few-layers WS_{0.3}Se_{1.7} having an oxidized region between source and drain (S/D) electrodes generated by the He/O₂ plasma exposure and the PL map; (b) Transfer characteristics of FETs with Au and Pt (S/D) electrodes; (c) corresponding output characteristics of FETs without and with He/O₂ plasma exposure for 60 s.

Figure 3.3.8a shows the schematic of the FETs structure with associated measuring circuit configuration. Figure 3.3.8b shows the transfer and output characteristics of the laser-irradiated WS_{0.3}Se_{1.7}/WO_x FETs at three different excitation wavelengths of 420, 532, and 650 nm for 60 s after the He/O₂ (60 s) plasma exposure. The I_{ds} -V_g curve changes from ambipolar to unipolar p-channel drive systematically as the laser excitation wavelength becomes shorter from 650 to 420 nm. The output characteristics for the corresponding laser-irradiated FETs at a V_g = 0.2 V are also shown in Figure 3.3.8c. The I_{ds} was negligibly small at the entire V_g region from -3 V to +0.5 V, whereas it increased markedly for V_g over 1 V. These behaviors are determined by the strong built-in field formed at the lateral p-n junction through the generation of the increased defective WSSe (O)_x few-layers which has higher electron affinity and promoted the hole doping to the underneath WS_{0.3}Se_{1.7} few-layer, formed p⁺ layer. Thus, an improved hole doping density from the high electron affinity WO_x to the underneath p-type WS_{0.3}Se_{1.7} layers, that develops the p⁺-n junction. In fact, the increase of hole injection level further was confirmed from the temperature dependence of I_{ds}-V_g characteristics utilizing the thermionic emission model, where the barrier height reduced from 0.19 eV to 0.09 eV by inserting WO_x layer between Pt/WSSe interface.

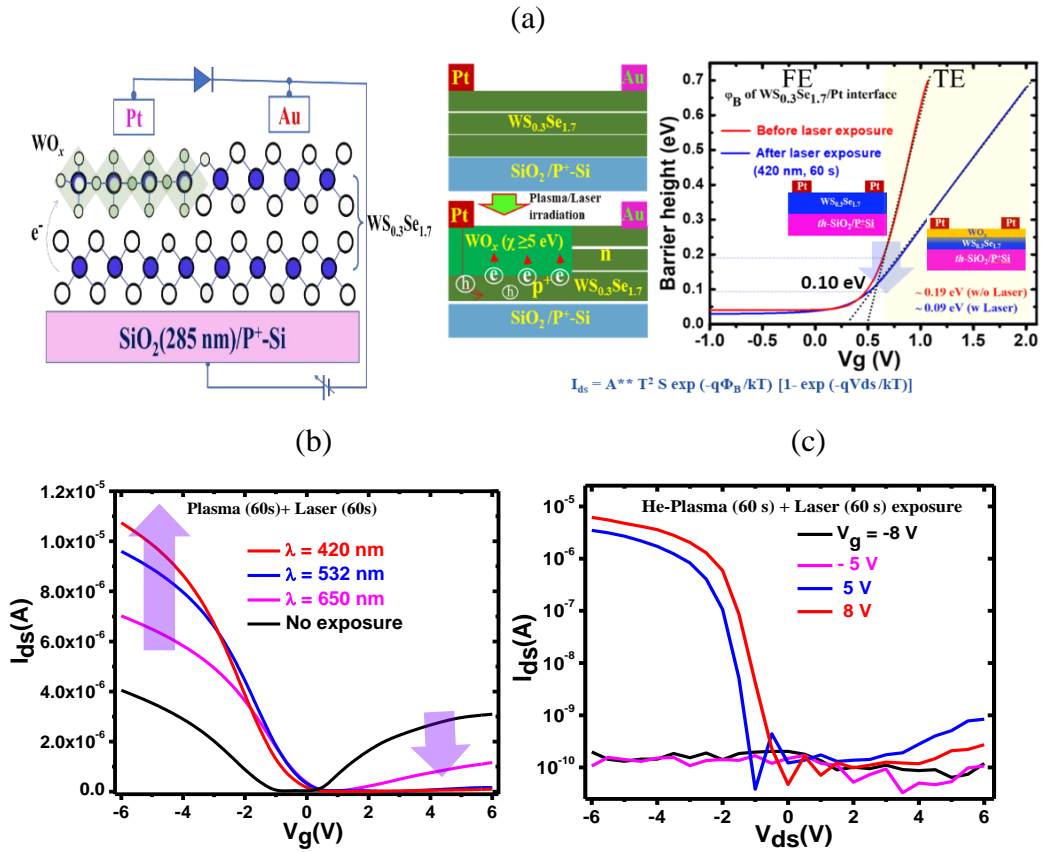


Figure 3.3.8. (a) the schematic of the FETs structure, associated circuit configuration, and barrier height obtained from temperature dependent I_{ds} - V_g characteristics using thermionic emission model; (b) transfer, and (c) output characteristics of the corresponding laser-irradiated $WS_{2-x}Se_x/WO_x$ FETs at three different excitation wavelengths of 420, 532, and 650 nm for 60 s after the O_2/He plasma exposure.

3.3.3 Photovoltaic properties in the FETs with lateral $WS_{0.3}Se_{1.7}/WO_x$ p⁺-n junction

Figure 3.3.9 shows the I_{ph} - V curves for the $WS_{0.3}Se_{1.7}/WO_x$ lateral p⁺-n junction devices before and after the He/ O_2 plasma exposure for 60 s. The device structure is schematized on the right. To ensure lower contact resistance, gold and platinum electrodes were formed on $WS_{0.3}Se_{1.7}$ and WO_x layers, respectively. The I_{ph} - V characteristic was found nearly linear and/or slightly non-linear due to the use of Au and Pt electrodes (electrode: length $L \sim 3.5$ nm, Width $W \sim 0.5$ mm, thickness $t \sim 50$ nm, channel length ~ 900 μ m) for as-deposited $WS_{0.3}Se_{1.7}$ layer. It showed a highly resistive in the -0.5 to 0.5 V region for the $WS_{0.3}Se_{1.7}/WO_x$ lateral p⁺-n junction devices formed by the He/ O_2 plasma exposure. The photovoltaic behavior was obtained under

simulated 100 mW/cm² solar light AM1.5G irradiation (exposure area, A~5 mm²) and the I_{ph} was an order of 10⁻⁶ A with a V_{oc} of ~1V, although the rectification behavior is still poor due to the influence of the thermal carrier.

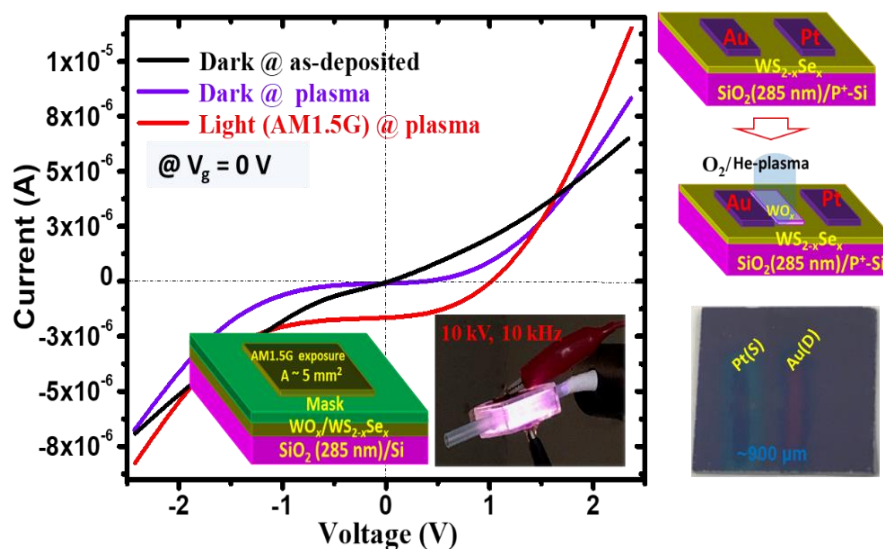
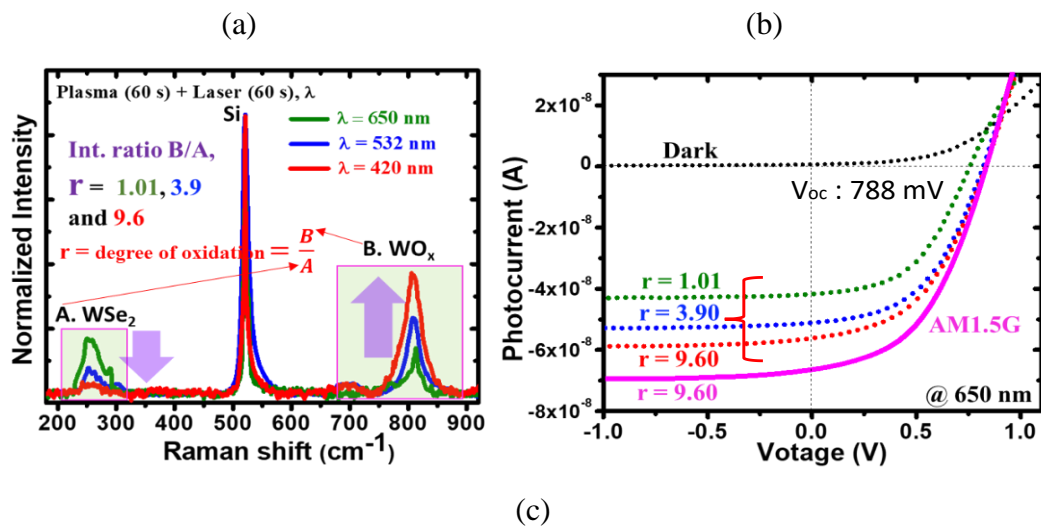


Figure 3.3.9. I_{ph} -V curves in the dark for the as-deposited WS_{0.3}Se_{1.7} few-layers and the He/O₂ plasma-treated devices for 60 s with gold and platinum electrodes when V_g = 0 V and under AM1.5G simulated solar light exposure for the device with a He/O₂ plasma exposure for 60 s.

Figure 3.3.10a shows the Raman spectra for the laser irradiation with three different wavelengths of 650, 532, and 420 nm after the plasma treatment of few-layers WS_{0.3}Se_{1.7} normalized by the transverse optical (TO) phonon peak intensity at 520 cm⁻¹ of a c-Si. The WSe₂-related peak intensity decreases, while WO_x-related peak intensity increases markedly for shorter wavelength laser exposure. The degree of oxidation is defined by “r” which is determined by the ratio of the intensity of WO₃ related Raman peak to the intensity of the WSe₂ peak. The degree of oxidation “r” was determined at 1.01, 3.9, and 9.6 corresponding to oscillation wavelengths of 650, 532, and 420 nm respectively. Figure 3.3.10b shows the current-voltage curves for the WS_{0.3}Se_{1.7}/WO_x lateral p⁺-n junction devices in the dark and under the illumination of the monochromatic 650 nm light exposure with different levels of the oxidized WO_x layer of 1.01, 3.9 and 9.6 corresponding to excitation wavelengths, 650, 532, and 420 nm. The photocurrent increased systematically with increased V_{oc} from 738.6 to 788.4 mV when r value increased from 1.01 to 9.6 corresponding to the laser wavelength from

650 to 420 nm. The I-V curve under the under simulated solar light AM1.5G 100 mW/cm² irradiation is also included for the well-oxidized WO_x p⁺-n junction with a r = 9.6. The I_{sc} was 71.7 × 10⁻⁹ A with an open-circuit voltage (V_{oc}) of 788.4 mV, a fill factor (FF) of 0.49. The photovoltaic performance is summarized in Table 3.3.3.

Figure 3.3.10c depicts the EQE for the corresponding WS_{0.3}Se_{1.7}/WO_x lateral p⁺-n junction device with Pt/Au as source/drain electrodes under 0 and ±0.5 V apply at a V_g = 0 V. The EQE values are very small because the ~4.0 nm thin as-deposited WS_{0.3}Se_{1.7} film corresponding 4-5 monolayers. The EQE shows a broad-band in the range of 250-1200 nm attributing to the optical absorption of WS_{0.3}Se_{1.7} and oxidized WO_x few layers. Apparently, when the forward bias of +0.5 V was applied between the source and drain electrodes, the carrier collection is preferentially predominated in the p-type WS_{0.3}Se_{1.7} layer with a lack of the response from the UV/visible region, whereas it was mainly predominated by defective WO_x layer at a reverse bias of -0.5 V. These findings imply that the carrier collection is mainly determined by the depletion region at the WS_{0.3}Se_{1.7}/WO_x lateral p⁺-n junction and the degree of oxidation of WO_x layer determine the hole injection level to the underneath WS_{0.3}Se_{1.7} few-layers of photovoltaic performance of WS_{0.3}Se_{1.7}/WO_x lateral p⁺-n junction devices.



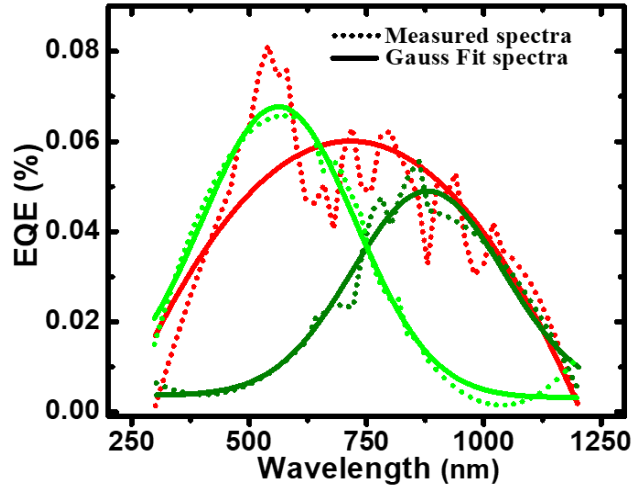


Figure 3.3.10. (a) Raman spectra for the laser irradiation with three different wavelengths of 650, 532, and 420 nm after the plasma treatment of few-layers $WS_{0.3}Se_{1.7}$ film; (b) I_{ph} -V curves for the $WS_{0.3}Se_{1.7}/WO_x$ lateral p^+ -n junction devices treated by the He/ O_2 plasma exposure for 60 s and followed by the laser irradiation at excitation wavelengths of 420 ($r = 9.60$), 532 ($r = 3.90$), and 650 nm ($r = 1.01$) (c) EQE for the corresponding WO_x lateral p^+ -n junction device with Au/Pt as source/drain electrodes under zero, forward, and reverse bias of 0 and ± 0.5 V at a $V_g = 0$ V.

Table 3.3.3. Summary of photovoltaic performance of $WS_{0.3}Se_{1.7}/WO_x$ lateral p^+ -n junction device.

λ (nm)	$r = WO_x/WS_{0.3}Se_{1.7}$	I_{sc} (nA)	V_{oc} (mV)	FF (%)
650	1.01	22.4	738.6	52.6
532	3.9	49.9	772.3	47.8
420	9.6	59.8	787.2	46.9
AM1.5G	9.6	71.7	788.4	49.6

Figure 3.3.11a depicts the I_{ph} -V curves for the well-oxidized lateral p^+ -n junction devices at a different light intensity at no gate bias. The I_{ph} increases linearly with increasing the light intensity, suggesting the free of space-charge in the interface region. In Figure 3.3.11b, the photocurrent–voltage curves of the $WS_{0.3}Se_{1.7}/WO_x$ lateral p^+ -n junction FETs measured at 532 nm light exposure under different gate bias V_g conditions are shown. As V_g changes from negative to positive, the photocurrent I_{ph}

increases with increasing the collecting (depletion) area owing to electrostatic doping³⁰. The lower carrier concentrations of non-irradiated region developed a wide depletion width compared with those of the laser-treated one. The as-deposited $\text{WS}_{0.3}\text{Se}_{1.7}$ becomes n-type at V_g of ≥ 0 V, a strong p-n junction forms between the laser-treated and as-deposited $\text{WS}_{0.3}\text{Se}_{1.7}$, thereby increasing the photocurrent to as much as ~ 80 nA, consequently, the photogenerated carriers can be effectively separated at high positive V_g . These results suggest that the atomically thin in-plane logic circuits can be addressed via laser-induced doping, which allows us to control the carrier type and doping concentration in 2D material-based electronic and optoelectronic devices. The relatively low-efficiency η is mainly due to low absorption along the thinner 2D TMDC channel in the lateral FET structure.

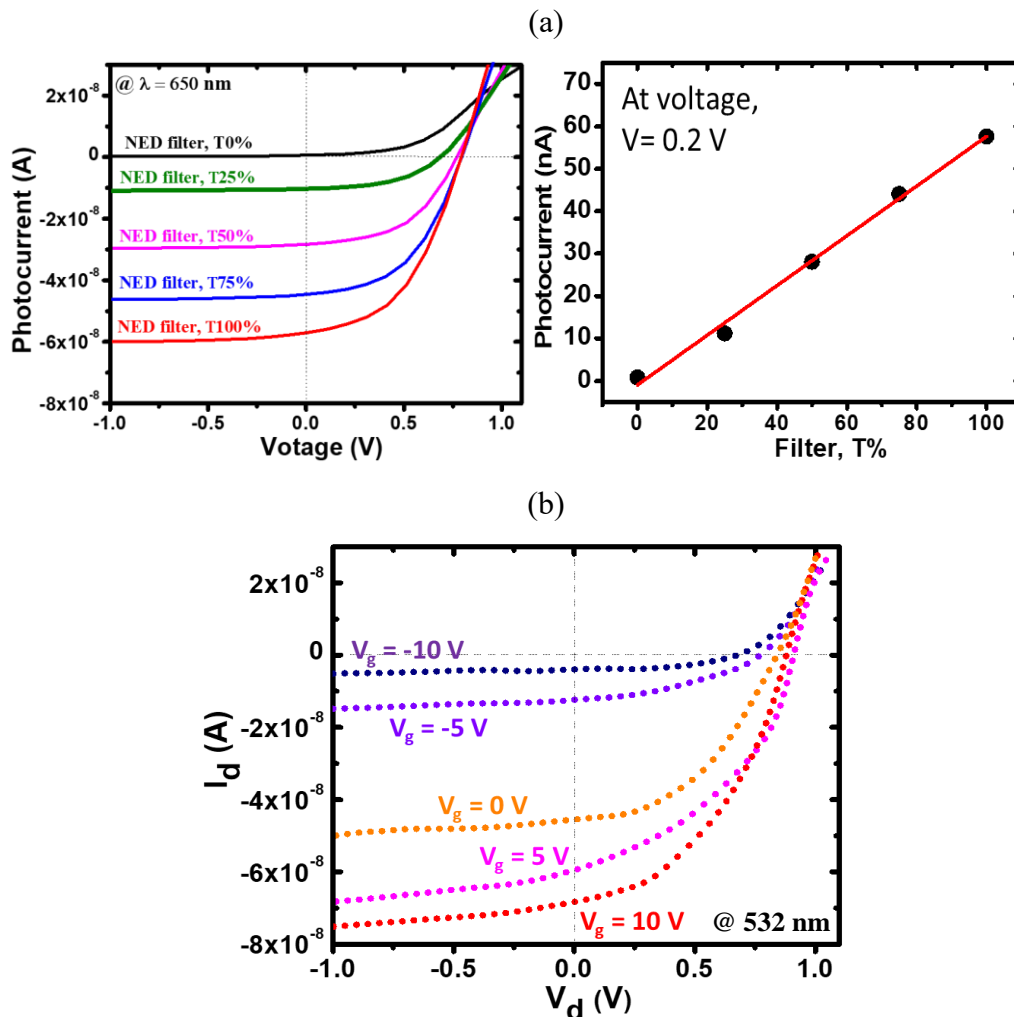


Figure 3.3.11. (a) The I_{ph} - V curves for the well-oxidized lateral p^+ - n junction devices at a different light intensity at no gate bias and photocurrent I_{ph} as a function of light intensity at 650 nm. (a) I_{ph} - V curves of the $\text{WS}_{0.3}\text{Se}_{1.7}/\text{WO}_x$ lateral p^+ - n junction FETs were measured at 532 nm light exposure under different gate bias V_g conditions.

Figure 3.3.12 shows a band diagram and corresponding schematic of $\text{WS}_{0.3}\text{Se}_{1.7}/\text{WO}_x$ lateral p^+-n junction at thermal equilibrium state under illumination. The change of photocurrent with bias voltage can be explained by the change of depletion width in $\text{WS}_{0.3}\text{Se}_{1.7}/\text{WO}_x$ junction with gate bias voltage. When the gate bias V_g increased from zero to positive, the gradient of carrier density between the exposed and un-exposed area increases, consequently, wider the depletion region results in a higher collection of photogenerated e-h pairs. Thus, the higher photocurrent at larger gate bias V_g is observed. The wide depletion width of the un-exposed region is attributed to its lower carrier concentrations compared with those of the exposed region. The tuning of depletion width of laser exposed WSe_2/WO_x lateral junction by gate bias V_g is described in detail elsewhere³⁰.

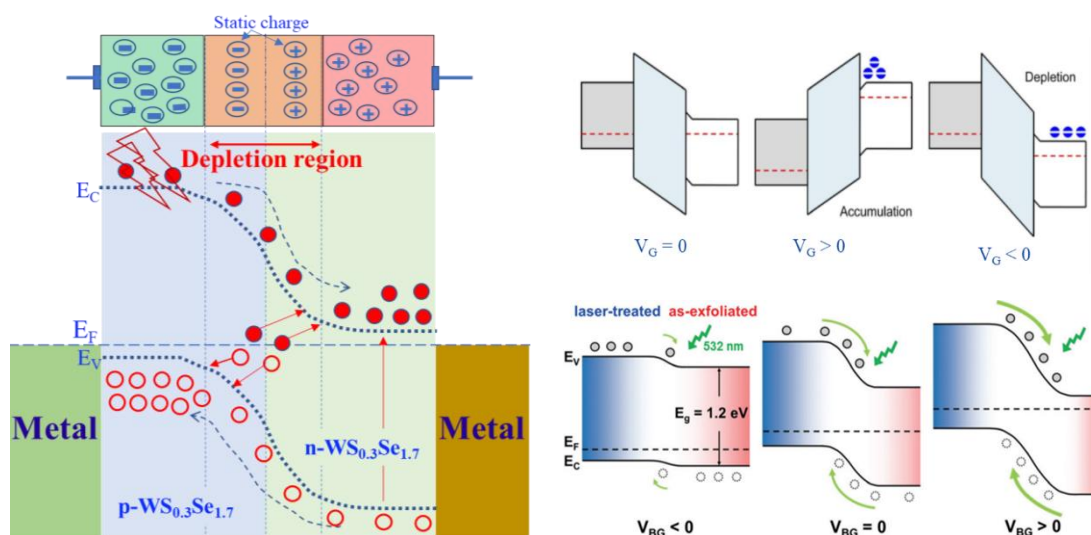


Figure 3.3.12. A band diagram and the schematic of $\text{WS}_{0.3}\text{Se}_{1.7}/\text{WO}_x$ lateral p^+-n junction at thermal equilibrium state under illumination. The change of depletion layer width with gate bias V_g .

Further improvement of the photocurrent I_{sc} is required to obtain the competitive photovoltaic performance. To this aim, metal mirror was inserted as a back reflector. Figure 3.3.13 shows the optical simulation result obtained from spectroscopic ellipsometry simulator at the normal incidence of light on $\text{ATO}/\text{Ag}/\text{Si}$ stacked layers with Ag and ATO thicknesses as variables to obtain a maximum back reflection in the entire UV/visible regions. Here, at the bottom, the extinction coefficient k spectra of ATO/Ag stacked layers using a bulk Ag and ATO. However, an insertion of Ag metal

mirror layer between ATO dielectric and Si substrate, higher reflectance around 95% of incident light observed with 100 nm-ATO and 80 nm thick-Ag layer by systematically simulation. This optimized thickness has been applied for improving the photocurrent.

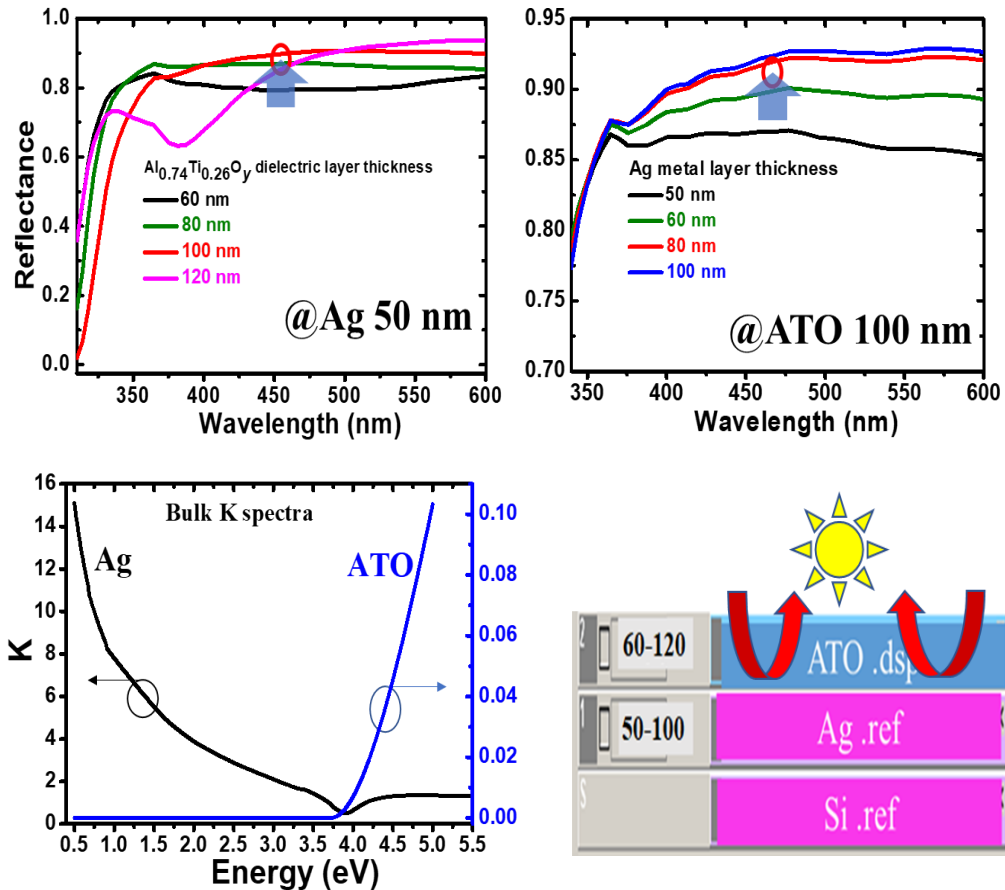
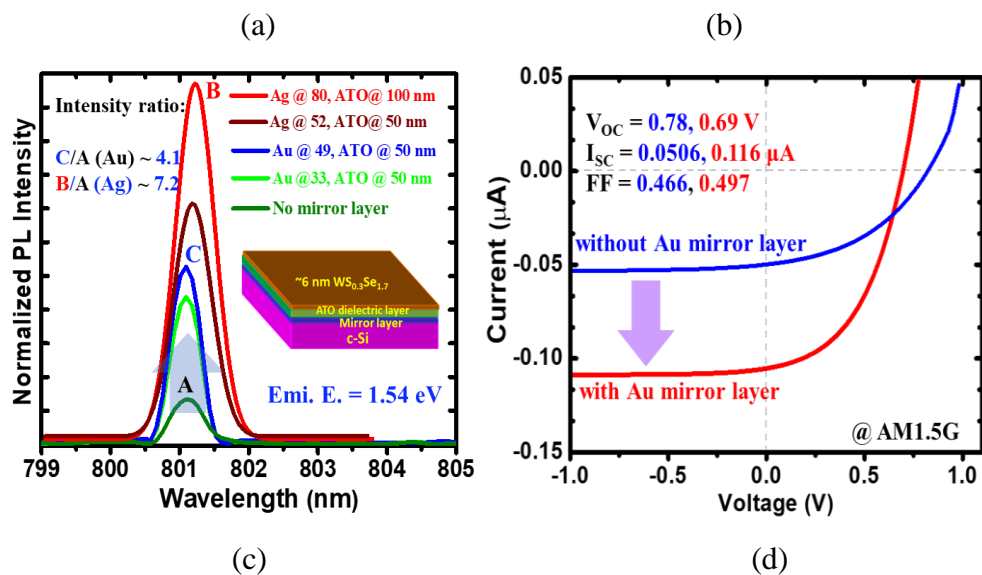


Figure 3.3.13. The simulation of optical reflectance at the normal incidence for the $\text{Al}_{0.74}\text{Ti}_{0.26}\text{O}_y$ (ATO)/Ag/Si stacked structures, the bulk extinction coefficient k-spectra corresponding to the optical absorption of ATO and Ag used in the simulation and its schematic diagram.

Figure 3.3.14a shows the PL spectra of few-layer $\text{WS}_{0.3}\text{Se}_{1.7}$ on a ATO dielectric layer with and without a gold/Ag mirror layer inserted between the dielectric ATO and p-Si substrate. A p-Si substrate with ATO/Au and ATO/Ag mirror layer was used to enhance the absorption of incident light, therefore a further improvement of I_{ph} . The PL intensity for the $\text{WS}_{0.3}\text{Se}_{1.7}/\text{WO}_x$ few-layer on a dielectric/gold mirror and dielectric/Ag mirror increased by 4 and 7 times respectively compared to that was with no mirror. This is owing to the enhanced light absorption in $\text{WS}_{0.3}\text{Se}_{1.7}$ layer. In Figure 3.3.14b, the $I_{\text{ph}}-V$ curve of $\text{WS}_{0.3}\text{Se}_{1.7}/\text{WO}_x$ lateral p^+-n junction fabricated on ATO/Au/p-Si and

ATO/Ag/p-Si in the dark and under simulated solar light exposure of AM1.5G illumination. The I_{ph} increased from 10^{-9} A to a 0.6×10^{-6} A and to a 1.97×10^{-6} A for Au and Ag layer respectively as back reflector due to the enhanced optical absorption. The details of back reflections of incident light in the metal back reflector are described elsewhere^{31,32}. In Figure 3.3.14c shows photocurrent –voltage curves are for the lateral p-n junction composed of $WS_{0.3}Se_{1.7}/WO_x$ at different gate biases under AM1.5 simulated solar light exposure. The I_{sc} increased by 25 times by the use of Ag mirror by gate bias apply. Furthermore, the I_{sc} increased to $2 \mu\text{A}$ using $\sim 50\text{-nm}$ -thick tin-oxide (SnO_2) as an antireflection layer at this stage (Figure 3.3.14c), although optical simulation showed the minimum reflectance in the UV-visible regions at $2\text{-}\mu\text{m}$ -thick SnO_2 layer. In addition, the V_{oc} of 1.34 V was obtained by series connection of two solar cells as preliminary study as shown in Figure 3.3.14d. However, this study releases several opportunities to explore this study including photochromic characteristics, lateral solar cell module, sensor and logic gates and so on. Thus, the photovoltaic properties of few layers $WS_{0.3}Se_{1.7}/WO_x(WS_{0.3}Se_{1.7})$ lateral p⁺-n junction with field-effect transistor structures reveals that I_{sc} of 2×10^{-6} A, V_{oc} of 0.805 V , and FF of 0.48 under AM1.5G simulated solar light exposure. Further, the series connection of two solar cells offers V_{oc} of 1.34 V .



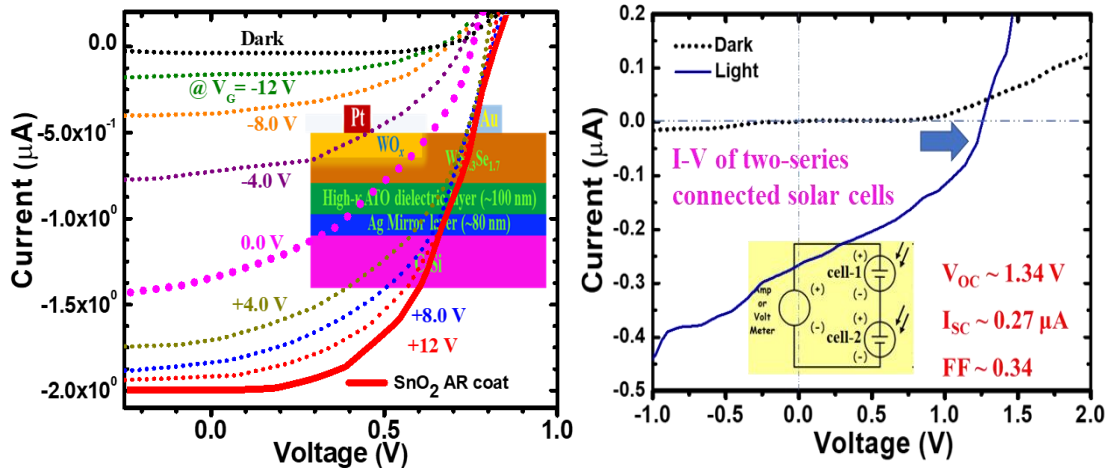


Figure 3.3.14 (a) PL spectra for few-layer $WS_{0.3}Se_{1.7}$ on 40-nm-thick ATO/p-Si with and without inserting gold mirror layer inserted between ATO dielectric layer and p-Si substrate; (b) I_{ph} -V curve in the dark and under simulated AM1.5G illumination solar light exposure for $WS_{0.3}Se_{1.7}/WO_x$ lateral p^+ -n junction device fabricated on ATO/Au/c-Si and (c) ATO/Ag/c-Si substrate; (d) the preliminary result of series connected two solar cells.

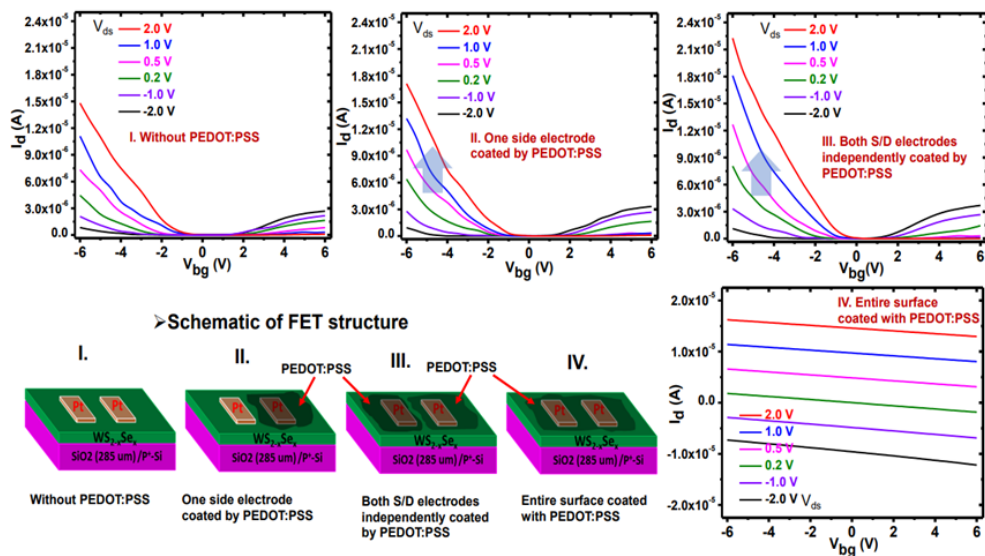
3.3.4 PEDOT:PSS/2D $WS_{0.3}Se_{1.7}/n$ -Si Heterojunction Solar Cells

The junction property at the PEDOT:PSS/n-Si interface and photovoltaic characteristics are explained in terms of p^+ -n junction in the dark and under light exposure using field-effect transistors (FETs) structure. Spin-coated $WS_{0.3}Se_{1.7}$ thin films on th -SiO₂/p⁺-Si substrate was pre-heating on a hot plate at 140 °C for 5 minutes and the selenium vapor was exposed at 600°C for 60 minutes under 50 sccm Ar+H₂ (5%) mixture gas. After that, the Pt source and drain (S/D) electrodes were sputtered on ~4 nm thick $WS_{0.3}Se_{1.7}$ and formed FETs structure. Finally, PEDOT:PSS (w/o ethylene glycol) was coated by drop cast near the S/D electrodes regions on the top of the TMDCs channel as PEDOT:PSS/ $WS_{0.3}Se_{1.7}$.

Figure 3.3.15a shows the transfer characteristics of p- $WS_{0.3}Se_{1.7}$ channel MOSFETs with and without PEDOT:PSS cap layer near one side and both sides at the S/D electrodes at V_{ds} of ± 2 V. The I_{ds} were increased by 1.6 times for PEDOT:PSS coated FETs near both S/D electrodes compare with FETs with no PEDOT:PSS cap layer. Figure 3.3.15b shows the corresponding output characteristics of p- $WS_{0.3}Se_{1.7}$ channel MOSFETs with and without PEDOT:PSS cap layer at V_g of -3 to 5 V. The output

current of I_{ds} was also found 1.5 times for PEDOT:PSS coated FETs. The heavily doped PEDOT:PSS capping layer underneath of metal contact reduced the contact resistance of Pt/ $WS_{0.3}Se_{1.7}$ interface and heavy doping of the channel region in proximity of the Pt contact reduced the Schottky barrier (SB) width, results in the hole injection through the SBs by tunnelling³³, therefore, increased the output current I_{ds} . These findings suggest that the conductive polymer like PEDOT:PSS enables to tune the carrier transport properties of FETs and explore the performance limits of TMDC devices.

(a)



(b)

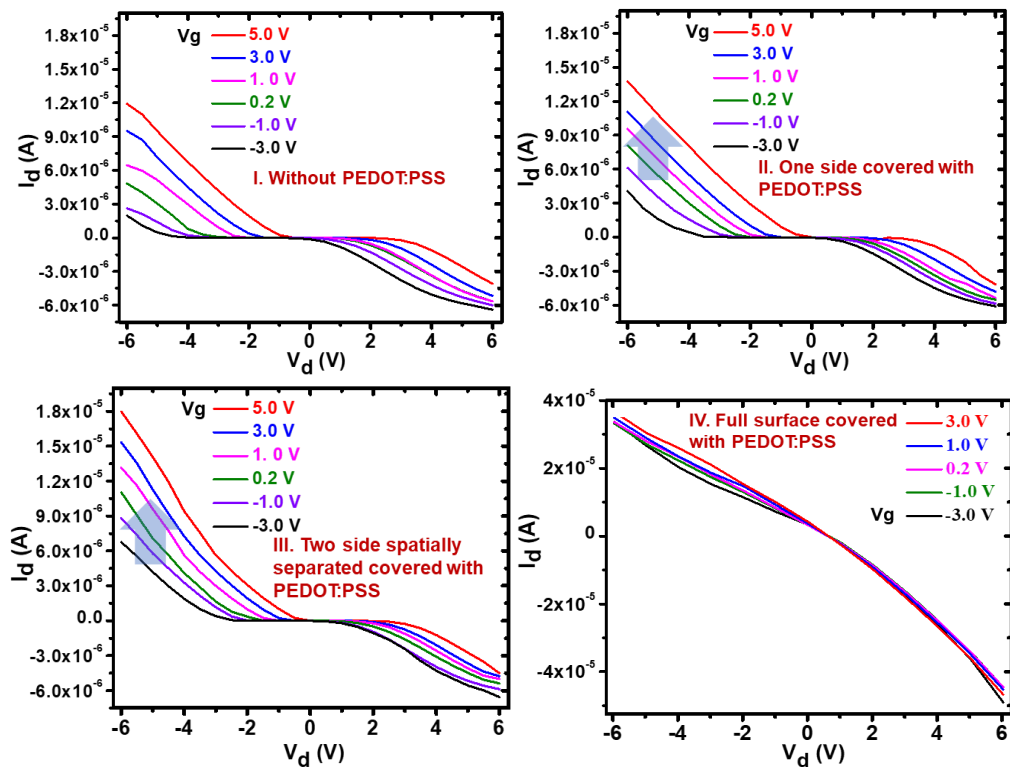


Figure 3.3.15. (a) Transfer and (b) output characteristics of $WS_{0.3}Se_{1.7}$ p-channel MOSFETs with and without PEDOT:PSS cap layer near one side and both sides at the S/D electrodes.

Figure 3.3.16 shows the I-V and EQE curve of PEDOT:PSS/ $WS_{0.3}Se_{1.7}$ p⁺-n junction solar cell with MOSFETs structure in the dark and under AM1.5G simulated solar illumination. A high resistive behavior under dark condition was observed, while the photocurrent I_{ph} of 1.6×10^{-5} A, V_{oc} of 0.613 V, and FF of 0.432 was obtained under AM1.5G solar illumination, while The EQE was found maximum at 700-900 nm. Contact resistance of metal/ $WS_{0.3}Se_{1.7}$ reduced by PEDOT:PSS increased photocurrent J_{sc} and V_{oc} .

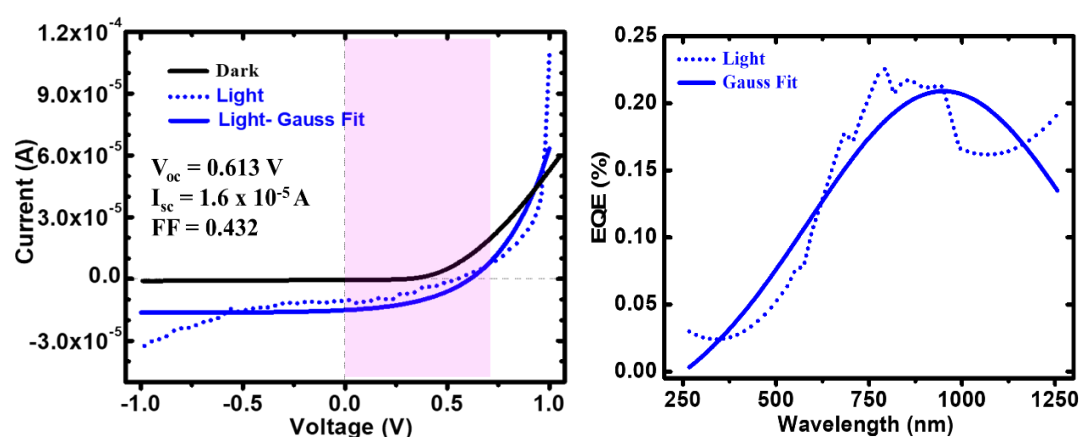


Figure 3.3.16. The I-V curve of PEDOT:PSS/ $WS_{0.3}Se_{1.7}$ lateral p⁺-n junction solar cell fabricated on *th*-SiO₂ (285 nm)/p⁺-Si in the dark and under simulated solar light exposure of AM1.5G illumination.

3.3.5 Growth of few-layer triangle-shape $WS_{0.3}Se_{1.7}$ flakes

Figure 3.3.17a shows AFM images of triangle-shaped $WS_{0.3}Se_{1.7}$ film synthesized at 4000 rpm for 60 s and subsequent Se-exposure at 600 °C for 60 minutes. A precursor of $(NH_4)_2WS_4$ dissolved in complex solvent (0.01 M/L) spin-coated thin film was pre-heated at 140 °C for 5 minutes, and placed on a boat in the three-zone selenization chamber. Ar gas flowed for 10 minutes to clean the chamber and after that, the H₂ gas (10 sccm) flowed only for 12-15 minutes to make H₂ rich environment in the chamber. Then, the Se-vapor was exposed at 600 °C for 60 minutes under a steady flow of Ar+H₂ (5%). The AFM thickness profile of synthesized $WS_{0.3}Se_{1.7}$ film reveals the thickness

of ~ 3.1 nm, which correspond to 3-4 monolayers with a uniform compositional distribution. A Raman peak at ~ 250 cm^{-1} is attributed to the in-plane and out-of-plane vibrations of trigonal phase WSe_2 with the 2nd order WS_2 related signals at 298 cm^{-1} (Figure 3.3.17b). The PL emission energy of $\text{WS}_{0.3}\text{Se}_{1.7}$ films is 1.52 eV with FWHM of ~ 18 nm confirming the film crystallinity. The high concentration of H_2 gas promotes desulfurization and chemical etching effect significantly³⁴. The evolution of pure triangular shape $\text{WS}_{0.3}\text{Se}_{0.7}$ flakes from spin-coated thin films as found in aforementioned studies can be deduced by the preferential substitution of unstable S-sites of WS_x and the stabilization of the Se-substituted S-edge energy in an active Se-atmosphere with a high H_2 content. An energetically adsorption of active Se-atoms on remained W-sites owing to enhanced desulfurization together with the thermal etching, results the formation of triangle-shape uniform $\text{WS}_{0.3}\text{Se}_{1.7}$ flakes with thickness down to 3 nm flakes from 4.0 nm film. These findings explore an effective way for achieving uniform triangle-shape ternary flakes from solution-processed thin films at a high content of H_2 gas in Se-atmosphere. Further, a detail study on the synthesis of triangle-shape large area $\text{WS}_{0.3}\text{Se}_{1.7}$ flakes is required.

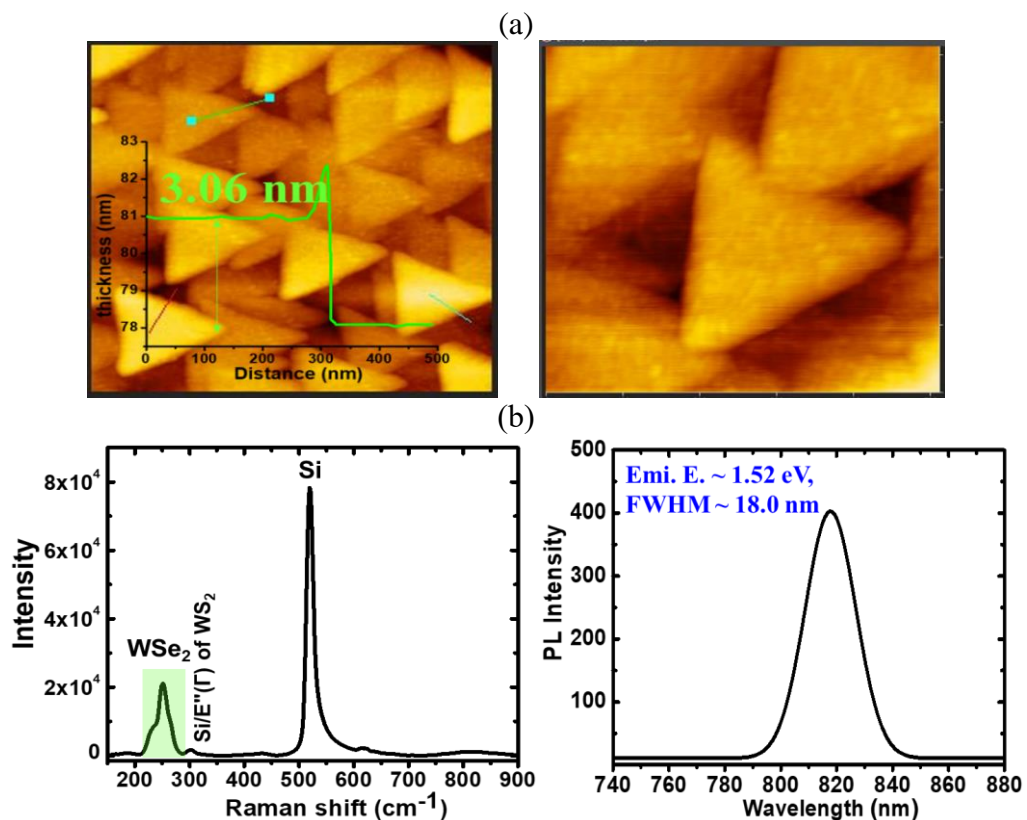
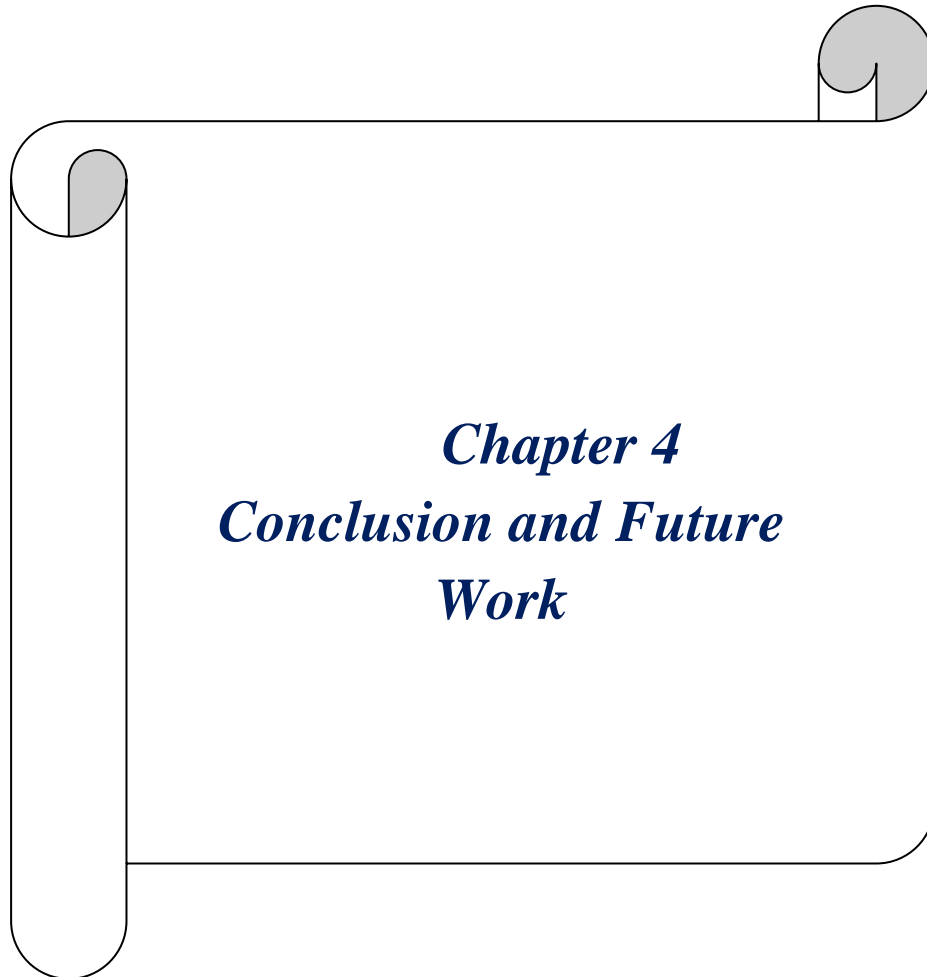


Figure 3.3.17. (a) AFM images of triangle-shape $\text{WS}_{0.3}\text{Se}_{1.7}$ (the inset shows the line profile); (b) Raman spectra and PL spectra of the corresponding $\text{WS}_{0.3}\text{Se}_{1.7}$ samples.

References

1. Kim, J., Higashimine, K., Haga, K. I. & Tokumitsu, E. Fabrication of MoS₂ thin films on oxide-dielectric-covered substrates by chemical solution process. *Phys. Status Solidi Basic Res.* **254**, 1–8 (2017).
2. Gupta, U. *et al.* Characterization of few-layer 1T-MoSe₂ and its superior performance in the visible-light induced hydrogen evolution reaction. *APL Mater.* **2**, (2014).
3. Yang, J. *et al.* Wafer-scale synthesis of thickness-controllable MoS₂ films via solution-processing using a dimethylformamide/n-butylamine/2-aminoethanol solvent system. *Nanoscale* **7**, 9311–9319 (2015).
4. Li, F. *et al.* Anomalous lattice vibrations of CVD-grown monolayer MoS₂ probed using linear polarized excitation light. *Nanoscale* **11**, 13725–30 (2019).
5. Rajib, A. *et al.* Mist chemical vapor deposition of Al_{1-x}Ti_xO_y thin films and their application to a high dielectric material. *J. Appl. Phys.* **131**, 105301 (2022).
6. Chen, J. *et al.* Chemical Vapor Deposition of High-Quality Large-Sized MoS₂ Crystals on Silicon Dioxide Substrates. *Adv. Sci.* **3**, 1600033 (2016).
7. Zhang, X. *et al.* Transition metal dichalcogenides bilayer single crystals by reverse-flow chemical vapor epitaxy. *Nat. Commun.* **10**, 598 (2019).
8. Bergeron, H. *et al.* Chemical vapor deposition of monolayer MoS₂ directly on ultrathin Al₂O₃ for low-power electronics. *Appl. Phys. Lett.* **110**, 053101 (2017).
9. Kim, H. *et al.* MoS₂ field-effect transistors by non-covalent functionalisation. *Nanoscale* **10**, 17557–17566 (2018).
10. Kuddus, A. *et al.* Mist chemical vapor deposition of crystalline MoS₂ atomic layer films using sequential mist supply mode and its application in field-effect transistors. *Nanotechnology* **33**, 045601 (2022).
11. Yokoyama, K., Kuddus, A., Hossain, F. & Shirai, H. Mesh Bias Controlled Synthesis of TiO₂ and Al_{0.74}Ti_{0.26}O₃ Thin Films by Mist Chemical Vapor Deposition and Applications as Gate Dielectric Layers for Field-Effect Transistors. **4**, 5, 2516–2524 (2022)
12. Li, S. Salt-assisted chemical vapor deposition of two-dimensional transition metal dichalcogenides. *iScience* **24**, 103229 (2021).
13. Wu, W. *et al.* High mobility and high on/off ratio field-effect transistors based on chemical vapor deposited single-crystal MoS₂ grains. *Appl. Phys. Lett.* **102**, 142106 (2013).
14. Cui, Y. *et al.* High-Performance Monolayer WS₂ Field-Effect Transistors on High-κ Dielectrics. *Adv. Mater.* **27**, 5230–5234 (2015).
15. Stoeckel, M. A. *et al.* Boosting and Balancing Electron and Hole Mobility in Single- and Bilayer WSe₂ Devices via Tailored Molecular Functionalization. *ACS Nano* **13**, 11613–11622 (2019).
16. Urban, F., Martucciello, N., Peters, L., McEvoy, N. & Di Bartolomeo, A. Environmental effects on the electrical characteristics of back-gated WSe₂

- field-effect transistors. *Nanomaterials* **8**, 901 (2018).
17. Kuddus, A. *et al.* Direct synthesis of submillimeter-sized few-layer WS₂ and WS_{0.3}Se_{1.7} by mist chemical vapor deposition and its application to complementary MOS inverter. *Semicond. Sci. Technol.* **37** 095020, (2022).
 18. Shimura, K. & Yoshida, H. Heterogeneous photocatalytic hydrogen production from water and biomass derivatives. *Energy Environ. Sci.* **4**, 2467–81 (2011).
 19. Zheng, B. *et al.* Band Alignment Engineering in Two-Dimensional Lateral Heterostructures. *J. Am. Chem. Soc.* **140**, 11193–11197 (2018).
 20. Forcherio, G. T. *et al.* Gold nanoparticles physicochemically bonded onto tungsten disulfide nanosheet edges exhibit augmented plasmon damping. *AIP Adv.* **7**, 075103 (2017).
 21. Wang, J. *et al.* Steep Slope p-type 2D WSe₂ Field-Effect Transistors with Van der Waals Contact and Negative Capacitance. *Tech. Dig. - Int. Electron Devices Meet. IEDM18*, 22.3.1-22.3.4 (2019).
 22. Varghese, A. *et al.* WSe₂/ReS₂ vdW heterostructure for versatile optoelectronic applications. *Device Res. Conf. - Conf. Dig. DRC2018*, 9–10 (2018).
 23. Shokouh, S. H. H. *et al.* High-Performance, Air-Stable, Top-Gate, p-Channel WSe₂ Field-Effect Transistor with Fluoropolymer Buffer Layer. *Adv. Funct. Mater.* **25**, 7208–7214 (2015).
 24. Yang, Y. *et al.* Tunable Polarity Behavior and High-Performance Photosensitive Characteristics in Schottky-Barrier Field-Effect Transistors Based on Multilayer WS₂. *ACS Appl. Mater. Interfaces* **10**, 2745–2751 (2018).
 25. Cho, A. J., Park, K. C. & Kwon, J. Y. A high-performance complementary inverter based on transition metal dichalcogenide field-effect transistors. *Nanoscale Res. Lett.* **10**, 1–6 (2015).
 26. Liu, X. *et al.* P-Type Polar Transition of Chemically Doped Multilayer MoS₂ Transistor. *Adv. Mater.* **28**, 2345–2351 (2016).
 27. Liu, E. *et al.* Integrated digital inverters based on two-dimensional anisotropic ReS₂ field-effect transistors. *Nat. Commun.* **6**, 1–7 (2015).
 28. Du, W. *et al.* Low-power-consumption CMOS inverter array based on CVD-grown p-MoTe₂ and n-MoS₂. *iScience* **24**, 0–9 (2021).
 29. Lin, Y. F. *et al.* Ambipolar MoTe₂ transistors and their applications in logic circuits. *Adv. Mater.* **26**, 3263–3269 (2014).
 30. Yang, S. *et al.* An in-plane WSe₂ p-n homojunction two-dimensional diode by laser-induced doping. *J. Mater. Chem. C* **8**, 8393–8398 (2020).
 31. Xu, H. Enhanced light-matter interaction of a MoS₂ monolayer with a gold mirror layer. *RSC Adv.* **7**, 23109–23113 (2017).
 32. Huang, X. *et al.* Fabry-Perot cavity enhanced light-matter interactions in two-dimensional van der Waals heterostructure. *Nano Energy* **62**, 667–673 (2019).
 33. Mahmut, T. *et al.* High-Gain Inverters Based on WSe₂ Complementary Field-Effect Transistors. *ACS Nano* **8**, 4948–4953 (2019).
 34. Xiao, L. *et al.* Role of hydrogen in chemical vapor deposition growth of MoS₂ atomic layers. *Nanoscale* **7**, 8398-8404 (2015).



Chapter 4
Conclusion and Future
Work

Chapter 4: Summary and future work

4.1 Summary of Results

- ❖ Submillimeter-size few-layer MoS₂, WS₂ and WS_{0.3}Se_{1.7} were obtained by mist CVD on high- κ a-Al_{0.74}Ti_{0.26}O_y/P⁺-Si by adjusting the deposition condition.
- ❖ The n-type characteristics of MoS₂ channel MOSFET.
- ❖ CMOS logic circuit cascading the n-WS₂ FET and p- WS_{0.3}Se_{1.7} channel FETs on ~ 45 nm- high- κ Al_{0.74}Ti_{0.26}O_y/P⁺-Si obtained.
- ❖ Ambipolar to a p-type unipolar characteristic in FETs by O₂/He plasma and laser irradiation with different wavelengths obtained.
- ❖ Improved photovoltaic effect in WS_{0.3}Se_{1.7}/WO_x(WS_{0.3}Se_{1.7}) lateral p⁺-n junction with well-oxidized high-affinity WO_x layers.
- ❖ Increased photocurrent I_{ph} in WS_{0.3}Se_{1.7}/WO_x(WS_{0.3}Se_{1.7}) solar cell owing to the improved optical absorption by silver mirror as back reflector.

4.2 Future Works

The synthesis of submillimeter-size few-layer TMDCs of MoS₂, WS₂, and WS_{0.3}Se_{1.7} and their application in electronic and photovoltaic devices lead to the following future issues:

- Direct synthesis of wafer-scale TMDCs films using mist CVD and their applications in cascaded integrated circuit photosensor, photodiode and photovoltaic devices.
- Photochromic and superconductive behaviors of mist CVD TMDCs films.
- Surface, interface and phase engineering of atomic layer mist CVD TMDCs films and their hetero/homo junction.
- Van der Waals/lateral junction properties of mist CVD TMDCs.
- Anti-reflection (AR) and mirror layer to improve the photocurrent I_{ph}.
- Multiple stacked p⁺-n junction solar cells-based module.